LINEAR RESPONSE DENSITY FUNCTIONAL THEORY FOR METAL SURFACES WITH APPLICATION TO SECOND HARMONIC GENERATION

By

Justin Droba

A DISSERTATION

Submitted to
Michigan State University
in partial fulfillment of the requirements
for the degree of

Applied Mathematics – Doctor of Philosophy

2014

ABSTRACT

By

Justin Droba

This thesis is a study of electronic excitations at metal surfaces, as described within the context of density functional theory (DFT). Before presenting any physics, the document develops an adaptive spline collocation method that is the workhorse for most of the numerical computations presented afterwards. The background and mathematical foundations of DFT are briefly explored. From there, two different techniques for computing ground state densities—orbital-free density functional theory and Kohn-Sham density functional theory—are fully realized. Development of algorithms for numerical computation is the primary component of the presentation, but both techniques are also given rigorous theoretical treatment in full proofs of asymptotic results. What follows next is a rigorous derivation of linear response theory from first principles. Great effort is then spent to develop a scheme for numerical computation of excited responses via linear response theory. Finally, the thesis concludes by demonstrating the application of the techniques developed in the previous chapters to a nonlinear optical phenomenon called second harmonic generation.

To my parents,
who have been with me since the beginning.
To my wife Yuqi,
who will be with me until the end.

ACKNOWLEDGMENTS

It is said that it takes a village to raise a child. I suppose the academic analog is that it takes a department to produce a PhD. Perhaps a whole department is a bit of an exaggeration, but I certainly would not have been able to reach this end without the selfless contributions of so many different people.

First and foremost, I must thank my parents, who have supported me financially and emotionally for the entirety of my long academic career. As far back as I can remember, they constantly inspired me to push myself to levels I thought attainable only by others and willingly sacrificed luxury to give me the finest education possible. It is certainly no exaggeration to say that without their love, support, and frienship, I never would have even come to Michigan State University to pursue my PhD, let alone complete it.

Had I not come to Michigan State, I never would have met my wife Yuqi. It is hard to fathom the odds defied in two people coming from two places so far apart, meeting in the insignificant town in the middle of Michigan, and discovering perfection in each other. When I reached my lowest points, when it seemed all hope was lost and I was on the verge of breaking, it was she who gave me the strength to perservere. Without her providing something greater for which to strive, I fear I would given up before reaching the end.

My greatest academic thanks goes to Prof. Gang Bao, who served as my advisor for four years. His generous support of research assistantships semester after semester allowed me to pursue research without distraction and freed up time to chase other academic ventures that greatly enriched my graduate experience. On top of that, he arranged for three visits to China, including a multiweek stay at Zhejiang University.

The man with the second greatest impact on my research is Prof. Hiroshi Ajiki. My project had stalled out before I arrived under his care at the Photon Pioneers Center at Osaka Unversity in June 2012. His guidence and tutelage revitalized my research and set me on a path to achievement. The trip would not have been possible without the East Asia and Pacific Summer Institutes (EAPSI) fellowship program and the sponsoring agencies, the National Science Foundation (NSF) and Japan Society for the Promotion of Science (JSPS), who provided the tremendous funds that paid for my twelve-week stay in Japan. A special thanks goes to Prof. Di Liu, who provided valuable suggestions that ultimately led to a successful proposal.

I would like to express my gratitude to my other professors at Michigan State, in particular Jeffrey Schenker and Keith Promislow, for keeping their doors open and allowing me to pick their brains when I was stuck on my research. I thank Andrew Christlieb, Jianliang Qian, and Casim Abbas for their service on my committee. I am greatful to Prof. Aklilu Zeleke for his continued friendship and for retaining me as mentor

for the REU for four summers, even when my travels limited my ability to participate fully. I would also like to acknowledge Professors Neepa Maitra and Ansgar Liebsch, who had no reason to take the time to answer the silly questions of a nagging graduate student far removed from their circles—but chose to do so anyway.

My journey through graduate school would not have been nearly as enjoyable without the good company that continuously surrounded me, sharing in the good moments and providing advice and emotional support in the bad. I would especially like to acknowledge my friends, who each contributed in a unique way:

- Eric Wolf, for reading my proposals and fellowship applications and providing suggestions that helped them to success, for always being willing to take time away from his own work to provide some thinking points when I was stuck on a problem, and for in so many ways being the best friend I've ever had.
- Kazuko Fuchi, without whose Japanese help my initial emails to Prof. Ajiki may have gone ignored.
- Jackie Dresch and Richard Shadrach, for being such amicable officemates for my first four years.
- Adam Giambrone and Faramarz Vafaee, my next-door neighbors after our move to the fifth floor, for always being ready and able to serve as a most welcome diversion from work.
- Luke Williams, for so many engaging philosophical conversations over lunches at Charlie Kang's.
- The alumni students and postdocs of Prof. Bao's group not already mentioned: Guanghui Hu, Xianliang Hu, Jun Lai, Peijun Li, Junshan Lin, Songting Luo, Russell Richins, Yuliang Wang, Xiang Xu, Zhengfu Xu, Hai Zhang, and Xinghui Zhong. I hope our paths will cross again one day.
- Jaylan Jones, who provided me with the light of hope in one of my darkest moments.

July 1, 2014

TABLE OF CONTENTS

LIST OF TABLES

LIST OF FIGURES

LIST OF ALGORITHMS

KEY TO ABBREVIATIONS AND SYMBOLS

Symbol	Meaning	Detailed in
BVP	Boundary value problem	Chapter 2
DFT	Density functional theory	Chapter 3
i.s.d	In the sense of distributions	Section 1.3
KS-DFT	Kohn-Sham density functional theory	Chapter 5
LDA	Local density approximation	Section 3.4.1
LRT	Linear response theory	Section 7.1.2
ODE	Ordinary differential equation	Chapter 2
OF-DFT	Orbital-free density functional theory	Chapter 4
SCF	Self-consistent field iteration	Section 5.6
SHG	Second harmonic generation	Chapter 8
TD-DFT	Time-dependent density functional theory	Section 7.1
TFDW	Thomas-Fermi-Dirac-von Weizsäcker	Section 4.2
$\mathbb{R}^d$	Set of d-tuples of real numbers	Standard
$\mathbb{N}$	Set of natural numbers	Standard
$\mathbb{C}$	Set of complex numbers	Standard
$i\mathbb{R}$	Set of purely imaginary numbers	Standard
$C^k(A)$	Set of k-times continuously differentiable functions on A	Standard
$C_0(A)$	Set of functions that vanish at infinity	Standard
$C_c^\infty(A)$	Set of infinitely-differentiable and compactly-supported functions	Standard
$L^p(A)$	For $1 \leq p < \infty$, the set of p-integrable functions on A	Standard
$L^p_{\mathrm{loc}}(A)$	The set of functions in $L^p(K)$ for each compact subset $K \subseteq A$	Standard
$L^\infty(A)$	The set of essentially bounded functions on A	Standard
$H^k(A)$	The set of L^2 functions with weak derivatives up to and including order k in $L^2(A)$	Standard
α_k	Coefficient of right asymptotic behavior of ψ_k	Section 5.3.1
γ_k	Phase shift of left asymptotic behavior of ψ_k	Section 5.3.2
ΔV	Surface barrier potential	Equation (5.3)
$\delta(\mathbf{x})$	Dirac delta distribution	Section 1.3
$\varepsilon(\omega)$	Dielectric constant	Equation (7.47)

$\varepsilon_{\mathbf{k}}, \varepsilon_k$	Energy of Kohn-Sham orbital corr. to momentum $\mathbf{k}$ or k	Equation (5.11)
$\epsilon_{\mathrm{c}}(n)$	Correlation kernel for local density approximation	Section 3.4.1
$\epsilon_{\mathbf{x}}(n)$	Exchange kernel for homogeneous electron gas	Equation (3.23)
$\epsilon_{\mathrm{xc}}(n)$	Exchange-correlation kernel under LDA	Section 3.4.1
η	Positive infinitesimal	End of Section 6.2.4
$\Theta(x)$	Unit step function	Section 1.3
θ	Polar angle (angle with respect to surface normal)	Figure 8.5
λ	Chapter 4: strength of von-Weizsäcker gradient correction	Equation (4.3)
	Chapter 5: strength of cut-off filter	Equation (5.35)
	Chapter 7: free parameter for Poisson integral equation	Theorem 7.3
λ_k	Exponent of right asymptotic behavior of ψ_k	Section 5.3.1
μ	Exponent of left asymptotic behavior of φ_1, φ_2	Equation (6.3)
$\mu_k^{\pm}$	Exponent of left asymptotic behavior of $\varphi_i(\cdot; \varepsilon_k \pm \omega)$	Section 7.4.1
ν	Exponent of right asymptotic behavior of φ_1, φ_2	Equation (6.4)
$\xi_1(x;\omega)$	Driving function for n_1 integral equation	Equation (7.56)
$\xi_2(x;\omega)$	Additional driving function for n_1 integral equation	Equation (7.71)
$\sigma(\omega)$	Zeroth moment of first-order density n_1	Equation (7.46)
$\sigma(\mathcal{A})$	Spectrum of the operator $\mathcal{A}$	Section 6.2.2
$\sigma_{\mathrm{ess}}(\mathcal{A})$	Essential spectrum of the operator $\mathcal{A}$	Section 6.2.2
$\sigma_{\mathrm{pt}}(\mathcal{A})$	Point spectrum of the operator $\mathcal{A}$	Section 6.2.2
ς	Boundary condition for electrostatic potential	Equation (5.27)
τ_a	Tolerance for adaptive spline method	Algorithm 2.3
τ_{sc}	Tolerance for SCF convergence	Algorithm 5.1
υ	Chemical exchange potential and Lagrange multiplier	Equation (4.7)
Φ_W	Work function	Equation (5.4)
$\phi(x)$	Electrostatic potential for ground state density	Equation (3.14)
$\phi_1(x;\omega)$	Quasi-electrostatic potential of linear response density	Equation (7.52)
$\phi_{\mathrm{est}}(x;\omega)$	Electrostatic potential for linear response density	Equation (7.19)
$\phi_{\mathrm{ext}}(x;\omega)$	Linear response external potential	Equation (7.20)
$\phi_{\mathrm{xc}}(x;\omega)$	Linear response exchange-correlation under ALDA	Equation (7.21)
ϕ	Spherical angle (angle with respect to plane of incidence)	Figure 8.5
$\varphi_1(x), \varphi_2(x)$	Basis functions for Green's function $G(x, y; \varepsilon)$	Equation (6.5)
$\chi_1(\mathbf{x}, \mathbf{y}, \omega)$	Linear response function	Section 7.2

$\Psi(\mathbf{x})$	Many-body wavefunction	Equation 3.1
$\psi_{\mathbf{k}}(x), \psi_k(x)$	Kohn-Sham wavefunction corr. to energy $\varepsilon_{\mathbf{k}}$, ε_k, resp.	Equation (5.10)
ω	Angular frequency (incident laser or Fourier domain)	Section 7.3
ω_p	Plasmon frequency	Equation (7.48)
$a(\omega)$	Parameter that determines second harmonic intensity	Equation (8.9)
A_p	Amplitude of contribution to SHG from p-polarization	Equation (8.7)
A_s	Amplitude of contribution to SHG from s-polarization	Equation (8.8)
$\mathbf{B}(\mathbf{x}, \omega)$	Time-harmonic magnetic induction	Section 8.1
$\mathcal{B}^{\pm}(x, k; \omega)$	Bulk contribution to ξ_1 corr. to $G(\cdot, \cdot; \varepsilon_k \pm \omega)$	Section 7.4
c	Chapter 5: location of cut-off filter	Equation (5.34)
	Outside Chapter 5: speed of light	Section 1.1
$\mathbf{D}(\mathbf{x}, \omega)$	Time-harmonic electric displacement	Section 8.1
D	Surface dipole barrier	Equation (5.2)
$d_{\perp}(\omega)$	Effective surface location of normal comp. of $\mathbf{E}$	Equation (7.50)
$\mathbf{E}(\mathbf{x}, \omega)$	Time-harmonic electric field	Section 8.1
$\mathcal{E}_0$	Magnitude of $\mathbf{E}_{\text{ext}}$	Equation (7.44)
E_F	Fermi energy	Equation (5.1)
$E_{\text{H}}[n]$	Energy functional corr. to Hartree interaction	Equation (3.9)
$\mathbf{E}_{\text{ext}}(\cdot)$	Electric field due to external potential	Equation (7.44)
$E_{\text{xc}}[n]$	Energy functional corr. to exchange-correlation	Sections 3.3 & 3.4
$\hat{f}(\xi)$	Ordinary Fourier transform of f	Section 1.3
$\mathcal{F}\{f\}(\xi)$	Same as $\hat{f}$ above	Section 1.3
$\mathfrak{F}\{f\}(\omega)$	Special non-unitary angular Fourier transform of f	Section 1.3
$F(\varepsilon)$	Fermi-Dirac distribution	Equations (5.5) & (5.6)
$F_c(x)$	Cut-off filter for density splitting	Equation (5.35)
$f_k, f_{\mathbf{k}}$	Fermi-Dirac occupation factor corr. to k, $\mathbf{k}$, resp.	End of Section 7.2.2
$f_{\text{xc}}(\mathbf{x})$	Derivative in n of V_{xc}	Equation (3.31)
$G(x, y; \varepsilon)$	Green's function for Schrödinger operator $\mathcal{H} - \varepsilon$	Equation (6.6)
$G_{\mathcal{L}}(\mathbf{x} - \mathbf{y})$	Green's function for Laplace operator $\mathcal{L}$	Sections 3.3 & 7.1
$g_{\text{xc}}(\mathbf{x})$	Second derivative in n of V_{xc}	Equation (3.33)
$\mathbf{H}(\mathbf{x}, \omega)$	Time-harmonic magnetic field	Section 8.1
k_F	Fermi wavevector	Section 5.1.1
$\mathcal{H}$	Hamiltonian of Kohn-Sham Schrödinger operator	Equation (6.1)

$\mathcal{I}_1(x;\varepsilon)$	Helper integral used in computing ξ_1 and ξ_2	Equation (7.64)
$\mathcal{I}_2(x;\varepsilon)$	Helper integral used in computing ξ_1 and ξ_2	Equation (7.65)
I_ω	Intensity of fundamental-frequency radiation	Section 8.3
$I_{2\omega}$	Intensity of second-harmonic radiation	Section 8.3
$\mathbf{J}(\mathbf{x},\omega)$	Time-harmonic current	Section 8.1
$\mathcal{L}$	Laplace operator scaled by $1/4\pi$ (except in Chapter 6)	Section 7.1
$\mathfrak{n}(\mathbf{x})$	Density operator (time-independent)	Equation (7.26)
$\mathfrak{n}(\mathbf{x},t)$	Density operator in Heisenberg picture	Equation (7.25)
$n_0(\mathbf{x})$	Ground state density	Chapter 3
$n_1(x;\omega)$	Linear response density	Section 7.3
$n_2(x;\omega)$	Nonlinear response density	Section 8.2.1
$n_+(x)$	Positive background charge in jellium system	Equation (4.1)
$n_\sigma(x)$	Screened density	Section 5.8
$n_{\mathrm{ind}}(x)$	Induced portion of ground state density	Equation (5.31)
$n_{\mathrm{qu}}(x)$	Quantum contribution to ground state density	Equation (5.37)
$\bar{n}$	Average electron density	Section 3.4.2
R_1	Left endpoint (as $-R_1$) of computational domain	Section 7.4
R_2	Right endpoint of computational domain	Section 7.4
r_s	Wigner-Seitz radius	Section 3.4.2
$\mathcal{S}^{\pm}(x,k;\omega)$	Surface contribution to ξ_1 corr. to $G(x,y;\varepsilon_k \pm \omega)$	Section 7.4
$\mathrm{sgn}(x)$	Sign (signum) function	Section 1.3
$T[n]$	True kinetic energy functional (interacting system)	Section 3.3
$T_s[n]$	Kinetic energy functional for noninteracting system	Section 3.3
$V(\mathbf{x})$	Kohn-Sham potential for self-contained system	Equation (3.15)
$V_{\mathrm{eff}}(\mathbf{x})$	Kohn-Sham potential (general)	Equation (3.11)
$V_{\mathrm{xc}}(\mathbf{x})$	LDA exchange-correlation potential (Perdew-Wang)	Equation (3.30)
W	Wronskian of Green's basis functions φ_1 and φ_2	Equation (6.9)
$\tilde{\mathbf{x}}$	Component of $\mathbf{x}$ parallel to the surface	Section 5.2

Chapter 1

Introduction

The project detailed in this dissertation originated when the author was charged with a very simple-sounding task by his advisor: investigate modeling and computation for second harmonic generation at metal/dielectric interfaces. In the course of his preliminary literature review, the author encountered a six-page paper on the application of density functional theory (DFT) to the phenomenon by Weber and Liebsch [113]. Dissatisfied with the conventional techniques, the author was intrigued by seemingly simpler and more flexible framework DFT offered. However, as the length of this document testifies, the DFT approach is anything but simple.

The original motivation for this work, second harmonic generation, does not make an appearance until nearly one hundred forty pages in. As time progressed, the purpose of the research behind this dissertation gradually shifted from attempting to describe a single phenomenon to becoming a comprehensive study in electronic excitations at metal surfaces, as described within the context of DFT. The subject of electronic excitations is rather broad and can be used to describe a host of physical phenomena, such as surface plasmons, van der Waals attraction, and nonlocal optics. Such applications are not the focus of this dissertation and second harmonic generation is offered as merely a novel demonstration of the techniques developed herein.

Trained as a mathematician and an engineer but never a physicist, the author undertook this project with no previous familiarity with the background material. Therefore, a foremost goal of this dissertation is self-containment. The author's intent is that a mathematically advanced reader lacking knowledge of DFT and solid state physics can acquire all the knowledge necessary to understand the document from within it.

There are two separate yet intertwined primary goals of this dissertation:

1. **Theoretical:** To present complete and rigorous derivations of all the fundamental equations and expressions used in the study. Too often, works of physics assert the validity of "mystery equations" as

though they were gospel. A major effort of this thesis has been to rigorize important concepts. While this endeavor is likely of more interest to mathematicians—and this is a thesis of *mathematics*—it serves the physics community by preserving the mathematical justification of critical quantities.

2. **Computational:** To develop fundamentally sound methods of numerical computation for the processes described in the theory sections and to implement them in redistributable, easy-to-use codes.

This thesis is divided into the following chapters:

- Chapter 2 details the adaptive spline collocation method for solving ordinary differential equations and boundary value problems. The method is the workhorse for most of the computations in this thesis, the only exception being the integral equations of Chapter 7.
- Chapter 3 is a background chapter that lays the theoretical foundations of DFT. In many ways, it is the true "introductory chapter," at least as the term is commonly applied to research publications. It introduces and analyzes the behavior of the Perdew-Wang correlation kernel that is used throughout the thesis. No computations are performed in this chapter. A true expert both on DFT and solid state physics will find little new information here, but the discussion on the Wigner-Seitz radius in Section 3.4.2 is critical to the understanding of this thesis for those familiar with only DFT.
- Chapter 4 first introduces the jellium model in which all computations are framed. A technique known as orbital-free density functional theory is detailed. The end of the chapter contains sample computations and the first of many uses the adaptive spline method of Chapter 2 in the thesis. The biggest contributions of the chapter are the asymptotic results contained in Section 4.4.
- Chapter 5 opens with additional solid state physics background needed to formulate Kohn-Sham density functional theory for jellium surfaces. Derivation of the Kohn-Sham system and boundary conditions is done from first principles. The proof of Theorem 5.2 may be considered the most substantial theoretical result of the thesis. The electrostatic potential for semi-infinite jellium systems is notoriously difficult to compute numerically. Section 5.5 details an algorithm that overcomes these issues due to long-range Coulomb interaction. A full self-consistent field iteration is then formulated with this fix. The last section before the Conclusion contains a myriad of numerical results generated by the aforementioned iteration process in conjunction with the adaptive spline method.
- Chapter 6 is the most mathematical chapter. The beginning section concerns the Green's function for the Kohn-Sham Schrödinger opertor. The remainder is comprised almost entirely of theorems and proofs for the spectrum of the operator, which culminates in a spectral representation for the Green's function. The representation is essential to a derivation in the following chapter.

- Chapter 7 is the longest, most technical, and most difficult chapter of the entire thesis. It begins with a complete rigorous derivation of linear response theory and the linear response function for jellium surfaces. The lengthy demonstration is not found in a single published work and is therefore a valuable compilation and rigorization of widely used results. A numerical scheme based on the adaptive spline method for computing the linear response is then introduced. The analytic computations of Section 7.4 have never been demonstrated before and represent a landmark advancement in efficiency and simplicity for such calculations. Finally, the chapter concludes with numerical results for linear response densities.
- Chapter 8 wraps up the thesis with a presentation of a tangible application of the results of the preceeding chapters. The application is second harmonic generation, a simple process in nonlinear optics. The chapter briefly discusses the history of the discovery of the process, as well as an overview of classical modeling techniques before demonstrating how DFT can be used to characterize it.

The remainder of this introductory chapter is dedicated to explicating the conventions and notation used throughout the document. The author has spent considerable time and effort ensuring that notation is clear, free of contradictions, and consistent with standard symbology whenever possible. The comprehensive list on the preceeding pages serves as not only a legend of symbols but also an index of concepts for the document.

1.1 Atomic Units

All computations are done in Hartree atomic units, denoted a.u. In this system, the following four fundamental quantities are taken to have value one:

Symbol	Physical meaning	Value in SI Units
m_e	Mass of electron	9.109383×10^{-31} kg
e	Charge of electron	1.602177×10^{-19} C
$\hbar$	Reduced Planck's constant	1.054572×10^{-34} J·s
ε_0	Permittivity of free space	8.987552×10^{8} $\mathrm{kg \cdot m^3 / s^2 \cdot C^2}$

Table 1.1: Unitary Quantities in Atomic Units. These values are redefined to be 1 in atomic units.

Another important constant is the speed of light c. In atomic units, $c = 137.036$.

While virtually every measurable quantity—including time and force—has a corresponding value in atomic units, of concern to us are only the following:

Dimension	Value in SI Units	Comments
Electric field	5.1422065×10^{11} V/m	One a.u. is strength of field between e^- and nucleus
Energy	4.359744×10^{-18} J	One Hartree, denoted E_h; equal to 27.211396 eV
Frequency	4.134137×10^{16} Hz	Denoted with "a.u." (no unique name)
Intensity	3.509455×10^{20} W/m^2	Measured at peak; also called electric flux density
Length	5.291772×10^{-11} m	One Bohr, denoted a_0

Table 1.2: Important SI Quantities in Atomic Units. This table lists correspondence of 1 a.u. to SI units for quantities that will appear in this thesis.

Aside from energy and length, none of the above has a name in atomic units; the above table gives the value of 1 a.u. in SI units. Otherwise, employment of these units in this thesis will be transparent to the reader.

1.2 Conventions

1.2.1 Asymptotic Behavior

A function ψ is said to *behave asymptotically like* g as $x \to \infty$ and is denoted $\psi \sim g$ if

$$\lim_{x\to\infty} \big(\psi(x) - g(x)\big) = 0$$

1.2.2 Complex Numbers and Conjugation

i always denotes the imaginary unit $i = \sqrt{-1}$. It is never used as an index except for iterations, when it will always appear as superscript (i). Complex conjugation is denoted by a superscipt $*$, so that

$$z = a + bi \Rightarrow z^* = a - bi$$

Hermitian adjoints do not appear in this thesis save for very briefly in Section 6.2.3, so no confusion can occur there. To avoid confusion with the critical parameter $\bar{n}$, we will not use an overbar to indicate conjugation.

1.2.3 Defined Quantities

When quantities are equated by definition, $\triangleq$ is used to indicate the assignment.

1.2.4 Function Notation

Within function notation, semicolons separate independent variables from parameters. In $f(x, y; \omega)$, x and y are the independent variables and ω is an input parameter that determines some properties of f. ω is allowed to be changed but not vary freely: if $f(x, y; \omega) = x + y + \omega^2$, then $f(x, y; 3\omega) = x + y + 9\omega^2$.

1.2.5 Norm, Absolute Value, and Inner Product

When used on a vector quantity, $|\cdot|$ denotes the standard Euclidean norm: $|\mathbf{x}|^2 = \sum x_k^2$. Per physics convention, we will frequently write $\mathbf{x}^2$ for $|\mathbf{x}|^2$. For scalar quantities, it denotes absolute value. The norm of a functional space $\mathscr{H}$ is denoted $\|\cdot\|_{\mathscr{H}}$; if $\mathscr{H}$ is a Hilbert space, its inner product is $\langle \cdot, \cdot \rangle_{\mathscr{H}}$.

1.2.6 Superscripts

In an iterative process, superscripts in parentheses indicate the iteration number from which a quantity comes. For example, if the quantity x is computed via an iterative process, then $x^{(5)}$ refers to the result after five such steps. The same notation is used for derivatives or order higher than three, below which primes are used, but the distinction should be clear from context.

1.2.7 Theorems and Lemmata

A "lemma" refers to a result used to prove another result; they are generally not referenced outside the section in which they appear. A "theorem" signifies a major result; frequently they are recalled multiple times, sometimes many pages after their appearance.

1.2.8 Vector Quantities

As per standard, vector quantities are denoted with boldface type.

1.3 Special Functions

1.3.1 Dirac Delta

$\delta(x)$ denotes the Dirac delta distribution. For $f \in C(\mathbb{R})$,

$$\int_{-\infty}^{+\infty} f(x)\delta(x - a)\, dx = f(a)$$

Likely to accompany usage of δ is the abbreviation "i.s.d," which stands for "in the sense of distributions." Because of its ubiquity in this document, δ never refers to anything else, including the Kronecker delta.

1.3.2 Fourier Transforms

The preferred Fourier transform is the "ordinary Fourier transform":

$$\mathcal{F}\{f\}(\xi) = \hat{f}(\xi) = \int_{-\infty}^{+\infty} f(x)e^{-2\pi i x\xi}\,dx$$

This definition of the Fourier transform is technically valid only for $f \in L^2(\mathbb{R})$ (via limiting argument), but we will often take Fourier transforms as (tempered) distributions for $f \in L^2_{\text{loc}}(\mathbb{R})$. In such a case, the choice of normalization is taken to be the above and the transform is understood to mean the (tempered) distribution $\hat{f}$ that satisfies the Plancherel identity

$$\left\langle \hat{f}, \varphi \right\rangle_{\mathcal{S}(\mathbb{R})} = \left\langle f, \hat{\varphi} \right\rangle_{\mathcal{S}(\mathbb{R})}$$
$$\int_{-\infty}^{+\infty} \hat{f}(x)\varphi(x)\,dx = \int_{-\infty}^{+\infty} f(x)\hat{\varphi}(x)\,dx$$

for all $\varphi \in \mathcal{S}(\mathbb{R})$, the set of Schwarz functions. The integral on the right is understood i.s.d and is more properly integration against a general measure. Fourier transforms of tempered distributions may be differentiated and all convolution formulas and identities hold for tempered distributions.

We will occasionally employ a non-unitary, angular frequency Fourier transform:

$$\mathfrak{F}\{f\}(\omega) = \int_{-\infty}^{+\infty} f(x)e^{i\omega x}\,dx$$

Take careful note of the positive sign in the exponential. This sign is used to be consistent with sign convention of time-harmonic fields. The change in sign has the effect of conjugating transforms of familiar functions, as the quantities we will transform will be real valued. The notation $\hat{f}$ is not used to denote this transform so that there is no confusion with the ordinary transform.

1.3.3 Step and Sign Functions

$\Theta(x)$ denotes the unit step function:

$$\Theta(x) = \begin{cases} 0 & x < 0 \\ 1 & x \geq 0 \end{cases}$$

$\mathrm{sgn}(x)$ denotes the sign (or signum) function:

$$\mathrm{sgn}(x) = \begin{cases} -1 & x < 0 \\ 1 & x \geq 0 \end{cases}$$

The values for both of these functions at $x = 0$ often differ in other sources, but the specific choice of this value is not important in this thesis.

1.4 Dirac Notation

On occasion, mostly notably in Chapters 6 and 7, we employ the Dirac notation commonplace in quantum mechanics. Let $\mathscr{H}$ be a Hilbert space. An element $\psi \in \mathscr{H}$ is called a *ket vector* or just a "ket" and is denoted $|\psi\rangle$. An element of the continuous dual space $\varphi \in \mathscr{H}^*$ is called a *bra vector*, or a "bra," and is denoted $\langle\varphi|$.

By the Riesz Representation Theorem, $\mathscr{H}^*$ is identified with $\mathscr{H}$ up to isometric isomorphism. If $\varphi^* \in \mathscr{H}^*$, then there is an element $\varphi \in \mathscr{H}$ such that

$$\varphi^*(\psi) = \langle \psi, \varphi \rangle_{\mathscr{H}}$$

Therein lies the motivation for Dirac notation: rather than work with elements from the dual space, which are functionals, we may take the inner product with the corresponding element from the main space. The action of the functional described by the bra $\langle\varphi|$ is written $\langle\varphi|\psi\rangle$ and is expressed in standard math notation

$$\langle\varphi|\psi\rangle = \langle \psi, \varphi \rangle_{\mathscr{H}}$$

If $\mathcal{A}$ is an operator on a subspace of $\mathscr{H}$, then the *matrix element* of $\mathcal{A}$ corresponding to φ and ψ is given by

$$\langle\varphi|\mathcal{A}|\psi\rangle = \langle \mathcal{A}\psi, \varphi \rangle_{\mathscr{H}}$$

Dirac notation is intuitive for physicists because it allows them to bypass the heavy mathematical machinery of dual spaces and easily manipulate elements of abstract Hilbert spaces as though they were vectors in $\mathbb{C}^d$. In particular, outer products become incredibly easy to represent and manipulate. Mathematically, the outer product of $\psi \in \mathscr{H}$ and $\varphi \in \mathscr{H}^*$ is the operator $\mathcal{P}_{\varphi,\psi}(\phi) = \langle \phi, \varphi \rangle \psi$. In Dirac notation, this operator is easily represented as $\mathcal{P}_{\varphi,\psi} = |\psi\rangle\langle\varphi|$ so that its action is obtained merely by writing symbols next to each other:

$$\mathcal{P}_{\varphi,\psi}|\phi\rangle = |\psi\rangle\langle\varphi\|\phi\rangle = |\psi\rangle\langle\varphi|\phi\rangle \quad \Longleftrightarrow \quad \mathcal{P}_{\varphi,\psi}(\phi) = \langle \phi, \varphi \rangle \psi$$

If φ_n is a complete orthonormal sequence, then the Fourier series representation of ψ is

$$\psi = \sum_n \langle \psi, \varphi_n \rangle \varphi_n$$

or in Dirac notation

$$\langle \psi | = \sum_n | \varphi_n \rangle \langle \varphi_n | \psi \rangle$$

which allows us to write the identity operator compactly as as

$$\hat{1} = \sum_n | \varphi_n \rangle \langle \varphi_n |$$

The action of the right side is immediately clear just by juxtaposing symbols. This representation is called a *completeness relation*. Mathematics notation does not allow for such an elegant representation if $\mathscr{H} \neq \mathbb{C}^d$. It is perhaps the ease of writing completeness relations that is the most attractive feature of Dirac notation.

To facilitate seemless transition from Dirac notation back to mathematics notation, if $\mathscr{H} = L^2(\mathbb{R}^d)$, then

$$\langle \varphi | \psi \rangle = \int_{\mathbb{R}^d} \varphi^*(\mathbf{x}) \psi(\mathbf{x}) \, d\mathbf{x}$$
$$\langle \varphi | \mathcal{A} | \psi \rangle = \int_{\mathbb{R}^d} \varphi^*(\mathbf{x}) \mathcal{A}\psi(\mathbf{x}) \, d\mathbf{x}$$

Chapter 2

Spline Collocation Method for Differential Equations

Before diving into the main content of this thesis, we open by presenting a method for solving ordinary differential equations that forms the basis for virtually all of the numerical computations of this work.

2.1 Overview

Definition 2.1 (Spline). *Let $a = x_1 < x_2 < \cdots < x_{N+1} = b$ and $S : [a, b] \to \mathbb{R}$ be a piecewise-defined function,*

$$S(x) = \begin{cases} s_1(x) & x_1 \le x < x_2 \\ s_2(x) & x_2 \le x < x_3 \\ \vdots & \vdots \\ s_N(x) & x_N \le x \le x_{N+1} \end{cases}$$

S is called a spline *of degree m if each s_k is a polynomial of degree m and $S \in C^{m-1}[a, b]$.*

While the definition calls S the spline, in a form of terminology overloading, we also refer to the pieces s_k as "splines." Because polynomials are C^∞, the only potential impediments to the global $m - 1$ continuous differentiability of S occur at the transition points x_k, called "nodes" or "knots." In particular, the continuity requirement means that we must have

$$\lim_{x \to x_{k+1}} \frac{\partial^p}{\partial x^p}\Big[s_k(x)\Big] = \lim_{x \to x_{k+1}} \frac{\partial^p}{\partial x^p}\Big[s_{k+1}(x)\Big]$$

for all $0 \le p \le m-1$ and $1 \le k \le N-1$.

Splines are most often used in the context of data interpolation and curve fitting, particularly in image processing, but following the work of Albasiny and Hoskins [1], they can also be used to solve differential equations and boundary value problems. Because an m degree spline can be written in the form

$$s_k(x) = a_m x^m + a_{m-1} x^{m-1} + \cdots + a_1 x + a_0$$

the spline collocation method for differential equations is nothing more than a search for coefficients. When used for curve fitting, the spline interpolates a set of given values. When used for solving differential equations, the spline interpolates the differential equation itself.

The specifics of the method are best explained by illustrative example. Consider the boundary value problem

$$u''(x) = f(x, u(x), u'(x))$$
$$u(a) = \alpha, u(b) = \beta$$

We first discretize the interval $[a, b]$ into the mesh $a = x_1 < x_2 < \cdots < x_N < x_{N+1} = b$, which need **not** be uniformly spaced. For this second-order equation, it is natural to use cubic splines to seek a C^2 solution. Each spline s_k must satisfy the following conditions:

$$\begin{aligned}
\text{DE conditions}: \quad & s_k''(x_k) = f(x_k, s_k(x_k), s_k'(x_k)) && 1 \le k \le N \\
& s_k''(x_{k+1}) = f(x_{k+1}, s_k(x_{k+1}), s_k'(x_{k+1})) && 1 \le k \le N \\
C^0\text{conditions}: \quad & s_k(x_{k+1}) = s_{k+1}(x_{k+1}) && 1 \le k \le N-1 \\
C^1\text{conditions}: \quad & s_k'(x_{k+1}) = s_{k+1}'(x_{k+1}) && 1 \le k \le N-1 \\
\text{Boundary conditions}: \quad & s_1(x_1) = \alpha \\
& s_N(x_{N+1}) = \beta
\end{aligned}$$

There are N splines in total, giving $4N$ total coefficients. The above gives $2N$ DE conditions, $N-1$ C^0 conditions, and $N-1$ C^1 conditions. The two boundary conditions complete the set of $4N$ equations. Figure 2.1 below provides a visual illustration of the placement of the conditions at each node.

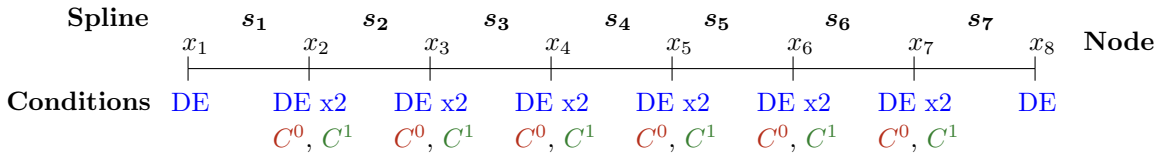

Figure 2.1: Placement of Spline Conditions. Example mesh with $N = 7$ splines. Each interval is labeled with the spline defined (only) there; beneath each node are the conditions that must be satisfied there. Boundary conditions are omitted because these can be placed anywhere.

We note that there is no need to enforce continuity conditions corresponding to the order of the differential equation. Continuing the example, at x_{k+1} the DE conditions

$$s_k''(x_{k+1}) = f(x_{k+1}, s(x_{k+1}), s'(x_{k+1}))$$
$$s_{k+1}''(x_{k+1}) = f(x_{k+1}, s_{k+1}(x_{k+1}), s_{k+1}'(x_{k+1}))$$

imply that $s_k''(x_{k+1}) = s_{k+1}''(x_{k+1})$. Thus, the DE conditions in conjunction with the C^0 and C^1 conditions automatically result in a C^2 solution. For an m^{th} order equation, the DE conditions always result in continuity of the m^{th} derivative, assuming f is continuous. For a quartic solution to this equation, we would need to write C^3 conditions beyond the previously prescribed C^0 and C^1 and the C^2 we get automatically.

The previous paragraph highlights the advantage of choosing polynomials of one degree higher than the order of the differential equation, but it is also possible to seek solutions of higher degree. Doing so results in additional degrees of freedom not covered by just the increased C^m conditions, and requires the invention of additional constraints—for example, additional regularity at endpoints, as is common in ordinary spline interpolation. However, we are always limited by the smoothness of the governing ODE; if f is only continuous, for instance, it would be unwise to seek quartic solutions to $u'' = f(x, u, u')$.

There are three particularly attractive benefits to the spline collation method. The first, and perhaps greatest, boasting point is that the method produces analytic-like solutions that can be evaluated at any point in the computational domain. This thesis will employ the spline method in a heirarchal process, a progression that requires the result from A to compute B, B to compute C, and so on. The spline method allows computation of each step without need to look upward—A can be computed on the best mesh for A without consideration of what will be needed for B yet compatibilty of meshes will still be guaranteed.

Secondly, the representation of the solution as polynomials allows elementary calculus operations to be performed easily and accurately. For instance, the definite integral of a spline S over $[\xi_1, \xi_2] \subset [x_k, x_{k+1}]$ for

some k is able to be computed exactly:

$$\int_{\xi_1}^{\xi_2} S(x)\,dx = \int_{\xi_1}^{\xi_2} s_k(x)\,dx = \sum_{p=1}^{m} a_p^{(k)}\left[\xi_1^p - \xi_2^p\right]$$

Integration over intervals not wholly contained in one of the $[x_k, x_{k+1}]$ are handled by decomposing the integral into a combination of subintervals that are. Of particular interest is the access to accurate derivative information, something most methods for differential equations do not provide. We shall use this ability many times over, most notably in formulating an adaptive version of the method in Section 2.4.

The third benefit is their excellent accuracy, which mirrors the accuracy when splines are used for interpolation, given in a result in Stoer and Bulirsch [103, p.105]:

Theorem 2.1. *Suppose that $g \in C^4[a,b]$ and $\left|g^{(4)}(x)\right| \le L$ for $x \in [a,b]$. Let $a = x_1 < \cdots < x_{N+1} = b$ be a partition of the interval $[a,b]$ and K be a constant such that for $k = 1, 2, \ldots, N$*

$$\frac{h}{x_{k+1} - x_k} \le K$$

$$h = \max_{1 \le k \le N} \left(x_{k+1} - x_k\right)$$

If S is the cubic spline function that interpolates the values of the function g at the knots $x_1, \cdots, x_{N+1}$ and satisfies $S'(x) = g'(x)$ at $x = a, b$, then there exist constants $C_k \le 2$ independent of the partition such that

$$\max_{x \in [a,b]} \left|g^{(m)} - S^{(m)}\right| \le C_k L K \cdot h^{4-m}$$

The corresponding result for the spline method for differential equations is given by Loscalzo and Talbot [70]

Theorem 2.2. *Let u be the true solution to the differential equation*

$$u'' = f(x, u, u')$$

with $f \in C^2$ of all its arguments and S be the cubic spline approximation computed by the spline collocation method. Then

$$\max_{x \in [a,b]} \left|u^{(m)}(x) - S^{(m)}(x)\right| = \mathcal{O}\left(h^{4-m}\right)$$

for $m = 0, 1, 2, 3$. At the nodes x_k, the derivatives $S'''(x_k)$ are to be interpreted as average values of the left

and right limits

$$S'''(x_k) \triangleq \frac{1}{2}\left[\lim_{x\to x_k^-} S'''(x) + \lim_{x\to x_k^+} S'''(x)\right]$$

We have given the accuracy result only for cubic splines; as all differential equations to which we will apply this method are second-order, we will always use cubic splines. Several of the equations we will solve have a discontinuous source term. Navigating the discontinuity will require specialized results and, unfortunately, the bag of tricks is not so deep that enough boundary conditions may be summoned to accomodate high-order splines. Furthermore, as detailed in [70], splines of higher degree can become unstable as $h \to 0$.

2.2 Application to Nonlinear Equations

To improve numerical conditioning, it is better to write the splines in the shifted form

$$s_k(x) = a_k(x - x_k)^3 + b_k(x - x_k)^2 + c_k(x - x_k) + d_k \tag{2.1}$$

for $x \in [x_k, x_{k+1}]$. Another advantage of this form is that evaluation at the node x_k is trivial.

The approach to applying the spline method to nonlinear equations is first to collect all the necessary equations as outlined in Figure 2.1. We assume f to be nonlinear in u and u', so we will need to employ a nonlinear solver. The venerable Newton's Method for systems [103, p.269] is the method of choice. To implement it, we will also need to find the Jacobian matrix of the collection of equations in terms of all the coefficients of all the splines; this will require computing derivatives of each of the equations in a_k, b_k, etc.

We begin with the DE conditions for s_k, which we denote $\mathcal{D}_k^1$ for x_k and $\mathcal{D}_k^2$ at x_{k+1}. (The k on the $\mathcal{D}$ corresponds to the k of s_k, not of the spatial coordinate x.) Let $h_k \triangleq h_{k+1} - h_k$. By (2.1), we have

$$\begin{aligned}
s_k(x_k) &= d_k & s_k(x_{k+1}) &= a_k h_k^3 + b_k h_k^2 + c_k h_k + d_k \\
s_k'(x_k) &= c_k & s_k'(x_{k+1}) &= 3a_k h_k^2 + 2b_k h_k + c_k \\
s_k''(x_k) &= 2b_k & s_k''(x_{k+1}) &= 6a_k h_k + 2b_k
\end{aligned}$$

To help simplify the notation, let $\mathbf{s}_k$ and $\mathbf{s}_{k+1}$ denote the ordered triples

$$\begin{aligned}
\mathbf{s}_k &\triangleq \Big(x_k, s_k(x_k), s_k'(x_k)\Big) &&= \Big(x_k, d_k, c_k\Big) \\
\mathbf{s}_{k+1} &\triangleq \Big(x_{k+1}, s_k(x_{k+1}), s_k'(x_{k+1})\Big) &&= \Big(x_{k+1}, a_k h_k^3 + b_k h_k^2 + c_k h_k + d_k, 3a_k h_k^2 + 2b_k h_k + c_k\Big)
\end{aligned}$$

With this notation, the DE conditions for s_k become

$$\mathcal{D}_k^0 = 2b_k - f(\mathbf{s}_k) \tag{2.2}$$

$$\mathcal{D}_k^1 = 6a_k h_k + 2b_k - f(\mathbf{s}_{k+1}) \tag{2.3}$$

To compute derivatives in the coefficients, it is easiest to use the chain rule

$$\begin{aligned}\frac{\partial f}{\partial a_k} &= \frac{\partial f}{\partial u}\cdot\frac{\partial u}{\partial a_k} + \frac{\partial f}{\partial u'}\cdot\frac{\partial u'}{\partial a_k}\\ &= h_k^3\cdot\frac{\partial f}{\partial u} + 3h_k^2\cdot\frac{\partial f}{\partial u'}\end{aligned}$$

and similarly for b_k, c_k, and d_k. In the above evaluation, we have $s_k = u$ but written partials of f in u to keep the notation cleaner. We can then write

$$\begin{aligned}
\frac{\partial \mathcal{D}_k^0}{\partial a_k} &= 0 & \frac{\partial \mathcal{D}_k^1}{\partial a_k} &= 6h_k - h_k^3\cdot\frac{\partial f}{\partial u}(\mathbf{s}_{k+1}) - 3h_k^2\cdot\frac{\partial f}{\partial u'}(\mathbf{s}_{k+1})\\
\frac{\partial \mathcal{D}_k^0}{\partial b_k} &= 2 & \frac{\partial \mathcal{D}_k^1}{\partial b_k} &= 2h_k - h_k^2\cdot\frac{\partial f}{\partial u}(\mathbf{s}_{k+1}) - 2h_k\cdot\frac{\partial f}{\partial u'}(\mathbf{s}_{k+1})\\
\frac{\partial \mathcal{D}_k^0}{\partial c_k} &= \frac{\partial f}{\partial u'}(\mathbf{s}_k) & \frac{\partial \mathcal{D}_k^1}{\partial c_k} &= -h_k\cdot\frac{\partial f}{\partial u}(\mathbf{s}_{k+1}) - \frac{\partial f}{\partial u'}(\mathbf{s}_{k+1})\\
\frac{\partial \mathcal{D}_k^0}{\partial d_k} &= \frac{\partial f}{\partial u}(\mathbf{s}_k) & \frac{\partial \mathcal{D}_k^1}{\partial d_k} &= -\frac{\partial f}{\partial u}(\mathbf{s}_{k+1})
\end{aligned}$$

It is convenient to use gradient notation, defining $\nabla_{\mathbf{c}_k} = \left[\frac{\partial}{\partial a_k}, \frac{\partial}{\partial b_k}, \frac{\partial}{\partial c_k}, \frac{\partial}{\partial d_k}\right]$. We can write the above derivatives more compactly as

$$\nabla_{\mathbf{c}_k}\mathcal{D}_k^0 = \left[0,2,0,0\right] \quad - \frac{\partial f}{\partial u}(\mathbf{s}_k)\cdot\left[0,0,0,1\right] \qquad - \frac{\partial f}{\partial u'}(\mathbf{s}_k)\cdot\left[0,0,1,0\right] \tag{2.4}$$

$$\nabla_{\mathbf{c}_k}\mathcal{D}_k^1 = \left[6h_k,2,0,0\right] - \frac{\partial f}{\partial u}(\mathbf{s}_{k+1})\cdot\left[h_k^3,h_k^2,h_k,1\right] - \frac{\partial f}{\partial u'}(\mathbf{s}_{k+1})\cdot\left[3h_k^2,2h_k,1,0\right] \tag{2.5}$$

Proceeding just as for the DE conditions, the C^0 and C^1 continuity conditions are

$$\mathcal{C}_k^0 = a_k h_k^3 + b_k h_k^2 + c_k h_k + d_k - d_{k+1}$$

$$\mathcal{C}_k^1 = 3a_k h_k^2 + 2b_k h_k + c_k - c_{k+1}$$

with derivatives

$$\nabla_{\mathbf{c}_k}\mathcal{C}_k^0 = \left[h_k^3,h_k^2,h_k,1\right] \qquad\qquad \nabla_{\mathbf{c}_{k+1}}\mathcal{C}_k^0 = -\left[0,0,0,1\right] \tag{2.6}$$

$$\nabla_{\mathbf{c}_k} \mathcal{C}_k^1 = \Big[3h_k^2, 2h_k, 1, 0\Big] \qquad\qquad \nabla_{\mathbf{c}_{k+1}} \mathcal{C}_k^1 = -\Big[0, 0, 1, 0\Big] \tag{2.7}$$

We have omitted equations for the boundary conditions. While the model problem has been written with Dirichlet conditions at both ends, the spline collation method is capable of handling Neumann conditions at either or both ends. The equations corresponding to the boundary conditions are incredibly simple, so it is left to the reader to derive them himself if he so desires to see them.

Let $\mathbf{c}$ be the vector of coefficients, stacked in descending powers and grouped by k:

$$\mathbf{c} = \Big(a_1, b_1, c_1, d_1, \cdots, a_N, \cdots, d_N\Big)^T$$

With the pieces finally in place, we present the complete algorithm below.

Algorithm 2.1. Spline Collocation Method for Nonlinear BVPs.

1. Generate an initial guess for the coefficient vector $\mathbf{c}^{(0)}$. **Enter the Newton iteration:**

2. For each k, add the contribution to the Jacobian matrix

$$\mathbf{J}\Big[\text{index} : 4k, \text{index} : 4(k+1)\Big] = \begin{pmatrix} \nabla_{\mathbf{c}_k} \mathcal{D}_k^0 & \mathbf{0} \\ \nabla_{\mathbf{c}_k} \mathcal{D}_k^1 & \mathbf{0} \\ \nabla_{\mathbf{c}_k} \mathcal{C}_k^0 & \nabla_{\mathbf{c}_{k+1}} \mathcal{C}_k^0 \\ \nabla_{\mathbf{c}_k} \mathcal{C}_k^1 & \nabla_{\mathbf{c}_{k+1}} \mathcal{C}_k^1 \end{pmatrix}$$

   where index $= 1 + 4(k-1)$ and $\mathbf{0} = \big[0, 0, 0, 0\big]$. The components are given in (2.4), (2.5), (2.6), and (2.7). This 4×8 block comprises all the nonzero entries in rows index to $4k$.

3. For each k, add the contribution to the equation vector

$$\mathbf{F}\Big[\text{index} : 4(k-1)\Big] = \begin{pmatrix} 2b_k - f(\mathbf{s}_k) \\ 6a_k h_k + 2b_k - f(\mathbf{s}_{k+1}) \\ a_k h_k^3 + b_k h_k^2 + c_k h_k + d_k - d_{k+1} \\ 3a_k h_k^2 + 2b_k h_k + c_k - c_{k+1} \end{pmatrix}$$

4. Add boundary conditions to the first and/or last rows of $\mathbf{J}$ and $\mathbf{F}$, depending on whether the conditions are imposed on the left or the right.

5. Update $\mathbf{c}$ by solving

$$\mathbf{J}\mathbf{c}^{(i+1)} = \mathbf{J}\mathbf{c}^{(i)} - \mathbf{F}$$

6. Repeat Steps 2 through 5 until

$$\left\| \mathbf{c}^{(i+1)} - \mathbf{c}^{(i)} \right\| < \tau_n$$

   where τ_n is the Newton solve tolerance, typically 10^{-12} or smaller. Any vector norm on $\mathbb{R}^{4N}$ may be used, although the max norm (ℓ^∞) is the most natural choice.

The matter of generating a suitable starting vector in Step 1 is highly context dependent. When used as part of an adaptive algorithm, as we shall develop in Section 2.4, the initial guess can come from a solution computed on the previous coarse grid. Before that, a trial solution may be generated based on intuition from the underlying physical problem or from something like a linearization of the problem.

Steps 2 and 3 are worded to suggest use of `for` or `while` loops, but such an implementation is likely to be slow. In fact, by exploiting patterns k of the components, the Jacobian matrix and equation vector can be assembled very quickly. We leave details of that for documentation in source code.

2.3 Application to Linear Equations

We will also apply this method to ordinary differential equations. In this thesis, all such ODEs are second-order linear equations of the form

$$u''(x) + g(x)u(x) = 0$$

$$u \sim b(x) \text{ as } x \to -\infty \text{ or } x \to -\infty$$

Fortunately, for problems of this form, the spline method is much simpler to implement than for nonlinear BVPs. For linear equations, obviously there is no need for Newton's method. By characterizing in terms of the moments $M_k = u''(x_k)$ and applying continuity of the first derivative, we can derive a simple recurrence relation involving $u(x_k)$, $u(x_{k-1})$, and $u(x_{k-2})$. The two starting values necessary to transform the method into a linear multi-step method are generated by evaluating the boundary function at the first or last two grid points. Consequently, there are no matrices to be formed and no equations to be solved.

Denote $u_k \triangleq u(x_k)$ and $g_k \triangleq g(x_k)$. The algorithm below has been modified from Albasiny [1] for use on a nonuniform grid. It is presented with the boundary condition on the left; a boundary condition on the right proceeds similarly and is explained afterwards.

Algorithm 2.2 assumes that a mesh $a = x_1 < x_2 < \cdots < x_{N+1} = b$ has already been chosen and that the domain is large enough that the asymptotic condition is approximately achieved at the finite endpoint.

Algorithm 2.2. Spline Collocation Method for Linear ODEs.

1. Set $u_1 = b(x_1)$ and $u_2 = b(x_2)$.

2. For each $k = 3, 4, \ldots, N+1$, set

$$u_k = \frac{h_{k-1}}{h_{k-2}}\left(1 + \frac{h_{k-1}^2}{6}g_k\right)^{-1}\left[u_{k-1}\left(1 + \frac{h_{k-2}}{h_{k-1}} - \left(\frac{h_{k-2}^2}{3} + \frac{h_{k-2}h_{k-1}}{3}\right)g_{k-1}\right) + u_{k-2}\left(1 + \frac{h_{k-2}^2}{6}g_{k-2}\right)\right]$$

3. For each k, set $M_k = -g_k u_k$.

4. The coefficients of the spline (2.1) are given in terms of the M_k by [103, p.98]

$$a_k = \frac{M_{k+1} - M_k}{6h_k} \qquad b_k = \frac{M_k}{2}$$
$$c_k = \frac{u_{k+1} - u_k}{h_k} - \frac{h_k\big(2M_k + M_{k+1}\big)}{6} \qquad d_k = u_k$$

If the boundary condition is instead posed as $x \to +\infty$, then set $u_N = b(x_N)$ and $u_{N-1} = b(x_{N-1})$ in Step 1; in Step 2, proceed over $k = N-2, N-3, \ldots, 1$ and replace k by $k+2$ in the formula for u_k.

2.4 Local Adaptivity

That the spline collocation method can be formulated on unstructured grids can be exploited to transform the method into a locally adaptive one. In this section, we describe how to do this.

Suppose we have computed a spline solution S on the mesh $\{x_1, \ldots, x_{N+1}\}$. By virtue of the DE conditions imposed at the nodes, $S''(x_k) = f\big(x_k, S(x_k), S'(x_k)\big)$ to machine precision. However, inside each interval $[x_k, x_{k+1}]$, S is not likely to satisfy the differential equation to such precision. The error estimate of Theorem 2.2 is helpful, but remember that big O notation provides an estimate in the limit $h \to 0$; the constant multiplying h^4 could be quite large, thus overwhelming a finite h.

To ensure that computed solutions are just as accurate inside the mesh as at the nodes, we take advantage of the spline method's ability to work on nonuniform grids and add in local adaptivity. At the midpoint nodes $x_{k+1/2} \triangleq \frac{1}{2}(x_k + x_{k+1})$, depicted below in Figure 2.2, consider the residual error:

$$\mathcal{E}_{k+1/2} \triangleq \left|S''(x_{k+1/2}) - f\big(x_{k+1/2}, S(x_{k+1/2}), S'(x_{k+1/2})\big)\right|$$

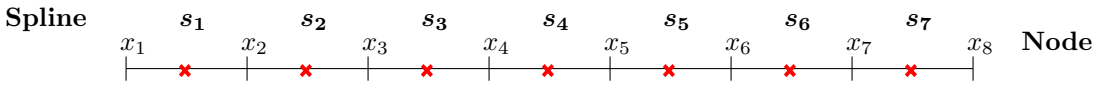

Figure 2.2: Adaptive Evaluation Points. The red × marks, which correspond to the midpoints between the existing nodes, are the test points for Algorithm 2.3.

Because the spline solution is an analytic expression known globally, the derivatives appearing in $\mathcal{E}_{k+1/2}$ can be computed easily without need of estimation. If $\mathcal{E}_{k+1/2} > \tau_a$, refine the mesh by adding the nodes $x_{k+1/3}$ and $x_{k+2/3}$. This augmentation results in three splines where there had been one, on the intervals $[x_k, x_{k+1/3}]$, $[x_{k+1/3}, x_{k+2/3}]$, and $[x_{k+2/3}, x_{k+1}]$. The process is illustrated in Figure 2.3 below.

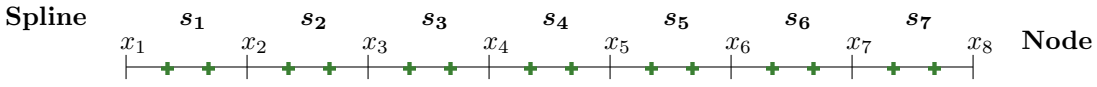

Figure 2.3: Adaptively Addable Points. The green plus marks, which correspond to the one-third and two-thirds points between the nodes, are the points that may be added via adaptivity, Algorithm 2.3.

Algorithm 2.3. Adaptive Spline Method Choose an adaptive tolerance τ_a.

1. Generate an uniform grid of $N+1$ points $x_k = a + (k-1)h$ where $h = \frac{b-a}{N}$.

2. Execute Algorithm 2.1 or 2.2 to compute the spline solution on this uniform grid.

3. Generate a test grid composed of the midpoints of the current grid

$$x_{k+1/2} = \frac{1}{2}(x_k + x_{k+1})$$

4. Compute the residual error at each test point

$$\mathcal{E}_{k+1/2} \triangleq \left|S''(x_{k+1/2}) - f\big(x_{k+1/2}, S(x_{k+1/2}), S'(x_{k+1/2})\big)\right|$$

   and set $\mathcal{E} = \max \mathcal{E}_{k+1/2}$.

5. If $\mathcal{E} < \tau_a$, terminate the procedure. Otherwise, for each k such that $\mathcal{E}_{k+1/2} > \tau_k$, add the points

$$x_{k+1/3} = \frac{1}{3}(x_k + x_{k+1}) \qquad\qquad x_{k+2/3} = \frac{2}{3}(x_k + x_{k+1})$$

   to the existing mesh $\{x_1, x_2, \cdots, x_{N+1}\}$.

6. Compute the spline solution on the new grid via Algorithm 2.1 or 2.2 and return to Step 3.

Chapter 3

Density Functional Theory

Density functional theory (DFT) is a computational method in quantum mechanics that attempts to characterize the electronic structure of a system of atoms or molecules by investigating its electron density. As the name implies, the objects of study are functionals—maps from a function space into a scalar field—of the electron density. DFT has been popular in computational physics since nearly its inception, but it is only in past twenty years or so that the technique has been considered accurate enough for deployment in quantum chemistry applications [27, p.252]. Since acceptance in that community, the number of publications about DFT has exploded from a few hundred per year to nearly 20,000, as shown below in Figure 3.1.

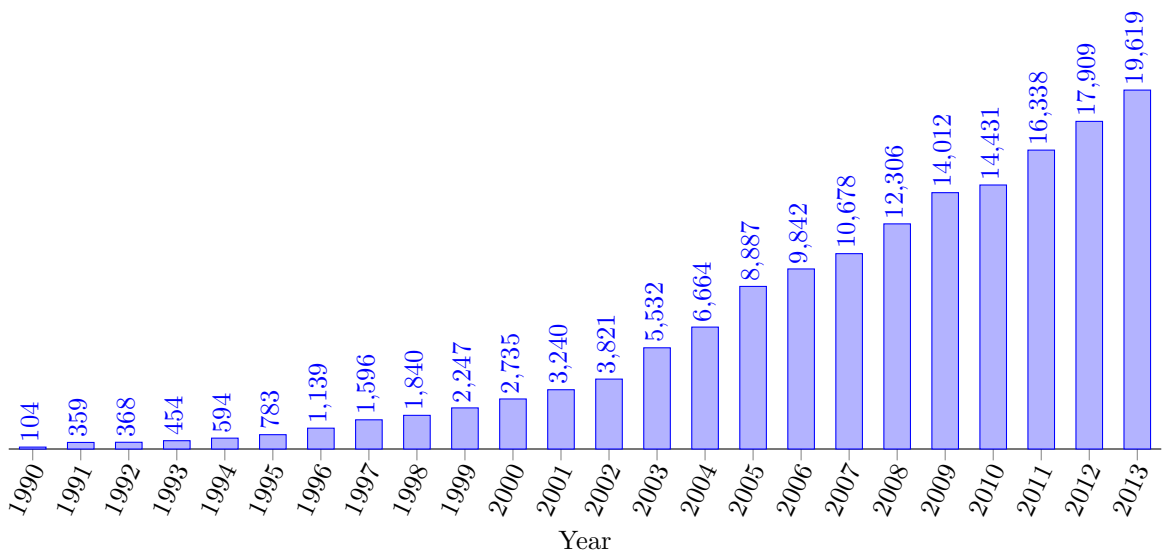

Figure 3.1: DFT Publications Per Year. This chart depicts the number of DFT publications per year as counted by searching for articles with topic containing "density functional theory" (as string literal) or "DFT" on the ISI Web of Science (`http://apps.webofknowledge.com`). At the time of completion of this thesis in early June, over 7000 articles had already been published on the subject in 2014.

This chapter provides an overview of ground state density functional theory. DFT has been adapted for time-dependent situations, one example of which will be seen in Chapter 7, but the term "density functional theory" specifically refers only to ground state computations. The intent of the next sections is not to provide a complete exposition on the subject; for a comprehensive examination from first principles, the reader is advised to consult one of the many available texts, such as Engel and Dreizler [24], Eschrig [25], or Parr and Yang [83]. The works of Elliot Lieb, in particular [62] and [64], may be of special interest to mathematicians.

3.1 The Big Idea

A system of N electrons in the ground state is described by the time-independent Schrödinger equation

$$\begin{aligned} \hat{H}\Psi(\mathbf{x}_1, \cdots, \mathbf{x}_N) &= E\Psi(\mathbf{x}_1, \cdots, \mathbf{x}_N) \\ \hat{H} &= -\frac{1}{2}\sum_{k=1}^{N} \nabla_{\mathbf{x}_k}^2 + \sum_{k=1}^{N} V(\mathbf{x}_k) + \sum_{\substack{k=1 \\ k<k'}}^{N} \mathcal{W}(\mathbf{x}_k, \mathbf{x}_{k'}) \end{aligned} \tag{3.1}$$

where $\mathcal{W}$ quantifies the interaction of electrons with each other. In a theoretical environment, there is no issue with this equation. Because each $\mathbf{x}_k \in \mathbb{R}^3$, the many-body wavefunction Ψ has domain $\mathbb{R}^{3N}$. Consequently, if N is larger than three or so, attempting numerical computation of Ψ is a foray into the impossible.

The goal of density functional theory is to resolve this difficulty by working directly with the electron density, which can be defined in terms of the many-body wavefunction

$$n(\mathbf{x}) = N \int_{\mathbb{R}^3 \times \cdots \times \mathbb{R}^3} |\Psi(\mathbf{x}, \mathbf{x}_2, \ldots, \mathbf{x}_N)|^2 \, d\mathbf{x}_2 \cdots d\mathbf{x}_N \tag{3.2}$$

As electrons are fermions, the wavefunction is anti-symmetric in each of its arguments, so it does not matter over which $N-1$ coordinates the integral is taken. Of course, the goal is to avoid the wavefunction entirely, so the above characterization is not terribly helpful.

3.2 The Hohenberg-Kohn Theorems

Density functional theory can trace its conceptual roots all the way back to 1927 in the works of Llewellyn Thomas [107] and Enrico Fermi [32, 33, 34], who independently argued that the distribution of electrons of an atom can be described in a statistical setting. Thomas wrote

> Electrons are distributed uniformly in the six-dimensional phase space for the motion of an electron at the rate of two for each h^3 of volume.

Without realizing what would follow some forty years later, Thomas established the groundwork for description of systems as electron densities. Assuming uniform distribution of electrons in space, his description is crude in comparison to the sophistication of the tag team of (3.1) and (3.2). Nevertheless, by considering regions of electrons in lieu of discrete point charges, this idea represents a breakthrough in concept.

The true genesis of DFT would not come until 1964 in the innoculously titled paper "Inhomogeneous Electron Gas" by Pierre Hohenberg and Walter Kohn [52], a work that has amassed nearly 29000 citations† since its publication. In a mere seven pages understandable to anyone with only basic knowledge of quantum mechanics, they spawned an entirely new field that would eventually lead Kohn to the award of the 1998 Nobel Prize in Chemistry. Below are the two theorems that begot density functional theory. Because of the surprising ease and elegance with which these landmark results are proven, the proofs are included.

Theorem 3.1 (**Hohenberg-Kohn I**). *If two systems of electrons with potentials V_1 and V_2 generate the same ground state density, then $V_1 - V_2 \equiv$ constant.*

Proof. Suppose that V_1 and V_2 generate the same ground state density but with respective wavefunctions Ψ_1 and Ψ_2. If $V_1 - V_2 \neq$ constant, then $\Psi_1 \neq \Psi_2$ because they satisfy different Schrödinger equations. Let

$$\hat{H}_k = -\frac{1}{2}\nabla^2 + V_k(\mathbf{x}) + \mathcal{W}(\mathbf{x})$$

so that $\hat{H}_k\Psi_k(\mathbf{x}) = E_k\Psi_k(\mathbf{x})$, where $\mathbf{x} \in \mathbb{R}^{3N}$, for $k = 1, 2$. Because the ground state energy is the minimum among all possible wavefunctions that can describe a system, we have

$$E_2 = \left\langle \Psi_2, \hat{H}_2\Psi_2 \right\rangle_{L^2(\mathbb{R}^{3N})} < \left\langle \Psi_1, \hat{H}_2\Psi_1 \right\rangle_{L^2(\mathbb{R}^{3N})} \Longrightarrow E_2 < E_1 + \int_{\mathbb{R}^{3N}} n(\mathbf{x})\big[V_1(\mathbf{x}) - V_2(\mathbf{x})\big]\, d\mathbf{x}$$

We can switch the indices and repeat the above to obtain the second inequality

$$E_1 < E_2 + \int_{\mathbb{R}^{3N}} n(\mathbf{x})\big[V_2(\mathbf{x}) - V_1(\mathbf{x})\big]\, d\mathbf{x}$$

Adding the two yields the contradiction

$$E_1 + E_2 < E_1 + E_2$$

■

Corollary 3.2. *The ground state density alone is sufficient to determine all properties of the system.*

†All citation numbers as counted by Google Scholar.

Theorem 3.3 (**Hohenberg-Kohn II**). *There exists a universal functional $F[n]$ such that*

$$E[n] = F[n] + \int_{\mathbb{R}^3} V(\mathbf{x}) n(\mathbf{x})\, d\mathbf{x}$$

which obtains a minimum on the set

$$\mathcal{N} = \left\{ n : \mathbb{R}^3 \to \mathbb{R} \,\middle|\, n(\mathbf{x}) \geq 0 \text{ and } \int_{\mathbb{R}^3} n(\mathbf{x})\, d\mathbf{x} = N \right\} \tag{3.3}$$

at the ground state density n_0. The value $E[n_0]$ is the ground state energy. The functional F is universal in the sense that it is valid for any number of particles and any external potential.

Proof. By (3.2), the density is a functional of the many-body wavefunction. Therefore, define

$$F[n] \triangleq \frac{1}{2}\left\langle \nabla\Psi, \nabla\Psi \right\rangle_{L^2(\mathbb{R}^{3N})} + \left\langle \Psi, \mathcal{W}\Psi \right\rangle_{L^2(\mathbb{R}^{3N})} \tag{3.4}$$

It is clear that $F[n]$ is universal in the claimed sense. For a fixed potential V, we can define

$$E[n] = F[n] + \int_{\mathbb{R}^3} V(\mathbf{x}) n(\mathbf{x})\, d\mathbf{x}$$

which obviously corresponds to the ground state energy E if the correct n is input. We now show that $E[n]$ assumes its minimum at the ground state density n_0. Let Ψ_0 be the wavefunction corresponding to n_0 and let $n \in \mathcal{N}$ correspond to wavefunction Ψ. Then because

$$E[n] = E[\Psi] = \left\langle \Psi, V\Psi \right\rangle_{L^2(\mathbb{R}^{3N})} + \frac{1}{2}\left\langle \nabla\Psi, \nabla\Psi \right\rangle_{L^2(\mathbb{R}^{3N})} + \left\langle \Psi, \mathcal{W}\Psi \right\rangle_{L^2(\mathbb{R}^{3N})}$$

we have $E[n_0] < E[n]$. Positivity is automatic from (3.2) and that n integrates to N follows from the unit normalization of Ψ:

$$\int_{\mathbb{R}^3} n(\mathbf{x})\, d\mathbf{x} = N \int_{\mathbb{R}^3} \int_{\mathbb{R}^3 \times \cdots \times \mathbb{R}^3} |\Psi(\mathbf{x}, \mathbf{x}_2, \ldots, \mathbf{x}_N)|^2 \, d\mathbf{x}_2 \cdots d\mathbf{x}_N \, d\mathbf{x} = N \int_{\mathbb{R}^{3N}} |\Psi(\mathbf{y})|^2 \, d\mathbf{y} = N \qquad \blacksquare$$

As Hohenberg and Kohn readily admitted, the universal functional is not easily constructed. It has been defined in terms of the wavefunction Ψ, which we cannot easily find from a given density—and the whole point of DFT is to sidestep the wavefunction entirely. The Hohenberg-Kohn Theorems alone are not enough to escape Schrödinger wave theory, even if they do establish the theoretical foundation of DFT. If we seek a computable theory, it seems there is more work that must be done.

3.3 The Kohn-Sham Equations

While the impact of the first DFT paper by Hohenberg and Kohn is nearly immeasurable, it can be argued that Kohn's subsequent publication the next year with Lu Jeu Sham [55] is even more monumental. In that work, Kohn and Sham brought the last piece to the DFT puzzle: a practical method for computation of ground state densities, without which the Hohenberg-Kohn theorems might have passed into obscurity.

Consider a system of noninteracting electrons so that in (3.1) the Hamiltonian has $\mathcal{W} \equiv 0$. Then if we define the single-particle wavefunctions ψ_k to be the solutions to

$$\left(-\frac{1}{2}\nabla^2 + V(\mathbf{x})\right)\psi_k(\mathbf{x}) = \varepsilon_k \psi_k(\mathbf{x})$$

and put Ψ to be the Slater determinant

$$\Psi(\mathbf{x}_1, \mathbf{x}_2, \ldots, \mathbf{x}_N) = \frac{1}{\sqrt{N!}} \det \begin{vmatrix} \psi_1(\mathbf{x}_1) & \psi_1(\mathbf{x}_2) & \cdots & \psi_1(\mathbf{x}_N) \\ \psi_2(\mathbf{x}_1) & \psi_2(\mathbf{x}_2) & \cdots & \psi_2(\mathbf{x}_N) \\ \vdots & \vdots & \ddots & \vdots \\ \psi_N(\mathbf{x}_1) & \psi_N(\mathbf{x}_2) & \cdots & \psi_N(\mathbf{x}_N) \end{vmatrix} \tag{3.5}$$

then this Ψ will be the solution to (3.1) as well with $E = \sum \varepsilon_k$. If we suppose that the ψ_k are orthogonal, then by (3.2), the density corresponding to this wave function will be

$$n_0(\mathbf{x}) = \sum_{k=1}^{N} |\psi_k(\mathbf{x})|^2$$

In the universal functional (3.4), the first quantity represents the kinetic energy

$$T[n] \triangleq \frac{1}{2}\left\langle \nabla\Psi, \nabla\Psi \right\rangle_{L^2(\mathbb{R}^{3N})} \tag{3.6}$$

For the noninteracting system with wavefunction (3.5) and orthogonalized ψ_k, this kinetic energy will be given exactly by

$$T_s[n] \triangleq \frac{1}{2}\sum_{k=1}^{N} \left\langle \nabla\psi_k, \nabla\psi_k \right\rangle_{L^2(\mathbb{R}^3)} \tag{3.7}$$

The matter of the kinetic energy is precisely the issue that plagues Hohenberg-Kohn theory: T is known only in terms of the many-body wavefunction Ψ, which we cannot compute. The single-particle wavefunctions ψ_k, however, exist on $\mathbb{R}^3$, which is certainly in the realm of feasible computation.

Kohn and Sham proposed a method that exploits the computational ease of T_s: instead of the full interacting system, we consider a noninteracting system with the same density. The kinetic energy of the noninteracting system will be given exactly by (3.7). Of course, the universal functionals for the interacting and noninteracting systems cannot be same. Kohn and Sham proposed a separation of the form

$$E[n] = \int_{\mathbb{R}^3} V_{\text{ext}}(\mathbf{x}) n(\mathbf{x})\, d\mathbf{x} + T_s[n] + E_{\text{H}}[n] + E_{\text{xc}}[n] \tag{3.8}$$

so that the first two pieces correspond to the noninteracting system. The third term is the classical Hartree contribution to the energy from the Coulombic interaction of electrons among themselves. It is given by

$$E_{\text{H}}[n] = \frac{1}{2} \int_{\mathbb{R}^3} \int_{\mathbb{R}^3} G_{\mathcal{L}}(\mathbf{x} - \mathbf{y}) n(\mathbf{x}) n(\mathbf{y})\, d\mathbf{x}\, d\mathbf{y} \tag{3.9}$$

where $G_{\mathcal{L}}$ denotes the Green's function for the Laplace operator $\mathcal{L} \triangleq -\frac{1}{4\pi}\nabla^2$; in three-dimensions, $G_{\mathcal{L}}(\mathbf{x}-\mathbf{y}) = |\mathbf{x} - \mathbf{y}|^{-1}$. The remainder of the differences between the interacting and noninteracting system are contained in E_{xc}; this somewhat mysterious term, called the exchange-correlation functional, will be explored in great detail in the next section. To find the minimum of (3.8), we seek the solution to the Euler-Lagrange equation given by taking the first variation (see Appendix A):

$$\frac{\delta T_s[n]}{\delta n(\mathbf{x})} + V_{\text{eff}}(\mathbf{x}) = \upsilon \tag{3.10}$$

where υ is the Lagrange multiplier associated with the constraint $\int n(\mathbf{x})\, d\mathbf{x} = N$ and V_{eff} is

$$V_{\text{eff}}(\mathbf{x}) = V_{\text{ext}}(\mathbf{x}) + \int_{\mathbb{R}^3} G_{\mathcal{L}}(\mathbf{x} - \mathbf{y}) n(\mathbf{y})\, d\mathbf{y} + \frac{\delta E_{\text{xc}}[n]}{\delta n(\mathbf{x})} \tag{3.11}$$

While it seems we've finally made it, it's the same old story: we don't know T_s in terms of n. Fortunately, the brilliance of Kohn and Sham comes to rescue us from this quagmire in which we have been repeatedly ensnared: they showed that (3.10) is precisely the equation obtained from the usual density functional theory when a *noninteracting system is subject to the external potential* $V_{\text{ext}} = V_{\text{eff}}$.

The Kohn-Sham approach to DFT is therefore to solve the celebrated Kohn-Sham equations

$$\left(-\frac{1}{2}\nabla^2 + V(\mathbf{x})\right)\psi_k(\mathbf{x}) = \varepsilon_k \psi_k(\mathbf{x}) \tag{3.12}$$

with $V = V_{\text{eff}}$ as in (3.11) and form the density via

$$n_0(\mathbf{x}) = \sum_{k=1}^{N} |\psi_k(\mathbf{x})|^2 \tag{3.13}$$

Because the Kohn-Sham energies ε_k are unknown, (3.12) are eigenvalue problems.

The derivation of the Kohn-Sham equations presented here lacks rigor and is valid only for non-degenerate ground states—a restriction shared by the Hohenberg-Kohn Theorems—and then only for such densities that are the ground-state of some noninteracting system. Extension of the result to remove this limitation has been performed by Levy [59, 60], Levy and Perdew [61], and Lieb [63], among others.

3.3.1 Kohn-Sham Potential in Self-Contained Systems

In (3.11), the "external potential" comes from any force not directly attributable to the electrons themselves. In a self-contained system, the only such source is the Coulomb repulsion from the positively charged nuclei:

$$E_{\text{ext}}[n] = -\int_{\mathbb{R}^d}\int_{\mathbb{R}^d} G_{\mathcal{L}}(\mathbf{x}-\mathbf{y})n_+(\mathbf{y})n(\mathbf{x})\,d\mathbf{y}\,d\mathbf{x}$$

where $n_+(\mathbf{x})$ is the positive charge distribution due to the nuclei. Taking the first variation yields the potential

$$V_{\text{ext}}(\mathbf{x}) = -\int_{\mathbb{R}^d} G_{\mathcal{L}}(\mathbf{x}-\mathbf{y})n_+(\mathbf{y})\,d\mathbf{y}$$

within V_{eff}, we may fold this contribution into the one from the Hartree electron-electron interaction. Rather than integrate against the Green's function, we may solve the corresponding Poisson equation:

$$\nabla^2\phi(\mathbf{x}) = -4\pi\big(n(\mathbf{x}) - n_+(\mathbf{x})\big) \tag{3.14}$$

This ϕ represents the total electrostatic potential. In conjunction with (3.14), we may write

$$V(\mathbf{x}) = \phi(\mathbf{x}) + \frac{\delta E_{\text{xc}}[n]}{\delta n(\mathbf{x})} \tag{3.15}$$

3.4 The Exchange-Correlation Functional

The exchange-correlation functional E_{xc} appears nowhere in the pioneering work of Hohenberg and Kohn. It is not a natural part of DFT but rather an artificial introduction due to Kohn and Sham, in part due to the "universal functional" Hohenberg and Kohn postulated but could not produce. The purpose of the

exchange-correlation functional is to compensate for two defects in the Kohn-Sham formulation:

1. The kinetic energy $T_s[n]$ of the noninteracting system is *not* the same as that of the true system.
2. The Hartree energy E_{H} is a strictly classical expression. Proper description of the interaction of electrons among themselves should include quantum-level effects.

As the name implies, there are two pieces to the correction. The *exchange* part is the energy change that occurs when spatial coordinates of two electrons are interchanged; this phenomenon is easily quantified. The more elusive of the two, the *correlation* portion, attempts to characterize behavior that is lost by representing the electrons as a density rather than point charges. When one point charge moves, the others adjust accordingly. Electrons are free to move in small regions without changing the overall density, so the individuality of the particles is lost. It is this direct influence that "correlation" attempts to recapture.

3.4.1 The Local Density Approximation (LDA)

Consider a homogeneous electron gas (HEG) of uniform density $\bar{n}$. Then if $\epsilon_{\mathrm{xc}}^{\mathrm{HEG}}(\bar{n})$ quantifies the ground state energy per electron from exchange and correlation for an HEG, the total energy due to the effect is

$$E_{\mathrm{xc}}^{\mathrm{HEG}} = \int_{\mathbb{R}^d} \bar{n}\epsilon_{\mathrm{xc}}^{\mathrm{HEG}}(\bar{n})\, d\mathbf{x} \tag{3.16}$$

An idea also due to Kohn and Sham, the issue of exchange-correlation energy for an inhomogeneous electron gas can be resolved by replacing the constant density $\bar{n}$ in (3.16) by the spatially varying density $n(\mathbf{x})$:

$$E_{\mathrm{xc}}^{\mathrm{LDA}}[n] = \int_{\mathbb{R}^d} n(\mathbf{x})\epsilon_{\mathrm{xc}}^{\mathrm{HEG}}\big(n(\mathbf{x})\big)\, d\mathbf{x} \tag{3.17}$$

This approximation is known as the *local density approximation* (LDA) because E_{xc} depends only on local coordinates of the density. A more sophisticated description known as the *generalized gradient approach* (GGA) includes contribution from the gradient of the density. However, the LDA is sufficient for the majority of applications and, for this reason, it is the most commonly used exchange-correlation functional.

The LDA *exchange-correlation potential* $V_{\mathrm{xc}}^{\mathrm{LDA}}$ is the first variation of the exchange-correlation functional. Following standard variational calculus, it is given by the expression

$$\begin{aligned} V_{\mathrm{xc}}^{\mathrm{LDA}}(\mathbf{x}) &\triangleq \frac{\delta E_{\mathrm{xc}}^{\mathrm{HEG}}[n]}{\delta n} = \frac{\partial}{\partial n}\big[n\epsilon_{\mathrm{xc}}^{\mathrm{HEG}}(n)\big] \\ &= \epsilon_{\mathrm{xc}}^{\mathrm{HEG}}(n(\mathbf{x})) + n(\mathbf{x})\frac{\partial \epsilon_{\mathrm{xc}}^{\mathrm{HEG}}}{\partial n}\big(n(\mathbf{x})\big) \end{aligned} \tag{3.18}$$

Because we work solely in the LDA in this thesis, we will drop the superscript LDA from all terms from here forward. Furthermore, because all exchange-correlation expressions technically describe only the homogeneous electron gas, we drop the superscript HEG as well. Due to its appearance in a functional defined by integration, we dub $\epsilon_{\text{xc}}(n)$ the exchange-correlation *kernel*.

Per the introduction to this section, ϵ_{xc} can be separated into exchange and correlation portions so that

$$\epsilon_{\text{xc}}(n) = \epsilon_{\text{x}}(n) + \epsilon_{\text{c}}(n) \tag{3.19}$$

In the coming subsections, we will explore expressions for the exchange kernel ϵ_{x} and correlation kernel ϵ_{c}.

3.4.2 The Wigner-Seitz Radius r_s

We now introduce two parameters: the average electron density $\bar{n}$ and the dimensionless Wigner-Seitz radius r_s. The two are related by

$$r_s = \left(\frac{3}{4\pi\bar{n}}\right)^{\frac{1}{3}} \quad \Longleftrightarrow \quad \bar{n} = \frac{3}{4\pi r_s^3} \tag{3.20}$$

Physically, r_s is the inverse ratio of the Bohr radius and the radius of the sphere occupied by a single "average electron." Values for elemental metals are known and contained in the periodic table on the next page.

It is more convenient to write the correlation kernel in terms of r_s instead of the density n. In doing so, r_s becomes a spatially varying function of $\mathbf{x}$, as opposed to its usual usage as a fixed constant set by the material under study. In this usage, for each $\mathbf{x}$, $r_s(\mathbf{x})$ and $n(\mathbf{x})$ are related just as in (3.20).

In what might be considered an abuse of notation, in later chapters we will use r_s as a constant. We will commonly write $V_{\text{xc}}(r_s)$, often right next to $V_{\text{xc}}(\mathbf{x}) = V_{\text{xc}}\big(n_0(\mathbf{x})\big)$. When evaluating, the meaning of the input should be placed in context and adjusted appropriately before insertion into the formula.

3.4.3 Exchange Kernel

The exact exchange energy for a homogeneous electron gas can be obtained using a perturbation approach within Hartree-Fock theory [25, Ch.7.1]:

$$E_{\text{x}}[n] = -\frac{3}{4}\left(\frac{3}{\pi}\right)^{\frac{1}{3}} \int_{\mathbb{R}^d} n^{4/3}(\mathbf{x})\, d\mathbf{x} \tag{3.21}$$

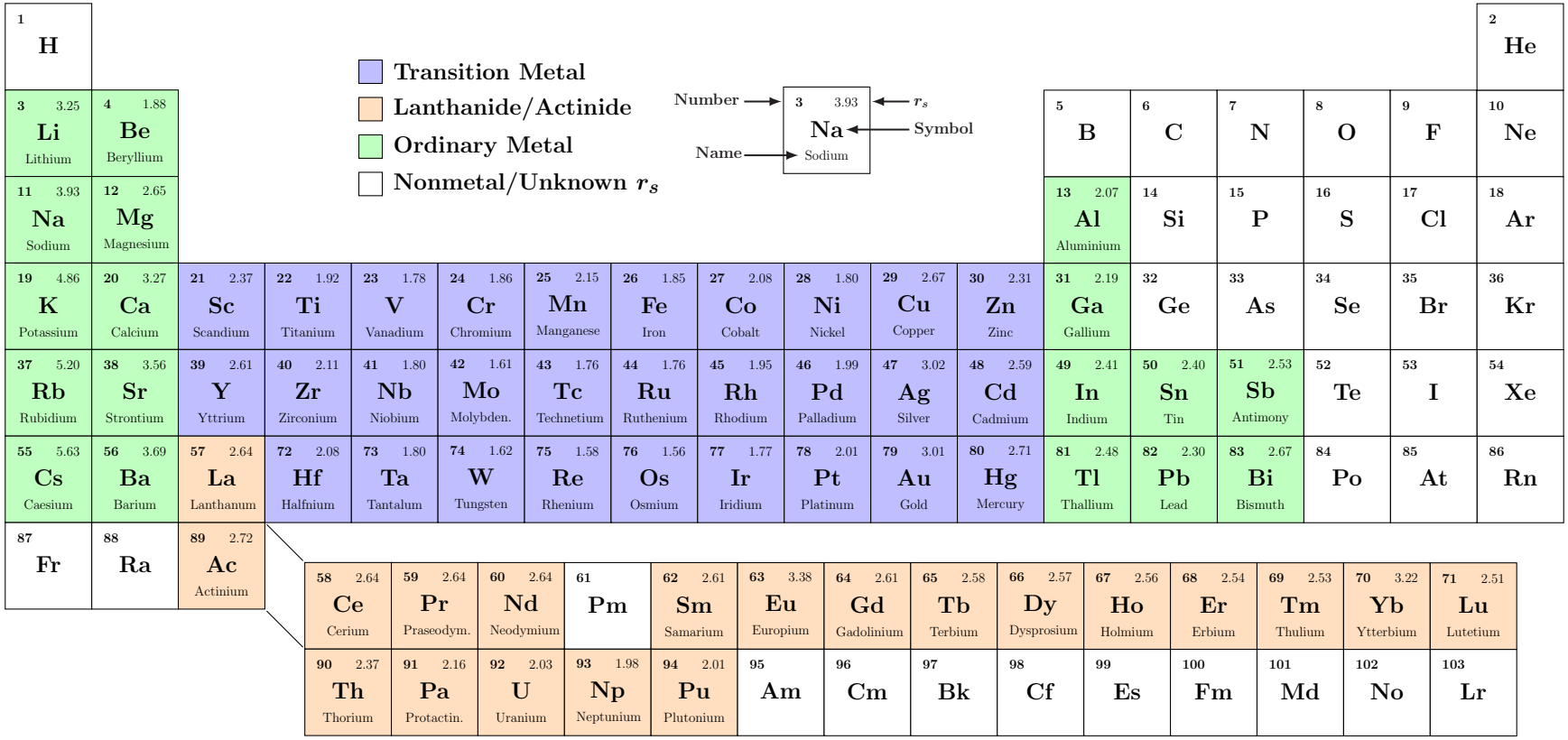

Figure 3.2: Periodic Table with r_s Values. All elements considered, we have $1.61 \leq r_s \leq 5.63$. For transition metals, we have $1.61 \leq r_s \leq 3.01$, with most elements under $r_s = 2$, with the notable exceptions of gold, silver, and copper. Ordinary metals average about $r_s \approx 2.4$ except for alkali metals, which all have $r_s > 3$. Lanthanides hover around $r_s \approx 2.6$, except for europium and ytterbium; the few actinides for which r_s is available typically have $r_s \approx 2$. This diagram constitutes a derivative work of LaTeX code written by Ivan Griffin and posted freely on `texample.net` and is fully compliant with the terms and conditions of the LaTeX Project Public License version 1.3. All r_s values taken from [7, p.89].

The exchange kernel is given by the variational derivative of E_{x}:

$$\epsilon_{\mathrm{x}}(n) = -\frac{3}{4}\left(\frac{3}{\pi}\right)^{\frac{1}{3}} n^{1/3} \tag{3.22}$$

or in terms of r_s,

$$\epsilon_{\mathrm{x}}(r_s) = -\frac{3}{4}\left(\frac{9}{4\pi^2}\right)^{\frac{1}{3}} \frac{1}{r_s} \tag{3.23}$$

The exchange kernel of this section is the one used in every published work the author of this thesis has ever encountered; the matter is considered completely resolved. The correlation kernel, however, is trickier and no perfect solution exists. The next subsections detail three popular expressions for ϵ_{c}. By no means do just these comprise an exhaustive complication. There are results due to Perdew and Zunger [86] and Cole and Perdew [17], certainly as well as others of which this author is unaware.

3.4.4 Correlation Kernel of Wigner

Before the development of modern correlation kernels, the standard workhorse was a kernel that goes all the way back to 1934 to the work of Wigner [115], a paper that has been cited over 2300 times. The Wigner exchange kernel is a compact and elegant expression:

$$\epsilon_{\mathrm{c}}^{\mathrm{Wig}}(n) = -\frac{n^{1/3}}{1.410 + 17.73n^{1/3}} \tag{3.24}$$

Despite predating DFT by thirty years and incorrect behavior in both high- and low-density limits, this kernel is surprisingly accurate across the range of relevant physical values $1 \leq r_s \leq 6$. For this reason, as well as the kernel's simplicity of form, it is still used today, especially in computational demonstration [87]. In particular, this functional has been employed by authors [15, 87, 113] wishing to compare their work to that of the past, especially that of Lang and Kohn, who performed many of the initial studies on DFT for solid state applications [56, 57, 58].

Various authors have made improvements on the Wigner kernel by correcting the poor behavior as $n \to 0$ and $n \to \infty$. Gell-Mann and Brueckner [40] addressed the high-density limit and Nozieres and Pines [80] crafted an improvement based on interpolation. Because the modern kernels of the coming sections are of more interest to this thesis, these results are mentioned only in passing.

3.4.5 Correlation Kernel of Vosko, Wilk, and Nusair

In formulating the first truly modern exchange kernel, Vosko, Wilk, and Nusair [112] took a fundamentally different approach. Instead of relying on pure theory, they used Padé interpolation of high quality data from Monte Carlo experiments from both para- and ferro-magnetic electron states to obtain a kernel that is accurate for not only a range of r_s values but also for a range of spin polarizations. For the unpolarized spin (paramagnetic) case, they wrote

$$\epsilon_{\mathrm{c}}^{\mathrm{VWN}}(r_s) = A\Bigg[\log\left(\frac{r_s}{X(r_s)}\right) + \frac{2b}{Q}\tan^{-1}\left(\frac{Q}{2\sqrt{r_s}+b}\right) - \frac{bx_0}{X(x_0^2)}\left\{\log\left(\frac{(\sqrt{r_s}-x_0)^2}{X(r_s)}\right) + \frac{2(2x_0+b)}{Q}\tan^{-1}\left(\frac{Q}{2\sqrt{r_s}+b}\right)\right\}\Bigg]$$

where $X(r_s) = r_s + b\sqrt{r_s} + c$ and $Q = \sqrt{4c-b^2}$. The reader interested in the precise values of the constants b,c, and x_0 is directed to consult the original work for their values.

The exchange kernel of Vosko, Wilk, and Nusair is widely used and is generally the kernel of choice when the Wigner form is not used. The original paper [112] has been cited almost 14000 times; any attempt to compile a coherent list of example usage would be an exercise in futility. While $\epsilon_{\mathrm{c}}^{\mathrm{VWN}}$ works well for ground-state only computations, the unwieldiness of the formula in regards to differentiation makes it cumbersome to use in excited-state computations. Consequently, $\epsilon_{\mathrm{c}}^{\mathrm{VWN}}$ is not the kernel of choice of this thesis.

3.4.6 Correlation Kernel of Perdew and Wang

Following the lead of Vosko, Wilk, and Nusair, Perdew and Wang [85] produced the following kernel from Monte Carlo data from Ceperley and Alder [14]:

$$\epsilon_{\mathrm{c}}^{\mathrm{PW}} = -2A(1+\alpha_1 r_s)\log\left(1 + \frac{1}{2A\left(\beta_1 r_s^{1/2} + \beta_2 r_s + \beta_3 r_s^{3/2} + \beta_4 r_s^{p+1}\right)}\right) \tag{3.25}$$

Like the trio before them, Perdew and Wang's expression can be adapted for different spin polarizations, although such generality is unnecessary here. They provided two sets of values for the constants p, A, α_1, and $\beta_1 \sim \beta_4$, one in the RPA[†] and one "beyond RPA." These values are presented in Table 3.1 below.

By standing on the shoulders of giants, Perdew and Wang were able to improve upon the already excellent accuracy of Vosko, Wilk, and Nusair. In addition, their formula is much easier to handle. For these two

[†]In the random phase approximation (RPA), electrons are assumed to respond only to an external potential and a screening potential. Other effects average out and only the total potential at wavevector $\mathbf{k}$ contributes.

reasons, this is the kernel with the "beyond RPA" parameters that is used in all computations in this thesis.

	$p^{\S}$	$A^{\S}$	α_1	β_1	β_2	β_3	β_4
$\epsilon_c^{\mathrm{RPA}}(r_s)$	0.75	0.031091	0.082477	5.1486	1.6483	0.23647	0.20614
$\epsilon_c(r_s)$	1.00	0.031091	0.21370	7.5957	3.5876	1.6382	0.49294

Table 3.1: Parameters for Perdew-Wang Exchange Kernel. These are the parameters in ϵ_c of (3.25). Parameters marked with § are constrained to exact values from Vosko, Wilk, and Nusair [112].

3.4.7 Analysis of the Perdew-Wang Exchange-Correlation Kernel

Combining (3.25) with (3.23), the complete exchange-correlation kernel of Perdew and Wang is

$$\epsilon_{xc}\big(r_s(n(\mathbf{x}))\big) = -\frac{3}{4}\left(\frac{9}{4\pi^2}\right)^{\frac{1}{3}}\frac{1}{r_s} - 2A(1+\alpha_1 r_s)\log\left(1+\frac{1}{2A\left(\beta_1 r_s^{1/2}+\beta_2 r_s+\beta_3 r_s^{3/2}+\beta_4 r_s^{p+1}\right)}\right) \tag{3.26}$$

The kernel itself is not what is needed to perform DFT calculations. What we really need is the exchange-correlation *potential* V_{xc}, given by (3.18). Of use in computing it are the chain rules

$$\frac{\partial r_s}{\partial n} = -\frac{1}{3}\left(\frac{3}{4\pi}\right)^{\frac{1}{3}}\frac{1}{n^{4/3}} = -\frac{4\pi r_s^4}{9} \tag{3.27}$$

$$\frac{\partial^2 r_s}{\partial n^2} = \frac{4}{9}\left(\frac{3}{4\pi}\right)^{\frac{1}{3}}\frac{1}{n^{7/3}} = \frac{64\pi^2 r_s^7}{27} \tag{3.28}$$

Employing these rules in (3.18) for the Perdew-Wang kernel, we have

$$V_{xc}(r_s) = \epsilon_{xc}(r_s) + \frac{3}{4\pi r_s^3}\frac{\partial \epsilon_{xc}(r_s)}{\partial r_s}\frac{\partial r_s}{\partial n} = \epsilon_{xc}(r_s) - \frac{r_s}{3}\frac{\partial \epsilon_{xc}(r_s)}{\partial r_s} \tag{3.29}$$

$$= -\left(\frac{9}{4\pi^2}\right)^{\frac{1}{3}}\frac{1}{r_s} - 2A\left(1+\tfrac{2}{3}\alpha_1 r_s\right)\log\left(1+\frac{1}{P(r_s)}\right) - \frac{2Ar_s}{3}\left(1+\alpha_1 r_s\right)\frac{P'(r_s)}{P^2(r_s)+P(r_s)} \tag{3.30}$$

where

$$P(r_s) \triangleq 2A\left(\beta_1 r_s^{1/2}+\beta_2 r_s+\beta_3 r_s^{3/2}+\beta_4 r_s^{p+1}\right)$$

$$P'(r_s) = 2A\left(\frac{1}{2}\beta_1 r_s^{-1/2}+\beta_2+\frac{3}{2}\beta_3 r_s^{1/2}+(p+1)\beta_4 r_s^{p}\right)$$

Necessary for excited state computations is $f_{\text{xc}} = V'_{\text{xc}}(n)$, found by the chain rule:

$$\begin{aligned} f_{\text{xc}}(r_s) = \Bigg[& \frac{1}{r_s^2}\left(\frac{9}{4\pi^2}\right)^{\frac{1}{3}} - \frac{4A\alpha_1}{3}\log\left(1+\frac{1}{P(r_s)}\right) + \frac{4A}{3}\frac{P'(r_s)}{P^2(r_s)+P(r_s)} \\ & - \frac{2Ar_s}{3}(1+\alpha_1 r_s)\left(\frac{P''(r_s)}{P^2(r_s)+P(r_s)} - \frac{\big(2P(r_s)+1\big)\big(P'(r_s)\big)^2}{\big(P^2(r_s)+P(r_s)\big)^2}\right)\Bigg] \cdot \left(\frac{-4\pi r_s^4}{9}\right) \end{aligned} \tag{3.31}$$

where P and P' are as before and

$$P''(r_s) = 2A\left(-\frac{1}{4}\beta_1 r_s^{-3/2} + \frac{3}{4}\beta_3 r_s^{-1/2} + p(p+1)\beta_4 r_s^{p-1}\right)$$

The second derivative $g_{\text{xc}} = V''_{\text{xc}}(n)$ will be needed later as well. By differentiating f_{xc} with help from the chain rule,

$$g_{\text{xc}}(r_s) = V''_{\text{xc}}(n) = \frac{\partial^2 V_{\text{xc}}}{\partial r_s^2}\left(\frac{\partial r_s}{\partial n}\right)^2 + \frac{\partial V_{\text{xc}}}{\partial r_s}\frac{\partial^2 r_s}{\partial n^2} \tag{3.32}$$

We can assemble the first term by differentiating the quantity in the brackets [ ] contained in (3.31) and using (3.27). The computational burden may be reduced for the second term by recognizing that

$$\frac{\partial V_{\text{xc}}}{\partial r_s} = -\frac{9}{4\pi r_s^4} f_{\text{xc}}(r_s)$$

Substituting the second chain rule expression (3.28) into the above, we have

$$g_{\text{xc}}(\mathbf{x}) = \frac{\partial^2 V_{\text{xc}}}{\partial r_s^2}\left(\frac{\partial r_s}{\partial n}\right)^2 - \frac{16\pi r_s^3}{3} f_{\text{xc}}$$

We can then compute the missing piece directly, finally obtaining:

$$\begin{aligned} g_{\text{xc}}(r_s) = \frac{16\pi^2 r_s^8}{81}\Bigg[& -\frac{2}{r_s^3}\left(\frac{9}{4\pi^2}\right)^{\frac{1}{3}} + \frac{4A\alpha_1}{3}\frac{P'}{P^2+P} + \frac{2A}{3}(1-2\alpha_1 r_s)\left(\frac{P''}{P^2+P} - \frac{\big(2P+1\big)\big(P'\big)^2}{\big(P^2+P\big)^2}\right) \\ & - \frac{2Ar_s}{3}(1+\alpha_1 r_s)\left(\frac{P'''}{P^2+P} + \frac{P'\big(2P+1\big)\big(2P+P''\big) + 2\big(P'\big)^3}{\big(P^2+P\big)^2}\right. \\ & \left. + \frac{2\big(2P+1\big)^2\big(P'\big)^3}{\big(P^2+P\big)^3}\right)\Bigg] - \frac{16\pi r_s^3}{3} f_{\text{xc}} \end{aligned} \tag{3.33}$$

Because exchange-correlation measures effects due to electrons, as the number of electrons in a region decreases, the magnitude of exchange-correlation should also decrease. Consequently, a "correct" V_{xc} should decay to zero as $n \to 0$, or equivalently, as $r_s \to +\infty$.

Theorem 3.4. *For the Perdew-Wang V_{xc} given in* (3.30)*, we have*

$$\lim_{r_s \to +\infty} V_{xc}(r_s) = 0$$

Proof. We first return to formal expression (3.29) for V_{xc} and separate into the exchange and correlation pieces, as in (3.19):

$$V_{\mathrm{xc}}(r_s) = \left[1 - \frac{r_s}{3}\frac{\partial}{\partial r_s}\right]\epsilon_{\mathrm{x}}(r_s) + \epsilon_{\mathrm{c}}(r_s) - \frac{r_s}{3}\frac{\partial \epsilon_{\mathrm{c}}(r_s)}{\partial r_s} \tag{3.34}$$

A quick examination of $\epsilon_{\mathrm{x}}(r_s)$, given in (3.23), reveals that $\frac{\partial^k \epsilon_{\mathrm{x}}(r_s)}{\partial r_s^k}$ is of the form $C r_s^{-(k+1)}$; accordingly, we need not perform further asymptotic analysis of the exchange contribution. Instead, we focus on

$$\epsilon_{\mathrm{c}}(r_s) = -2A(1+\alpha_1 r_s)\log\left(1 + \frac{1}{P(r_s)}\right) \tag{3.35}$$

$$\frac{\partial \epsilon_{\mathrm{c}}(r_s)}{\partial r_s} = -2A\alpha_1 \log\left(1 + \frac{1}{P(r_s)}\right) - 2A(1+\alpha_1 r_s)\frac{P'(r_s)}{P^2(r_s) + P(r_s)} \tag{3.36}$$

Let $q_k(r_s)$ be a polynomial in r_s of degree $k \geq 1$. Then we can directly compute

$$\begin{aligned}\lim_{r_s \to +\infty}\left[q_k(r_s)\log\left(1 + \frac{1}{P(r_s)}\right)\right] &= \lim_{r_s \to +\infty} \frac{\log\left(1 + \frac{1}{P(r_s)}\right)}{\frac{1}{q_k(r_s)}} \\ &= \lim_{r_s \to +\infty} \frac{q_k^2(r_s)}{q_k'(r_s)}\frac{P'(r_s)}{P^2(r_s) + P(r_s)}\end{aligned}$$

Because P is a polynomial-type expression of "degree" $p+1$ and q_k has degree 1, from the above expression we have that

$$\lim_{r_s \to +\infty}\left[q_k(r_s)\log\left(1 + \frac{1}{P(r_s)}\right)\right] \sim \lim_{r_s \to +\infty} \frac{r_s^{p+2k}}{r_s^{2p+k+1}} = 0$$

when $p > k-1$. Further, we note that when this condition holds, $\log\left(1 + \frac{1}{P(r_s)}\right)$ vanishes like r_s^{k-1-p}. Now we turn attention to

$$\lim_{r_s \to +\infty}\left[q_k(r_s)\frac{P'(r_s)}{P^2(r_s) + P(r_s)}\right]$$

Unlike in the previous case, in which the function whose limit we were computing contained terms with only positive powers of r_s, P' contains terms with negative exponents. We need not pay special attention to these, as they may be split off into terms of the form $1/\left(r_s^a \mathcal{P}(r_s)\right)$ with $a > 0$ and $\mathcal{P}$ of all positive exponents;

such terms clearly vanish at infinity. Using the ~ symbol to characterize the slowest rate of decay, we have

$$\lim_{r_s\to+\infty}\left[q_k(r_s)\frac{P'(r_s)}{P^2(r_s)+P(r_s)}\right]\sim\lim_{r_s\to+\infty}\frac{r_s^{p+k}}{r_s^{2p+2}}=0 \tag{3.37}$$

whenever $p > k-2$. For choices of p given in Table 3.1, per (3.35) and (3.36) and the above results, we have

$$\lim_{r_s\to+\infty}\epsilon_{\mathrm{c}}(r_s)=0 \qquad\qquad \lim_{r_s\to+\infty}\frac{r_s}{3}\frac{\partial\epsilon_{\mathrm{c}}(r_s)}{\partial r_s}=0$$

Consequently,

$$\lim_{r_s\to+\infty}V_{\mathrm{xc}}(r_s)=0$$ ■

Before we begin to analyze the behavior of f_{xc}, it is convenient to write it in a form similar to (3.34):

$$\begin{aligned}
f_{\mathrm{xc}}(r_s)&=\frac{\partial}{\partial r_s}\left[\left(1-\frac{r_s}{3}\frac{\partial}{\partial r_s}\right)\epsilon_{\mathrm{x}}(r_s)+\epsilon_{\mathrm{c}}(r_s)-\frac{r_s}{3}\frac{\partial\epsilon_{\mathrm{c}}(r_s)}{\partial r_s}\right]\cdot\frac{\partial r_s}{\partial n}\\
&=\left[\frac{2}{3}\frac{\partial\epsilon_{\mathrm{x}}(r_s)}{\partial r_s}-\frac{r_s}{3}\frac{\partial^2\epsilon_{\mathrm{x}}(r_s)}{\partial r_s^2}+\frac{2}{3}\frac{\partial\epsilon_{\mathrm{c}}(r_s)}{\partial r_s}-\frac{r_s}{3}\frac{\partial^2\epsilon_{\mathrm{c}}(r_s)}{\partial r_s^2}\right]\cdot\frac{\partial r_s}{\partial n}\\
&=-\frac{8\pi r_s^4}{27}\frac{\partial\epsilon_{\mathrm{x}}(r_s)}{\partial r_s}+\frac{4\pi r_s^4}{27}\frac{\partial^2\epsilon_{\mathrm{x}}(r_s)}{\partial r_s^2}-\frac{8\pi r_s^4}{27}\frac{\partial\epsilon_{\mathrm{c}}(r_s)}{\partial r_s}+\frac{4\pi r_s^5}{27}\frac{\partial^2\epsilon_{\mathrm{c}}(r_s)}{\partial r_s^2}
\end{aligned} \tag{3.38}$$

In the brief discussion that follows (3.34), we stated that $\frac{\partial^k\epsilon_{\mathrm{x}}(r_s)}{\partial r_s^k}\propto r_s^{-(k+1)}$; therefore, via the first two terms of (3.38), it is clear that $|f_{\mathrm{xc}}|\to+\infty$ as $r_s\to+\infty$. However, this is not the behavior of concern. Whenever f_{xc} will appear, it will always do so as nf_{xc}. Consequently, it is Theorem 3.5 that really matters.

Theorem 3.5. *Using the Perdew-Wang correlation kernel, f_{xc} as defined in* (3.31) *has*

$$\lim_{r_s\to+\infty}n(r_s)\,f_{xc}(r_s)=0$$

Proof. Using (3.20) and (3.38), we have

$$n(r_s)\,f_{\mathrm{xc}}(r_s)=-\frac{2r_s}{9}\frac{\partial\epsilon_{\mathrm{x}}(r_s)}{\partial r_s}+\frac{r_s^2}{3}\frac{\partial^2\epsilon_{\mathrm{x}}(r_s)}{\partial r_s^2}-\frac{2r_s}{9}\frac{\partial\epsilon_{\mathrm{c}}(r_s)}{\partial r_s}+\frac{r_s^2}{9}\frac{\partial^2\epsilon_{\mathrm{c}}(r_s)}{\partial r_s^2}$$

The first two terms vanish as $r_s\to+\infty$ per the discussion before the theorem statement. The proof of Theorem 3.4 shows that $\frac{\partial\epsilon_{\mathrm{c}}(r_s)}{\partial r_s}\to 0$. Consequently, we need only focus on the last term; we proceed from (3.36) and compute

$$\frac{\partial^2\epsilon_{\mathrm{c}}(r_s)}{\partial r_s^2}=-4A\alpha_1\frac{P'(r_s)}{P^2(r_s)+P(r_s)}-2A(1+\alpha_1 r_s)\left[\frac{P''(r_s)}{P^2(r_s)+P(r_s)}-\frac{\big(2P(r_s)+1\big)\big(P'(r_s)\big)^2}{\big(P^2(r_s)+P(r_s)\big)^2}\right] \tag{3.39}$$

When we compute the limit

$$\lim_{r_s \to +\infty} \frac{r_s^2}{9} \frac{\partial^2 \epsilon_c(r_s)}{\partial r_s^2}$$

the result of (3.37) handles the first term from (3.39), as $k = 2$ in this case. Next, because P'' is polynomial-type with degree $p - 1$, we have

$$\lim_{r_s \to +\infty} \left[q_k(r_s) \frac{P''(r_s)}{P^2(r_s) + P(r_s)} \right] \sim \lim_{r_s \to +\infty} \frac{r_s^{p+k-1}}{r_s^{2(p+1)}} = 0$$

whenever $p > k - 3$. Finally, we address the last term:

$$\lim_{r_s \to +\infty} \left[q_k(r_s) \frac{\big(2P(r_s) + 1\big)\big(P'(r_s)\big)^2}{\big(P^2(r_s) + P(r_s)\big)^2} \right] \sim \lim_{r_s \to +\infty} \frac{r_s^{3p+k+1}}{r_s^{4(p+1)}} = 0$$

again whenever $p > k - 3$. Combining all these results, we have

$$\lim_{r_s \to +\infty} \frac{r_s^2}{9} \frac{\partial^2 \epsilon_c(r_s)}{\partial r_s^2} = 0$$

That completes the proof of the theorem. ■

Chapter 4

The Ground State: Orbital-Free DFT

4.1 The Jellium Model

In the Drude-Sommerfeld model, also known as the free electron model, the valence of electrons of a crystalline metallic solid are assumed to be detached from their nuclei and thus free to wander about as gas particles in a box. An extension of Drude-Sommerfeld, which neglects to include even Coulombic electron-electron repulsion, the jellium model is the simplest model for delocalized, interacting electrons of a metal solid.

The ansatz that powers the jellium model is that the positive charge, due to the nuclei sans the wandering valence electrons, is uniformly distributed in space. In the macroscopic view, the symmetric arrangement of the nuclei in the metal crystal structure creates an environment where positive charges smear out in space. Ignoring the location of the nuclei and neglecting the structure of the atomic lattice makes jellium especially suited for studies concerning effects due to the quantum behavior of electrons.

The name "jellium" is attributed to Conyers Herring, co-receipient with Phillip Nozieres of the 1984/5 Wolf Prize in physics for their "fundamental theory of solids, especially of the behavior of electrons in metals" [36], who likened the uniform charge distribution to a spreading of "positive electron jelly" on bread [28].

Jellium is well-suited for studying electronic excitations at metal surfaces. Combined with the LDA in a DFT setting, the use of jellium is attractive for several reasons [67, p.10]:

1. It provides an accurate, self-consistent description of the density distribution in the surface region.
2. Electronic excitations in the bulk are absent for input frequencies below the bulk plasma frequency. Electronic surface excitations can be examinined in the jellium model without concern that bulk excitations will interfere with and invariably obscure or corrupt the surface excitation processes.

3. Since the jellium model is translationally invariant parallel to the surface, the reduction of dimension it provides makes the computational effort significantly simpler than for three-dimensional systems.

We model a solid as a block that extends infinitely in all but one direction. In atomic units, the unit length is the Bohr radius and has value 5.291772×10^{-11} m. As 1 mm of material is 1.89×10^{7} a.u, a macroscopic sample is, practically speaking, infinite. A true free-space formulation greatly simplifies the problem formulation and the underlying analysis at the cost of complicating the numerics, as we shall see.

Mathematically, if we assume the metal to lie in the negative half-space $\{x \in \mathbb{R}^3 : x_3 < 0\}$, the positive background charge $n_+(\mathbf{x}) = n_+(x)$ of the positive nuclei is given by

$$n_+(x) = \bar{n}\Theta(-x) = \begin{cases} \bar{n} & x \le 0 \\ 0 & x > 0 \end{cases} \tag{4.1}$$

where $\bar{n}$ is the average electron radius of (3.20). This is the reduction of dimension of the third point above.

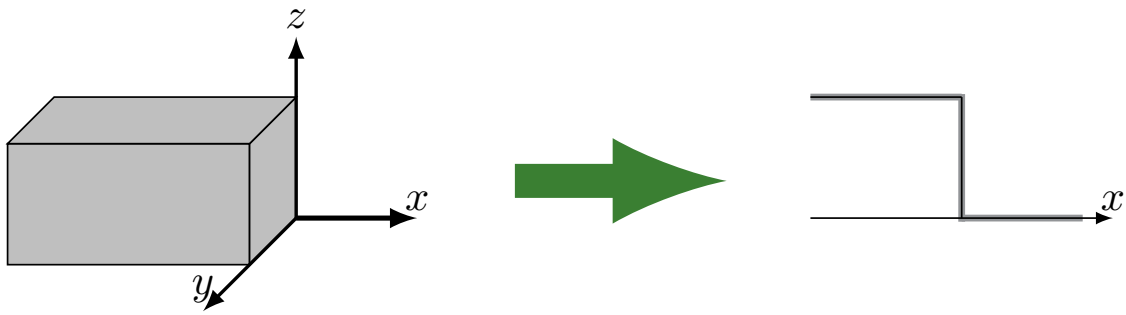

Figure 4.1: Reduction of Dimension in Semi-infinite Jellium. The surface is assumed to extend infinitely in the y-, z-, and negative x-directions. By assuming uniformity of charge in space, jellium transforms the three-dimensional block on the right to the one-dimensional line on the left in computations.

The term "bulk" refers to the portion of the metal that is too distant to feel surface effects, typically no more than a handful of atoms in. Mathematically, this region begins around $x \approx -10$ and ends at $-\infty$.

4.1.1 Properties of Exact Electron Density

The *exact* electron density of a jellium system and its corresponding electrostatic potential (3.14) satisfy several properties. The first is a theorem due to Budd and Vannimenus [12] that links the electrostatic potential at the surface to the electron energy in the bulk material.

Theorem 4.1 (**Budd-Vannimenus**). *The electrostatic potential ϕ satisfies*

$$\phi(0) - \phi(-\infty) = \bar{n}\frac{\partial \varepsilon_T}{\partial n}\big(\bar{n}\big)$$

where ε_T is the total energy per electron in the system:

$$\varepsilon_T(n) = \frac{3}{5}(3\pi^2)^{2/3}n^{5/3} + \varepsilon_{xc}(n)$$

In the presence of an external electric field, the Budd-Vannimenus Theorem takes a slightly different form. The generalization below is due to Theophilou [106].

Theorem 4.2 (**Budd-Vannimenus in Electric Field**). *For a semi-infinite jellium surface in the presence of a strong electric field, the Budd-Vannimenus Theorem takes the form*

$$\phi(0) - \phi(-\infty) = \bar{n}\frac{\partial \varepsilon_T}{\partial n}\big(\bar{n}\big) + \frac{2\pi\varsigma^2}{\bar{n}}$$

where the strength of the field is $E_0 = 2\pi\varsigma$. This corresponds to the boundary condition $\phi'(+\infty) = -4\pi\varsigma$.

Corollary 4.3. *In the local density approximation, the result of Theorem 4.2 becomes*

$$\phi(0) - \phi(-\infty) = \frac{1}{5}\big(3\pi^2\bar{n}\big)^{2/3} + V_{\mathrm{xc}}(\bar{n}) - \varepsilon_{\mathrm{xc}}(\bar{n}) + \frac{2\pi\varsigma^2}{\bar{n}} \tag{4.2}$$

Proof. Under the local density approximation, $V_{\mathrm{xc}}(n) = \frac{\partial}{\partial n}\big[n\varepsilon_{\mathrm{xc}}(n)\big]$. As a result,

$$\begin{aligned} V_{\mathrm{xc}}(n) &= n\frac{\partial \varepsilon_{\mathrm{xc}}}{\partial n} + \varepsilon_{\mathrm{xc}}(n) \\ \Longrightarrow n\frac{\partial \varepsilon_{\mathrm{xc}}}{\partial n} &= V_{\mathrm{xc}}(n) - \varepsilon_{\mathrm{xc}}(n) \end{aligned}$$

After differentiating the first term of ε_T in n directly and evaluating at $\bar{n}$, we arrive at (4.2). ∎

There is also a result about the value of the density at the surface from Perdew [84].

Theorem 4.4. *In the high-density limit, the value of the density at the surface edge results from the Thomas-Fermi model:*

$$n(0) = \bar{n}\left(\frac{3}{5}\right)^{3/2}$$

The high-density limit [76] means that r_s should be "small." The limit $r_s \to 0$ refers to an extreme high-density limit, so the high-density limit does not imply r_s must be infinitesimal. A close examination of

Kohn-Sham densities of Chapter 5 would reveal that Theorem 4.4 is satisfied reasonably well even for $r_s = 3$. However, the range of validity of this relation is not an investigation point of this study.

It is important to understand that the density obtained from DFT is merely an approximation of the exact density, and these theorems only hold for the latter. Consequently, we cannot expect computed densities to satisfy them automatically. Rather, they will be called upon to overcome computational difficulties.

4.2 The Kinetic Energy Functional

The Kohn-Sham approach detailed in Section 3.3 is the most popular method of resolving the conundrum of kinetic energy. As we shall see in the next chapter, specifically in Section 5.6, it comes at a high computational price—the equations that construct the density are implicit and must be solved by iterative methods.

An alternative approach that bypasses Schrödinger wavefunctions entirely is to write an explicit functional for the kinetic energy in terms of the density. This is, of course, no easy task—if it were, there would be no reason for the Kohn-Sham equations to exist. For a crude solution, we hearken back all the way to the origins of DFT and write the Thomas-Fermi kinetic energy functional

$$T_{\mathrm{TF}}[n] = \frac{3}{10}(3\pi^2)^{2/3}\int_{\mathbb{R}^d} n^{5/3}(\mathbf{x})\,d\mathbf{x}$$

As one might expect, use of T_{TF} alone does not lead to terribly good results. In the absence of the nonlinear exchange-correlation term, it is possible to solve the resultant Euler-Lagrange equation for a single-atom system semi-analytically. It can then be shown that $n \sim |x|^{-3/2}$ as $|x| \to 0$ so that the density blows up near the nucleus. This is clearly incorrect—the positive nucleus should repel electrons, not collect them!

The second purpose of E_{xc} was to quantify the non-classical electron-electron interaction. Even with a perfectly exact kinetic energy, we still have a need for this correction. It seems reasonable that a plausible revision to the Thomas-Fermi functional is to include the exchange energy (3.21), giving

$$T_{\mathrm{TFD}}[n] = \frac{3}{10}(3\pi^2)^{2/3}\int_{\mathbb{R}^d} n^{5/3}(\mathbf{x})\,d\mathbf{x} - \frac{3}{4}\left(\frac{3}{\pi}\right)^{\frac{1}{3}}\int_{\mathbb{R}^d} n^{4/3}(\mathbf{x})\,d\mathbf{x}$$

This functional is called the Thomas-Fermi-Dirac kinetic energy functional, so named because the exchange energy is actually due to Dirac [20]. While this seems like an improvement, the density under T_{TFD} has the same problems at the origin as before and further underestimates the kinetic energy [83, p.113].

The primary shortcoming of both T_{TF} and T_{TFD} is that they are based on homogeneity of the density; we recall the quote from Thomas at the beginning of Section 3.2 and remember that the Dirac exchange energy is for the homogeneous electron gas. An attempt to incorporate inhomogeneous effects first came from von Weizsacker [111], who suggested a gradient correction to Thomas-Fermi kinetic energy. Application of his idea within DFT results in the Thomas-Fermi-Dirac-von Weizsacker (TFDW) functional:

$$T_{\mathrm{TFDW}}[n] = \frac{3}{10}(3\pi^2)^{2/3}\int_{\mathbb{R}^d} n^{5/3}(\mathbf{x})\,d\mathbf{x} + \frac{\lambda}{8}\int_{\mathbb{R}^d}\left|\nabla\sqrt{n(\mathbf{x})}\right|^2 d\mathbf{x} - \frac{3}{4}\left(\frac{3}{\pi}\right)^{\frac{1}{3}}\int_{\mathbb{R}^d} n^{4/3}(\mathbf{x})\,d\mathbf{x} \tag{4.3}$$

von Weizsäcker used the value $\lambda = 1$ in his work, but the canonical value has been established to be $\lambda = \frac{1}{9}$. Still, this value is not set in stone; following the lead of Chizmeshya and Zaremba [15], who employed the TFDW functional for use in second harmonic generation, we will take $\lambda = \frac{1}{4}$. Regardless of the value of λ, the TFDW functional constitutes a monumental improvement over the others of this section. In addition to providing more accurate kinetic energy estimates, it results in densities that are finite near the nucleus.

The TFDW functional (4.3) incorporates the exchange energy yet ignores the correlation energy. Because the correlation contribution to E_{xc} attempts to capture important behavior that is still lost in representing as densities, it is more natural to remove the exchange from the kinetic energy, replacing $T_s[n]$ by

$$T[n] = \frac{3}{10}(3\pi^2)^{2/3}\int_{\mathbb{R}^d} n^{5/3}(\mathbf{x})\,d\mathbf{x} + \frac{\lambda}{8}\int_{\mathbb{R}^d}\left|\nabla\sqrt{n(\mathbf{x})}\right|^2 d\mathbf{x} \tag{4.4}$$

in (3.8) and including the entirety of E_{xc}.

The functionals here each produce very different mathematical problems of uniqueness, existence, and solution space of minimizers to (3.8). For an extensive compilation of such knowledge, see Lieb [62]. Despite the document's age, the author believes its information is still current and its open questions remain so.

4.3 Orbital-Free Density Functional Theory

The kinetic energy functionals of Section 4.2 form the basis for a technique known as *orbital-free density functional theory* (OF-DFT). It is so named because it lacks the wavefunctions that correspond to the non-physical orbitals of the Kohn-Sham equations. The benefit of OF-DFT over Kohn-Sham DFT (KS-DFT) is the explicit equations it produces; the cost is inaccuracy in kinetic energy.

With (4.4) in hand, formulation of orbital-free density functional theory proceeds in exactly the same manner

as the Kohn-Sham approach does. We take the first variation of the energy functional

$$E[n] = \int_{\mathbb{R}^3} n_+(\mathbf{x})n(\mathbf{x})\,d\mathbf{x} + T[n] + E_{\mathrm{H}}[n] + E_{\mathrm{xc}}[n]$$

to yield the Euler-Lagrange equation for the ground state density n_0

$$\frac{\delta T[n]}{\delta n_0(\mathbf{x})} + \underbrace{\phi(\mathbf{x}) + V_{\mathrm{xc}}\big(n_0(\mathbf{x})\big)}_{V_{\mathrm{eff}}(\mathbf{x})} = \upsilon$$

This semi-complete form highlights the similarity with (3.10) that appeared in the derivation of the Kohn-Sham equations. The same V_{eff} reappears in the above, in the form (3.15) because the jellium system is a self-contained one. ϕ is the total electrostatic potential and satisfies the Poisson equation

$$\nabla^2\phi(\mathbf{x}) = -4\pi\big(n_0(\mathbf{x}) - n_+(\mathbf{x})\big)$$

However, in stark contrast to the Kohn-Sham approach, the kinetic energy is known explicitly in terms of the density, and we don't need any hocus pocus to find the variation $\frac{\delta T[n]}{\delta n_0(\mathbf{x})}$. Instead, we can directly apply the formula for the first variation of a functional defined by integration (see Appendix A):

$$\frac{\delta T[n]}{\delta n_0(\mathbf{x})} = \frac{1}{2}(3\pi^2)^{2/3}n_0^{2/3}(\mathbf{x}) + \frac{\lambda}{8}\left(\frac{\nabla n_0(\mathbf{x})}{n_0(\mathbf{x})}\right)^2 - \frac{\lambda}{4}\frac{\nabla^2 n_0(\mathbf{x})}{n_0(\mathbf{x})}$$

Consequently, the Euler-Lagrange equation becomes the coupled system

$$\frac{1}{2}(3\pi^2)^{2/3}n_0^{2/3}(x) + \frac{\lambda}{8}\left(\frac{n_0'(x)}{n_0(x)}\right)^2 - \frac{\lambda}{4}\frac{n_0''(x)}{n_0(x)} + \phi(x) + V_{\mathrm{xc}}\big(n_0(x)\big) - \upsilon = 0 \tag{4.5}$$

$$\phi''(x) = -4\pi\big(n_0(x) - n_+(x)\big) \tag{4.6}$$

Because the background charge n_+ depends only on the depth into the metal x, the equations reduce to one-dimension and partial derivatives transform into ordinary ones. Finally, the Lagrange multiplier υ is the chemical exchange potential [79] and is equal to

$$\upsilon = \frac{1}{2}(3\pi^2\bar{n})^{2/3} + V_{\mathrm{xc}}(\bar{n}) = \frac{1}{2}k_F^2 + V_{\mathrm{xc}}(\bar{n}) \tag{4.7}$$

Traditionally, this Lagrange multiplier is denoted μ, which is also the symbol ordinarily used for the Fermi level, which coincides with the Fermi energy $\frac{1}{2}k_F^2$ at zero temperature. To make the distinction between

Fermi level and (4.7), which includes an exchange-correlation contribution, v is used for the multiplier. The Lagrange multiplier accounts for the integral constraint in the set of minimization (3.3) of the energy functional, but the positivity one has so far been unenforced. In KS-DFT, this requirement is handled automatically by (3.13), but in OF-DFT, it is not. To that end, let

$$n_0(x) = Y^2(x) \quad \Longrightarrow \quad n_0' = 2YY' \quad \Longrightarrow \quad n_0'' = 2YY'' + 2(Y')^2$$

which yields the set of equations

$$Y'' = \frac{1}{2}(3\pi^2)^{2/3}\lambda^{-1}\,Y^{7/3} + 2\lambda^{-1}Y\big(V_{\mathrm{xc}}(Y^2) + \phi - v\big) \tag{4.8}$$

$$\phi'' = -4\pi(Y^2 - n_+) \tag{4.9}$$

Deep inside the metal, we require that $n_0 \to \bar{n}$ as $x \to -\infty$; electrons cannot get infinitely far away from the surface, so n_0 must vanish at $+\infty$. We also normalize so that the electrostatic potential vanishes inside the metal, or $\phi(-\infty) = 0$. These assertions give the set of boundary conditions

$$\begin{aligned} Y(-\infty) &= \sqrt{\bar{n}} \qquad \phi(-\infty) = 0 \\ Y(+\infty) &= 0 \qquad\quad \phi'(+\infty) = -4\pi\varsigma \end{aligned} \tag{4.10}$$

The last of these corresponds to the charge condition

$$\phi'(+\infty) = -4\pi \int_{-\infty}^{+\infty} \big(n_0(x) - n_+(x)\big)\,dx = -4\pi\varsigma$$

As will be discussed in the next chapter, ς represents screening charge; for a charge-neutral system, $\varsigma = 0$.

4.4 Asymptotic Behavior of the Orbital-Free Density

To prove a result about the asymptotic behavior of the density determined by (4.8)–(4.9), we will call upon the following theorem, a mainstay in theory of control of time-varying systems. The result is necessary because integrability of f is not sufficient to imply existence of a *limit* at infinity.

Theorem 4.5 (**Barbălat's Lemma**). *If $f : [a, +\infty) \to \mathbb{R}$ is uniformly continuous and*

$$\lim_{t \to +\infty} \int_a^t f(s)\,ds$$

exists and is finite, then $f \to 0$ *as* $t \to 0$.

Proof. See, for example, Khalil [53, p.323]. ∎

Corollary 4.6. *If f(t) has a finite limit as* $t \to +\infty$ *and either* f' *is uniformly continuous or* f'' *is bounded, then* $f' \to 0$ *as* $t \to +\infty$.

Proof. By the Fundamental Theorem of Calculus,

$$f(t) = f'(a) + \int_a^t f'(s)\, ds$$

If f' is uniformly continuous and f has a finite limit as $t \to +\infty$, then all the hypothesis of Barbălat's Lemma are satisfied and $f' \to 0$. If f'' is bounded, then f' is Lipschitz, and hence, uniformly continuous. ∎

Theorem 4.7. *The TFDW OF-DFT density* n_0 *satisfies*

$$\lim_{x \to -\infty} n_0'(x) = 0 \qquad\qquad \lim_{x \to -\infty} n_0''(x) = 0$$

Proof. By evaluating (4.8) at the boundary conditions $Y(-\infty) = \sqrt{\bar{n}}$ and $\phi(-\infty) = 0$, we see that $Y''(-\infty) = 0$. Continuity of the right-hand side of (4.8) implies Y'' is too, so we have $Y'' \in C_0(-\infty, a]$ for at least $a < 0$. Since Y has a finite limit at $-\infty$ by imposition, $Y' \to 0$ as $x \to -\infty$ by Corollary 4.6. Then because $n_0' = 2YY'$ and $n_0'' = 2YY'' + 2(Y')^2$, we have both $n_0' \to 0$ and $n_0'' \to 0$ as $x \to -\infty$. ∎

Theorem 4.7 is nice and ultimately necessary for the next result, but it is not terribly enlightening. What we really seek are results that characterize the behavior of the density itself. Below are two such results that give the asymptotic behavior at each infinite endpoint. The first of these was shown by Utreras-Diaz [109]; the proof here mirrors his except that this one contains considerably more detail and makes a farther reaching conclusion. In particular, analytic expressions for the decay factor and oscillation period are part of the theorem statement here, while Utreras-Diaz left them as unknowns.

Theorem 4.8. *As* $x \to -\infty$, *the TFDW OF-DFT density* n_0 *exhibits oscillatory exponentially decay:*

$$n_0(x) \sim \bar{n} + Ae^{\theta x} \cos(\zeta x + \gamma)$$

where the amplitude A *and phase shift* γ *are unknown, but*

$$\theta = \frac{\sqrt{\sqrt{\alpha^2 + D^2} + \alpha}}{2} > 0 \qquad\qquad \zeta = \frac{\sqrt{\sqrt{\alpha^2 + D^2} - \alpha}}{2}$$

where α and D are given by

$$\alpha = \frac{4}{\lambda}\left(\frac{1}{3}\left(3\pi^2\bar{n}\right)^{2/3} + \bar{n}f_{xc}(\bar{n})\right) \qquad D = \operatorname{Im}\sqrt{\alpha^2 - \frac{64\pi\bar{n}}{\lambda}}$$

Furthermore, n_0', ϕ, ϕ', and ϕ'' all decay to zero in the same manner with rate θ and frequency ζ.

Proof. Rather than work with Y, it is more convenient this time to write (4.8) and (4.9) directly in n_0:

$$n_0'' = \frac{4n_0}{\lambda}\left[\frac{1}{2}(3\pi^2)^{2/3}n_0^{2/3} + \frac{\lambda}{8}\frac{(n_0')^2}{n_0} + V_{\mathrm{xc}}(n_0) + \phi - \upsilon\right] \tag{4.11}$$

$$\phi'' = -4\pi(n_0 - n_+) \tag{4.12}$$

Our analysis is based on linearization. Define $\rho_1 \triangleq n_0$ and $\rho_2 \triangleq n_0'$ so that (4.11) becomes

$$\begin{aligned}\rho_1' &= \rho_1\\ \rho_2' &= \frac{4\rho_1}{\lambda}\left[(3\pi^2)^{2/3}\rho_1^{2/3} + \frac{\lambda}{8}\frac{\rho_2^2}{\rho_1} + V_{\mathrm{xc}}(\rho_1) + \phi - \upsilon\right] \triangleq f(\rho_1, \rho_2, \phi, \phi')\end{aligned}$$

Because $n_+ = \bar{n}$ for $x < 0$, Corollary 4.6 gives that $\phi' \to 0$ as $x \to -\infty$. The boundary conditions $n_0(-\infty) = \bar{n}$ and $\phi(-\infty) = 0$ plus Theorem 4.7 imply that the equilibrium point about which we are linearizing is $(\rho_1, \rho_2, \phi, \phi') = (\bar{n}, 0, 0, 0)$. We first compute the partial of f with respect to ρ_1:

$$\frac{\partial f}{\partial \rho_1} = \frac{4}{\lambda}\left[\frac{1}{2}(3\pi^2)^{2/3}\rho_1^{2/3} + \frac{\lambda}{8}\frac{\rho_2^2}{\rho_1} + V_{\mathrm{xc}}(\rho_1) + \phi - \upsilon\right] + \frac{4\rho_1}{\lambda}\left[\frac{1}{3}(3\pi^2)^{2/3}\rho_1^{-1/3} - \frac{\lambda}{8}\left(\frac{\rho_2}{\rho_1}\right)^2 + f_{\mathrm{xc}}(\rho_1)\right]$$

where $f_{\mathrm{xc}} = V_{\mathrm{xc}}'$ as in (3.31). Now we evaluate:

$$\frac{\partial f}{\partial \rho_1}(\bar{n}, 0, 0, 0) = \frac{4}{\lambda}\left[\frac{1}{3}\left(3\pi^2\bar{n}\right)^{2/3} + \bar{n}f_{\mathrm{xc}}(\bar{n})\right]$$

wherein we used the value of υ in (4.7). Partials of f with respect to ρ_2 and ϕ are easily seen:

$$\frac{\partial f}{\partial \rho_2}(\bar{n}, 0, 0, 0) = 0 \qquad \frac{\partial f}{\partial \phi}(\bar{n}, 0, 0, 0) = 4\bar{n}\lambda^{-1}$$

Noting that (4.12) is already linear, after defining $\phi_1 \triangleq \phi$, and $\phi_2 \triangleq \phi'$, we can cast the linearization of (4.8)

and (4.9) into the matrix system

$$\frac{\partial}{\partial x}\begin{pmatrix}\rho_1\\ \rho_2\\ \phi_1\\ \phi_2\end{pmatrix} = \begin{pmatrix}0 & 1 & 0 & 0\\ \alpha & 0 & 4\bar{n}\lambda^{-1} & 0\\ 0 & 0 & 0 & 1\\ -4\pi & 0 & 0 & 0\end{pmatrix}\begin{pmatrix}\rho_1\\ \rho_2\\ \phi_1\\ \phi_2\end{pmatrix} \triangleq A\begin{pmatrix}\rho_1\\ \rho_2\\ \phi_1\\ \phi_2\end{pmatrix} \tag{4.13}$$

where

$$\alpha \triangleq \frac{4}{\lambda}\left(\frac{1}{3}(3\pi^2\bar{n})^{2/3} + \bar{n}f_{\mathrm{xc}}(\bar{n})\right)$$

The solution to (4.13) may be characterized by the eigenvalues of A, which can be computed analytically:

$$\lambda_1 = \frac{1}{2}\sqrt{2\alpha + 2\sqrt{\alpha^2 - 64\pi\bar{n}\lambda^{-1}}} \qquad \lambda_2 = -\lambda_1$$
$$\lambda_3 = \frac{1}{2}\sqrt{2\alpha - 2\sqrt{\alpha^2 - 64\pi\bar{n}\lambda^{-1}}} \qquad \lambda_4 = -\lambda_3$$

We now need to examine the quantities λ_1 and λ_3 closer. First, define the function of $\bar{n}$

$$\Delta(\bar{n}) \triangleq \alpha^2 - 64\pi\bar{n}\lambda^{-1} = \frac{16}{\lambda^2}\left[\frac{1}{3}(3\pi^2\bar{n})^{2/3} + \bar{n}f_{\mathrm{xc}}(\bar{n})\right]^2 - \frac{64\pi\bar{n}}{\lambda}$$

Plotted below in terms of r_s, which from the periodic table in Figure 3.2 we know ranges from $1.61 \le r_s \le 5.63$ for elemental metals, we see that $\Delta(\bar{n}) < 0$ for relevant values of λ in Figure 4.2 below.

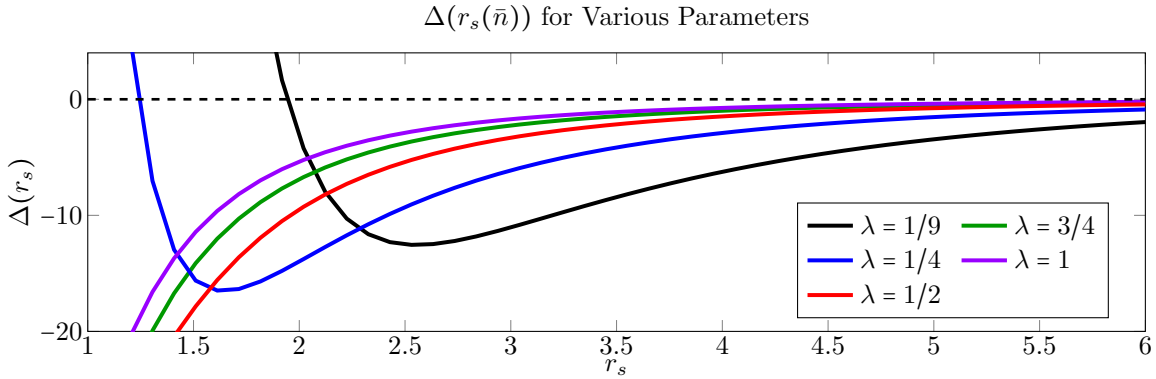

Figure 4.2: $\Delta(\bar{n})$ for Relevant r_s Values. For physical values of r_s and appropriate λ, we have $\Delta(\bar{n}) < 0$. For $\lambda = \frac{1}{9}$, we have $\Delta < 0$ for $r_s > 1.9427$ or $\bar{n} = 3.2560 \times 10^{-2}$. For $\lambda = \frac{1}{4}$, Δ crosses zero at $r_s = 1.2380$, well below the lowest possible physical value of the parameter.

Because $\sqrt{\Delta(\bar{n})} \in i\mathbb{R}$, define $D \triangleq \mathrm{Im}\sqrt{\Delta}$ with $D > 0$. Then we have

$$\lambda_1 = \frac{\sqrt{2}}{2}\sqrt{\alpha + iD} \qquad \lambda_3 = \frac{\sqrt{2}}{2}\sqrt{\alpha - iD}$$

Using the formula for the square root of a complex number (principle branch),

$$\sqrt{a+bi} = \frac{1}{\sqrt{2}}\sqrt{\sqrt{a^2+b^2}+a} \; + \; i\,\frac{\operatorname{sgn}(b)}{\sqrt{2}}\sqrt{\sqrt{a^2+b^2}-a}$$

we may express λ_1 and λ_3 as

$$\lambda_1 = \frac{1}{2}\left[\sqrt{\sqrt{\alpha^2+D^2}+\alpha} + i\sqrt{\sqrt{\alpha^2+D^2}-\alpha}\right]$$
$$\lambda_3 = \frac{1}{2}\left[\sqrt{\sqrt{\alpha^2+D^2}+\alpha} - i\sqrt{\sqrt{\alpha^2+D^2}-\alpha}\right]$$

We observe that $\lambda_3 = \bar{\lambda}_1$. Because $\mathrm{Re}(\lambda_1), \mathrm{Re}(\lambda_3) > 0$ and $\lambda_2 = -\lambda_1$, $\lambda_4 = -\lambda_3$ and $\rho_1 \to \bar{n}$, we know that the modes corresponding to λ_2 and λ_4 must be not active in the solution for ρ_1. Therefore, we have

$$\rho_1(x) \sim \bar{n} + K_1 e^{\lambda_1 x} + K_2 e^{\lambda_3 x} = K_1 e^{\lambda_1 x} + K_2 e^{\bar{\lambda}_1 x}$$

Defining

$$\theta \triangleq \frac{\sqrt{\sqrt{\alpha^2+D^2}+\alpha}}{2} \qquad\qquad \zeta \triangleq \frac{\sqrt{\sqrt{\alpha^2+D^2}-\alpha}}{2}$$

so that $\lambda_1 = \theta + i\zeta$, we have

$$\begin{aligned}
\rho_1(x) &\sim \bar{n} + K_1 e^{\theta x}\left[\cos\zeta x + i\sin\zeta x\right] + K_2 e^{\theta x}\left[\cos\zeta x - i\sin\zeta x\right] \\
&\sim \bar{n} + e^{\theta x}\left[(K_1+K_2)\cos\zeta x + i(K_1-K_2)\sin\zeta x\right] \\
&\sim \bar{n} + e^{\theta x}\left[\tilde{K}_1\cos\zeta x + \tilde{K}_2\sin\zeta x\right]
\end{aligned} \tag{4.14}$$

We note that $K_1, K_2 \in \mathbb{C}$ but in the above expression, we must have $\tilde{K}_1, \tilde{K}_2 \in \mathbb{R}$. Thus, we may write

$$\rho_1(x) \sim \bar{n} + e^{\theta x}\sqrt{\tilde{K}_1^2+\tilde{K}_2^2}\left[\frac{\tilde{K}_1}{\sqrt{\tilde{K}_1^2+\tilde{K}_2^2}}\cos\zeta x + \frac{\tilde{K}_2}{\sqrt{\tilde{K}_1^2+\tilde{K}_2^2}}\sin\zeta x\right] \tag{4.15}$$

Accordingly, there exists $\gamma \in \mathbb{R}$ such that

$$\cos\gamma = \frac{\tilde{K}_1}{\sqrt{\tilde{K}_1^2+\tilde{K}_2^2}} \qquad\qquad \sin\gamma = -\frac{\tilde{K}_2}{\sqrt{\tilde{K}_1^2+\tilde{K}_2^2}}$$

so that (4.15) becomes

$$\rho_1(x) = n_0(x) \sim \bar{n} + e^{\theta x}\sqrt{\tilde{K}_1^2 + \tilde{K}_2^2}\Big[\cos\gamma\cos\zeta x - \sin\gamma\sin\zeta x\Big]$$
$$\sim \bar{n} + Ae^{\theta x}\cos(\zeta x + \gamma)$$

after applying the standard difference formula from elementary trigonometry.

Because $\rho_2 = n_0'$, $\phi_1 = \phi$, and $\phi_2 = \phi'$ all decay to zero, the linearized solution for each takes the form (4.14), except without the $\bar{n}$. We may repeat the analysis that led to the asymptotic form of ρ_1. The constants K_1 and K_2 come from the first component of the eigenvector corresponding to λ_1; θ and ζ come from the eigenvalue and are independent of the entries of the eigenvector. Consequently, each of $n_0', \phi, \phi' \sim e^{\theta x}\cos(\zeta x + \gamma)$ as $x \to -\infty$, with each having its own proportionality constant. That ϕ'' also exhibits this behavior is clear from the dynamics (4.12). This completes the proof. ■

Remark 4.1. Utreras-Diaz asserted that the decay is still exponentially oscillatory even the absence of exchange-correlation. However, this is not the case for all metals. If $V_{\text{xc}} \equiv 0$, then $\Delta(\bar{n})$ becomes

$$\Delta(\bar{n}) = \frac{16}{9\lambda^2}(3\pi^2\bar{n})^{4/3} - \frac{64\pi\bar{n}}{\lambda}$$

Using the relation $k_F = (3\pi^2\bar{n})^{1/3}$, we can write

$$\Delta(k_F) = \frac{16}{3\lambda}k_F^3\left(\frac{1}{3\lambda}k_F - \frac{4}{\pi}\right)$$

which is positive until $k_F = 12\lambda\pi^{-1}$. For $\lambda = \frac{1}{9}$, this happens at $k_F = 0.4244$ or $r_s = 4.5219$, well-within the range of physical values. Utreras-Diaz expressed surprise at his result and had pegged exchange-correlation as the likely source of oscillation. His intuition was correct but his analysis clearly erred somewhere. For $\lambda = \frac{1}{4}$, the transition occurs at $k_F = 0.9549$ or $r_s = 2.0097$, which is at the bottom of the physical range. ■

Remark 4.2. It is possible to compute both the amplitude A and γ analytically, but the formulas are so cumbersome and unwieldy that they are not illustrative. They have accordingly been omitted here. ■

The table below gives values of the decay rate θ and frequency of oscillation ζ for common materials.

The following result appears in several sources [15],[67, p.14], yet no hint of its derivation or reference thereto is ever provided. We have therefore produced a rigorous proof of this very important property.

Material	r_s	θ	ζ
Platinum	2.01	1.4132	0.6589
Zinc	2.31	1.2354	0.6686
Copper	2.67	1.0726	0.6614
Silver/Gold	3.01	0.9530	0.6469
Sodium	3.93	0.7283	0.5990
Potassium	4.86	0.5832	0.5537

Table 4.1: TFDW Decay Rate and Frequency of Oscillation. The values for the decay rate θ and frequency of oscillation ζ for common materials. This values differ from those appearing in Utreras-Diaz because he used the Wigner correlation kernel; these were computed with Perdew-Wang.

Theorem 4.9. *As $x \to +\infty$, the TFDW OF-DFT density n_0 for charge-neutral systems decays exponentially:*

$$n_0 \sim B \exp\left(-2x\sqrt{\frac{2\big(\upsilon - \phi(+\infty)\big)}{\lambda}}\right) \tag{4.16}$$

where B is an undetermined constant.

Proof. The starting point is the original Euler-Lagrange equations (4.5)–(4.6). The method of attack for proving this theorem is the method of dominant balance [5, p.83]: suppose that $n_0 \sim e^{\theta x}$ for some $\theta < 0$. Then we can characterize the behavior of the various terms appearing in the top equation as follows:

$$\text{Terms that approach constants:} \quad \left(\frac{n_0'(x)}{n_0(x)}\right)^2,\ \frac{n_0''(x)}{n_0(x)},\ \phi(x),\ \upsilon$$

$$\text{Terms that go to 0 exponentially:} \quad n_0^{2/3}(x),\ V_{\text{xc}}\big(n_0(x)\big)$$

The proof of Theorem 3.4 shows that the slowest decaying piece of V_{xc} behaves as r_s^{-1}. While $\phi \to \phi(+\infty) \neq 0$, it does so at an exponential rate; this is apparent from (4.6), after integrating twice, if $n_0 \sim e^{\theta x}$ is assumed. Therefore, for large x, we must have

$$\frac{\lambda}{8}\left(\frac{n_0'(x)}{n_0(x)}\right)^2 - \frac{\lambda}{4}\frac{n_0''(x)}{n_0(x)} + \phi(+\infty) - \upsilon = 0$$

Define $K \triangleq 8\lambda^{-1}\big(\phi(+\infty) - \upsilon\big) > 0$. (See Remark 4.4 afterwards for a demonstration of positivity.) We then must solve

$$\left(\frac{n_0'(x)}{n_0(x)}\right)^2 = 2\,\frac{n_0''(x)}{n_0(x)} - K \tag{4.17}$$

Motivated by the observation that

$$\frac{\partial}{\partial x}\left[\frac{n_0'}{n_0}\right] = -\left(\frac{n_0'}{n_0}\right)^2 + \frac{n_0''}{n_0}$$

we subtract $2\left(\frac{n_0'}{n_0}\right)^2$ from both sides of (4.17) and use that $\frac{\partial}{\partial x}\big[\log n_0\big] = \frac{n_0'}{n_0}$ to obtain

$$-\left(\frac{n_0'(x)}{n_0(x)}\right)^2 = 2\left[\frac{n_0''(x)}{n_0(x)} - \left(\frac{n_0'(x)}{n_0(x)}\right)^2\right] - K$$
$$-\left[\frac{\partial}{\partial x}\big(\log n_0\big)\right]^2 = 2\,\frac{\partial}{\partial x^2}\Big[\log n_0\Big] - K$$

Making the substitution $g \triangleq \frac{\partial}{\partial x}\big[\log n_0\big]$, what we must solve is then

$$g' + \frac{1}{2}g^2 = \frac{1}{2}K \tag{4.18}$$

To solve (4.18), introduce another substitution:

$$g(x) \triangleq -\sqrt{K} + h(x) \quad \Longrightarrow g'(x) = h'(x)$$
$$\Longrightarrow \quad g^2 = K - 2h\sqrt{K} + h^2$$

Then (4.18) becomes

$$h' - h\sqrt{K} + \frac{1}{2}h^2 = 0 \quad \Longrightarrow \quad \frac{h'}{h\sqrt{K} - \frac{1}{2}h^2} = 1$$

We may solve by converting to partial fractions,

$$\frac{1}{\sqrt{K}}\left(\frac{1}{h} + \frac{1}{2\sqrt{K} - h}\right)h' = 0$$

and then integrating to obtain

$$\log h - \log\left(2\sqrt{K} - h\right) = x\sqrt{K} + A$$

Solving for h yields

$$h(x) = 2\sqrt{K}\,\frac{Ae^{x\sqrt{K}}}{Ae^{x\sqrt{K}} + 1}$$

Using the definitions of h and g yields the following simple equation for n_0:

$$\frac{\partial}{\partial x}\big[\log n_0\big] = -\sqrt{K} + 2\sqrt{K}\,\frac{Ae^{x\sqrt{K}}}{Ae^{x\sqrt{K}} + 1}$$

which may be integrated directly and then solved for n_0:

$$n_0 = Be^{-x\sqrt{K}}\left(Ae^{x\sqrt{K}} + 1\right)^2$$

Finally, because $n_0 \to 0$, we know that $A = 0$ (B remains undetermined), so we have

$$n_0 = B\exp\left(-2x\sqrt{\frac{2\big(\upsilon - \phi(+\infty)\big)}{\lambda}}\right) \qquad \blacksquare$$

Remark 4.3. The method of dominant balance supposes behavior of the form $e^{S(x)}$ and then solves a differential equation for S. We know that without the exchange-correlation term, the TFDW density decays exponentially [83, p.133]. It is therefore a reasonable supposition that the result should still hold in its presence, so we put $S(x) = \theta x$ from the outset to reach the inevitable conclusion with greater celerity. $\blacksquare$

Remark 4.4. In the above proof, we asserted the positivity of K without explanation. That $K > 0$ follows readily from the work function Φ_W, which will not be detailed until Section 5.1.2. The author did not wish to clutter the proof with a lengthy aside on this concept. Based on its physical interpretation, Φ_W is always positive. If $\lambda = 1$, then the exponential decay rate is exactly $2\Phi_W$. By (4.7), we have

$$\begin{aligned}\phi(+\infty) - \upsilon &= \phi(+\infty) - \frac{1}{2}k_F^2 - V_{\mathrm{xc}}(\bar{n}) \\ &= D - V_{\mathrm{xc}}(-\infty) - E_F = \Phi_W\end{aligned}$$

The physical significance is that the gradient correction forces the density to decay twice the energy it takes to remove them. As λ decreases to zero, the rate of decay increases, meaning that a weak gradient correction forces the electrons to remain closer to the surface. As $\lambda \to 0$, electrons improperly bunch up at the surface, reflecting that the $\lambda \to 0$ limit of the TFDW model is Thomas-Fermi-Dirac. $\blacksquare$

Because n_+ is discontinuous, $n_0 - n_+ \notin H^2(\mathbb{R})$ because requisite absolute continuity is lacking at the origin. However, as a direct consequence of Theorems 4.8 and 4.9 in tandem, we can assert the following.

Corollary 4.10. *$n_0 - \bar{n} \in W^{2,p}(-\infty, 0)$ and $n_0 \in W^{2,p}(0, +\infty)$ for $1 \le p \le \infty$, where $W^{2,p}$ is the Sobolev space*

$$W^{2,p}(A) = \left\{f \in L^p(A) : f', f'' \in L^p(A)\right\}$$

Remark 4.5. The specifics of V_{xc} were not used in any of the proofs of Theorems 4.9 and 4.8, aside from requiring that the decay of V_{xc} be dominated by some homogeneous term so that the overall decay remains

exponential and that V_{xc} vanish as $n \to 0$. As seen in the proof of Theorem 3.4, the exchange energy decays like r_s^{-2}. Neglecting correlation but including exchange, which is the Thomas-Fermi-Dirac model, leads to a density that exhibits polynomial decay $|x|^{-6}$ as $|x| \to +\infty$ (for a single atom) [83, p.112].

Without correlation, the TFDW density decays as $|x|^{-2} e^{-C|x|}$ for single-atom systems [83, p.133]. Here, with correlation, we have a purely exponential rate of decay. Again recalling the proof of Theorem 3.4, the correlation exhibits slower decay than the exchange, which accounts for the difference.

What can be concluded from all this is that it is the gradient correction that give the exponential decay; correlation is not insignificant, however, as its inclusion slows the decay rate by a factor of $|x|^2$. ∎

The section has one final asymptotic result, which concerns the value of the electrostatic potential at $+\infty$.

Theorem 4.11. *For a charge neutral system (i.e., $\phi'(+\infty) = 0$) normalized so that $\phi(-\infty) = 0$,*

$$\phi(+\infty) = 4\pi \int_{-\infty}^{+\infty} y\big[n_0(y) - n_+(y)\big]\, dy \tag{4.19}$$

Proof. The Green's function for the Poisson equation in 1D is $G(x-y) = -2\pi|x-y|$; we may obtain the solution to (4.6) by integrating against G. The exponential decay of both $n_0 - n_+ \to 0$ at both endpoints makes the integral

$$\phi(x) = -2\pi \int_{-\infty}^{+\infty} |x-y| \big[n_0(y) - n_+(y)\big]\, dy$$

well-defined and absolutely convergent (not a principle value). Then for $x > 0$,

$$\begin{aligned} -\frac{1}{2\pi}\left(\phi(x) - \phi(-x)\right) &= \int_{-\infty}^{x} (x-y)\big[n_0(y) - n_+(y)\big]\, dy + \int_{x}^{+\infty} (y-x)\big[n_0(y) - n_+(y)\big]\, dy \\ &\quad - \int_{-\infty}^{-x} (-x-y)\big[n_0(y) - n_+(y)\big]\, dy - \int_{-x}^{+\infty} (y+x)\big[n_0(y) - n_+(y)\big]\, dy \\ &= 2x \int_{-\infty}^{-x} \big[n_0(y) - n_+(y)\big]\, dy - 2\int_{-x}^{x} y\big[n_0(y) - n_+(y)\big]\, dy \end{aligned}$$

Now consider

$$\lim_{x\to+\infty} x \int_{-\infty}^{-x} \big[n_0(y) - n_+(y)\big]\, dy = \lim_{x\to+\infty} \frac{\int_{-\infty}^{-x} \big[n_0(y) - n_+(y)\big]\, dy}{1/x}$$

Because $n_0 - n_+$ is integrable due to its exponential decay, the numerator tends to zero as $x \to +\infty$. It is therefore valid to apply L'Hopital's Rule, followed by the change of variables $x \mapsto -x$:

$$\lim_{x\to+\infty} x \int_{-\infty}^{-x} \big[n_0(y) - n_+(y)\big]\, dy = \lim_{x\to-\infty} \frac{n_0(x) - n_+(x)}{1/x^2} = \lim_{x\to-\infty} x^2\big(n_0(x) - \bar{n}\big) = 0$$

because the exponential squashes the x^2. Consequently,

$$\lim_{x\to+\infty}\left(\phi(x)-\phi(-x)\right) = 4\pi \lim_{x\to+\infty}\int_{-x}^{x} y\big[n_0(y)-n_+(y)\big]\,dy$$

Then because ϕ is finite at both $+\infty$ and $-\infty$, we have

$$\begin{aligned}\phi(+\infty) &= \phi(-\infty) + 4\pi \lim_{x\to+\infty}\int_{-x}^{x} y\big[n_0(y)-n_+(y)\big]\,dy\\ &= 4\pi\int_{-\infty}^{\infty} y\big[n_0(y)-n_+(y)\big]\,dy\end{aligned}$$

with the last line following from that $\phi(-\infty)=0$. ■

4.5 Numerical Implementation

The numerical method we will use to solve (4.8)–(4.9) is the adaptive spline method of Chapter 2 detailed in Algorithm 2.3. However, a challenge in applying the spline method is that (4.9) contains a discontinuous term in n_+. It is well-known that attempts to interpolate across discontinuities fail dramatically. A simple fix for jump discontinuities (as n_+ has) is to place the discontinuity at a node and break into right-hand and left-hand problems, using the appropriate limit values to make the function seem continuous to the interpolation technique. However, doing so requires the value of the function to be known at the break.

Fortunately, Theorems 4.2 and 4.4 provide just the information needed to remedy the issue. First, let

$$f(Y,\phi) \triangleq \frac{1}{2\lambda}\left(3\pi^2\right)^{2/3} Y^{7/3} + \frac{2}{\lambda}\, Y\big(V_{\mathrm{xc}}(Y^2)+\phi-\upsilon\big)$$

Instead of (4.8) and (4.9) with the boundary conditions (4.10), we consider the left and right problems

$$\begin{array}{lllll}
\text{Left problem:} & Y'' = f(Y,\phi) & Y(-\infty)=\sqrt{\bar{n}} & Y(0)=\sqrt{\bar{n}}\left(\frac{3}{5}\right)^{3/4} \\
& \phi'' = -4\pi(Y^2-\bar{n}) & \phi(-\infty)=0 & \phi(0)=\phi_{\mathrm{BV}} \\
\text{Right problem:} & Y'' = f(Y,\phi) & Y(0)=\sqrt{\bar{n}}\left(\frac{3}{5}\right)^{3/4} & Y(+\infty)=0 \\
& \phi'' = -4\pi Y^2 & \phi(0)=\phi_{\mathrm{BV}} & \phi'(+\infty)=0
\end{array}$$

where $\phi_{BV} \triangleq \frac{1}{5}\left(3\pi^2\bar{n}\right)^{2/3} + V_{\mathrm{xc}}(\bar{n}) - \varepsilon_{\mathrm{xc}}(\bar{n})$. Computation will be restricted to charge-neutral systems for the scope of this demonstration so that $\varsigma = 0$ or $\phi'(+\infty)=0$.

Of the two spline method algorithms, Algorithm 2.1 is the one applicable to nonlinear BVPs. To complete

the recipe for the spline method detailed in Section 2.2, we need the derivatives

$$\frac{\partial f}{\partial Y} = \frac{7}{6\lambda}(3\pi^2)^{2/3}\, Y^{4/3} + \frac{2}{\lambda}\big(V_{\mathrm{xc}}(Y^2) + \phi - \upsilon\big) + \frac{2Y^2}{\lambda} f_{\mathrm{xc}}(Y^2)$$
$$\frac{\partial f}{\partial \phi} = \frac{2Y}{\lambda}$$

Note that Theorem 3.5 ensures that $Y^2 f_{\mathrm{xc}}(Y^2)$ will behave for large x when $Y \to 0$. The derivatives in Y of the equations for ϕ'' are trivial to compute, so they are not presented here.

To extend the spline method from single equations to systems, let a_k, b_k, c_k, d_k be the coefficients of the k^{th} spline for Y and $\bar{a}_k, \bar{b}_k, \bar{c}_k, \bar{d}_k$ be those for ϕ. Then we interweave these as sets to form the coefficient vector

$$\mathbf{c} = \Big(a_1, b_1, c_1, d_1, \bar{a}_1, \bar{b}_1, \bar{c}_1, \bar{d}_1, \cdots, a_N, \cdots, d_N, \bar{a}_N, \cdots, \bar{d}_N\Big)^T$$

The equations go in corresponding procession, with the two DE, the C^0, and then C^1 conditions for the k^{th} spline for Y first, followed by the ones for ϕ. This arrangement retains the banded structure of the Jacobian matrix $\mathbf{J}$ that allows for efficient solution, although the bandwidth will double from four to eight.

Per Step 1 of Algorithm 2.1, Newton's method needs an initial guess. For this, we use the trial density

$$n^{(0)} = \frac{1}{1 + e^{10x}}$$

and then perform standard spline interpolation on the initial mesh. We then take $\phi^{(0)} \equiv 0$.

To extend the mechanism of adaptive grid generation to the system, we form the errors

$$\mathcal{E}_{k+1/2} = \max\left\{ \left|Y_k''(x_{k+1/2}) - f\big(Y_k(x_{k+1/2}), \phi_k(x_{k+1/2})\big)\right|, \left|\phi_k''(x_{k+1/2}) + 4\pi\big(Y_k(x_{k+1/2}) - n_+(x_{k+1/2})\big)\right| \right\}$$

where Y_k and ϕ_k denote the k^{th} spline in the numerical solution for Y and ϕ, respectively. Points are then added just as before. In this manner, Y and ϕ are solved on the same grid.

After computation, we form n_0 by squaring the spline solution for Y using spline arithmetic. See Appendix C for details. This results in sixth degree polynomials, although they remain only C^2 and $\mathcal{O}(h^4)$ accurate.

4.6 Computational Results

In this example, $r_s = 3$ and the infinite domain was truncated to $[-20, 10]$. With the exponential decay of the density on both sides, even this domain is larger than necessary. An adaptive tolerance of $\tau_a = 10^{-7}$ was used. The results are compiled below in Figures 4.3, 4.4, and 4.5.

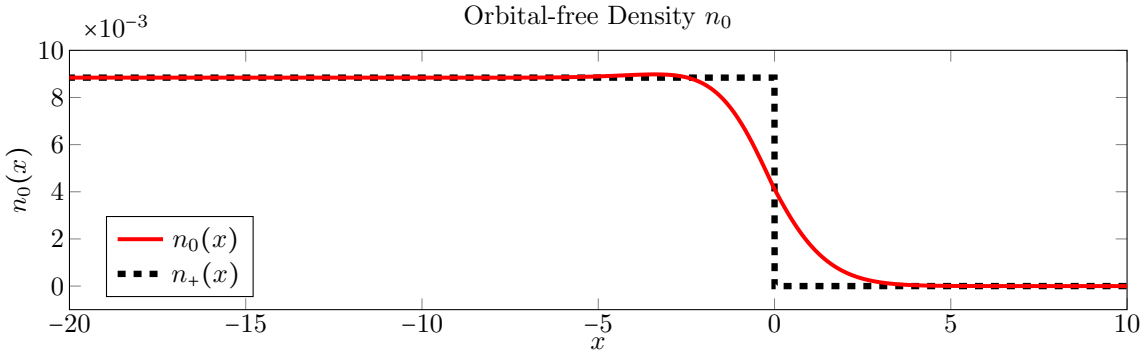

Figure 4.3: Orbital-free Density for $r_s = 3$. This figure depicts the TFDW OF-DFT ground state density There is little overshoot of the background charge and convergence to limits is incredibly rapid.

The density itself is rather unremarkable and there is little to say about it. The profile decays rapidly to its limits $\bar{n}$ in the bulk metal and zero in the vacuum. Figure 4.4 highlights the oscillations.

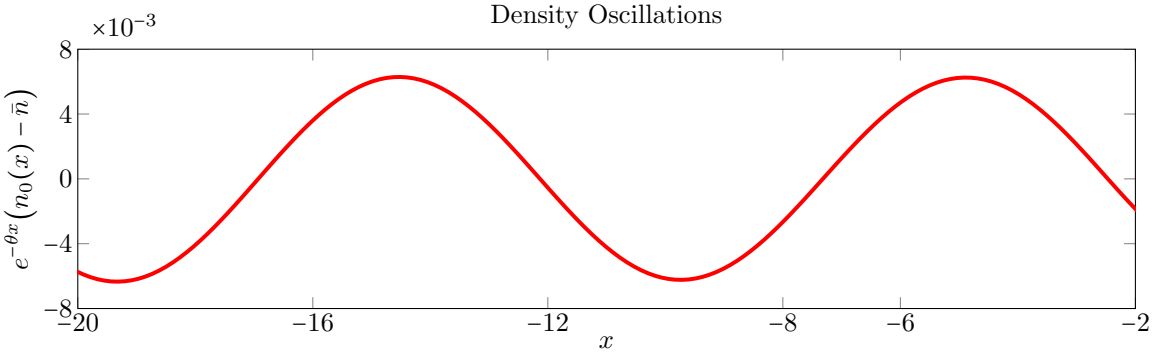

Figure 4.4: Highlight of Density Oscillations. By depicting $e^{-\theta x}\left(n_0(x) - \bar{n}\right)$, this figure highlights the oscillations in the density. Computed per Theorem 4.8, $\theta = 0.9562$. By equating $A\cos(\zeta x + \gamma)$ with the numerical solution evaluated at the points $x_1 = -18$ and $x_2 = -15$, we find $A = -6.337 \times 10^{-3}$ and $\gamma = -0.04312$. Although not shown, substitution of these values into $A\cos(\zeta x + \gamma)$, with $\zeta = 0.6474$ per Theorem 4.8, yields excellent agreement with the depicted plot throughout the domain.

The corresponding electrostatic potential settles into its limit values just as quickly as the density. There is large a dip near the surface. The low point does not correspond to the peak overshoot in n_0, which is located approximately one unit farther into the bulk material.

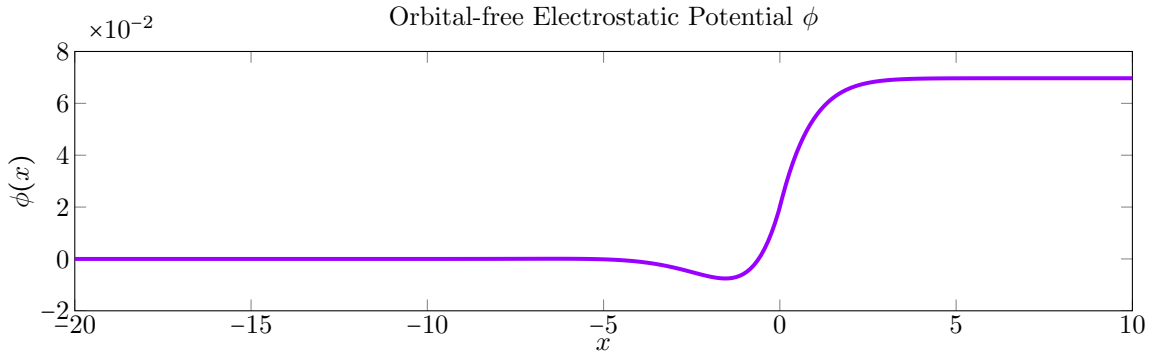

Figure 4.5: Orbital-free Electrostatic Potential. This figure shows the electrostatic potential corresponding to Figure 4.3. Convergence is very rapid, with limits nearly attained by $x = -5$ and $x = 5$.

The number line of Figure 4.6 portrays the distribution of splines across the domain. On the very left, there is no refinement of the initial mesh, which had spacing $h = 0.02$.

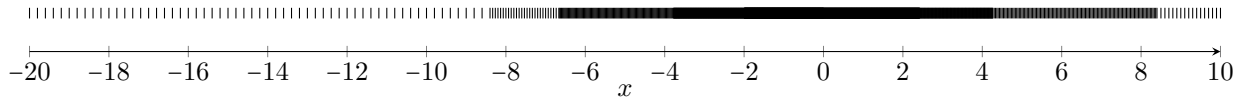

Figure 4.6: Spline Distribution for OF-DFT Computation. Solving the right problem to tolerance $\tau_a = 10^{-7}$ required 1262 splines; the left needed 960. As we see, the splines are concentrated near the origin, where the transition is sharpest. Very few are needed in flat areas at both ends of the domain.

4.7 Conclusion

Because of the liberties that must be taken in the kinetic energy, OF-DFT is less often deployed than its cousin KS-DFT. For very large systems, however, when the Kohn-Sham method becomes intractable, OF-DFT offers a very reasonable approximation, especially if the alternative is nothing at all. The adaptive spline method presented here is capable of finding highly accurate solutions in just a few seconds.

The primary contributions of this chapter are the proofs of Theorems 4.8 and 4.9. A less advanced version of the first was presented in a published source, and due to an error in computation, reached an erroneous conclusion about the source of the oscillations. The more illustrative proof produced here allowed the mistake to be discovered and provides support for the original author's intuition that exchange-correlation plays an important role in the oscillatory nature of TFDW densities.

The result of the second theorem appears in [15], but no reference to its proof is provided. Only a heuristic

argument based on the nature of electrons near the Fermi level was given to support the validity of the claim. Making a rigorous proof of this fundamental result available serves mathematical and physics audiences alike.

The computational methodology here marks an advancement in the OF-DFT techniques for jellium of Chizmeshya and Zaremba [15]. Their work includes a third equation in total charge $Q = \phi'$ to contain the boundary condition $Q(+\infty) = \varsigma = -\frac{1}{4\pi}\phi'(+\infty)$ so that standard BVP methods can be applied. Placing the boundary condition directly on ϕ' reduces the size of the computation by one-third. Furthermore, the novelty of employing the Budd-Vanninemus Theorem and Theorem 4.4 to circumvent the discontinuity in n_+ must not be discounted. The decomposition into left and right problems expands the set of usable numerical solvers from those that can handle discontinuities to virtually anything that works on BVPs.

Chapter 5

The Ground State: Kohn-Sham DFT

5.1 Introduction to Solid-State Physics

The previous chapter introduced a solid-state physics model for interacting electrons within a metal solid called jellium. This section discusses a few needed concepts from solid-state physics in brevity.

5.1.1 The Fermi Surface and Fermi Sphere

The most rudimentary concepts of solid-state physics are inherently linked to the construction of an N-electron atom. The Pauli Exclusion Principle states that no more than two electrons can occupy the same energy level (orbital) at the same time. Following this principle, electrons are shuffled into the discrete energy levels described by quantum mechanics as follows:

1. Place two electrons at energy level zero.
2. Proceed to the orbital corresponding to the next energy level and place two electrons.
3. Repeat Step 2 until the supply of electrons has been exhausted.

If $\mathbf{k}$ is the momentum of a particle, then its energy ε is given by

$$\varepsilon = \frac{1}{2}\mathbf{k}^2$$

so that we may index particles by energy or (magnitude of) momentum interchangeably. This fact, along with Figure 5.1 on the next page, motivates a slew of "Fermi" terminology:

- **Fermi wavevector**: k_F, momentum at the highest energy level.

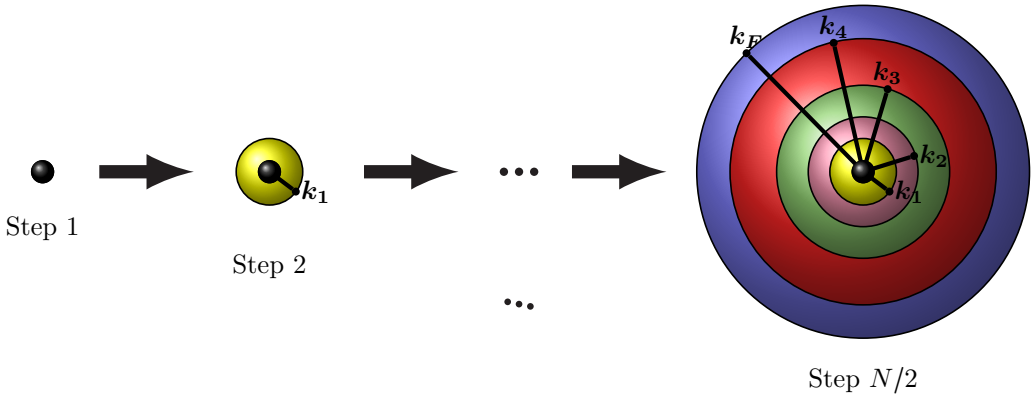

Figure 5.1: Placement of N electrons. In Step 1, two electrons are placed at momentum $k = 0$. In Step 2, two electrons are placed at k_1. The process continues until step $N/2$ when the final electrons are placed at momentum level k_F, called the Fermi wavevector.

- **Fermi sphere**: sphere of radius k_F (outermost layer). It encloses all occupied energy levels.
- **Fermi surface**: surface of the Fermi sphere. It separates occupied from unoccupied orbitals.
- **Fermi energy**: energy level of the highest occupied particles. It is given by

$$E_F = \frac{1}{2}k_F^2 \tag{5.1}$$

Some care is needed with the term "Fermi energy." It is more properly the energy difference between the highest and lowest occupied energy levels and can only be defined at zero temperature. Zero-temperature models are excellent approximations for ordinary finite temperatures and are accordingly used in this thesis.

5.1.2 Three Important Physical Quantities

In this section, we introduce some physical quantities of critical importance in solid-state and surface physics. Because of their limited role in this thesis, characterization here will be restricted to a brief description and mathematical definition. Comprehensive discussions can be found in Ashcroft [2], for example.

Definition 5.1 (**Surface dipole barrier**). *The* surface dipole barrier D *is a dipole layer formed at the surface due to the spill-out of electrons from the material into the vacuum. It is given by*

$$D \triangleq \phi(+\infty) - \phi(-\infty) \tag{5.2}$$

Definition 5.2 (**Surface barrier potential**). *The* surface barrier potential *is the total height of the barrier potential seen by an electron on the surface. It is given by*

$$\begin{aligned}\Delta V &\triangleq V(+\infty) - V(-\infty) \\ &= D - V_{xc}(-\infty)\end{aligned} \tag{5.3}$$

with the second line coming because V_{xc} vanishes as $x \to +\infty$.

Definition 5.3 (**Work function).** *The* work function *is the energy required to remove an electron from the Fermi level (or electron with energy equal to E_F at zero temperature) from a solid to a point far enough away from the surface that it is no longer influenced by electric fields in the vacuum emanating from the surface. Mathematically, it is defined by the expression*

$$\begin{aligned}\Phi_W &\triangleq \Delta V - E_F \\ &= D + V_{xc}(-\infty) - E_F\end{aligned} \tag{5.4}$$

Per the last line, D can be viewed as the surface contribution to the work function, while the bulk contribution is represented in the V_{xc} term. The E_F appears because it is the energy difference between the current state and one far away; if electromagnetic effects didn't exist, for instance, E_F would be precisely the energy required to remove an electron. Table 5.1 lists values of these three quantities for various jellium surfaces.

r_s	E_F	Φ_W	D	ΔV	Example Material (actual r_s)
2.0	12.52	3.89	6.80	16.41	Platinum (1.99)
2.5	8.01	3.72	3.83	11.73	Cadmium (2.59)
3.0	5.57	3.50	2.32	9.07	Gold (3.01)
3.5	4.09	3.26	1.44	7.35	Strontium (3.56)
4.0	3.13	3.06	0.91	6.19	Sodium (3.93)

Table 5.1: Ground State Energies for Jellium Surfaces. Adapted from Lang and Kohn [57], this table contains values of the Fermi energy E_F, the work function Φ_W, dipole barrier D, and surface barrier potential ΔV for jellium surfaces of various average densities r_s. All quantities are in eV. Reproduced with express permission from the American Physical Society and Norton Lang.

5.1.3 Fermi-Dirac Statistics

As fermions (identical particles that obey Pauli Exclusion Principle), electrons in metals obey Fermi-Dirac statistics, first noted by Sommerfeld [102]. Fermi-Dirac statistics describe the probability of finding a fermion at energy level ε via the distribution

$$F(\varepsilon) = \frac{1}{e^{(\varepsilon-\mu)/k_B T} + 1} \tag{5.5}$$

where μ is chemical potential or Fermi level[†], k_B is Boltzman's constant, and T is absolute (Kelvin) temperature. The Fermi level is the energy level that has a 50% probability of occupation—which happens when the exponential is zero. At zero temperature, this value coincides with the Fermi energy so that

$$\mu = E_F = \frac{1}{2}k_F^2$$

With this knowledge, as we take $T \to 0^+$ in (5.5), we can deduce the zero-temperature limit of the Fermi-Dirac distribution, expressed in terms of $\mathbf{k}$,

$$F(\varepsilon) = \begin{cases} 1 & |\mathbf{k}| < k_F \\ 0 & |\mathbf{k}| > k_F \end{cases} \tag{5.6}$$

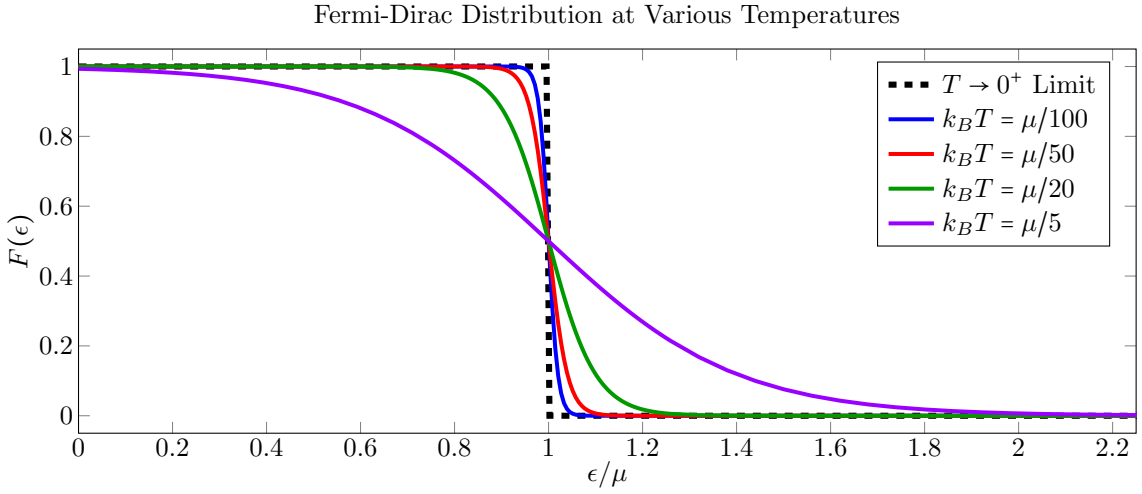

Figure 5.2: Fermi-Dirac Distribution. Considering $k_BT = \mu/f$, for fixed μ, low T corresponds to large f. For gold ($\mu \approx 0.2046$), the values $f = 100, 50, 20, 5$ depicted correspond to temperatures of 373°C, 1019°C, 2978°C, and 12650°C, respectively. A temperature of 20°C corresponds to $f \approx 220.5$.

Figure 5.2 shows what an excellent approximation (5.6) makes to (5.5) for ordinary temperatures. In atomic units, $k_B = 3.1668 \times 10^{-6}$ Rydberg/K. As room temperature is around 300 K, it follows that $k_BT \approx 10^{-3}$; since $\mu = E_F \in (0, 0.5)$ per the table in Appendix B, all cases of interest have $f > 200$, with f as in the figure. Thus, the full Fermi-Dirac distribution is well-approximated by the $T \to 0^+$ limit for such cases.

Suppose that there are $\mathcal{N}(\varepsilon)\,d\varepsilon$ states at energy level ε. Then the total number of electrons n is [117, p.136]

$$n = \int_0^\infty F(\varepsilon)\mathcal{N}(\varepsilon)\,d\varepsilon \tag{5.7}$$

[†]The Lagrange multiplier of the previous chapter was denoted v to avoid confusion with this Fermi level.

Inserting the Fermi-Dirac distribution (5.6) and taking the volume element in $\mathbf{k}$ space $d\varepsilon \mapsto \dfrac{d\mathbf{k}}{(2\pi)^3}$, we have

$$n = \frac{1}{(2\pi)^3} \int_{|\mathbf{k}|<k_F} \mathcal{N}(\varepsilon)\, d\mathbf{k}$$

The state counter $\mathcal{N}$ is given in terms of the Kohn-Sham wavefunctions, indexed in momentum

$$\mathcal{N}(\varepsilon) = 2\,|\psi_{\mathbf{k}}(\mathbf{x})|^2$$

The factor of 2 comes from that two electrons are allowed for each value of $\mathbf{k}$ (or ε). Because the wavefunctions only give us a probabilistic sense of whether an electron is at position $\mathbf{x}$, the left-hand side of (5.7) is more appropriately interpreted as the ground state *density* rather than the actual number of electrons, so

$$n_0(\mathbf{x}) = \frac{1}{4\pi^3} \int_{|\mathbf{k}|<k_F} |\psi_{\mathbf{k}}(\mathbf{x})|^2\, d\mathbf{k} \tag{5.8}$$

5.2 Effect of Jellium

Let $\mathbf{k} = (k, k_2, k_3)^T$. Denote the components parallel to the metal surface using a tilde, mathematically defined as $\tilde{\mathbf{k}} = \mathbf{k} - (\mathbf{k}\cdot\boldsymbol{\nu})\,\boldsymbol{\nu}$, where $\boldsymbol{\nu}$ denotes the unit normal vector pointed outward of the surface. Because the surface is assumed to occupy the yz-plane, $\boldsymbol{\nu} = (1,0,0)^T$, we have $\tilde{\mathbf{k}} = (0, k_2, k_3)^T$.

Because of the symmetry of the jellium surface, the wave functions $\psi_{\mathbf{k}}$ (indexed by *vector* subscripts) can be decomposed into a plane wave parallel to the surface and a wave function ψ_k (indexed by scalar subscript) depending only on the perpendicular direction:

$$\psi_{\mathbf{k}}(\mathbf{x}) = e^{i\tilde{\mathbf{k}}\cdot\tilde{\mathbf{x}}}\,\psi_k(x) \tag{5.9}$$

Because $\tilde{\mathbf{k}}\cdot\tilde{\mathbf{x}} = k_2x_2 + k_3x_3$, substituting (5.9) into Kohn-Sham equations (3.12) yields

$$\left(-\frac{1}{2}\frac{\partial^2}{\partial x^2} + \frac{1}{2}k_2^2 + \frac{1}{2}k_3^2 + V(\mathbf{x}) - \varepsilon_{\mathbf{k}}\right) e^{i\tilde{\mathbf{k}}\cdot\tilde{\mathbf{x}}}\,\psi_k(x) = 0$$

Because we have $\varepsilon_{\mathbf{k}} = \frac{1}{2}\mathbf{k}^2 + V(-\infty) = \frac{1}{2}\tilde{\mathbf{k}}^2 + \frac{1}{2}k^2 + V(-\infty)$, each ψ_k satisfies a one-dimensional Schrödinger equation of the form

$$\left(-\frac{1}{2}\frac{\partial^2}{\partial x^2} + V(x) - \varepsilon_k\right)\psi_k(x) = 0 \tag{5.10}$$

where

$$\varepsilon_k = \frac{1}{2}k^2 + V(-\infty) \tag{5.11}$$

We are able to reduce the dimension from $\mathbf{x}$ to x in V by noting that because of (5.9) the Kohn-Sham representation of the density (5.8) becomes

$$n_0(\mathbf{x}) \equiv n_0(x) = \frac{1}{4\pi^3}\int_{|\mathbf{k}|<k_F} \psi_k^2(x)\, d\mathbf{k}$$

We can remove the absolute value because the ψ_k are real-valued (because ε_k is). Now, because the integrand depends only on the perpendicular component of $\mathbf{k}$, we can integrate analytically over the parallel momenta:

$$\begin{aligned} n_0(x) &= \frac{1}{4\pi^3}\int_{-k_F}^{k_F} \psi_k^2(x) \int_{-\sqrt{k_F^2-k^2}}^{\sqrt{k_F^2-k^2}} \int_{-\sqrt{k_F^2-k^2-k_3^2}}^{\sqrt{k_F^2-k^2-k_3^2}} dk_2\, dk_3\, dk \\ &= \frac{1}{2\pi^3}\int_{-k_F}^{k_F} \psi_k^2(x) \int_{-\sqrt{k_F^2-k^2}}^{\sqrt{k_F^2-k^2}} \sqrt{k_F^2-k^2-k_3^2}\, dk_3\, dk \end{aligned}$$

Using the integral formula

$$\int \sqrt{a^2-x^2}\, dx = \frac{x}{2}\sqrt{a^2-x^2} + \frac{a^2}{2}\tan^{-1}\left(\frac{x}{\sqrt{a^2-x^2}}\right)$$

the inner integral may be computed exactly:

$$n_0(x) = \frac{1}{4\pi^2}\int_{-k_F}^{k_F} (k_F^2-k^2)\, \psi_k^2(x)\, dk$$

By virtue of (5.11), the integrand is even in k, so we can write

$$n_0(x) = \frac{1}{2\pi^2}\int_0^{k_F} \left(k_F^2-k^2\right)\psi_k^2(x)\, dk \tag{5.12}$$

5.3 Boundary Conditions for Wavefunctions

Next, we will use the representation (5.12) to formulate asymptotic boundary conditions for the ψ_k's. The following result will of great usefulness in doing so:

Theorem 5.1. *Let $V \in C(\mathbb{R})$ be such that*

$$\lim_{x\to+\infty} V(x) = V(+\infty) \qquad\qquad \lim_{x\to-\infty} V(x) = V(-\infty)$$

and let ψ be a solution to the Schrödinger equation

$$\left(-\frac{1}{2}\frac{\partial^2}{\partial x^2} + V(x) - \varepsilon\right)\psi = 0$$

Then ψ behaves like

$$\psi \sim \begin{cases} \beta_1 e^{i\hat{\kappa}x} + \beta_2 e^{-i\hat{\kappa}x} & x \to -\infty \\ \alpha_1 e^{i\hat{\lambda}x} + \alpha_2 e^{-i\hat{\lambda}x} & x \to +\infty \end{cases}$$

where $\hat{\kappa}^2 = 2\varepsilon - 2V(+\infty)$ and $\hat{\lambda}^2 = 2\varepsilon - 2V(-\infty)$. Note that either or both of $\hat{\kappa}$ or $\hat{\lambda}$ may be imaginary, as no assumption is made on ε in relation to $V(-\infty)$ and $V(+\infty)$.

It is easy to understand the intuition of this result: by continuity of solutions to differential equations in their coefficients, as x reaches $+\infty$, it seems reasonable that ψ should approach the solution to

$$\left(-\frac{1}{2}\frac{\partial^2}{\partial x^2} + V(+\infty) - \varepsilon\right)\psi = 0$$

and similarly for $-\infty$. A rigorous proof of this theorem, however, requires far more machinery than the simple ideas from which it was conceptualized and involves asymptotics of Jost solutions for Strum-Liouville equations. For details, see Theorem 9.2.3 in Promislow and Kapitula [88, p.256].

5.3.1 Asymptotic Conditions at $+\infty$

To apply Theorem 5.1 with $\varepsilon = \varepsilon_k$, we first compute $\hat{\lambda}_k^2$ via (5.11)

$$\hat{\lambda}_k^2 = k^2 - 2V(-\infty) + 2V(+\infty) = 2\left(\frac{1}{2}k^2 - \Delta V\right)$$

where ΔV is the surface barrier potential of (5.3). Based on its physical interpretation, the work function (5.4) is always positive, so $\Delta V > E_F$. Because $k < k_F \implies \frac{1}{2}k^2 < E_F$, we have $\frac{1}{2}k^2 - \Delta V < 0$, so $\hat{\lambda}_k^2 < 0$. Define

$$\lambda_k \triangleq \sqrt{2V(+\infty) - 2\varepsilon_k} \qquad \implies \qquad \hat{\lambda}_k = i\lambda_k$$

with the square root taken to produce a positive imaginary part. Then the asymptotic form of ψ_k becomes

$$\psi_k \sim \alpha_1(k)\, e^{-\lambda_k x} + \alpha_2(k)\, e^{\lambda_k x}$$

We note that all quantities in the above expression are real. Because we require that $n_0 \to 0$ as $x \to +\infty$, we must have $\alpha_2(k) = 0$ for all k, as $\lambda_k > 0$ and this exponentially growing mode would preclude the possibility of satisfying the required decay condition. We therefore have as $x \to +\infty$

$$\psi_k \sim \alpha_k e^{-\lambda_k x} \tag{5.13}$$

5.3.2 Asymptotic Conditions at $-\infty$

Again appealing to Theorem 5.1, we compute

$$\hat{\kappa}^2 = k^2 + 2V(-\infty) - 2V(-\infty) = k^2$$

so that as $x \to -\infty$ we have the asymptotic behavior

$$\psi_k \sim \beta_1(k)\, e^{ikx} + \beta_2(k)\, e^{-ikx}$$

Because ψ_k is real-valued, we must have $\beta_1 = \beta_2^*$. Thus, we may write the above as

$$\psi_k \sim \beta_k\, e^{ikx} + \beta_k^*\, e^{-ikx} \tag{5.14}$$

We may substitute (5.14) into (5.12) to obtain

$$\begin{aligned} n_0 &\sim \frac{1}{2\pi^2} \int_0^{k_F} \left(k_F^2 - k^2\right) \left[2\left|\beta_k\right|^2 + \beta_1^2 e^{2ikx} + (\beta_1^*)^2 e^{-2ikx}\right] dk \\ &\sim \frac{1}{2\pi^2} \Bigg[\int_0^{k_F} 2\left|\beta_k\right|^2 \left(k_F^2 - k^2\right) dk + \underbrace{\int_0^{k_F} \beta_k^2 \left(k_F^2 - k^2\right) e^{2ikx}\, dk}_{\triangleq A} + \underbrace{\int_0^{k_F} (\beta_k^*)^2 \left(k_F^2 - k^2\right) e^{-2ikx}\, dk}_{\triangleq B} \Bigg] \end{aligned}$$

To prove that $A, B \to 0$, we will need the following famous lemma [43, p.105]:

Lemma 5.1 (Riemann-Lebesgue). *If $f \in L^1(\mathbb{R}^d)$, then its Fourier transform $\hat{f}(\boldsymbol{\xi})$ has*

$$\lim_{|\boldsymbol{\xi}| \to \infty} \hat{f}(\boldsymbol{\xi}) = 0$$

Claim. *$A, B \to 0$ as $x \to -\infty$.*

Proof. Because $\psi_k = \psi_{-k}$ so that $\beta_k = \beta_{-k}$, by sending $k \mapsto -k$

$$A = \int_{-k_F}^{0} \beta_k^2 \left(k_F^2 - k^2\right) e^{-2ikx}\, dk = \int_{\mathbb{R}} \underbrace{\beta_k^2 \left(k_F^2 - k^2\right) \left[\Theta(k + k_F) - \Theta(k)\right]}_{\triangleq f(k)} e^{-2ikx}\, dk = \hat{f}\left(\frac{x}{\pi}\right)$$

where $\hat{f}$ denotes the ordinary Fourier transform of f if this quantity is well-defined. By continuity of $k \mapsto \beta_k$, f is bounded and compactly supported, so $f \in L^1(\mathbb{R})$. Hence, by the Riemann-Lebesgue Lemma, $\hat{f} \to 0$ as $|x| \to \infty$, so we have $A \to 0$ as desired. Turning our attention to B, we have that

$$B = \int_{\mathbb{R}} \underbrace{(\beta_k^*)^2 \left(k_F^2 - k^2\right) \left[\Theta(k) - \Theta(k - k_F)\right]}_{\triangleq\, g(k)} e^{-2ikx}\, dk = \hat{g}\left(\frac{x}{\pi}\right)$$

Hence, by the same argument as above, $B \to 0$. ∎

Because $n_0 \to \bar{n}$ as $x \to -\infty$, we have

$$\bar{n} = \frac{1}{\pi^2} \int_0^{k_F} |\beta_k|^2 \left(k_F^2 - k^2\right) dk \tag{5.15}$$

We return to (5.14) and express it in a more familiar form:

$$\begin{aligned} \psi_k &\sim |\beta_k| \left(e^{i\vartheta_k} e^{ikx} + e^{-i\vartheta_k} e^{-ikx}\right) \\ &= 2\,|\beta_k| \cos(kx - \vartheta_k) \\ &= -2\,|\beta_k| \sin(kx - \gamma_k) \end{aligned}$$

where $\vartheta_k \triangleq \text{angle}(\beta_1)$ and $\gamma_k \triangleq \vartheta_k - \frac{\pi}{2}$. If we choose $|\beta_k| \equiv \frac{1}{\sqrt{2}}$ for each k, via (5.15), the asymptotic value for n will be correct:

$$\lim_{x \to -\infty} n_0(x) = \frac{1}{2\pi^2} \int_0^{k_F} \left(k_F^2 - k^2\right) dk = \frac{k_F^3}{3\pi^2} = \bar{n}$$

The last equality follows from Appendix B. Therefore, taking each ψ_k to have asymptotic behavior

$$\psi_k \sim -\frac{2}{\sqrt{2}} \sin(kx - \gamma_k) = -\sqrt{2} \sin(kx - \gamma_k) \tag{5.16}$$

as $x \to -\infty$ yields the correct result for the density n. Furthermore, because ψ_k appears only as ψ_k^2 in (5.12) (or as $\psi_k(x)\psi_k(y)$ in spectral forms), we may remove the negative sign; because the ψ_k are generated by linear equations, we can absorb the factor of $\frac{1}{2}$ in (5.12) into the ψ_k, giving

$$\psi_k \sim \sin(kx - \gamma_k) \tag{5.17}$$

5.3.3 Summary and Consequences

As shown in the preceding subsections, in order for the wavefunctions ψ_k to produce the correct asymptotic behavior of the ground state density n_0, they must behave like

$$\psi_k \sim \begin{cases} \sin(kx - \gamma_k) & x \to -\infty \\ \alpha_k e^{-\lambda_k x} & x \to +\infty \end{cases}$$

In deriving the boundary condition at $-\infty$, we began with (5.12), which has a factor of $\frac{1}{2}$ out front. However, in the above boundary conditions, we incorporated that factor into the ψ_k, so with this choice of normalization, the density is instead given by

$$n_0(x) = \frac{1}{\pi^2} \int_0^{k_F} \left(k_F^2 - k^2\right) \psi_k^2(x)\, dk \tag{5.18}$$

5.4 Asymptotic Behavior of the Kohn-Sham Density

The following definition and lemma appear in Lighthill [69, p.56]:

Definition 5.4. *A distribution f is said to be* well-behaved at infinity *if there exists $R > 0$ such that $f - F \in L^1\big((-\infty, -R)\big) \cap L^1\big((R, +\infty)\big)$, where F is a linear combination of the functions for $\beta, k \in \mathbb{R}$*

$$e^{ikx}|x|^\beta \quad e^{ikx}|x|^\beta \operatorname{sgn}(x) \quad e^{ikx}|x|^\beta \log|x| \quad e^{ikx}|x|^\beta \log|x| \operatorname{sgn}(x)$$

Lemma 5.2. *If F and all its derivatives exist as functions for $x \geq 0$ and are well-behaved at infinity, then*

$$\int_0^\infty F(x)\sin(2\pi xy) \sim \frac{F(0)}{2\pi y} - \frac{F''(0)}{(2\pi y)^3} + \frac{F^{(4)}(0)}{(2\pi y)^5} - \cdots \tag{5.19}$$

$$\int_0^\infty F(x)\cos(2\pi xy) \sim -\frac{F'(0)}{(2\pi y)^2} + \frac{F'''(0)}{(2\pi y)^4} - \frac{F^{(5)}(0)}{(2\pi y)^6} + \cdots \tag{5.20}$$

We will use the above lemma in proving the following asymptotic formula for the density n_0. The result appears frequently throughout the literature (e.g., [54, p.89]), but always without reference to any proof.

Theorem 5.2. *As $x \to -\infty$, the Kohn-Sham density given by* (5.18) *has asymptotic behavior*

$$n_0(x) \sim \bar{n}\left(1 + \frac{3\cos(2xk_F - 2\gamma_{k_F})}{(2xk_F)^2}\right) + \mathcal{O}\left(\frac{1}{x^3}\right) \tag{5.21}$$

Proof. We begin by using the asymptotic form of the wavefunction given in (5.17) in (5.18)

$$n_0 \sim \frac{1}{\pi^2} \int_0^{k_F} \left(k_F^2 - k^2\right) \sin^2(kx - \gamma_k)\, dk$$

$$
\begin{aligned}
&\sim \frac{1}{2\pi^2}\int_0^{k_F}\left(k_F^2-k^2\right)\left(1-\cos(2kx-2\gamma_k)\right)dk\\
&\sim \frac{1}{2\pi^2}\int_0^{k_F}\left(k_F^2-k^2\right)dk-\frac{1}{2\pi^2}\int_0^{k_F}\left(k_F^2-k^2\right)\cos(2kx-2\gamma_k)\,dk\\
&\sim \bar{n}-\frac{1}{2\pi^2}\int_0^{k_F}\left(k_F^2-k^2\right)\cos(2kx-2\gamma_k)\,dk
\end{aligned}
\tag{5.22}
$$

We applied the standard power-reducing formula to $\sin^2$ to reach line two from line one; to obtain the final line, we have once again used that $k_F^3 = 3\pi^2\bar{n}$. Formally, we may write

$$
\int_0^{k_F}\left(k_F^2-k^2\right)\cos(2kx-2\gamma_k)\,dk=\int_0^{\infty}\left(k_F^2-k^2\right)\cos(2kx-2\gamma_k)\,dk-\int_{k_F}^{\infty}\left(k_F^2-k^2\right)\cos(2kx-2\gamma_k)\,dk
$$

where the integrals of the right-hand side are to be interpreted as distributions (i.s.d), as they do not converge to actual functions. We will compute asymptotic behavior of these distributions. Write

$$
\int_0^{\infty}\left(k_F^2-k^2\right)\cos(2kx-2\gamma_k)\,dk=\int_0^{\infty}\left(k_F^2-k^2\right)\cos 2\gamma_k\cos 2kx\,dk+\int_0^{\infty}\left(k_F^2-k^2\right)\sin 2\gamma_k\sin 2kx\,dk
$$

The functions

$$
\begin{aligned}
F_1(k)&\triangleq\left(k_F^2-k^2\right)\cos 2\gamma_k\\
F_2(k)&\triangleq\left(k_F^2-k^2\right)\sin 2\gamma_k
\end{aligned}
$$

satisfy all the hypotheses for Lemma 5.2, so we may apply the results (5.19) and (5.20):

$$
\int_0^{\infty}\left(k_F^2-k^2\right)\cos(2kx-2\gamma_k)\,dk=\frac{F_2(0)}{2x}-\frac{F_1'(0)}{(2x)^2}-\frac{F_2''(0)}{(2x)^3}+\mathcal{O}\left(\frac{1}{x^4}\right)
$$

The relevant derivatives are given by

$$
\begin{aligned}
F_1'(k)&=-2k\cos 2\gamma_k-2\frac{\partial\gamma_k}{\partial k}\cdot\left(k_F^2-k^2\right)\sin 2\gamma_k\\
F_2''(k)&=-2\left(4k\frac{\partial\gamma_k}{\partial k}-\left(k_F^2-k^2\right)\cdot\frac{\partial^2\gamma_k}{\partial k^2}\right)\cos 2\gamma_k-2\left(1+2\left(k_F^2-k^2\right)\cdot\left(\frac{\partial\gamma_k}{\partial k}\right)^2\right)\sin 2\gamma_k
\end{aligned}
$$

Because $\gamma_0 = 0$, we have

$$
\begin{aligned}
F_2(0)&=0\\
F_1'(0)&=0\\
F_2''(0)&=2k_F^2\left.\frac{\partial^2\gamma_k}{\partial k^2}\right|_{k=0}
\end{aligned}
$$

And so

$$\int_0^\infty \left(k_F^2 - k^2\right)\cos(2kx - 2\gamma_k)\,dk = -\left(\frac{k_F^2}{4}\left.\frac{\partial^2\gamma_k}{\partial k^2}\right|_{k=0}\right)\frac{1}{x^3} + \mathcal{O}\left(\frac{1}{x^4}\right) \tag{5.23}$$

To resolve the integral over $[k_F, \infty)$, we first make the change of variables $k \mapsto k - k_F$ so that we have

$$\begin{aligned}\int_{k_F}^\infty \left(k_F^2 - k^2\right)\cos(2kx - 2\gamma_k)\,dk &= \int_0^\infty \left(k_F^2 - \left(k + k_F\right)^2\right)\cos(2kx + 2xk_F - 2\gamma_{k+k_F})\,dk \\ &= \int_0^\infty \left(k_F^2 - \left(k + k_F\right)^2\right)\cos(2xk_F - 2\gamma_{k+k_F})\cos 2kx\,dk \\ &\quad + \int_0^\infty \left(k_F^2 - \left(k + k_F\right)^2\right)\sin(2xk_F - 2\gamma_{k+k_F})\sin 2kx\,dk\end{aligned}$$

Defining

$$\begin{aligned}G_1(k) &\triangleq \left(k_F^2 - \left(k + k_F\right)^2\right)\cos(2xk_F - 2\gamma_{k+k_F}) \\ G_2(k) &\triangleq \left(k_F^2 - \left(k + k_F\right)^2\right)\sin(2xk_F - 2\gamma_{k+k_F})\end{aligned}$$

we can apply Lemma 5.2

$$\int_{k_F}^\infty \left(k_F^2 - k^2\right)\cos(2kx - 2\gamma_k)\,dk = \frac{G_2(0)}{2x} - \frac{G_1'(0)}{(2x)^2} - \frac{G_2''(0)}{(2x)^3} + \mathcal{O}\left(\frac{1}{x^4}\right)$$

The required derivatives are

$$\begin{aligned}G_1'(k) &= -2\left(k + k_F\right)\cos(2xk_F - 2\gamma_{k+k_F}) + 2\frac{\partial\gamma_{k+k_F}}{\partial k}\cdot\left(k_F^2 - \left(k + k_F\right)^2\right)\sin(2xk_F - 2\gamma_{k+k_F}) \\ G_2''(k) &= 2\left(4\left(k + k_F\right)\frac{\partial\gamma_{k+k_F}}{\partial k} - \left(k_F^2 - \left(k + k_F\right)^2\right)\cdot\frac{\partial^2\gamma_{k+k_F}}{\partial k^2}\right)\cos(2xk_F - 2\gamma_{k+k_F}) \\ &\quad - 2\left(1 + 2\left(k_F^2 - \left(k + k_F\right)^2\right)\cdot\left(\frac{\partial\gamma_{k+k_F}}{\partial k}\right)^2\right)\sin(2xk_F - 2\gamma_{k+k_F})\end{aligned}$$

so that we have

$$\begin{aligned}G_2(0) &= 0 \\ G_1'(0) &= -2k_F\cos(2xk_F - 2\gamma_{k_F}) \\ G_2''(0) &= \left(8k_F\left.\frac{\partial^2\gamma_{k+k_F}}{\partial k^2}\right|_{k=0}\right)\cos(2xk_F - 2\gamma_{k_F}) - 2\sin(2xk_F - 2\gamma_{k_F})\end{aligned}$$

The derivative of γ_k term can be explained by rewriting γ_k using standard function notation:

$$\begin{aligned} \gamma_k \equiv \gamma(k) \quad &\implies \quad \frac{\partial \gamma_k}{\partial k} = \gamma'(k) \\ \gamma_{k+k_F} \equiv \gamma(k+k_F) \quad &\implies \quad \frac{\partial \gamma_{k+k_F}}{\partial k} = \gamma'(k+k_F) \\ &\implies \quad \frac{\partial^2 \gamma_{k+k_F}}{\partial k^2} = \gamma''(k+k_F) \end{aligned}$$

so that

$$\left.\frac{\partial^2 \gamma_{k+k_F}}{\partial k^2}\right|_{k=0} = \gamma''(k_F) = \left.\frac{\partial^2 \gamma_k}{\partial k^2}\right|_{k=k_F}$$

Plugging in these evaluations gives

$$\int_{k_F}^{\infty} \left(k_F^2 - k^2\right) \cos(2kx - 2\gamma_k)\, dk = -\frac{2k_F \cos(2xk_F - 2\gamma_{k_F})}{(2x)^2} - \frac{G_2''(0)}{(2x)^3} + \mathcal{O}\left(\frac{1}{x^4}\right) \tag{5.24}$$

Combining (5.23) and (5.24) and substituting into (5.22), we have the asymptotic behavior for n_0:

$$n_0(x \to -\infty) = \bar{n} + \frac{k_F}{\pi^2} \frac{\cos(2xk_F - 2\gamma_{k_F})}{(2x)^2} + \frac{\zeta}{x^3} + \mathcal{O}\left(\frac{1}{x^4}\right) \tag{5.25}$$

with

$$\zeta \triangleq \frac{k_F^2}{8\pi^2} \left.\frac{\partial^2 \gamma_k}{\partial k^2}\right|_{k=0} + \frac{k_F}{2\pi^2} \cos(2xk_F - 2\gamma_{k_F}) \cdot \left.\frac{\partial^2 \gamma_k}{\partial k^2}\right|_{k=k_F} - \frac{1}{8\pi^2} \sin(2xk_F - 2\gamma_{k_F})$$

To further simplify (5.25), we can multiply and divide the second term by $3k_F^2$ and again use that $k_F^3 = 3\pi^2 \bar{n}$. Furthermore, because γ_k is not known analytically as a function of k, the x^{-3} term is not particularly helpful. Discarding it gives the form claimed in (5.21). ∎

5.4.1 Friedel Oscillations

Theorem 5.2 says that the Kohn-Sham density exhibits *Friedel Oscillations* [38], which are alternating regions of positive and negative charge due to impurities in the electron jelly. These oscillations always look like

$$\rho(\mathbf{x}) \sim \rho_0(\mathbf{x}) + \frac{A \cos(2k_F |\mathbf{x}| + \gamma)}{|\mathbf{x}|} \tag{5.26}$$

The source of this phenomenon is the nonzero de Broglie wavelength of electrons at low temperatures, which causes a scattering-like effect that smears out charge in space; at high temperatures, the range of electron wavelength widens, and there is no coherent collective smearing of charge. Only electrons near the Fermi energy can participate in this effect, as the oscillations are due to electrons jumping to unoccupied states

above their current energy level and no such states exist for electrons below the Fermi energy. This is reflected in the period of oscillation $\frac{\pi}{k_F}$, which is half the de Broglie wavelength of the outermost electrons. The de Broglie wavelength of particles at the Fermi energy is also known as the Fermi wavelength $\lambda_F = \frac{2\pi}{k_F}$.

Within the jellium model, it can be thought of as a Gibbs-type phenomenon. The positive background density terminates abruptly at the interface, yet the electron density is continuous. Because of the charge neutrality condition

$$\int_{-\infty}^{+\infty} \big(n_0(x) - n_+(x)\big)\, dx = 0$$

one can think of the continuous n_0, which is a sum of of sine waves for $x \gg 0$, as attempting to approximate the discontinuous n_+. A Gibbs-like overshoot occurs near the interface and ripples through the domain.

5.5 Electrostatic Potential: A Deceptively Hard Problem

The total electrostatic potential associated with the density is the solution to the Poisson equation

$$\begin{aligned} \phi''(x) &= -4\pi\big(n_0(x) - n_+(x)\big) \\ \phi(-\infty) = 0, \phi'(+\infty) &= -4\pi\varsigma \end{aligned} \tag{5.27}$$

The right boundary condition is the total charge condition and enforces the requirement that

$$\int_{-\infty}^{+\infty} \big(n_\varsigma(x) - n_+(x)\big)\, dx = \varsigma \tag{5.28}$$

For a charge-neutral system, $\varsigma = 0$; $\varsigma \neq 0$ describes systems with surface screening charge. A naïve approach to solving (5.27) would be to proceed we did in the orbital-free computation: truncate the infinite domain to a large finite one $[R_1, R_2]$ and enforce the boundary conditions $\phi(R_1) = 0$ and $\phi'(R_2) = -4\pi\varsigma$. A more sophisticated attempt would make use of the known analytic behavior of n_0 from (5.13) and (5.17):

$$n_0(x) \sim \begin{cases} \displaystyle\int_0^{k_F} \big(k_F^2 - k^2\big) \sin^2(kx - \gamma_k)\, dk & x \ll 0 \\ \displaystyle\int_0^{k_F} \big(k_F^2 - k^2\big)\, \alpha_k^2 e^{-2\lambda_k x}\, dk & x \gg 0 \end{cases}$$

With the help of Fourier transforms, distributions, and complex contour integrals, the exact values of $\phi(R_1)$ and $\phi'(R_2)$ can be computed exactly. Following either the naïve or sophisticated path for truncating the domain and then using any standard ODE solver (finite difference, linear multi-step method, finite element, etc.) results in an incorrect solution, depicted below in Figure 5.3.

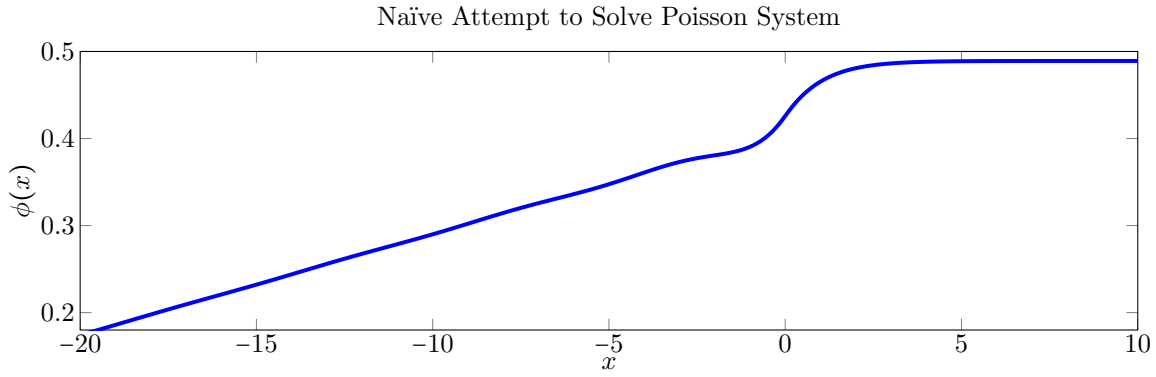

Figure 5.3: Failure of Standard Methods. A second-order finite difference method was used to solve (5.27) in the naïve formulation described above with $\varsigma = 0$. Note the linear behavior on the left.

Liebsch cites "long-range Coulomb potential due to charge imbalance" [67, p.39] as the reason for the difficulty in solving (5.27) and advocates an approached pioneered by Manninen *et al.* [75]. In this technique, a parameter $\lambda > 0$ is chosen and the Poisson equation is reformulated as an implicit integral equation

$$\phi(x) = \int_{-\infty}^{+\infty} e^{-\lambda|x-y|} \left[\frac{2\pi}{\lambda}\big(n_0(y) - n_+(y)\big) + \frac{\lambda}{2}\phi(y) \right] dy \tag{5.29}$$

The exponential decay of the kernel suppresses the problematic interactions. When combined with integration by parts, the integral equation allows for an exact (in principle) determination on a truncated interval. Furthermore, following the work of Causley [13], the integral may be computed on a uniform grid of N points in $\mathcal{O}(N)$ time. Unfortunately, the integral operator is incapable of seeing boundary conditions other than $\varsigma = 0$, so despite its upsides, it is unsuitable for cases of nonzero screening charge.

One may be tempted to conclude that the integral equation formulation includes these "long-range Coulomb effects" by concentrating wide-ranging Coulombic effects over $(-\infty, +\infty)$ into a finite interval, thereby transforming the infinite domain into a finite one. Accordingly, it would seem that a suitable fix would be to employ Fourier transforms. Information over all of $\mathbb{R}$ could be incorporated into the solution by decomposing into three contributions over $(-\infty, R_1)$, $[R_1, R_2]$, and $(R_2, +\infty)$. Over the "numerical" domain $[R_1, R_2]$, an FFT would suffice and the analytic asymptotic forms would be used over the semi-infinite pieces. This method also fails, indicating that the core problem is far deeper than complications from truncation.

The issue is a fundamental incompatibility between the boundary conditions for the Poisson equation and the spatial distribution of the electron density. Illustrated in [99], consider a simple integration of (5.27):

$$\phi'(x) = \phi'(0) - 4\pi \int_0^x \big(n_0(y) - n_+(y)\big)\, dy$$

$$\phi(x) = \phi(0) + x\phi'(x) - 4\pi \int_0^x y\big(n_0(y) - n_+(y)\big)\, dy$$

If we are to have $|\phi(\pm\infty)| < \infty$, then $x\phi'(x) \to 0$ as $|x| \to \infty$ and thus

$$\phi(+\infty) = -4\pi \int_{-\infty}^{+\infty} y\big(n_0(y) - n_+(y)\big)\, dy$$
$$\phi'(0) - 4\pi\varsigma = 4\pi \int_0^{+\infty} \big(n_0(y) - n_+(y)\big)\, dy$$

If these relations do not hold, then it is impossible to obtain the correct ϕ by solving (5.27) with a known right-hand side; it is exceptionally unlikely everything will just fall into place if we use an intermediate density from the Kohn-Sham process. Because the density depends on the electrostatic potential and potential depends on the density, the problem is one of self-consistency—or rather, lack there of.

To remedy the incompatibility, we follow the procedure detailed in [87] to replace the long-range Coulomb interaction with a screened interaction over finite range. To do this, we consider a splitting of the density:

$$n_0(x) = n_{\text{ind}}(x) + n_{\text{qu}}(x) \tag{5.30}$$

The induced density n_{ind} is given by

$$n_{\text{ind}}\big(\phi(x)\big) = \frac{2^{3/2}}{3\pi^2}\Big[E_F - \phi(x) - V_{\text{xc}}\big(n_0(x)\big)\Big]^{3/2} \tag{5.31}$$

The remainder n_{qu} represents quantum corrections to the quasiclassical electron distribution. With this separation of the density, the Poisson equation (5.27) becomes

$$\phi''(x) + 4\pi n_{\text{ind}}(x) = 4\pi\big(n_+(x) - n_{\text{qu}}(x)\big) \tag{5.32}$$

It is critical to note that the representation (5.31) is valid only if

$$\frac{\partial n_{\text{ind}}}{\partial \phi} < 0 \tag{5.33}$$

This condition generally fails to hold when the density is small (such as in the vacuum) and thus the significance of the exchange-correlation potential falls to the same level as that of the electrostatic potential. While an expression for the induced density may exist, it is **not** given by (5.31). Because the electron density decays rapidly away from the interface, Coulombic effects from the vacuum are negligible. Consequently, we

may take $n_{\text{ind}} \equiv 0$ when (5.33) no longer holds. Let c be the first point such that

$$\frac{\partial n_{\text{ind}}}{\partial \phi}(c) = 0 \tag{5.34}$$

and define for $\lambda > 0$

$$F_c(x) \triangleq \frac{1}{1 + e^{\lambda(x-c)}} \tag{5.35}$$

For λ large enough, F_c is a C^∞ approximation to the step function $\Theta(c - x)$ so that $F_c \approx 0$ for $x > c$ and $F_c \approx 1$ for $x < c$. While it is possible to construct a smooth function that is exactly 1 for $-R < x < c$ and exactly 0 outside this range, this F_c is precise enough. Employing this filter, n_{ind} is redefined to be

$$n_{\text{ind}}\big(\phi(x)\big) = \frac{2^{3/2}}{3\pi^2}\Big[E_F - \phi(x) - V_{\text{xc}}\big(n_0(x)\big)\Big]^{3/2} \cdot F_c(x) \tag{5.36}$$

n_{qu} is still defined as the difference

$$n_{\text{qu}} = n_0 - n_{\text{ind}} \tag{5.37}$$

and the modified Poisson equation (5.32) remains the same. How to find c is the subject of Section 5.7.3.

5.6 Self-Consistent Field Iteration (SCF)

The Schrödinger equations (5.10) that the wavefunctions satisfy are linear differential equations. However, the wavefunctions generate the density n_0, which is part of the potential $V = \phi + V_{\text{xc}}(n_0)$ that generates the wavefunctions. In physics, this circular dependence is known as *self-consistency*. With the Kohn-Sham equations, we generate a density (via wavefunctions) with an *a priori* potential—the density does not generate the potential used to compute that density, so the two are not self-consistent.

To square this otherwise circular process, we perform what is known as a *self-consistent field iteration* (SCF): we assume that we know the potential and then use that to compute the density. That newly computed density is then used to generate a new potential, which in turn is used to generate another density, depicted below in Figure 5.4. The process can be thought of as a fixed-point iteration and is continued until the potential and density generate each other in some approximate sense.

The above figure is a mere overview of the process. Not only does the density appear explicitly in V through the V_{xc} term but it also does so implicitly through ϕ, which satisfies the Poisson equation (5.27), in which n_0 appears on the right-hand side. The difficulty in solving for ϕ detailed at length in Section 5.5 can be

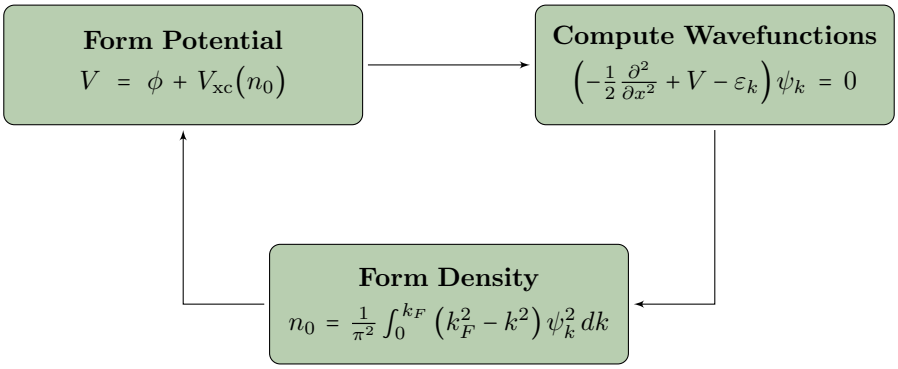

Figure 5.4: Self-consistent Field Iteration. The potential V is needed to compute the density n_0 and the density is needed to compute the potential. In contrast to orbital-free techniques, the Kohn-Sham process is not capable of solving for these quantities simultaneously, so iteration becomes necessary.

directly attributed to the issue of self-consistency—the "form potential" step is easier said than done! In order for the iteration of Figure 5.4 to work, we need to incorporate the fixes of the previous section.

While based on the work of Posvyanskii and Shul'man [87], the algorithm below differs slightly from theirs. The excellent starting density and potential afforded by OF-DFT allows rearrangment of the steps.

Algorithm 5.1. Complete SCF Iteration.

1. Compute initial $n_0^{(0)}$ and $\phi^{(0)}$ using OF-DFT techniques of Chapter 4. **Enter iteration:**

2. Form the Kohn-Sham effective potential

$$V^{(i+1)}(x) = \phi^{(i)}(x) + V_{\text{xc}}\left(n_0^{(i)}(x)\right)$$

3. For an appropriate set of discrete k values, compute the wavefunctions

$$\left(-\frac{1}{2}\frac{\partial^2}{\partial x^2} + V^{(i+1)}(x) - \varepsilon_k\right)\psi_k(x) = 0$$

4. Form the density from the wavefunctions computed in Step 3 via

$$n_0^{(i+1)}(x) = \frac{1}{\pi^2}\int_0^{k_F}\left(k_F^2 - k^2\right)\psi_k^2(x)\,dk$$

5. Determine the cut-off filter of (5.35). (See Algorithm 5.3 in Section 5.7.3.)

6. Update the quantum contribution n_{qu} to the density via the formula

$$n_{\mathrm{qu}}^{(i+1)}(x) = n_0^{(i+1)}(x) - \underbrace{\frac{2^{3/2}}{3\pi^2}\Big[E_F - \phi^{(i)}(x) - V_{\mathrm{xc}}\big(n_0^{(i+1)}(x)\big)\Big]^{3/2} \cdot F_c^{(i+1)}(x)}_{n_{\mathrm{ind}}^{(i+1)}(x)}$$

7. Solve the nonlinear Poisson equation

$$\partial_{xx}\phi^{(i+1)} + \frac{2^{7/2}}{3\pi}\Big[E_F - \phi^{(i+1)} - V_{\mathrm{xc}}\big(n_0^{(i+1)}\big)\Big]^{3/2} \cdot F_c^{(i+1)}(x) = 4\pi\big(n_+ - n_{\mathrm{qu}}^{(i+1)}\big)$$
$$\phi^{(i+1)}(-\infty) = 0, \partial_x\phi^{(i+1)}(+\infty) = -4\pi\varsigma$$

8. Compute the L^∞ error between successive densities ("previous-to-current-iterate error")

$$\mathcal{E} = \left\| n_0^{(i+1)} - n_0^{(i)} \right\|_{L^\infty}$$

If $\mathcal{E} < \tau_{sc}$, terminate the process. Otherwise, return to Step 2.

A visual illustration of Algorithm 5.1 as a flowchart is depicted in Figure 5.5 on the next page. The description above merely tells what is to be computed; the details of *how* are the subject of the next section.

The iteration indexing used in Algorithm 5.1 warrants clarification. In Step 2, the $(i+1)^{\mathrm{th}}$ potential is computed using $n_0^{(i)}$ and $\phi^{(i)}$. It may seem that this potential should be numbered $V^{(i)}$, but doing so leads to an index mismatch. In the utilized numbering scheme, the $(i)^{\mathrm{th}}$ V is used to compute the $(i)^{\mathrm{th}}$ density, which is then used to compute the $(i)^{\mathrm{th}}$ electrostatic potential. The progression is more intuitively

$$\big\{n_0^{(0)}, \phi^{(0)}\big\} \longrightarrow V^{(1)} \longrightarrow n_0^{(1)} \longrightarrow \phi^{(1)} \longrightarrow V^{(2)} \longrightarrow \cdots$$

instead of

$$\big\{n_0^{(0)}, \phi^{(0)}\big\} \longrightarrow V^{(0)} \longrightarrow n_0^{(1)} \longrightarrow \phi^{(1)} \longrightarrow V^{(1)} \longrightarrow \cdots$$

In Step 6, the underbrace is labeled $n_{\mathrm{ind}}^{(i+1)}$ even though it is generated by $\phi^{(i)}$. We do this so that $n_0^{(i+1)} = n_{\mathrm{qu}}^{(i+1)} + n_{\mathrm{ind}}^{(i+1)}$, even though doing so is really an index mismatch. In Step 7, we solve an equation that involves the unknown $n_{\mathrm{ind}}\big(\phi^{(i+1)}\big)$. Because double use of n_{ind} would be overly confusing, Algorithm 5.1 eliminates the symbol n_{ind}. It is provided in Step 6 merely to connect to a previously introduced concept.

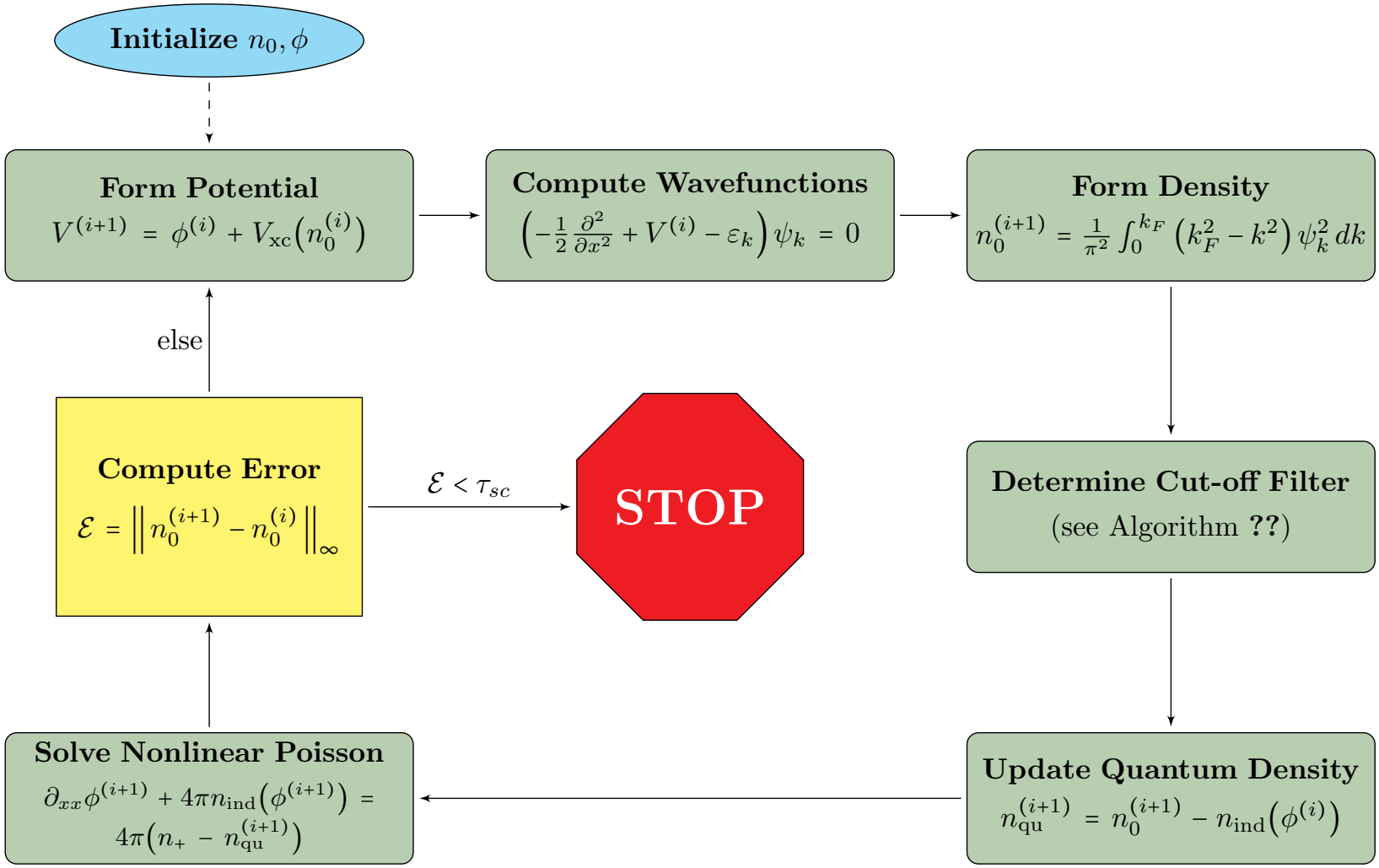

Figure 5.5: Complete SCF Algorithm. This is a visual representation of Algorithm 5.1.

5.7 Numerical Implementation

5.7.1 Determining a Wavefunction ψ_k (Step 3)

Recall that ψ_k is subject to the asymptotic boundary conditions (5.13) and (5.17). Unfortunately, both of those expressions contain unknown values: α_k in the right condition and γ_k in the left one. By the linearity of (5.10), if $a\psi$ is a solution, then so is ψ. Consequently, we can remedy the issue by first solving

$$\begin{gathered}\left(-\frac{1}{2}\frac{\partial^2}{\partial x^2} + V(x) - \varepsilon_k\right)\tilde{\psi}_k(x) = 0 \\ \tilde{\psi}_k \sim e^{-\lambda_k x} \text{ as } x \to +\infty\end{gathered} \tag{5.38}$$

and then renormalizing $\tilde{\psi}_k$ to form the correct ψ_k:

$$\psi_k = \frac{1}{A}\tilde{\psi}_k \tag{5.39}$$

where A is the amplitude of

$$\tilde{\psi}_k \sim A\sin(kx - \gamma_k) \text{ as } x \to -\infty \tag{5.40}$$

To solve (5.38), we use the adaptive spline method prescribed in Algorithm 2.3. The system (5.38) fits the mold of Section 2.3 exactly, so we employ Algorithm 2.2 in conjunction with the adaptive one.

5.7.1.1 Finding the Phase

The kink in the renormalization technique (5.39) is that γ_k is unknown, so (5.40) alone doesn't determine A. Fortunately, the spline method's ability to compute accurate derivatives comes to the rescue.

If $\tilde{\psi}$ behaves as in (5.40), then $\tilde{\psi}_k'$ behaves like

$$\tilde{\psi}_k' \sim Ak\cos(kx - \gamma_k) \text{ as } x \to -\infty$$

By assumption, the asymptotic conditions are achieved to satisfactory accuracy at x_1. Put

$$f_1 \triangleq \tilde{\psi}_k(x_1) \qquad\qquad f_2 \triangleq \tilde{\psi}_k'(x_1)$$

Then we have

$$\frac{f_1}{f_2} = \frac{1}{k}\tan\left(kx_1 - \gamma_k\right) \Longrightarrow \gamma_k \qquad\qquad = kx_1 - \tan^{-1}\left(\frac{kf_1}{f_2}\right)$$

In order to adjust γ_k so that it lies between $-\pi$ and π, we instead take

$$\gamma_k = kx_1 \bmod \pi - \tan^{-1}\left(\frac{kf_1}{f_2}\right) \tag{5.41}$$

We further wish to have $0 \le \gamma_k \le \dfrac{\pi}{2}$, so we follow Algorithm 5.2 below to make that happen.

Algorithm 5.2. Adjustment of γ_k

1. If γ_k as computed by (5.41) has $\gamma_k > \dfrac{\pi}{2}$, put $\gamma_k \leftarrow \pi - \gamma_k$.
2. If $\gamma_k < 0$, then put $\gamma_k \leftarrow -\gamma_k, A \leftarrow -A$.

Because the inverse tangent has range $\left(-\dfrac{\pi}{2}, \dfrac{\pi}{2}\right)$, (5.41) produces a value in $\left(-\dfrac{\pi}{2}, \dfrac{3\pi}{2}\right)$. After Step 1 of Algorithm 5.2, we will have $\gamma_k \in \left(-\dfrac{\pi}{2}, \dfrac{\pi}{2}\right)$ and Step 2 takes care of negative values.

5.7.1.2 Renormalizing

With γ_k in hand, we can find the amplitude A by taking

$$A = \frac{\tilde{\psi}_k(x_1)}{\sin(kx_1 - \gamma_k)}$$

and then taking ψ_k as in (5.39).

5.7.2 Forming the Density (Step 4)

To form the density via (5.18) the integral must be approximated by a sum of finitely many k values. The question becomes how many values of k should be used and how should they be distributed in $[0, k_F]$? At each k value, we must solve an ODE, so using more values than necessary creates a high computational burden; using too few can lead to an inaccurate result, which is ultimately self-defeating.

The answer comes in the form of Gaussian quadrature, which allows for computation of highly accurate approximations to integrals with just a handful of function evaluations [3, p.270]. The idea is to write

$$\int_{-1}^{1} g(x)\,dx \approx \sum_{q=1}^{N} w_q g(x_q)$$

for a set of nodes x_q and weights w_q. Table 5.2 below presents these values for a few N-point rules.

Points	Nodes x_q	Weights w_q
5	±0.9061798459	0.2369268851
	±0.5384693101	0.4786286705
	0	0.5688888889
6	±0.9324695142	0.1713244924
	±0.6612093865	0.3607615730
	±0.2386191861	0.4679139346
7	±0.9491079123	0.1294849662
	±0.7415311856	0.2797053915
	±0.4058451514	0.3818300505
	0	0.4179591837

Table 5.2: Gaussian Quadrature Nodes and Weights. This table lists the nodes x_q and weights w_q for high-order Gauss-Legendre quadrature rules.

Gaussian quadrature rules are always written for integrals over $[-1,1]$. Integrals over $[a,b]$ are transformed into ones over $[-1,1]$ via change of variables:

$$\int_a^b g(x)\,dx \approx \frac{b-a}{2}\int_{-1}^{1} g\left(\frac{a+b+x(b-a)}{2}\right)dx \tag{5.42}$$

Then the weights and nodes can be extracted from Table 5.2.

This formula is especially useful in formulating a composite rule for even greater accuracy. To compute the integral over $[a,b]$, we divide up the interval into d equally spaced intervals of the form $[\xi_p, \xi_{p+1}]$ with $\xi_1 = a$ and $\xi_{d+1} = b$. Then we write

$$\int_a^b g(x)\,dx = \sum_{p=1}^{d}\int_{\xi_p}^{\xi_{p+1}} g(x)\,dx$$

and apply the change of variables (5.42) to each of the integrals on the right-hand side.

5.7.3 Setting the Cut-off Filter (Step 5)

The next order of business is to describe how to determine the value of c for the cut-off filter (5.35) of Step 5 of Algorithm 5.1. The definition (5.34) is inconvenient because n_{ind} as defined in (5.31) is implicit: n_0 depends on n_{ind} and n_0 appears in the right-hand side within V_{xc}. The "inverse"

$$\phi\big(n_{\text{ind}}\big) = E_F - \frac{1}{2}\left(3\pi^2\right)^{2/3} n_{\text{ind}}^{2/3} - V_{\text{xc}}\big(n_{\text{ind}} + n_{\text{qu}}\big) \tag{5.43}$$

is a more convenient subject of analysis. The relevant condition (5.34) for c then becomes

$$\frac{\partial \phi}{\partial n_{\text{ind}}}(c) = 0$$

The needed derivative can be computed explicitly:

$$\begin{aligned} G(n_{\text{ind}}) \triangleq \frac{\partial \phi}{\partial n_{\text{ind}}} &= -\frac{1}{3}\left(3\pi^2\right)^{2/3} n_{\text{ind}}^{-1/3} - V_{\text{xc}}'(n_0) \\ &= -\frac{1}{3}\left(3\pi^2\right)^{2/3} n_{\text{ind}}^{-1/3} - f_{\text{xc}}(n_0) \end{aligned} \tag{5.44}$$

We therefore need to find the value of c such that $G\big(n_{\text{ind}}(c)\big) = 0$, solving the above nonlinear equation which is parameterized in x. An important distinction is to be made here: we are looking for an x value that makes (5.44) zero. We could solve this for a value of $n_{\text{ind}} = n_c$ and then find c such that $n_{\text{ind}}(c) = n_c$; this is a poor method because it requires solving nonlinear equations twice. It is more efficient to solve directly for c.

The method of choice for solving nonlinear equations is Newton's method. Newton's method can be a bit temperamental, especially when a reasonably good initial guess is not used. Fortunately, we can generate a suitable starting value by evaluating (5.44) on the mesh $\{x_m\}$ that constitutes the nodes of the splines of the density n_0 and locating the first index m such that $x_{m-1} < 0$ and $x_m > 0$. We can then make $c^{(0)}$ to be the midpoint of these values. To implement Newton's method, we need the derivative of (5.44) in x:

$$\frac{\partial G}{\partial x} = \frac{1}{9}\left(3\pi^2\right)^{2/3} n_{\text{ind}}^{-4/3} \cdot \frac{\partial n_{\text{ind}}}{\partial x} - \frac{\partial f_{\text{xc}}}{\partial n} \cdot \frac{\partial n_0}{\partial x}$$

We have written all the derivatives in Leibnitz notation at the moment for the sake of clarity. Recall that f_{xc} is a function of n and that $g_{\text{xc}} = f_{\text{xc}}'$ was previously defined in (3.32). Therefore, the above expression can be simplified using usual prime notation:

$$G'(x) = \frac{1}{9}\left(3\pi^2\right)^{2/3} n_{\text{ind}}^{-4/3}(x) n_{\text{ind}}'(x) - g_{\text{xc}}\big(n_0(x)\big)\, n_0'(x) \tag{5.45}$$

The remaining necessary derivative n_{ind}' can be computed by differentiating (5.31) directly:

$$n_{\text{ind}}'(x) = -\frac{\sqrt{2}}{\pi^2}\Big[E_F - \phi - V_{\text{xc}}(n_0)\Big]^{1/2} \cdot \big(\phi' + f_{\text{xc}}\big(n_0(x)\big)\, n_0'(x)\big) \tag{5.46}$$

Thanks to the spline method, we have access to accurate values for n_0' and ϕ' anywhere within the computational domain. Having assembled all the needed pieces, the complete algorithm is:

Algorithm 5.3. Determining the Cut-off Filter.

Let $x_1 < x_2 < \cdots < x_{N+1}$ be the nodes of the splines for the density n_0.

1. Find the first index m such that $G(x_{m-1}) < 0$ and $G(x_m) > 0$. Put $c^{(0)} = \dfrac{x_{m-1} + x_m}{2}$.

2. Newton Step:
$$c^{(i)} = c^{(i-1)} - \frac{G\left(c^{(i-1)}\right)}{G'\left(c^{(i-1)}\right)}$$
G and G' are given by formulas (5.44) and (5.45) with help from (5.46).

3. Repeat Step 2 until
$$\left|c^{(i)} - c^{(i-1)}\right| < \tau$$
for some desired tolerance $\tau \approx 10^{-12}$.

The last matter is the value of λ in (5.35). While a larger λ will make F_c more like a step function, the cutoff filter doesn't need to be so precise. Local adaptivity can handle a steep transition with as little effort as possible, but the overhead is ultimately unnecessary. Taking $\lambda = 50$ is a good compromise; such a value approximates a step function reasonably well while not being too sharp (cf. the red curve in Figure 5.2).

5.7.4 Solving the Nonlinear Poisson Equation (Step 7)

The last detail to be resolved is the crafting of a solution to the nonlinear Poisson equation

$$\phi''(x) + \frac{2^{7/2}}{3\pi}\Big[E_F - \phi(x) - V_{\mathrm{xc}}\big(n_0(x)\big)\Big]^{3/2} \cdot F_c(x) = 4\pi\big(n_+(x) - n_0(x)\big)$$
$$\phi(-\infty) = 0, \phi'(+\infty) = -4\pi\varsigma$$

Because of the nonlinearity in ϕ, we appeal to Algorithm 2.1 when the adaptive Algorithm 2.3 calls for it. There is one major wrinkle we must iron out before proceeding: the background charge function n_+ is discontinuous at $x = 0$, so a naïve application of the spline method will not work well.

To remedy the issue with the discontinuity, we appeal to the Budd-Vannimenus Theorem (or more explicitly, Corollary 4.3) as in the orbital-free computation to decompose the problem into

Left problem: $\phi''(x) = f_L(x, \phi)$, $\phi(-\infty) = 0, \phi(0) = \phi_{BV}$

Right problem: $\phi''(x) = f_R(x, \phi)$, $\phi(0) = \phi_{BV}, \phi'(+\infty) = -4\pi\varsigma$

where $\phi_{BV} \triangleq \frac{1}{5}\left(3\pi^2\bar{n}\right)^{2/3} + V_{\mathrm{xc}}(\bar{n}) - \varepsilon_{\mathrm{xc}}(\bar{n}) + \frac{2\pi\varsigma^2}{\bar{n}}$ and

$$f_L(x,\phi) \triangleq 4\pi\big(\bar{n} - n_{\mathrm{qu}}(x)\big) - \frac{2^{7/2}}{3\pi}\Big[E_F - \phi(x) - V_{\mathrm{xc}}\big(n_0(x)\big)\Big]^{3/2} \cdot F_c(x)$$

$$f_R(x,\phi) \triangleq -4\pi n_{\mathrm{qu}}(x)$$

The location of the cutoff filter c occurs near the surface but always within the metal so that we always have $c < 0$. Thus, $F_c \equiv 0$ wipes out the nonlinear term in the right problem. Even though the right problem is a linear equation, we still use Algorithm 2.1. In applying the nonlinear algorithm to linear equations, all the derivative terms that appear in (2.4) and (2.5) vanish and the Jacobian matrix is the system matrix for a formulation of the method for linear BVPs. The "Newton iteration" will converge in one step.

For the left side, though, the derivative contributions contained in (2.4) and (2.5) do not vanish. Since f_L does not involve ϕ', we need only compute

$$\frac{\partial f_L}{\partial \phi} = -\frac{2^{5/2}}{\pi}\Big[E_F - \phi(x) - V_{\mathrm{xc}}\big(n_0(x)\big)\Big]^{1/2} \cdot F_c(x)$$

The solutions to the left and right problems are glued together by interpolating the complete set of nodes and computed values with a cubic spline. We cannot simply juxtapose the two half-solutions because the composite result will not be differentiable at 0. Thanks to Theorem 2.1, the interpolation error is same order as local truncation error, so resplining does not introduce additional error.

5.8 Computational Results

For the simulations depicted in this section, $\tau_a = 10^{-7}$ was used for the adaptive tolerance and $\tau_{sc} = 10^{-6}$ for convergence of the SCF iteration. The infinite domain was truncated to $[-35, 10]$. A composite seven-point rule of $d = 4$ divisions (28 k points total) was used in forming the density. Rules for other domains were also investigated. Five divisions were needed for $[-50, 10]$; $d = 4$ was insufficient to damp the strong oscillations that appear for $x \ll 0$. Two divisions were enough for $[-20, 10]$ while $[-120, 10]$ required ten.

For $r_s = 3$ and $\varsigma = 0$, we were able to obtain a ground state density profile after 12 iterations of SCF (Algorithm 5.1), terminating with a final previous-to-current-iterate error of 8.987029×10^{-7}. Table 5.3 below lists this error after each iteration. Figure 5.7 on the next page shows all the densities.

Figure 5.6 below shows the final density. When $x \ll 0$, we see the dying Friedel oscillations described in Section 5.4.1 about the limit value $\bar{n}$, plotted as the broken black line depicting the background charge n_+.

Iteration	Error	Iteration	Error	Iteration	Error
1	5.203366×10^{-4}	5	2.595343×10^{-5}	9	3.137688×10^{-6}
2	5.520106×10^{-5}	6	1.900946×10^{-5}	10	6.433941×10^{-6}
3	1.204258×10^{-4}	7	2.475704×10^{-5}	11	4.434425×10^{-6}
4	9.385186×10^{-5}	8	1.200144×10^{-5}	12	8.987029×10^{-7}

Table 5.3: Error Per Step of SCF Iteration. The desired error 10^{-6} was achieved after 12 iterations.

We also see that some electrons spill out into the vacuum and that the density decays exponentially from just outside the surface; this is the cause of the surface dipole barrier (see Definition 5.1).

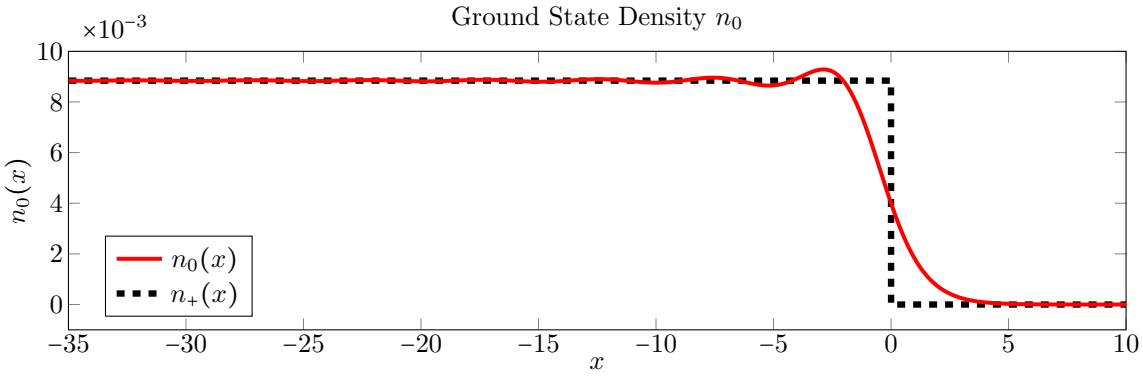

Figure 5.6: Ground State Density n_0 for $r_s = 3$ and $\varsigma = 0$. The density profile is shown in red; the broken black line is positive background charge. Algorithm 5.1 converged to this solution after 12 iterations.

Figure 5.8 depicts the corresponding electrostatic potential ϕ, computed as described in Section 5.7.4. The potential displays Friedel oscillations for $x < 0$, although they are not as pronounced as the ones in the density. This is the behavior that standard numerical methods applied directly to the Poisson equation fail to reproduce, although for $x > 0$ they do well qualitatively—but not quantitatively! (recall Figure 5.3).

We take a detour to highlight one of the benefits of adaptivity: each ψ_k can be computed on the best grid for that function. While each ψ_k can be computed quickly, even on large grids, because we must compute twenty to thirty wavefunctions per iteration and expect perform a dozen or more iterations, even a savings of one second per ψ_k can cut the time required to complete the SCF process significantly.

Table 5.4 presents the number of splines required to drive the residual error of wavefunctions below $\tau_a = 10^{-7}$. Only twelve are shown in the table, but in all, twenty-eight were used for n_0. Because $\psi_k \sim \sin(kx - \gamma_k)$ for

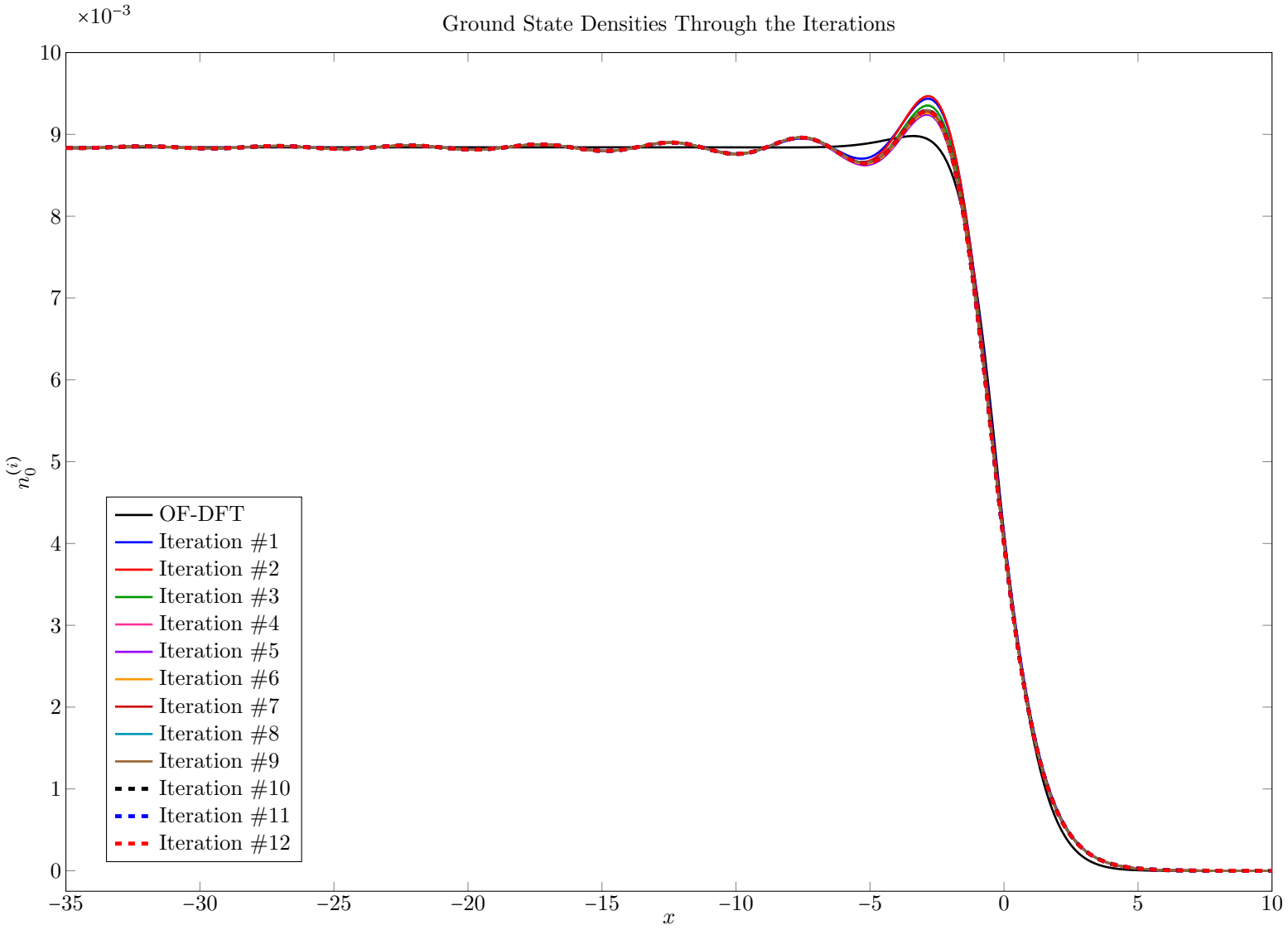

Figure 5.7: Density After Each Iteration. The starting density computed by the orbital-free methods of Chapter 4 is indicated by the solid black line. Note the much larger overshoot of Kohn-Sham densities compared to the orbital-free density.

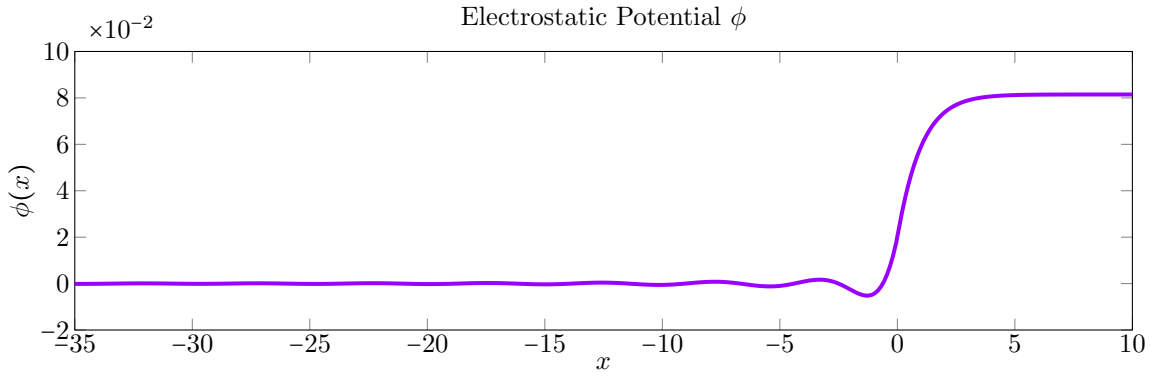

Figure 5.8: Electrostatic Potential ϕ for $r_s = 3$ and $\varsigma = 0$. This potential corresponds to the density depicted in Figure 5.6. The boundary condition $\varsigma = 0$ forces ϕ to approach a limit on the right end.

$x \ll 0$, fewer splines are needed for small k, as ψ_k oscillates slower in the asymptotic region as k decreases. The qualitative differences of low and high k wavefunctions is shown in Figure 5.9 beneath the table.

k	Splines	k	Splines	k	Splines
0.0041	2991	0.1559	3171	0.3674	6009
0.0475	2889	0.2074	3333	0.4591	6853
0.0800	2831	0.2723	4131	0.5273	7189
0.1124	2785	0.3158	5449	0.6191	7831

Table 5.4: Adaptive Splines in Action. This table lists the number of splines needed to compute the wavefunction ψ_k to residual error of $\tau_a = 10^{-7}$. For $r_s = 3$, $k_F = 0.6397$. In all, 28 k-values were used.

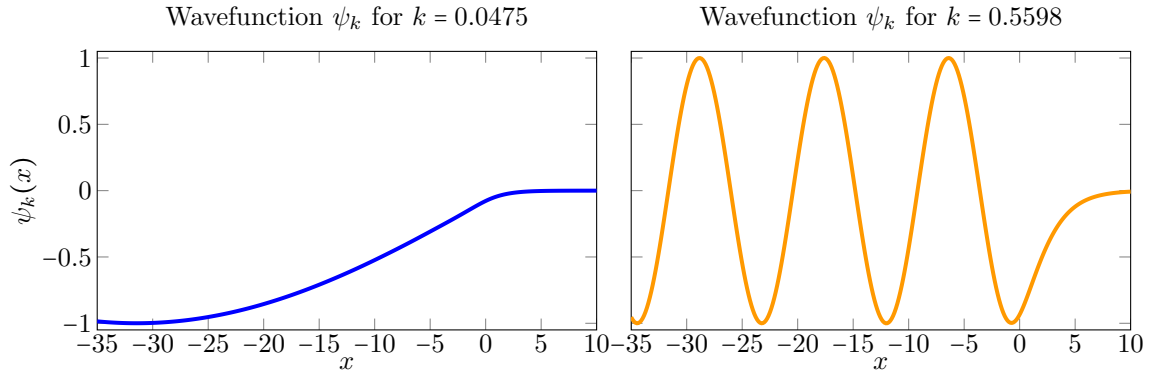

Figure 5.9: Wavefunctions ψ_k. Two ψ_k, corresponding to $k = 0.0475$ (left) and $k = 0.5598$ (right), used to form the density in Figure 5.6. The period of oscillation is $\frac{2\pi}{k}$, so small k means slower oscillation.

Below in Figure 5.10 is a density profile computed when $\varsigma = 5 \times 10^{-4}$ was taken as the boundary condition for $\phi'(+\infty)$. Because this density does not satisfy charge neutrality, we refer to it as a "screened density,"

as ς should more properly be interpreted as screening charge[†] than actual charge.

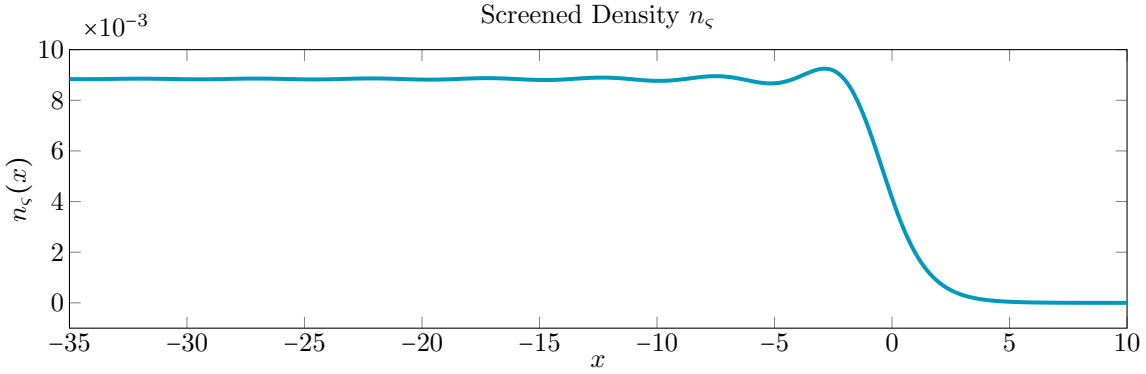

Figure 5.10: Screened Density n_ς for $r_s = 3$ and $\varsigma = 5 \times 10^{-4}$. This result was obtained after 15 iterations of SCF and concluded with the same final error of 5.8948×10^{-7}.

The screened profile looks nearly identical to the ground state one, but the corresponding electrostatic potential, depicted below in Figure 5.11, is obviously different: instead of flattening out to a steady-state value, ϕ decreases linearly on the right end of the domain. Since $\phi'(+\infty) = -4\pi\varsigma < 0$, this should be expected. Physically, this result shows that the effect of screening increases as we move farther from the surface.

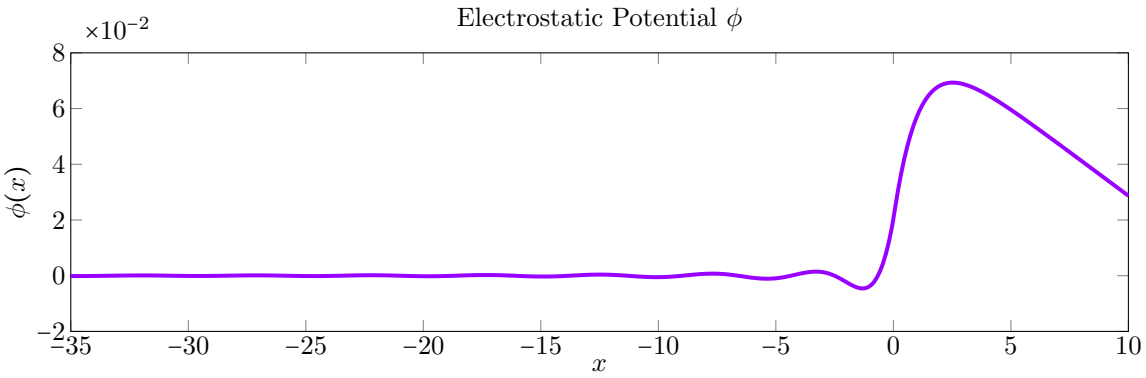

Figure 5.11: Electrostatic Potential ϕ for $r_s = 3$ and $\varsigma = 5 \times 10^{-4}$. This potential corresponds to the density depicted in Figure 5.10. Note how ϕ decreases linearly at the right end of the domain.

The last figure for $r_s = 3$ shows that there are quantitative differences between n_0 and n_ς. As Figure 5.12 shows, the largest differences are concentrated near zero. Since screening is a surface effect, it is natural that the greatest contributions to screening occur in the immediate region of the interface. Because the ultimate

[†]Electrons each possess their own electric fields. These fields cause electrons to repel each other, which creates little "bubbles" in which no other electron is present. At far enough distances, this bubble can be perceived as a sheet of positive charge that serves to negate the electrons' electric fields. The term "screening charge" refers to the collective effect of this.

goal for n_ς is in describing second harmonic generation in Chapter 8, ς has been limited to small values (weak-electric fields), which explains the small difference between n_0 and n_ς. As ς increases, the screened density deviates from the ground state one significantly; see, for example, Gies and Gerhardts [42].

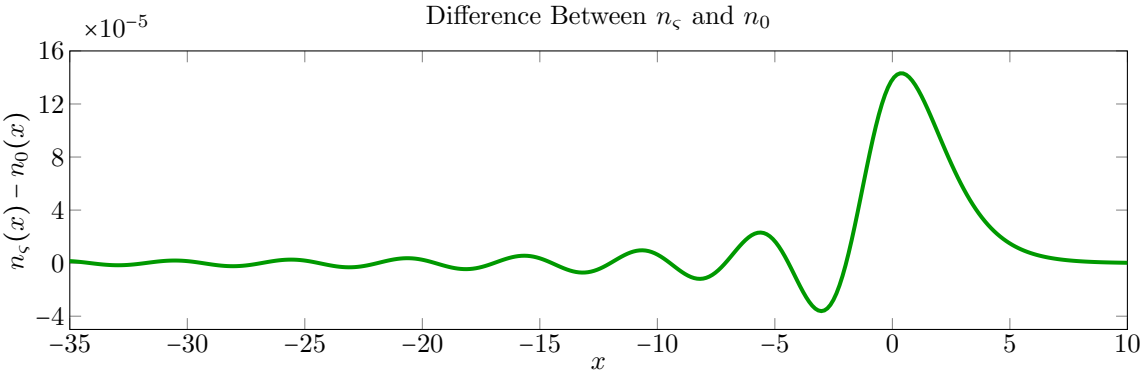

Figure 5.12: Difference between n_0 and n_ς for $r_s = 3$. That largest difference occurs inside the metal in the immediate vicinity of the surface reflects the nature of screening as a surface phenomenon.

The last result is the ground state density for $r_s = 2$ in Figure 5.13 below. Lower tolerances of $\tau_a = 5 \times 10^{-7}$ and $\tau_{sc} = 2 \times 10^{-5}$ were used for this run. Significantly many more splines are required for high accuracy, leading to instabilities and long computation times. The result is unremarkable when compared to the $r_s = 3$, except that Friedel oscillations are much less pronounced.

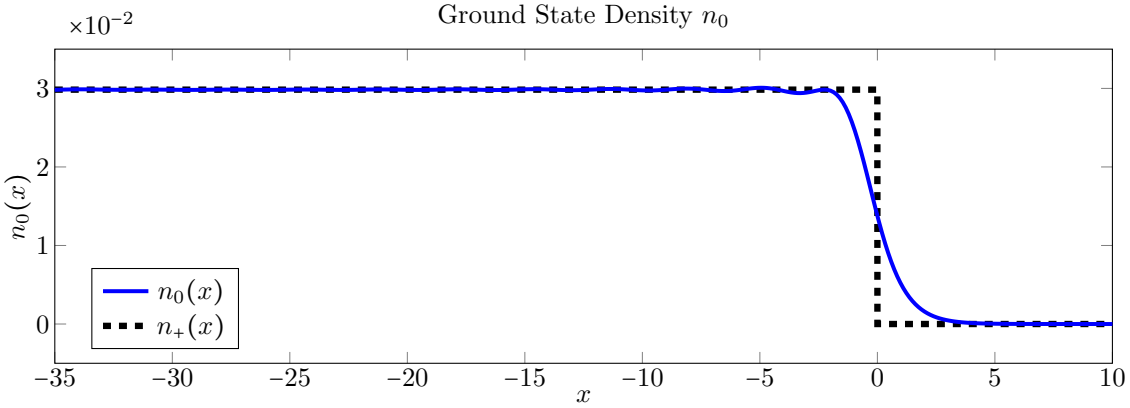

Figure 5.13: Ground State Density n_0 for $r_s = 2$ and $\varsigma = 0$. The density profile is shown in blue; the broken black line is positive background charge. Convergence took 8 iterations and error 1.5584×10^{-5}.

Finally, a word on computation time. The workstation used was a quad-core Intel Core i7 875K overclocked to 3464 MHz with 16GB of DDR3-1333 RAM, running MATLAB 2010a and Windows Vista Business x64. From the beginning of the first wavefunction computation to solving for ϕ, each iteration required 77 seconds on average. To obtain convergence to $\tau_{sc} = 10^{-6}$, the process took 15 minutes and 27 seconds in totality.

5.9 Conclusion

Kohn-Sham calculations for the ground state in jellium systems are not new. However, despite the saturation of the topic, this chapter has put forth both noteworthy theoretical and significant numerical advancements.

Outside the detailed presentation of the setup of KS-DFT for jellium systems in the early sections, the primary theoretical contribution of this chapter is the proof of the asymptotic formula in Theorem 5.2. Friedel oscillations are a distinguishing feature of jellium densities, and while the result of the theorem is common knowledge in the field, the proof has not been disseminated in any measure of publicity.

Numerically, the foremost contribution of this work is the adaptive spline collation method for ψ_k. The spline method facilitates obtainment of highly accurate results without need for analysis from the user aside from selection of a tolerance. The method maintains maximum efficiency by tailoring grids for each equation. Previous works universally used the Numerov method [81] on fixed grids, the use of which in atomic structure calculations can be traced back to Hartree [49, p.71] and has perpetuated for forty years [66, 87].

The direct method employed in this thesis for solving the Poisson equation for the electrostatic potential is a very welcome advancement. Since its first development by Manninen [75], conversion of the differential equation to the implicit integral equation (5.29) has been a staple in virtually every DFT for jellium computation. The method carries several significant disadvantages, all of which are resolved by the nonlinearization of the Poisson equation presented here:

1. (5.29) must be solved iteratively and concurrent with the Kohn-Sham system.
2. (5.29) leads to instability unless some sort of mixing scheme is used on successive density iterates.
3. (5.29) cannot handle the nonzero boundary conditions of charged systems.

The density splitting scheme was first proposed by Shul'Man [99] and solidified into a coherent algorithm by Posvyanskii and Shul'man [87]. This thesis greatly improves upon the latter's method in several ways:

1. Invocation of the Budd-Vanninemus Theorem allows for satisfactory sidestepping of the discontinuity in the background charge. Posvyanskii and Shul'man used a relaxation method that complicates the equation by introducing a time variable and then seeks the steady-state solution.
2. The adaptive spline method provides accurate derivative information that facilitates computation of the phase shifts γ_k so that ψ_k can be properly normalized. Posvyvanskii and Shul'man stuck with the traditional Numerov method, using a Taylor series to find the needed values.

3. Algorithm 5.3 provides a means to set the cutoff filter for arbitrary V_{xc}. Posvyanskii and Shul'man used the Wigner correlation kernel (3.24), exploiting its simple form to find c analytically.

Chapter 6

Green's Functions and Spectra

The subject of Green's functions, especially in the context of quantum mechanics [22] and even time-dependent density functional theory [110, p.86], is a deep one of paramount importance. In physics, particularly in many-body theory [71], the term "Green's function" is used liberally to refer to any one of several different, unrelated concepts, reaching as far as correlation functions of creation and annhilation operators.

Throughout this thesis, "Green's function" will used strictly in the mathematical sense: it is the fundamental solution to a linear differential equation. If G is the Green's function of a differential operator $\mathcal{A}$, then a solution to $\mathcal{A}u = f$ may be obtained by integrating $G(x,y)f(y)$ in y. This chapter investigates the Green's function for the Schrödinger operator $\mathcal{H}$ that generates the Kohn-Sham wavefunctions via (5.10):

$$\mathcal{H} \triangleq -\frac{1}{2}\frac{\partial^2}{\partial x^2} + V(x) \tag{6.1}$$

6.1 Derivation of Green's Function

Recalling Theorem 5.1 and the techniques used to generate boundary conditions for ψ_k in Sections 5.3.1 and 5.3.2, we know that solutions to $\big(\mathcal{H} - \varepsilon\big)\varphi = 0$ behave like

$$\varphi \sim \begin{cases} ae^{i\mu x} + be^{-i\mu x} & x \to -\infty \\ ce^{i\nu x} + de^{-i\nu x} & x \to +\infty \end{cases} \tag{6.2}$$

where the two exponents are[†], with help from Theorem 3.4 and the boundary condition $\phi(-\infty) = 0$,

[†]This definition of ν differs the one used in other sources, e.g., [67]. Because $\phi(+\infty) \ll 1$, giving $V(+\infty) \approx 0$, this quantity is traditionally neglected without explanation. We include it because there is little reason not to.

$$\mu \triangleq \sqrt{2\varepsilon - 2V(-\infty)} = \sqrt{2\varepsilon - 2V_{\mathrm{xc}}(r_s)} \tag{6.3}$$

$$\nu \triangleq \sqrt{2\varepsilon - 2V(+\infty)} = \sqrt{2\varepsilon - 2\phi(+\infty)} \tag{6.4}$$

We allow $\varepsilon \in \mathbb{C}$, so we must specify the branch of the complex square root to be used. We take the branch cut removing the negative real axis and taking the argument θ of z to lie in $(0, 2\pi)$. Then we take

$$\sqrt{z} = \sqrt{r}e^{i\theta/2}$$

This choice of argument ensures that $\mathrm{Im}(\mu) \geq 0$ and $\mathrm{Im}(\nu) \geq 0$. We can generate two linearly independent solutions ("basis functions") φ_1 and φ_2 by imposing the asymptotic conditions

$$\varphi_1 \sim \begin{cases} ae^{i\mu x} + be^{-i\mu x} & x \to -\infty \\ e^{i\nu x} & x \to +\infty \end{cases} \qquad \varphi_2 \sim \begin{cases} e^{-i\mu x} & x \to -\infty \\ ce^{i\nu x} + de^{-i\nu x} & x \to +\infty \end{cases} \tag{6.5}$$

Let $G(x, y; \varepsilon)$ be the Green's function to the operator $\mathcal{H} - \varepsilon$. It satisfies the equation

$$\big(\mathcal{H} - \varepsilon\big)G(x, y; \varepsilon) = -\delta(x - y) \tag{6.6}$$

and must have the following properties [21, p.36]:

1. (Continuity) $G(\cdot, \cdot; \varepsilon)$ is continuous on $\mathbb{R} \times \mathbb{R}$
2. (Continuity of derivative) $\dfrac{\partial G}{\partial x}(\cdot, y; \varepsilon)$ is continuous on $\mathbb{R}\backslash\{y\}$
3. (Jump condition) $\dfrac{\partial G}{\partial x}(x, y; \varepsilon)\Big|_{x=y^-}^{x=y^+} = \lim\limits_{x \to y^+} \dfrac{\partial G}{\partial x}(x, y; \varepsilon) - \lim\limits_{x \to y^-} \dfrac{\partial G}{\partial x}(x, y; \varepsilon) = \dfrac{1}{-\frac{1}{2}} = -2.$
4. (Symmetry) $G(x, y; \varepsilon) = G(y, x; \varepsilon)$

In 1D, the Green's function "switches" between the two linearly independent solutions. To this end, put

$$G(x, y; \varepsilon) = \begin{cases} A(y)\varphi_1(x), & -\infty < x \leq y \\ B(y)\varphi_2(x), & y < x \leq \infty \end{cases} \tag{6.7}$$

By Properties (1) and (3), the basis functions φ_1 and φ_2 must satisfy

$$\begin{aligned} A(y)\varphi_1(y) - B(y)\varphi_2(y) &= 0 \\ A(y)\varphi_1'(y) - B(y)\varphi_2'(y) &= 2 \end{aligned} \tag{6.8}$$

To solve the system of equations (6.8), we shall employ Cramer's Rule. First, recall the Wronskian

$$W(\varphi_1, \varphi_2)(y) \triangleq \det \begin{bmatrix} \varphi_1(y) & \varphi_2(y) \\ \varphi_1'(y) & \varphi_2'(y) \end{bmatrix} \tag{6.9}$$

and that scaling a column of a matrix changes its determinant by the same factor. Therefore,

$$-W(\varphi_1, \varphi_2)(y) = \det \begin{bmatrix} \varphi_1(y) & -\varphi_2(y) \\ \varphi_1'(y) & -\varphi_2'(y) \end{bmatrix}$$

By Cramer's Rule, the coefficients A and B are given by

$$A(y) = -\frac{1}{W(\varphi_1, \varphi_2)(y)} \det \begin{bmatrix} 0 & -\varphi_2(y) \\ 2 & -\varphi_2'(y) \end{bmatrix} = -\frac{2\varphi_2(y)}{W(\varphi_1, \varphi_2)(y)}$$

$$B(y) = -\frac{1}{W(\varphi_1, \varphi_2)(y)} \det \begin{bmatrix} \varphi_1(y) & 0 \\ \varphi_1'(y) & 2 \end{bmatrix} = -\frac{2\varphi_1(y)}{W(\varphi_1, \varphi_2)(y)}$$

By properties of determinants $-W(\varphi_1, \varphi_2) = W(\varphi_2, \varphi_1)$. Using this fact on the above solutions A and B, substitution of the result into (6.7) yields the revised formula for G:

$$G(x, y; \varepsilon) = \begin{cases} 2\dfrac{\varphi_1(x)\varphi_2(y)}{W(\varphi_2, \varphi_1)(y)}, & -\infty < x \le y \\ 2\dfrac{\varphi_1(y)\varphi_2(x)}{W(\varphi_2, \varphi_1)(y)}, & y < x \le \infty \end{cases}$$

The derivation will be complete after an appeal to the well-known Abel's Identity [7, p.118]:

Lemma 6.1 (**Abel's Identity**). *Let ζ_1 and ζ_2 be two linearly independent solutions to*

$$\zeta''(y) + p(y)\zeta'(y) + q(y)\zeta(y) = 0$$

Then the Wronksian W satisfies

$$W(\zeta_1, \zeta_2)(y) = W(\zeta_1, \zeta_2)(y_0) \exp\left(-\int_{y_0}^{y} p(t)\, dt\right)$$

In the case of $\mathcal{H} - \varepsilon$, $p \equiv 0$, so for any $y_0 \in \mathbb{R}$

$$W(\varphi_2, \varphi_1)(y) = W(\varphi_2, \varphi_1)(y_0) \equiv \text{constant}$$

In light of this, the constant W may be computed in the limit $y \to -\infty$ or $y \to +\infty$ by appealing to the asymptotic boundary conditions (6.5):

$$\begin{aligned} W(\varphi_2, \varphi_1) &= \lim_{y \to -\infty} \left[\varphi_2(y)\varphi_1'(y) - \varphi_2'(y)\varphi_1(y) \right] \\ &= \lim_{y \to -\infty} \left[e^{-i\mu x}\left(ia\mu e^{i\mu y} - ib\mu e^{-i\mu y} \right) + i\mu e^{-i\mu y}\left(ae^{i\mu y} + be^{-i\mu y} \right) \right] \\ &= 2i\mu a \end{aligned} \tag{6.10}$$

or

$$\begin{aligned} W(\varphi_2, \varphi_1) &= \lim_{y \to +\infty} \left[\varphi_2(y)\varphi_1'(y) - \varphi_2'(y)\varphi_1(y) \right] \\ &= \lim_{y \to +\infty} \left[\left(ae^{i\nu y} + be^{-i\nu y} \right) i\nu e^{i\nu y} - \left(ia\nu e^{i\nu y} - ib\nu e^{-i\nu y} \right) e^{i\nu y} \right] \\ &= 2i\nu c \end{aligned} \tag{6.11}$$

Because φ_1, φ_2, and W (which can now be written sans arguments) all depend on ε, it is preferable to write

$$G(x, y; \varepsilon) = \begin{cases} \dfrac{2}{W_\varepsilon} \varphi_1(x; \varepsilon)\varphi_2(y; \varepsilon) & -\infty < x \le y \\ \dfrac{2}{W_\varepsilon} \varphi_1(y; \varepsilon)\varphi_2(x; \varepsilon), & y < x \le \infty \end{cases} \tag{6.12}$$

6.2 Spectral Theory

6.2.1 The Operator $\mathcal{H}$

The nature of the Kohn-Sham potential V has a large effect on the spectrum of $\mathcal{H}$. Consequently, an examination of the specifics of V is necessary before we can proceed farther.

Depicted in Figure 6.1 is the Kohn-Sham potential for $r_s = 3$. Perhaps more important than any properties it possesses are the properties it does *not* have:

- V is not monotonic
- As $V(\pm\infty) \neq 0$, V is not integrable, nor is $V - c\Theta(x)$ or $V - c\Theta(-x)$ for any constant c
- V attains both positive and negative values

By applying standard results from scattering theory and the theory of one-dimensional Schrödinger operators [100, p.63], if V possessed one of these properties, the spectrum of $\mathcal{H}$ would be easily obtained.

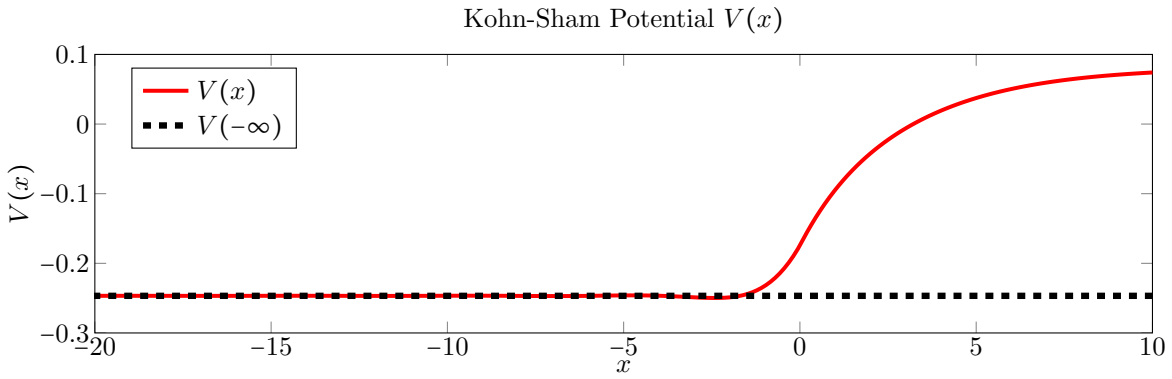

Figure 6.1: Kohn-Sham Potential V. Depicted for $r_s = 3$ is the Kohn-Sham potential $V = \phi + V_{\text{xc}}(n_0)$ and the limit value $V(-\infty)$. n_0 and ϕ are the ones shown in Figures 5.6 and 5.8, respectively.

Figure 6.2 below shows the detail of the potential and showcases the oscillations in V due to the Friedel oscillations of density. The diagram depicts just $r_s = 3$. Other r_s values of interest have similar potentials, although there are quantitative differences, of course. For $r_s = 2$, for example, the smaller and less pronounced oscillations in the density lead to a corresponding effect in the potential.

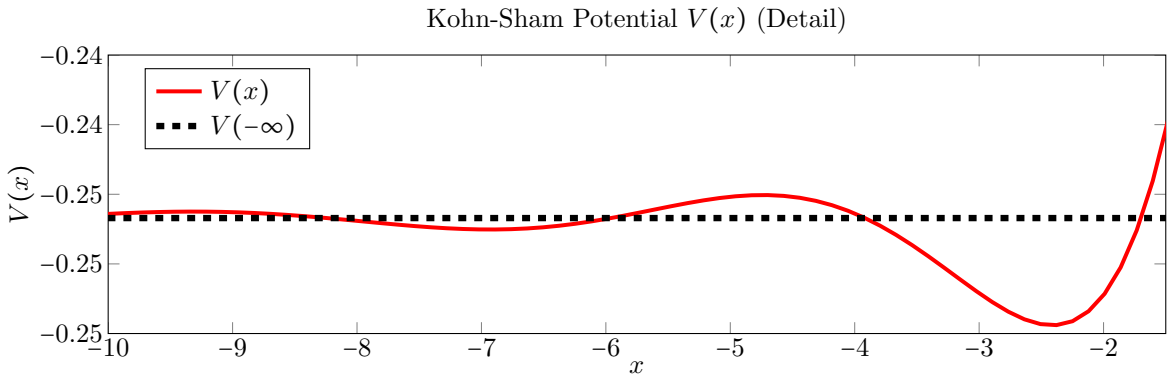

Figure 6.2: Detail of Kohn-Sham Potential V. This highlight of V (for $r_s = 3$) shows the oscillations in the Kohn-Sham potential due to the Friedel oscillations of n_0.

6.2.2 Review of Functional Analysis

This section briefly reviews important background from functional analysis. For an in-depth discussion, the reader is directed to consult one of the many texts on the subject, such as Rudin [92] or Conway [18]. The theorem and definition statements appearing throughout Section 6.2 are adapted from Teschl [105].

Definition 6.1 (Spectrum). *Let $\mathscr{B}$ be a Banach space over $\mathbb{C}$ and $\mathcal{A} : \mathfrak{D} \to \mathscr{B}$ be a linear operator defined on a dense subspace $\mathfrak{D} \subseteq \mathscr{B}$. The* spectrum *of $\mathcal{A}$ is the set*

$$\sigma(\mathcal{A}) = \left\{\lambda \in \mathbb{C} : \mathcal{A} - \lambda \text{ does not have a bounded inverse}\right\}$$

The operator $\mathcal{A} - \lambda$ can fail to have a bounded inverse in several different ways:

1. $\big(\mathcal{A} - \lambda\big)^{-1}$ exists but is not bounded
2. $\text{range}\big(\mathcal{A} - \lambda\big) \neq \mathscr{B}$ or $\text{range}(\mathcal{A} - \lambda)$ is not dense in $\mathscr{B}$ and $\mathcal{A} - \lambda$ is not bounded below.
3. $\mathcal{A} - \lambda$ is not one-to-one

If $\mathcal{A}$ is bounded, then its inverse, if it exists, must also be bounded, so item 1 is only possible for unbounded operators (e.g., any differential operator). If item 3 fails, then there exists $\psi \in \mathscr{B}\backslash\{0\}$ such that $\big(\mathcal{A} - \lambda\big)\psi = 0$; in this case, λ is called an *eigenvalue* and ψ is an *eigenstate* (physics) or *eigenvector* (mathematics).

The spectrum can be decomposed into several important subsets, defined below.

Definition 6.2 (**Point Spectrum**). *The* point spectrum $\sigma_{\text{pt}}(\mathcal{A})$ *is the set of eigenvalues of* $\mathcal{A}$.

Definition 6.3 (**Essential Spectrum**). *The* essential spectrum*, denoted* $\sigma_{\text{ess}}(\mathcal{A})$*, is the spectrum minus the set of eigenvalues that are isolated points with finite-dimensional eigenspace:*

$$\sigma_{\text{ess}}(\mathcal{A}) = \sigma(\mathcal{A})\backslash\Big\{\lambda : 0 < \dim \text{range}\big(\mathcal{A} - \lambda\big) < \infty \text{ and } \exists r > 0 \text{ s.t. } B_r(\lambda)\backslash\{\lambda\} \cap \sigma(\mathcal{A}) = \varnothing\Big\}$$

6.2.3 Characterization of the Spectrum of $\mathcal{H}$

Definition 6.3 of the essential spectrum is not terribly useful, as it requires knowledge of all eigenvalues and their eigenspaces. In practice, such information is incredibly difficult to obtain. An important result credited to Weyl concisely characterizes the essential spectrum of a self-adjoint operator defined on a dense subspace of a Hilbert space in a way that can be easily checked.

Definition 6.4 (**Symmetric and Self-adjoint Operators**). *Let* $\mathcal{A} : \mathfrak{D} \to \mathscr{H}$ *be a densely-defined operator.* $\mathcal{A}$ *is called* symmetric *if for all* $\psi, \varphi \in \mathfrak{D}$*,*

$$\big\langle \psi, \mathcal{A}\varphi \big\rangle_{\mathscr{H}} = \big\langle \mathcal{A}\psi, \varphi \big\rangle_{\mathscr{H}}$$

The adjoint operator $\mathcal{A}^*$ *is defined by*

$$\mathfrak{D}(\mathcal{A}^*) = \Big\{\psi \in \mathscr{H} \,\Big|\, \exists \tilde{\psi} \in \mathscr{H} : \big\langle \psi, \mathcal{A}\varphi \big\rangle_{\mathscr{H}} = \big\langle \tilde{\psi}, \varphi \big\rangle_{\mathscr{H}} \; \forall \varphi \in \mathfrak{D}(\mathcal{A})\Big\}$$
$$\mathcal{A}^*\psi = \tilde{\psi}$$

If $\mathcal{A} = \mathcal{A}^*$*, then the operator is said to be* self-adjoint.

Remark 6.1. While all self-adjoint operators are symmetric, the converse is not true. The domain of the adjoint operator may be different from that of the original operator. A self-adjoint operator is therefore a symmetric operator such that $\mathfrak{D}(\mathcal{A}) = \mathfrak{D}(\mathcal{A}^*)$. ■

Remark 6.2. Although not a direct consequence of the definition, self-adjoint operators have $\sigma(\mathcal{A}) \subseteq \mathbb{R}$.

Lemma 6.2 (**Weyl Criterion**). *$\lambda \in \sigma_{\text{ess}}(\mathcal{A})$ if and only if there is a sequence ψ_n such that $\|\psi_n\| = 1$, $\langle \psi_m, \psi_n \rangle = 0$ for $n \neq m$, and $\|(\mathcal{A} - \lambda)\psi_n\| \to 0$. Such a sequence is called a singular Weyl sequence for λ.*

Before proceeding to the critical result in Theorem 6.1, we need another definition and lemma.

Definition 6.5 (**Relatively bounded**). *An operator $\mathcal{B} : \mathfrak{D}(\mathcal{B}) \to \mathscr{H}$ is called* relatively bounded *with respect to another operator $\mathcal{A} : \mathfrak{D}(\mathcal{A}) \to \mathscr{H}$ if $\mathfrak{D}(\mathcal{A}) \subseteq \mathfrak{D}(\mathcal{B})$ and there are constants $a, b \geq 0$ such that*

$$\|\mathcal{B}\psi\|_{\mathscr{H}} \leq a\|\mathcal{A}\psi\|_{\mathscr{H}} + b\|\psi\|_{\mathscr{H}}$$

*for all $\psi \in \mathfrak{D}(\mathcal{A})$. The $\mathcal{A}$-*bound *of $\mathcal{B}$ is the value*

$$a^* = \inf\left\{a \,\middle|\, \exists b \geq 0 \text{ such that } \|\mathcal{B}\psi\|_{\mathscr{H}} \leq a\|\mathcal{A}\psi\|_{\mathscr{H}} + b\|\psi\|_{\mathscr{H}} \ \forall \psi \in \mathfrak{D}(\mathcal{A})\right\}$$

Remark 6.3. If $\mathcal{B}$ is a bounded operator, then it is necessarily relatively bounded with respect to any other operator $\mathcal{A}$ (then $\mathfrak{D}(\mathcal{B}) = \mathscr{H}$ and we can take $a = 0$). ■

Lemma 6.3 (**Kato-Rellich**). *Suppose that $\mathcal{A}$ is self-adjoint and $\mathcal{B}$ is symmetric and relatively bounded with $\mathcal{A}$-bound less than one. Then $\mathcal{A} + \mathcal{B}$, $\mathfrak{D}(\mathcal{A} + \mathcal{B}) = \mathfrak{D}(\mathcal{A})$ is also self-adjoint.*

The Weyl Criterion and Kato-Rellich lemma are the easiest route to proving the result below, which appears as an exercise in [105, p.148].

Theorem 6.1. *Let $q \in L^\infty(\mathbb{R})$ be real-valued and $\mathcal{A} = -\frac{1}{2}\frac{\partial^2}{\partial x^2} + q(x)$ with domain $\mathfrak{D} = H^2(\mathbb{R})$. Then $\mathcal{A}$ is self-adjoint. If*

$$-u''(x) + q(x)u(x) = \lambda u(x)$$

has a solution for which u and u' are bounded but $u \notin L^2(\mathbb{R})$, then $\lambda \in \sigma_{\text{ess}}(\mathcal{H})$.

Proof. First, we prove that $\mathcal{A}$ is self-adjoint. Define the free Schrödinger operator $\mathcal{H}_0 \triangleq -\frac{1}{2}\frac{\partial^2}{\partial x^2}$ and the multiplication operator $\mathcal{Q}\psi(x) \triangleq q(x)\psi(x)$. It is well known that $\mathcal{H}_0$ is self-adjoint when $\mathfrak{D}(\mathcal{H}_0) = H^2(\mathbb{R})$ [105, p.168]. Because $q \in L^\infty(\mathbb{R})$, $\mathcal{Q}$ is a bounded operator on $L^2(\mathbb{R})$:

$$\|\mathcal{Q}\psi\|^2_{L^2(\mathbb{R})} = \int_{\mathbb{R}} |q(x)\psi(x)|^2 \, dx \leq \|q\|^2_{L^\infty(\mathbb{R})} \|\psi\|^2_{L^2(\mathbb{R})} \tag{6.13}$$

Furthermore, because q is real-valued, $\mathcal{A}$ is also symmetric: for any $\psi, \varphi \in L^2(\mathbb{R})$

$$\big\langle \psi, \mathcal{Q}\varphi \big\rangle_{L^2(\mathbb{R})} = \int_{\mathbb{R}} \psi(x)\big(q(x)\varphi(x)\big)^* \, dx = \int_{\mathbb{R}} \big(q(x)\psi(x)\big)\varphi^*(x) \, dx = \big\langle \mathcal{Q}\psi, \varphi \big\rangle_{L^2(\mathbb{R})}$$

Consequently, by Remark 6.3 and the Kato-Rellich lemma, $\mathcal{A}$ is self-adjoint with domain $\mathfrak{D}(\mathcal{A}) = H^2(\mathbb{R})$.

Now, let (u, λ) be a solution and value satisfying the properties of the theorem statement. For $n \in \mathbb{N}$, let $K_n \triangleq [-n, n]$ and $\varphi_n \in C_c^\infty(\mathbb{R})$ be such that

$$\varphi_n(x) = \begin{cases} 1 & x \in K_n \\ 0 & x \notin K_n \end{cases}$$

A continuous function meeting the above specifications exists by Urysohn's lemma [90, p.179]; a C_c^∞ version can be constructed by convolving with a standard mollifier [26, p.629]. Define

$$\psi_n \triangleq \frac{1}{c_n} u \cdot (\varphi_{n+1} - \varphi_n)$$

where c_n is chosen so that $\| \psi_n \|_{L^2(\mathbb{R})} = 1$, which is well defined because $u \in L^\infty(\mathbb{R})$. Note that

$$\begin{aligned} c_n = \| u \cdot (\varphi_{n+1} - \varphi_n) \|_{L^2(\mathbb{R})} &\leq \big\| u^2 \big\|_{L^\infty(\mathbb{R})} \| \varphi_{n+1} - \varphi_n \|_{L^2(\mathbb{R})} \\ &= \| u \|^2_{L^\infty(\mathbb{R})} \left[\int_{\mathbb{R}} \big(\varphi_{n+1} - \varphi_n\big)^2 \, dx \right]^{1/2} \\ &= \| u \|^2_{L^\infty(\mathbb{R})} \left[\int_{-n-1}^{-n} dx + \int_n^{n+1} dx \right]^{1/2} = \sqrt{2} \| u \|^2_{L^\infty(\mathbb{R})} \end{aligned}$$

so the c_n are uniformly bounded. Next, observe that ψ_n forms an orthonormal sequence, as ψ_n and ψ_m have disjoint support whenever $n \neq m$. Because

$$\frac{\partial^2}{\partial x^2}\big[u\varphi_n\big] = u''\varphi_n + 2u'\varphi_n' + u\varphi_n''$$

we have

$$\begin{aligned} c_n\big(\mathcal{A} - \lambda\big)\psi_n &= \big(\mathcal{A} - \lambda\big)u \cdot \big(\varphi_{n+1} - \varphi_n\big) - 2u'\varphi_{n+1}' - u\varphi_{n+1}'' + 2u'\varphi_n' + u\varphi_n'' \\ &= -2u' \cdot \big(\varphi_{n+1}' - \varphi_n'\big) - u \cdot \big(\varphi_{n+1}'' - \varphi_n''\big) \end{aligned}$$

because $\big(\mathcal{A}-\lambda\big)u=0$. As a consequence of (6.13), we have the estimate

$$\big\|\big(\mathcal{A}-\lambda\big)\psi_n\big\|_{L^2(\mathbb{R})}\leq\sqrt{2}\,\|u'\|^2_{L^\infty(\mathbb{R})}\,\|\varphi'_{n+1}-\varphi'_n\|_{L^2(\mathbb{R})}+\sqrt{2}\,\|u\|^2_{L^\infty(\mathbb{R})}\,\|\varphi''_{n+1}-\varphi''_n\|_{L^2(\mathbb{R})}$$

Because φ'_n and φ''_n vanish outside of very small regions near the points n and $-n$, we have $\varphi'_n\to 0$ and $\varphi''_n\to 0$ pointwise as $n\to 0$. An application of Fatou's Lemma [91, p.23] gives

$$\big\|\big(\mathcal{A}-\lambda\big)\psi_n\big\|_{L^2(\mathbb{R})}\longrightarrow 0$$

Therefore, ψ_n forms a singular Weyl sequence for λ, so $\lambda\in\sigma_{\text{ess}}(\mathcal{H})$. ∎

Corollary 6.2. $\big[V(-\infty),+\infty\big)\subset\sigma_{\text{ess}}(\mathcal{H})$. *In particular, each* ε_k *defined by* (5.11) *is an element of* $\sigma_{\text{ess}}(\mathcal{H})$.

Proof. Let $\varepsilon\in\big[V(-\infty),+\infty\big)$, then $\mu^2\geq 0$. Consequently, following Theorem 5.1 the solution u corresponding to ε is oscillatory as $x\to-\infty$; hence, it is is bounded near $-\infty$ but not square integrable. Since $\nu^2<0$ as well, u can be chosen to decay exponentially as $x\to+\infty$, so it is bounded everywhere. ∎

Theorem 6.1 motivates a defining a new concept highly applicable to the Kohn-Sham wavefunctions ψ_k:

Definition 6.6 (**Extended Eigenvector**). *For* $\lambda\in\sigma_{\text{ess}}(\mathcal{A})\backslash\sigma_{\text{pt}}(\mathcal{A})$, ψ *is called an* extended eigenvector (eigenstate) *if* $\big(\mathcal{A}-\lambda\big)\psi=0$ *but* $\psi\notin\mathfrak{D}(\mathcal{A})$.

There are a number of issues in the above definition, chief among them is that if $\psi\notin\mathfrak{D}(\mathcal{A})$, then to which space does it belong? Is it even possible to define $\mathcal{A}$ on another space? These matters can only be by considering the specifics of the space $\mathscr{H}$, the operator $\mathcal{A}$, and its domain $\mathfrak{D}$.

In the proof of Theorem 6.1, we were able to construct a Weyl sequence by beginning with a classical solution $u\in C^2(\mathbb{R})\cap L^\infty(\mathbb{R})$. The construction fundamentally depended on the ability to define the operator $\mathcal{A}$ on a space different but "not too different" from $H^2(\mathbb{R})$. In this case, we were able work with $C_c^\infty(\mathbb{R})$ functions because both $L^2(\mathbb{R})$ and $H^2(\mathbb{R})$ are completions of $C_c^\infty(\mathbb{R})$ in their respective norms.

In essence, what we have done is replace the original Hilbert space with what is known as a *rigged Hilbert Space*. Without digressing into the rigors, the idea to take a subspace $\Phi\subseteq\mathscr{H}$ with a continuously embedded topology. By using the inner product on $\mathscr{H}$ to form linear functionals and identifying $\mathscr{H}$ with its continuous dual space $\mathscr{H}^*$ by Riesz Representation, we extend $\mathscr{H}$ by sandwiching between dual spaces: $\Phi\subseteq\mathscr{H}\subseteq\Phi^*$. In the context of $H^2(\mathbb{R})$, we consider the dense subspace $\Phi=C_c^\infty(\mathbb{R})$, whose dual space is the set of ordinary distributions. It is i.s.d. under which extended eigenvectors are to be understood.

Remark 6.4. Per Corollary 6.2, each ψ_k is an extended eigenvector for $\mathcal{H}$ corresponding to ε_k. ■

We return to "regular" eigenvalues and eigenvectors and characterize the point spectrum of $\mathcal{H}$:

Theorem 6.3. $\text{pt spec}(\mathcal{H}) = \big(-\infty, V(-\infty)\big)$

Proof. The proof is by construction of an eigenvector. Let $\varepsilon \in \big(-\infty, V(-\infty)\big)$. Invoking the highly useful Theorem 5.1, the asymptotic behavior of solutions is

$$\psi \sim \begin{cases} ae^{i\mu x} + be^{-i\mu x} & x \to -\infty \\ ce^{i\nu x} + de^{-i\nu x} & x \to +\infty \end{cases}$$

By (6.4), it is clear that $\mu^2 < 0$. Put $\tau \triangleq \varepsilon - V(-\infty) < 0$. Then

$$\begin{aligned} \frac{1}{2}\nu^2 &= \varepsilon - V(+\infty) = \varepsilon - V(-\infty) + V(-\infty) - V(+\infty) \\ &= \tau - \Delta V < 0 \end{aligned}$$

because $\Delta V > 0$ as well. Therefore, if we set $a = 0$ and $d = 0$, we will have a solution that behaves like

$$\psi \sim \begin{cases} be^{-i\mu x} & x \to -\infty \\ ce^{i\nu x} & x \to +\infty \end{cases}$$

so that ψ decays exponentially as $|x| \to +\infty$, meaning that $\psi \in L^2(\mathbb{R})$. Now because $\psi'' = 2\big(V(x) - \varepsilon\big)\psi$ and as we saw in the proof of Theorem 6.1, $V - \varepsilon \in L^\infty(\mathbb{R}) \implies 2\big(V(x) - \varepsilon\big)\psi \in L^2(\mathbb{R})$, we have $\psi'' \in L^2(\mathbb{R})$. Because the H^2 norm can be taken to be

$$\|\psi\|^2_{H^2(\mathbb{R})} = \|\psi\|^2_{L^2(\mathbb{R})} + \|\psi''\|^2_{L^2(\mathbb{R})}$$

we can conclude $\psi \in H^2(\mathbb{R})$ for each $\varepsilon < V(-\infty)$, meaning each such ε is an eigenvalue.

By the proof of Corollary 6.2, if $\varepsilon \geq V(-\infty)$, then we cannot find a square integrable solution to $\big(\mathcal{H} - \varepsilon\big)\psi = 0$ because we can only choose two values of a, b, c, and d to set to zero. Because $\nu^2 < 0$, to have any chance of integrability, d must be zero. But then we will be left with at least non-decaying (but bounded) term on the left, so we cannot find a square integrable solution for $\varepsilon \geq V(-\infty)$. ■

Corollary 6.4. *The spectrum of $\mathcal{H}$ is all of $\mathbb{R}$.*

The *discrete* spectrum consists of all isolated eigenvalues whose eigenspaces are finite-dimensional; it is the complement of the essential spectrum. As $\mathcal{H}$ has no isolated eigenvalues, its discrete spectrum is empty; the essential spectrum, continuous spectrum, and spectrum are all the same sets for $\mathcal{H}$.

6.2.4 Spectral Representation for G

Unlike in finite-dimensional spaces, it is not true that every self-adjoint operator $\mathcal{A}$ on a Hilbert space possesses a complete set of eigenvectors. When it does, eigenvectors corresponding to distinct eigenvalues are orthogonal and we have the completeness relation[†]

$$\sum_n |\psi_n\rangle\langle\psi_n| = \hat{1}$$

when $\|\psi_n\|_{\mathscr{H}} = 1$ for each n and $\hat{1}$ denotes the identity operator. Considering $\mathcal{A}$ on a rigged Hilbert space and including extended eigenvectors, we have an equivalent completeness relation

$$\sum_m |\psi_m\rangle\langle\psi_m| + \int_{\sigma_{\text{ess}}(\mathcal{A})} |\psi_\lambda\rangle\langle\psi_\lambda| \, d\lambda = \hat{1} \tag{6.14}$$

where $|\psi_m\rangle$ are in the discrete spectrum and ψ_λ is normalized to 1 in the rigged space. The identity is to be taken in the rigged space; elements from the original space belong to the rigged space, but not vice versa.

If $\psi : \mathbb{R} \to \mathbb{C}$ is continuous, then

$$\int_{\mathbb{R}} \psi(y)\delta(x-y)\, dy = \psi(x)$$

By considering the duality pairing on distributions (which coincides with our rigged Hilbert space), we encode the above relation in the symbol[‡] $\langle x|$, which acts on a state $|\psi\rangle$ as

$$\langle x|\psi\rangle = \psi(x)$$

We can then write $\delta(x-y) = \langle x|y\rangle$. As in Economou [22, p.4], we may write

$$\begin{aligned} \langle x|G(\varepsilon)|y\rangle &= G(x,y;\varepsilon) \\ \langle x|\mathfrak{H}|y\rangle &= \delta(x-y)\mathcal{H} \end{aligned} \tag{6.15}$$

where $G(\varepsilon)$ and $\mathfrak{H}$ are the operators such that

$$(\mathfrak{H} - \varepsilon)\mathcal{G}(\varepsilon) = -\hat{1} \tag{6.16}$$

[†]This subsection employs Dirac notation. See Section 1.4 for an explanation.
[‡]In quantum mechanics, $\langle x|$ is the eigenvector of the position operator. Such abstract machinery is not needed here.

We now show that (6.16) is equivalent to (6.6) by computing the matrix elements

$$\langle x \,|\, \mathfrak{H}\mathcal{G} \,|\, y \rangle - \varepsilon \langle x \,|\, \mathcal{G}(\varepsilon) \,|\, y \rangle = \langle x \,|\, \hat{1} \,|\, y \rangle = -\delta(x-y)$$

Inserting the completeness relation

$$\int_{\mathbb{R}} |\, z \rangle \langle z \,|\, dz = \hat{1}$$

inbetween the $\mathfrak{H}$ and $\mathcal{G}$ gives us

$$\begin{gathered}
\int_{\mathbb{R}} \langle x \,|\, \mathfrak{H} \,|\, z \rangle \langle z \,|\, \mathcal{G}(\varepsilon) \,|\, y \rangle \, dz - \varepsilon \langle x \,|\, \mathcal{G}(\varepsilon) \,|\, y \rangle = -\delta(x-y) \\
\int_{\mathbb{R}} \delta(x-z) \mathcal{H} \langle z \,|\, \mathcal{G}(\varepsilon) \,|\, y \rangle \, dz - \varepsilon \langle x \,|\, \mathcal{G}(\varepsilon) \,|\, y \rangle = -\delta(x-y) \\
\mathcal{H} \langle x \,|\, \mathcal{G}(\varepsilon) \,|\, y \rangle \, dz - \varepsilon \langle x \,|\, \mathcal{G}(\varepsilon) \,|\, y \rangle = -\delta(x-y)
\end{gathered}$$

which is the same as (6.6) after restoring to coordinate representation via (6.15). The operator $\mathcal{H}$ is the coordinate representation of $\mathfrak{H}$. Since we will work with (6.16) from here forward, we will instead write[†]

$$\mathcal{G}(\varepsilon) = (\varepsilon - \mathfrak{H})^{-1} = \frac{1}{\varepsilon - \mathfrak{H}}$$

For $\varepsilon \notin \sigma(\mathcal{H}) = \mathbb{R}$, $\mathcal{G}(\varepsilon)$ is bounded, and therefore, continuous. In the completeness relation (6.14) for $\mathcal{H}$, the sum term is vacuous; inserting it into the above, we have

$$\mathcal{G}(\varepsilon) = \frac{1}{\varepsilon - \mathfrak{H}} \int_{\mathbb{R}} |\, \psi_\lambda \rangle \langle \psi_\lambda \,|\, d\lambda = \int_{\mathbb{R}} \frac{1}{\varepsilon - \mathfrak{H}} |\, \psi_\lambda \rangle \langle \psi_\lambda \,|\, d\lambda$$

For an analytic function f, Borel functional calculus [105, chap.3] defines $f(\mathcal{A}) |\, \psi \rangle = f(\lambda) |\, \psi \rangle$ whenever (λ, ψ) are an extended eigenpair. Thus,

$$\mathcal{G}(\varepsilon) = \int_{\mathbb{R}} \frac{1}{\varepsilon - \lambda} \cdot |\, \psi_\lambda \rangle \langle \psi_\lambda \,|\, d\lambda$$

which we may write in coordinate representation as

$$G(x, y; \varepsilon) = \int_{\mathbb{R}} \frac{\psi_\lambda(x) \psi_\lambda^*(y)}{\varepsilon - \lambda} \, d\lambda$$

We are interested in evaluating the above integral for $\varepsilon \in \mathbb{R}$, for which there is a nonintegrable singularity.

[†]The very right-hand side, being an arithmetic expression involving operators, cannot be taken literally, may be considered an abuse of notation but is standard. This relation indicates that $\mathcal{G}(\varepsilon)$ is the resolvent of $\varepsilon - \mathfrak{H}$.

Therefore, the integral must be interpreted as a principal value. The Cauchy Principle Value

$$\text{p.v.} \int_{\mathbb{R}} \frac{\psi_\lambda(x)\psi_\lambda^*(y)}{\varepsilon - \lambda}\, d\lambda = \lim_{\eta \to 0^+} \int_{\mathbb{R}\setminus[\varepsilon-\eta,\varepsilon+\eta]} \frac{\psi_\lambda(x)\psi_\lambda^*(y)}{\varepsilon - \lambda}\, d\lambda$$

is one choice, but it is preferrable to use a branch cut by defining

$$\text{p.v.} \int_{\mathbb{R}} \frac{\psi_\lambda(x)\psi_\lambda^*(y)}{\varepsilon - \lambda}\, d\lambda = \lim_{\eta \to 0^+} \int_{\mathbb{R}} \frac{\psi_\lambda(x)\psi_\lambda^*(y)}{\varepsilon - \lambda + i\eta}\, d\lambda$$

In this expression, $\eta \to 0^+$ is implicit and therefore we can drop the limit and write

$$G(x, y; \varepsilon) = \int_{\mathbb{R}} \frac{\psi_\lambda(x)\psi_\lambda^*(y)}{\varepsilon - \lambda + i\eta}\, d\lambda \tag{6.17}$$

One can view the above as $G(\cdot, \cdot; \varepsilon + i\eta)$ with η taken as a positive infinitesimal in the original formula; this resolves the issue with the singularity but requires us to evaluate at an "incorrect value." Often, physicists will often use the formula with finite η to incorporate the effects of phonon damping, which is the interaction of electrons with the positively charged nucleus and full electron shell [72, p.157].

6.3 Conclusion

This chapter has two purposes: to introduce the Green's function and to rigorize its spectral representation (6.17). The Green's function will be an important computational tool in the next chapter on linear response. The spectral result (6.17) appears often in physics literature, but any justification is woefully omitted. Establishment of this result required an examination into the spectrum of the underlying operator $\mathcal{H}$ and involved many topics from advanced branches of mathematics. Perhaps such machinery is out of place in physics texts but it is certainly most welcome in a thesis of mathematics.

Chapter 7

The Excited State: Linear Response

7.1 Time-Dependent Density Functional Theory

The subject of time-dependent density functional theory (TD-DFT) is a deep one despite its young age. Ground state DFT can trace its genealogy to Thomas-Fermi theory of the 1920s and was formalized with the Hohenberg-Kohn theorems in 1964. TD-DFT has no such illustrious pedigree and was not conceptualized until 1984, sharing a birth year with the author of this thesis. Here, we explore just one technique from this rapidly growing field; Marques *et al.* have compiled an excellent set of lecture notes [77] with contributions from the pioneers of TD-DFT that surveys the wide variety of topics encompassed by TD-DFT.

First introduced way back in Section 3.3, let $G_{\mathcal{L}}$ be the Green's function to the Laplace operator $\mathcal{L} = -\frac{1}{4\pi}\nabla^2$ so that results generalize to $\mathbb{R}^d$ for $d = 1, 2, 3$. To remind the reader,

$$\begin{aligned} d = 1: &\qquad G_{\mathcal{L}}(x - y) = -2\pi\,|x - y| \\ d = 2: &\qquad G_{\mathcal{L}}(\mathbf{x} - \mathbf{y}) = -2\log|\mathbf{x} - \mathbf{y}| \\ d = 3: &\qquad G_{\mathcal{L}}(\mathbf{x} - \mathbf{y}) = |\mathbf{x} - \mathbf{y}|^{-1} \end{aligned}$$

7.1.1 The Runge-Gross Theorem

As discussed in Section 3.2, ground state DFT is powered by the two Honenberg-Kohn theorems, without which the field would not exist. In the same vein, TD-DFT owes its existence to three theorems from the work of Erich Runge and Eberhard K. U. Gross, who published the seminal paper "Density Functional Theory for Time-Dependent Systems" [94] exactly twenty years after the Hohenberg-Kohn Theorems.

Theorem 7.1 (**Runge-Gross I**). *For a given initial state* $\left|\Psi_0\right\rangle$*, for* $t \in [t_0, t_1]$ *there is a one-to-one*

correspondence between the set of external potentials analytic in time,

$$\mathcal{V} = \left\{ V(\mathbf{x},t) \,\middle|\, V(\mathbf{x},t) = \sum_{k=0}^{\infty} \frac{(t-t_0)^k}{k!} \left.\frac{\partial^k V}{\partial t^k}\right|_{t=t_0} \right\} \Big/ \left\{ c(t) \,\middle|\, c : [t_0, t_1] \to \mathbb{R} \right\}$$

and the set of densities

$$\mathcal{N} = \left\{ n(\mathbf{x},t) \,\middle|\, n(\mathbf{x},t) = \left\langle \Psi(t) \middle| \mathfrak{n}(\mathbf{x}) \middle| \Psi(t) \right\rangle \text{ and } i\frac{\partial \Psi(\mathbf{x},t)}{\partial t} = \mathcal{H}\Psi(\mathbf{x},t), \Psi(\mathbf{x},t_0) = \left| \Psi_0 \right\rangle \text{ where } \right.$$
$$\left. \mathcal{H} = -\frac{1}{2}\nabla^2 + \int_{\mathbb{R}^d} \mathfrak{n}(\mathbf{x}) V(\mathbf{x},t)\, d\mathbf{x} + \mathcal{W} \text{ for some } V \in \mathcal{V} \right\}$$

The operator $\mathcal{W}$ quantifies the interaction of electrons among themselves. $\mathfrak{n}(\mathbf{x})$ is the density operator. (It will be explored in the coming section.)

Remark 7.1. The quotient space in the definition of $\mathcal{V}$ means that potentials differing by a time-varying function cannot be distinguished by this theorem. This is the analog of the first Hohenberg-Kohn Theorem, which can only identify potentials up to an additive constant. The "constant" is always with respect to spatial variance, which in the case of TD-DFT, means time-varying functions. ■

Remark 7.2. It is insufficient to specify the initial density $n_0(\mathbf{x}) = n(\mathbf{x}, t_0) = \left\langle \Psi_0 \middle| \mathfrak{n}(\mathbf{x}) \middle| \Psi_0 \right\rangle$. The initial *state* $\left| \Psi_0 \right\rangle$ is what is necessary, unless the system is in its ground state until time t_0. At t_0, the Honenberg-Kohn Theorem would apply, allowing creation of a unique state that corresponds to the given initial density. This idea is, in essence, the backbone of the linear response theory of the next subsection. ■

One might suppose that the theorem is proved in a manner similar to the Hohenberg-Kohn Theorems by attempting to minimize the action integral

$$\mathcal{A}(t_0, t_1) \triangleq \int_{t_0}^{t_1} \left\langle \Psi(t) \middle| i\hbar\partial_t - \mathcal{H} \middle| \Psi(t) \right\rangle dt \tag{7.1}$$

Unfortunately, the Rayleigh-Ritz variational principle used to *prove* the Hohenberg-Kohn Theorems fails because (7.1) has no minimum, so the proof of the Runge-Gross Theorem is significantly more involved. We omit the proof here and refer the interested reader to either the original paper or Englel and Dreizler [24, p.311], whose proof is slightly more comprehensive and detailed than that of Runge and Gross.

While variational principles cannot be used to prove the one-to-one correspondence, a consequence of this bjiection is that states can be constructed from the density up to some phase function:

$$\left| \Psi(t) \right\rangle = e^{-i\alpha(t)} \left| \mathbf{\Psi}[n, \Psi_0](t) \right\rangle$$

Consequently, we do have a variational principle:

Theorem 7.2 (**Runge-Gross III**). *If the potential V is chosen such that $V - W \neq c(t)$ for any $W \in \mathcal{V}$, the action integral is a functional of the density:*

$$\mathcal{A}[n] = \mathcal{B}[n] - \int_{t_0}^{t_1} \int_{\mathbb{R}^d} n(\mathbf{x}, t) V(\mathbf{x}, t)\, d\mathbf{x}\, dt$$

The functional $\mathcal{B}$ is a universal functional of the density in the sense that the same dependence on n holds for all such choices of V. The exact density of the system is given by the stationary point of the system, or the solution to the Euler-Lagrange equation

$$\frac{\delta \mathcal{A}}{\delta n}(\mathbf{x}, t) = 0$$

The reader has surely noticed that we proceeded from Runge-Gross I to Runge-Gross III. Despite omission of an intermediate theorem appearing in the original work, the labeling of Runge and Gross has been retained.

7.1.2 Linear Response Theory

Applying Runge-Gross III, we can write the density $n(\mathbf{x}, t)$ as a functional of the external potential V_{ext}:

$$n(\mathbf{x}, t) = n[V_{\text{ext}}](\mathbf{x}, t) \tag{7.2}$$

Linear response theory (LRT) considers potentials of the form

$$\begin{aligned} V_{\text{ext}}(\mathbf{x}, t) &= \begin{cases} V_0(\mathbf{x}) & t \leq t_0 \\ V_0(\mathbf{x}) + V_1(\mathbf{x}, t) & t > t_0 \end{cases} \\ &= V_0(\mathbf{x}) + V_1(\mathbf{x}, t)\Theta(t - t_0) \end{aligned}$$

The system is in the ground state up to time t_0, at which time a time-varying potential turns on. This describes precisely a host of physical situations, among them incident laser fields in particular. More importantly, though, is that this switching allows the ground state density to uniquely determine the initial state of the time-varying one, as noted in Remark 7.2.

It is more notationally convenient and better suited to our end to perform the derivation of LRT in frequency domain; for a time-domain derivation, see, for example, Gross, Dobson, and Petersilka [45, p.101]. After a Fourier transform in time, LRT begins by writing a functional Taylor series for (7.2):

$$n(\mathbf{x},\omega) = n_0(\mathbf{x}) + n_1(\mathbf{x},\omega) + n_2(\mathbf{x},\omega) + \cdots \tag{7.3}$$

n_0 is the ground state density under the potential V_0; it may be found using the KS-DFT of Chapter 5. As before, V_0 is the positive background charge due to the nuclei sans valence electrons.

Following Taylor's Theorem for functionals, the first frequency-dependent term of (7.3) is given by

$$n_1(\mathbf{x},\omega) = \int_{\mathbb{R}^d} \chi(\mathbf{x},\mathbf{y},\omega) V_1(\mathbf{y},\omega)\, d\mathbf{y} \tag{7.4}$$

$$\chi(\mathbf{x},\mathbf{y},\omega) \triangleq \left.\frac{\delta n[V_{\text{ext}}](\mathbf{x},\omega)}{\delta V_{\text{ext}}(\mathbf{y},\omega)}\right|_{V=V_0} \tag{7.5}$$

If we had a closed-form expression for $n[V_{\text{ext}}]$, then we would be able to perform the above integration and obtain the linear density immediately. Unfortunately, all the functionals encountered so far have been in terms of n. In principle, these functionals can be inverted, but this is, practically speaking, impossible to execute. Instead, we take a different course of action and consider the Kohn-Sham potential

$$V(\mathbf{x}) = V_{\text{ext}}(\mathbf{x}) + \int_{\mathbb{R}^d} G_{\mathcal{L}}(\mathbf{x}-\mathbf{y}) n(\mathbf{y})\, d\mathbf{y} + V_{\text{xc}}(n(\mathbf{x})) \tag{7.6}$$

Our goal is to use (7.6) and make repeated use of the variational chain rule to transform χ into something we can actually compute explicitly. We begin with

$$\begin{aligned}\frac{\delta n[V_{\text{ext}}](\mathbf{x},\omega)}{\delta V_{\text{ext}}(\mathbf{y},\omega)} &= \int_{\mathbb{R}^n} \frac{\delta n[V](\mathbf{x},\omega)}{\delta V(\mathbf{x}',\omega)} \frac{\delta V(\mathbf{x}',\omega)}{\delta V_{\text{ext}}(\mathbf{y},\omega)}\, d\mathbf{x}' \\ &= \int \chi_1(\mathbf{x},\mathbf{x}',\omega) \frac{\delta V(\mathbf{x}',\omega)}{\delta V_{\text{ext}}(\mathbf{y},\omega)}\, d\mathbf{x}'\end{aligned} \tag{7.7}$$

where we have defined

$$\chi_1(\mathbf{x},\mathbf{y},\omega) \triangleq \left.\frac{\delta n[V](\mathbf{x},\omega)}{\delta V(\mathbf{y},\omega)}\right|_{V=V_0} \tag{7.8}$$

While we do not have a closed form expression for the functional $n[V]$, χ_1 can be obtained by appealing to the underlying state and using standard perturbation theory. This is the subject of the next section.

The remaining variational derivative in the integrand of (7.7) will come from the chain rule. For a fixed $\mathbf{x}$, we may treat V of (7.6) as a functional of n. Consequently, by the variational chain rule for functionals,

$$\begin{aligned}\frac{\delta V(\mathbf{x}',\omega)}{\delta V_{\text{ext}}(\mathbf{y},\omega)} &= \int_{\mathbb{R}^d} \frac{\delta V(\mathbf{x}',\omega)}{\delta n(\mathbf{x}'',\omega)} \frac{\delta n[V_{\text{ext}}](\mathbf{x}'',\omega)}{\delta V_{\text{ext}}(\mathbf{y},\omega)}\, d\mathbf{x}'' \\ &= \delta(\mathbf{x}'-\mathbf{y}) + \int_{\mathbb{R}^d} \left(G_{\mathcal{L}}(\mathbf{x}'-\mathbf{x}'') + \frac{\delta V_{\text{xc}}[n](\mathbf{x}')}{\delta n(\mathbf{x}'')} \right) \frac{\delta n(\mathbf{x}'',\omega)}{\delta V_{\text{ext}}(\mathbf{y},\omega)}\, d\mathbf{x}''\end{aligned} \tag{7.9}$$

The δ comes from the special case of the variational chain rule for functionals described in Appendix A applied to the first term from (7.6):

$$\delta(\mathbf{x}' - \mathbf{y}) = \int_{\mathbb{R}^d} \frac{\delta V_{\text{ext}}(\mathbf{x}', \omega)}{\delta n(\mathbf{x}'', \omega)} \frac{\delta n(\mathbf{x}'', \omega)}{\delta V_{\text{ext}}(\mathbf{y}, \omega)} \, d\mathbf{x}''$$

We recall (7.5) and define

$$\mathcal{K}(\mathbf{x}, \mathbf{y}, \omega) \triangleq G_{\mathcal{L}}(\mathbf{x} - \mathbf{y}) + f_{\text{xc}}(\mathbf{x}, \mathbf{y}, \omega) \tag{7.10}$$

$$f_{\text{xc}}(\mathbf{x}, \mathbf{y}, \omega) \triangleq \left. \frac{\delta V_{\text{xc}}[n](\mathbf{x}, \omega)}{\delta n(\mathbf{y}, \omega)} \right|_{n=n_0} \tag{7.11}$$

It is tempting to jump to the conclusion that f_{xc} is as in (3.31). For the moment, the reader should put that connection aside and pretend that (7.11) is different. With these, (7.9) simplifies to

$$\frac{\delta V(\mathbf{x}', \omega)}{\delta V_{\text{ext}}(\mathbf{y}, \omega)} = \delta(\mathbf{x}' - \mathbf{y}) + \int_{\mathbb{R}^d} \mathcal{K}(\mathbf{x}', \mathbf{x}'', \omega) \chi(\mathbf{x}'', \mathbf{y}, \omega) \, d\mathbf{x}'' \tag{7.12}$$

Next, we substitute (7.12) into (7.7) and equate the result with (7.5)

$$\chi(\mathbf{x}, \mathbf{y}, \omega) = \chi_1(\mathbf{x}, \mathbf{y}, \omega) + \int_{\mathbb{R}^d} \chi_1(\mathbf{x}, \mathbf{x}', \omega) \int_{\mathbb{R}^d} \mathcal{K}(\mathbf{x}', \mathbf{x}'', \omega) \, \chi(\mathbf{x}'', \mathbf{y}, \omega) \, d\mathbf{x}'' \, d\mathbf{x}' \tag{7.13}$$

Finally, we multiply both sides of (7.13) by $V_1(\mathbf{y}, \omega)$ and integrate over $\mathbf{y}$:

$$\begin{aligned} \int_{\mathbb{R}^d} \chi(\mathbf{x}, \mathbf{y}, \omega) V_1(\mathbf{y}, \omega) \, d\mathbf{y} &= \int_{\mathbb{R}^d} \chi_1(\mathbf{x}, \mathbf{y}, \omega) V_1(\mathbf{y}, \omega) \, d\mathbf{y} \\ &\quad + \underbrace{\int_{\mathbb{R}^d} V_1(\mathbf{y}, \omega) \int_{\mathbb{R}^d} \chi_1(\mathbf{x}, \mathbf{x}', \omega) \int_{\mathbb{R}^d} \mathcal{K}(\mathbf{x}', \mathbf{x}'', \omega) \chi(\mathbf{x}'', \mathbf{y}, \omega) \, d\mathbf{x}'' \, d\mathbf{x}' \, d\mathbf{y}}_{\triangleq \mathcal{I}} \end{aligned}$$

We freely interchange the order of integration within $\mathcal{I}$, performing the $\mathbf{y}$ integral first:

$$\begin{aligned} \mathcal{I} &= \int_{\mathbb{R}^d} \chi_1(\mathbf{x}, \mathbf{x}', \omega) \int_{\mathbb{R}^d} \mathcal{K}(\mathbf{x}', \mathbf{x}'', \omega) \left[\int_{\mathbb{R}^d} V_1(\mathbf{y}, \omega) \chi(\mathbf{x}'', \mathbf{y}, \omega) d\mathbf{y} \right] d\mathbf{x}'' \, d\mathbf{x}' \\ &= \int_{\mathbb{R}^d} \chi_1(\mathbf{x}, \mathbf{x}', \omega) \int_{\mathbb{R}^d} \mathcal{K}(\mathbf{x}', \mathbf{x}'', \omega) n_1(\mathbf{x}'', \omega) \, d\mathbf{x}'' \, d\mathbf{x}' \end{aligned}$$

after using (7.4). This finally gives the expression (after some switching of dummy variables)

$$\begin{aligned} n_1(\mathbf{x}, \omega) &= \int_{\mathbb{R}^d} \chi_1(\mathbf{x}, \mathbf{y}, \omega) \left[V_1(\mathbf{y}, \omega) + \int_{\mathbb{R}^d} \mathcal{K}(\mathbf{y}, \mathbf{y}', \omega) \, n_1(\mathbf{y}', \omega) \, d\mathbf{y}' \right] d\mathbf{y} \\ &= \int_{\mathbb{R}^d} \chi_1(\mathbf{x}, \mathbf{y}, \omega) \, V_{1,\text{scf}}(\mathbf{y}, \omega) \, d\mathbf{y} \end{aligned} \tag{7.14}$$

where $V_{1,\mathrm{scf}}(\mathbf{y},\omega)$ denotes the self-consistent potential

$$V_{1,\mathrm{scf}}(\mathbf{y},\omega) \triangleq V_1(\mathbf{y},\omega) + \int_{\mathbb{R}^d} \mathcal{K}(\mathbf{y},\mathbf{y}',\omega) n_1(\mathbf{y}',\omega)\, d\mathbf{y}' \tag{7.15}$$

7.1.3 Adiabatic Local Density Approximation (ALDA)

The exchange-correlation functional appearing in f_{xc} should, in principle, depend on the frequency. In the derivation of the preceding section, it appears we pulled a Fourier transform inside a nonlinear functional

$$\mathcal{F}\big\{n[V_{\mathrm{ext}}](\mathbf{x},\cdot)\big\}(\omega) = n\big[\mathcal{F}\big\{V_{\mathrm{ext}}(\mathbf{x},\cdot)\big\}(\omega)\big] = n[V_0(\mathbf{x}) + V_1(\mathbf{x},\omega)]$$

when we implicitly assumed that $n_0(\mathbf{x})$ corresponds to $V_0(\mathbf{x})$ and $n_1(\mathbf{x},\omega)$ corresponds to $V_1(\mathbf{x},\omega)$. The hang-up is the exchange-correlation portion, as it is the only nonlinear piece of the functional. To be proper, we should have written the functional Taylor series in time-domain and then transformed at the end.

Runge-Gross III speaks of a universal functional $\mathcal{B}[n]$; much like the second Hohenberg-Kohn theorem, it says nothing of what it looks like. Recalling KS-DFT, one might imagine that $\mathcal{B}$ looks something like

$$\mathcal{B}[n] = T_s[n] + \frac{1}{2}\int_{t_0}^{t_1}\int_{\mathbb{R}^d}\int_{\mathbb{R}^d} \mathcal{W}(\mathbf{x}-\mathbf{y}) n(\mathbf{x},t) n(\mathbf{y},t)\, d\mathbf{x}\, d\mathbf{y}\, dt + A_{\mathrm{xc}}[n]$$

where $A_{\mathrm{xc}}[n]$ is a time-dependent version of the exchange-correlation functional. The extension of $T_s[n]$ to time-varying systems is easy to visualize, but then the question becomes: how can one incorporate explicit time-dependence into exchange and correlation? Formulating reasonable approximations in the ground state is a daunting enough task. An easy solution is to take existing exchange-correlation functionals and merely replace the ground-state density with the time-varying one:

$$A_{\mathrm{xc}}^{\mathrm{ALDA}}[n] = \int_{t_0}^{t_1}\int_{\mathbb{R}^d} n(\mathbf{x},t)\epsilon_{\mathrm{xc}}\big(n(\mathbf{x},t)\big)\, d\mathbf{x}\, dt$$

Then the first variation is given by

$$\begin{aligned}\frac{\delta A_{\mathrm{xc}}^{\mathrm{ALDA}}[n](\mathbf{x},t)}{\delta n(\mathbf{y},\tau)} &= \delta(t-\tau)\delta(\mathbf{x}-\mathbf{y})\left.\frac{\partial[n\epsilon_{\mathrm{xc}}(n)]}{\partial n}\right|_{n=n(\mathbf{x},t)} \\ &= \delta(t-\tau)\left.\frac{\delta E_{\mathrm{xc}}[n](\mathbf{x})}{\delta n(\mathbf{y})}\right|_{n=n(\mathbf{x},t)}\end{aligned} \tag{7.16}$$

This replacement of time-varying functionals with static ones is known as the *adiabatic local density approximation* (ALDA). Although it is quite robust and sufficient in most applications of TD-DFT, it fails for some

computations, such as those involving charge transfer [73] and double excitations [74, 108].

Inspired by (7.16), if we now write the functional Taylor series for $E_{\text{xc}}[n]$ to first order,

$$E_{\text{xc}}[n_0 + n_1] = E_{\text{xc}}[n_0] + \int_{\mathbb{R}^d} \left.\frac{\delta E_{\text{xc}}[n](\mathbf{x})}{\delta n(\mathbf{y})}\right|_{n=n_0} n_1(\mathbf{y}, t)\, d\mathbf{y}$$

after taking the first variation and using that

$$\frac{\delta E_{\text{xc}}[n](\mathbf{x})}{\delta n(\mathbf{y})} = V_{\text{xc}}\big(n_0(\mathbf{x})\big)\delta(\mathbf{x}-\mathbf{y}) \tag{7.17}$$

we have

$$\frac{\delta A_{\text{xc}}^{\text{ALDA}}[n](\mathbf{x},t)}{\delta n(\mathbf{y},\tau)} = \delta(t-\tau)\delta(\mathbf{x}-\mathbf{y})\left[V_{\text{xc}}\big(n_0(\mathbf{x})\big) + n_1(\mathbf{y},t)\left.\frac{\delta V_{\text{xc}}[n](\mathbf{x})}{\delta n(\mathbf{y})}\right|_{n=n_0}\right]$$

or after Fourier transforming in $\tau \mapsto \omega'$ and then $t \mapsto \omega$ and recognizing (7.11)

$$\frac{\delta A_{\text{xc}}^{\text{ALDA}}[n](\mathbf{x},\omega)}{\delta n(\mathbf{y},\omega')} = \delta(\mathbf{x}-\mathbf{y})\delta(\omega-\omega')\Big[V_{\text{xc}}\big(n_0(\mathbf{x})\big) + n_1(\mathbf{y},\omega) f_{\text{xc}}(\mathbf{x},\mathbf{y})\Big]$$

which is precisely the result of the previous section. The ω argument has been removed from f_{xc} because it is a static kernel. The δ's will disappear when $\mathbf{x} = \mathbf{y}$ and $\omega = \omega'$ are taken in the Euler-Lagrange equation.

This discussion has provided insight to simplify (7.15). In light of (7.17), we can compute f_{xc} from (7.11)

$$\begin{aligned} f_{\text{xc}}(\mathbf{x},\mathbf{y}) &= \left.\frac{\partial V_{\text{xc}}}{\partial n}\right|_{n=n_0(\mathbf{x})} \delta(\mathbf{x}-\mathbf{y}) \\ &= V_{\text{xc}}'\big(n_0(\mathbf{x})\big)\delta(\mathbf{x}-\mathbf{y}) \end{aligned} \tag{7.18}$$

which upon substitution into (7.15) yields

$$V_{1,\text{scf}}(\mathbf{y},\omega) = V_1(\mathbf{y},\omega) + V_{\text{xc}}'\big(n_0(\mathbf{y})\big)n_1(\mathbf{y},\omega) + \int_{\mathbb{R}^d} G_{\mathcal{L}}(\mathbf{y}-\mathbf{y}')n_1(\mathbf{y}',\omega)\, d\mathbf{y}'$$

Rather than integrate against the Green's function for the Laplace operator, we can solve the corresponding differential equation. Let ϕ_{est} be the solution to

$$\nabla^2\phi_{\text{est}}(\mathbf{x},\omega) = -4\pi n_1(\mathbf{x},\omega) \tag{7.19}$$

We denote it "est" because it represents the electrostatic potential corresponding to the linear response density. To symmetrize our notation in subscripted varieties of ϕ, define

$$\phi_{\text{ext}}(\mathbf{x},\omega) \triangleq V_1(\mathbf{x},\omega) \tag{7.20}$$

$$\phi_{\text{xc}}(\mathbf{x},\omega) \triangleq V'_{\text{xc}}\big(n_0(\mathbf{x})\big)n_1(\mathbf{x},\omega) \tag{7.21}$$

In terms of these newly defined potentials, we can write the equation (7.14) for $n_1(\mathbf{x},\omega)$ instead as

$$n_1(\mathbf{x},\omega) = \int_{\mathbb{R}^d} \chi_1(\mathbf{x},\mathbf{y},\omega)\big[\phi_{\text{ext}}(\mathbf{y},\omega) + \phi_{\text{est}}(\mathbf{y},\omega) + \phi_{\text{xc}}(\mathbf{y},\omega)\big]\,d\mathbf{y} \tag{7.22}$$

Finally, perhaps much to the relief of the anxious reader, we note that the f_{xc} of this section is, in fact, the same one we computed way back in (3.31) and have used many times since. And therefore we have

$$\phi_{\text{xc}}(\mathbf{x},\omega) = f_{\text{xc}}(\mathbf{x})n_1(\mathbf{x},\omega) \tag{7.23}$$

7.2 Linear Response Function

In this section, we derive a spectral ("Lehmann") representation for the linear response function χ_1 in terms of ground state orbitals. We will begin in the time-domain and derive a frequency-domain representation in Section 7.2.1. From there, we will find an expression using Kohn-Sham orbitals in Section 7.2.2. Finally, we will arrive at the response function specific to the jellium model in the final subsection.

7.2.1 Frequency Domain Representation

While the primary sources include Wehrum and Hermeking [114], Fetter and Walecka [35], and Senatore and Subbaswamy [97], the derivation here follows the outline of Gross and Maitra [46], filling in all the details left out of their presentation. We begin with the time-domain representation of the first-order response function:

$$\mathcal{X}_1(\mathbf{x},\mathbf{y},t-\tau) = -i\Theta(t-\tau)\big\langle\Psi_0\big|\big[\mathfrak{n}(\mathbf{x},t),\mathfrak{n}(\mathbf{y},\tau)\big]\big|\Psi_0\big\rangle \tag{7.24}$$

where brackets denote the standard commutator of two (self-adjoint) operators

$$\big[\mathcal{A},\mathcal{B}\big] = \mathcal{A}\mathcal{B} - \mathcal{B}\mathcal{A},$$

Ψ_0 denotes the $t=0$ state, and $\mathfrak{n}(\mathbf{x},t)$ denotes the density operator in the Heisenberg picture [11, p.88]

$$\mathfrak{n}(\mathbf{x},t) = e^{i\mathcal{H}t}\mathfrak{n}(\mathbf{x})e^{-i\mathcal{H}t} \tag{7.25}$$

$$\mathfrak{n}(\mathbf{x}) = \sum_k \delta(\mathbf{x}-\hat{\mathbf{x}}_k) \tag{7.26}$$

We have overloaded the symbol $\mathfrak{n}$, using it for both time-dependent and independent operators, as the latter is the former with t set to zero. The notation for $\mathfrak{n}(\mathbf{x})$ is perhaps a bit perplexing. As we shall see when we apply it to states, the notation implicitly encodes how it operates.

What we seek is the linear response function, which is the angular frequency Fourier transform[†] of $\mathcal{X}_1$:

$$\chi_1(\mathbf{x}, \mathbf{y}, \omega) = \mathfrak{F}\{\mathcal{X}_1\}(\omega)$$

We begin by analyzing the commutator term of (7.24). Expanding by definition, we have

$$\big[\mathfrak{n}(\mathbf{x}, t), \mathfrak{n}(\mathbf{y}, \tau)\big] = \mathfrak{n}(\mathbf{x}, t)\mathfrak{n}(\mathbf{y}, \tau) - \mathfrak{n}(\mathbf{y}, \tau)\mathfrak{n}(\mathbf{x}, t)$$

Because the two terms are merely permutations of $(\mathbf{x}, t)$ and $(\mathbf{y}, \tau)$, we need only examine one of them and assert the result for the second. By inserting the completeness relation over excited (exc) states

$$\sum_j^{\text{exc}} \big|\, \Psi_j \big\rangle \big\langle \Psi_j \,\big| = \hat{1} \tag{7.27}$$

we have

$$\begin{aligned} \big\langle \Psi_0 \,\big|\, \mathfrak{n}(\mathbf{x}, t)\mathfrak{n}(\mathbf{y}, \tau) \,\big|\, \Psi_0 \big\rangle &= \big\langle \Psi_0 \,\big|\, \mathfrak{n}(\mathbf{x}, t)\, \hat{1}\, \mathfrak{n}(\mathbf{y}, \tau) \,\big|\, \Psi_0 \big\rangle \\ &= \sum_j^{\text{exc}} \big\langle \Psi_0 \,\big|\, \mathfrak{n}(\mathbf{x}, t) \,\big|\, \Psi_j \big\rangle \big\langle \Psi_j \,\big|\, \mathfrak{n}(\mathbf{y}, \tau) \,\big|\, \Psi_0 \big\rangle \end{aligned}$$

In deriving the spectral representation for the Green's function at the beginning of Section 6.2.4, we discussed extended states and rigged Hilbert spaces. The derivation of this section is also done in this context, although no appeal to the structures of the underlying L^2 or distribution space will be necessary.

Using the definition of the time-dependent density operator (7.25), the first matrix element becomes

$$\begin{aligned} \big\langle \Psi_0 \,\big|\, \mathfrak{n}(\mathbf{x}, t) \,\big|\, \Psi_j \big\rangle &= \big\langle \Psi_0 \,\big|\, e^{i\mathcal{H}t}\mathfrak{n}(\mathbf{x})e^{-i\mathcal{H}t} \,\big|\, \Psi_j \big\rangle \\ &= \big\langle e^{-i\mathcal{H}t}\Psi_0 \,\big|\, \mathfrak{n}(\mathbf{x}) \,\big|\, e^{-i\mathcal{H}t}\Psi_j \big\rangle \end{aligned}$$

Because $\mathcal{H}\Psi_j = E_j\Psi_j$, by Borel functional calculus again, we have $e^{-i\mathcal{H}t}\Psi_j = e^{-iE_jt}\Psi_j$, so

$$\begin{aligned} \big\langle \Psi_0 \,\big|\, \mathfrak{n}(\mathbf{x}, t) \,\big|\, \Psi_j \big\rangle &= \big\langle e^{-iE_0t}\Psi_0 \,\big|\, \mathfrak{n}(\mathbf{x}) \,\big|\, e^{-iE_jt}\Psi_j \big\rangle \\ &= e^{i(E_0 - E_j)t} \big\langle \Psi_0 \,\big|\, \mathfrak{n}(\mathbf{x}) \,\big|\, \Psi_j \big\rangle \end{aligned} \tag{7.28}$$

[†]See Section 1.3 for the definition of this transform. It does not conform to usual mathematical conventions.

Therefore, using the transitivity of symbols, we have

$$\left\langle \Psi_0 \middle| \mathfrak{n}(\mathbf{x},t)\mathfrak{n}(\mathbf{y},\tau) \middle| \Psi_0 \right\rangle = \sum_j^{\text{exc}} e^{i(E_0-E_j)(t-\tau)} \left\langle \Psi_0 \middle| \mathfrak{n}(\mathbf{x}) \middle| \Psi_j \right\rangle \left\langle \Psi_j \middle| \mathfrak{n}(\mathbf{y}) \middle| \Psi_0 \right\rangle$$

Applying this result to (7.24), we have

$$\mathcal{X}_1(\mathbf{x},\mathbf{y},t,\tau) = \sum_j^{\text{exc}} -i\Theta(t-\tau)\Big[e^{i(E_0-E_j)(t-\tau)} \left\langle \Psi_0 \middle| \mathfrak{n}(\mathbf{x}) \middle| \Psi_j \right\rangle \left\langle \Psi_j \middle| \mathfrak{n}(\mathbf{y}) \middle| \Psi_0 \right\rangle - e^{i(E_j-E_0)(t-\tau)} \left\langle \Psi_0 \middle| \mathfrak{n}(\mathbf{y}) \middle| \Psi_j \right\rangle \left\langle \Psi_j \middle| \mathfrak{n}(\mathbf{x}) \middle| \Psi_0 \right\rangle \Big]$$

Finally, because we assume the perturbation turns on adiabatically [48, p.14], we insert an $\eta \to 0^+$ infinitesimal term into the exponentials and take the Fourier transform with respect to $t' = t - \tau$:

$$\mathfrak{F}\Big\{ \Theta(t') e^{\eta t'} e^{i(E_0-E_j)t'} \Big\}(\omega) = \frac{1}{i\big(\omega - (E_0 - E_j)\big) - \eta} = \frac{1}{i\big(\omega + (E_j - E_0) + i\eta\big)} \tag{7.29}$$

Taking $\chi_1 = \mathfrak{F}\{\mathcal{X}_1\}$ and applying the above, we obtain the general spectral representation

$$\chi_1(\mathbf{x},\mathbf{y},\omega) = \sum_j^{\text{exc}} \left[\frac{\left\langle \Psi_0 \middle| \mathfrak{n}(\mathbf{x}) \middle| \Psi_j \right\rangle \left\langle \Psi_j \middle| \mathfrak{n}(\mathbf{y}) \middle| \Psi_0 \right\rangle}{\omega - \big(E_j - E_0\big) + i\eta} - \frac{\left\langle \Psi_0 \middle| \mathfrak{n}(\mathbf{y}) \middle| \Psi_j \right\rangle \left\langle \Psi_j \middle| \mathfrak{n}(\mathbf{x}) \middle| \Psi_0 \right\rangle}{\omega + \big(E_j - E_0\big) + i\eta} \right] \tag{7.30}$$

7.2.2 Spectral ("Lehmann") Representation using Kohn-Sham Orbitals

Within the TD-DFT LRT framework, the wavefunctions of (7.30) are expressed in terms of Kohn-Sham orbitals ψ_k. Because the system is noninteracting, Ψ_0 is a Slater determinant[†] [89, p.14]; in Dirac notation,

$$\left| \Psi_0 \right\rangle = \left| \psi_1 \psi_2 \cdots \psi_N \right\rangle$$

or in coordinate notation

$$\Psi_0(\mathbf{x}_1,\mathbf{x}_2,\ldots,\mathbf{x}_N) = \frac{1}{\sqrt{N!}} \det \begin{vmatrix} \psi_1(\mathbf{x}_1) & \psi_1(\mathbf{x}_2) & \cdots & \psi_1(\mathbf{x}_N) \\ \psi_2(\mathbf{x}_1) & \psi_2(\mathbf{x}_2) & \cdots & \psi_2(\mathbf{x}_N) \\ \vdots & \vdots & \ddots & \vdots \\ \psi_N(\mathbf{x}_1) & \psi_N(\mathbf{x}_2) & \cdots & \psi_N(\mathbf{x}_N) \end{vmatrix}$$

$$= \sum_P \text{sgn}(P) \psi_1(\mathbf{x}_{k_1}) \psi_2(\mathbf{x}_{k_2}) \cdots \psi_N(\mathbf{x}_{k_N})$$

[†]In Section 3.3, we associated the ground state wavefunction with a Slater determinant. There, we constructed a noninteracting system with such a wavefunction. Here, we assert the reverse: that Ψ for a noninteracting system has this form.

$P = \{k_1, k_2, \ldots, k_N\}$ is a permutation of $\{1, 2, \ldots, N\}$ and $\mathrm{sgn}(P) = (-1)^{s(P)}$, where $s(P)$ counts the number of switches from numerical order in P. The energy of the ground state is then

$$E_0 = \sum_k \varepsilon_k$$

An excited state Ψ_j is generated by moving an electron from the occupied orbital ψ_m to an unoccupied one ψ_j. The resultant wave function is

$$|\Psi_j\rangle = |\psi_1 \cdots \psi_{m-1} \psi_j \psi_{m+1} \cdots \psi_N\rangle$$

and energy of the excited state is

$$E_j = \varepsilon_j + \sum_{k \neq m} \varepsilon_k$$

which means that the change in energy is given by

$$E_j - E_0 = \varepsilon_j - \varepsilon_m \tag{7.31}$$

7.2.2.1 Bra-kets Involving $\mathfrak{n}(\mathbf{x})$: Two-electron Systems

To resolve the bra-ket terms, such as $\langle \Psi_j | \mathfrak{n}(\mathbf{x}) | \Psi_0 \rangle$, it is illustrative to derive the result for a two-electron system. Larger systems result in an unwieldy number of terms (a Slater determinant contains $N!$ terms), which in turn requires cumbersome and difficult-to-read notation to represent compactly.

When $N = 2$, the wavefunction of the initial state is

$$\Psi_0(\mathbf{x}_1, \mathbf{x}_2) = \frac{1}{\sqrt{2}} \Big(\psi_1(\mathbf{x}_1)\psi_2(\mathbf{x}_2) - \psi_1(\mathbf{x}_2)\psi_2(\mathbf{x}_1) \Big)$$

Generate an excited state by moving an electron from $1 \mapsto j$. Then denoting $\Psi_j \equiv \Psi_{1 \mapsto j}$

$$\Psi_{1 \mapsto j}(\mathbf{x}_1, \mathbf{x}_2) = \frac{1}{\sqrt{2}} \Big(\psi_j(\mathbf{x}_1)\psi_2(\mathbf{x}_2) - \psi_j(\mathbf{x}_2)\psi_2(\mathbf{x}_1) \Big) \tag{7.32}$$

We have $\mathfrak{n}(\mathbf{x}) = \delta(\mathbf{x} - \mathbf{x}_1) + \delta(\mathbf{x} - \mathbf{x}_2)$, so let us concentrate on the first term. We have

$$\begin{aligned} \langle \Psi_{1 \mapsto j} | \delta(\mathbf{x} - \mathbf{x}_1) | \Psi_0 \rangle &= \frac{1}{2} \langle \psi_j(\mathbf{x}_1)\psi_2(\mathbf{x}_2) - \psi_j(\mathbf{x}_2)\psi_2(\mathbf{x}_1) \,|\, \delta(\mathbf{x} - \mathbf{x}_1) \,|\, \psi_1(\mathbf{x}_1)\psi_2(\mathbf{x}_2) - \psi_1(\mathbf{x}_2)\psi_2(\mathbf{x}_1) \rangle \\ &= \frac{1}{2} \Big[\mathcal{A}_1 + \mathcal{B}_1 + \mathcal{C}_1 + \mathcal{D}_1 \Big] \end{aligned}$$

with

$$\mathcal{A}_1 \triangleq \left\langle \psi_j(\mathbf{x}_1)\psi_2(\mathbf{x}_2) \middle| \delta(\mathbf{x}-\mathbf{x}_1) \middle| \psi_1(\mathbf{x}_1)\psi_2(\mathbf{x}_2) \right\rangle \qquad \mathcal{C}_1 \triangleq \left\langle \psi_j(\mathbf{x}_2)\psi_2(\mathbf{x}_1) \middle| \delta(\mathbf{x}-\mathbf{x}_1) \middle| \psi_1(\mathbf{x}_1)\psi_2(\mathbf{x}_2) \right\rangle$$
$$\mathcal{B}_1 \triangleq \left\langle \psi_j(\mathbf{x}_1)\psi_2(\mathbf{x}_2) \middle| \delta(\mathbf{x}-\mathbf{x}_1) \middle| \psi_1(\mathbf{x}_2)\psi_2(\mathbf{x}_1) \right\rangle \qquad \mathcal{D}_1 \triangleq \left\langle \psi_j(\mathbf{x}_2)\psi_2(\mathbf{x}_1) \middle| \delta(\mathbf{x}-\mathbf{x}_1) \middle| \psi_1(\mathbf{x}_2)\psi_2(\mathbf{x}_1) \right\rangle$$

We first compute $\mathcal{A}_1$:

$$\begin{aligned}
\mathcal{A}_1 &= \int_{\mathbb{R}^3}\int_{\mathbb{R}^3} \psi_j^*(\mathbf{x}_1)\psi_2^*(\mathbf{x}_2)\psi_1(\mathbf{x}_1)\psi_2(\mathbf{x}_2)\delta(\mathbf{x}-\mathbf{x}_1)\,d\mathbf{x}_1\,d\mathbf{x}_2 \\
&= \left(\int_{\mathbb{R}^3} \psi_j^*(\mathbf{x}_1)\psi_1(\mathbf{x}_1)\delta(\mathbf{x}-\mathbf{x}_1)\,d\mathbf{x}_1\right)\left(\int_{\mathbb{R}^3} \psi_2^*(\mathbf{x}_2)\psi_2(\mathbf{x}_2)\,d\mathbf{x}_2\right) \\
&= \psi_j^*(\mathbf{x})\psi_1(\mathbf{x})
\end{aligned}$$

since $\left\langle \psi_2 \middle| \psi_2 \right\rangle = 1$. We proceed to $\mathcal{B}_1$:

$$\mathcal{B}_1 = \left(\int_{\mathbb{R}^3} \psi_j^*(\mathbf{x}_1)\psi_2(\mathbf{x}_1)\delta(\mathbf{x}-\mathbf{x}_1)\,d\mathbf{x}_1\right)\left(\int_{\mathbb{R}^3} \psi_2^*(\mathbf{x}_2)\psi_1(\mathbf{x}_2)\,d\mathbf{x}_2\right) = 0$$

because $\left\langle \psi_2 \middle| \psi_1 \right\rangle = 0$. $\mathcal{C}_1$ and $\mathcal{D}_1$ are similar to the previous case:

$$\mathcal{C}_1 = \left(\int_{\mathbb{R}^3} \psi_2^*(\mathbf{x}_1)\psi_1(\mathbf{x}_1)\delta(\mathbf{x}-\mathbf{x}_1)\,d\mathbf{x}_1\right)\left(\int_{\mathbb{R}^3} \psi_j^*(\mathbf{x}_2)\psi_2(\mathbf{x}_2)\,d\mathbf{x}_2\right) = 0$$
$$\mathcal{D}_1 = \left(\int_{\mathbb{R}^3} \psi_2^*(\mathbf{x}_1)\psi_2(\mathbf{x}_1)\delta(\mathbf{x}-\mathbf{x}_1)\,d\mathbf{x}_1\right)\left(\int_{\mathbb{R}^3} \psi_j^*(\mathbf{x}_2)\psi_1(\mathbf{x}_2)\,d\mathbf{x}_2\right) = 0$$

again because both $\left\langle \psi_j \middle| \psi_2 \right\rangle = 0$ and $\left\langle \psi_j \middle| \psi_1 \right\rangle = 0$. Therefore,

$$\left\langle \Psi_{1\mapsto j} \middle| \delta(\mathbf{x}-\mathbf{x}_1) \middle| \Psi_0 \right\rangle = \frac{1}{2}\psi_j^*(\mathbf{x})\psi_1(\mathbf{x}) \tag{7.33}$$

Next, we follow the same procedure to calculate

$$\left\langle \Psi_{1\mapsto j} \middle| \delta(\mathbf{x}-\mathbf{x}_2) \middle| \Psi_0 \right\rangle$$

Define $\mathcal{A}_2$–$\mathcal{D}_2$ as before, except with the $\mathbf{x}_1$ in the δ replaced by $\mathbf{x}_2$. Then

$$\mathcal{A}_2 = \left(\int_{\mathbb{R}^3} \psi_j^*(\mathbf{x}_1)\psi_1(\mathbf{x}_1)\,d\mathbf{x}_1\right)\left(\int_{\mathbb{R}^3} \psi_2^*(\mathbf{x}_2)\psi_2(\mathbf{x}_2)\delta(\mathbf{x}-\mathbf{x}_2)\,d\mathbf{x}_2\right) = 0$$
$$\mathcal{B}_2 = \left(\int_{\mathbb{R}^3} \psi_j^*(\mathbf{x}_1)\psi_2(\mathbf{x}_1)\,d\mathbf{x}_1\right)\left(\int_{\mathbb{R}^3} \psi_2^*(\mathbf{x}_2)\psi_1(\mathbf{x}_2)\delta(\mathbf{x}-\mathbf{x}_2)\,d\mathbf{x}_2\right) = 0$$
$$\mathcal{C}_2 = \left(\int_{\mathbb{R}^3} \psi_2^*(\mathbf{x}_1)\psi_1(\mathbf{x}_1)\,d\mathbf{x}_1\right)\left(\int_{\mathbb{R}^3} \psi_j^*(\mathbf{x}_2)\psi_1(\mathbf{x}_2)\delta(\mathbf{x}-\mathbf{x}_2)\,d\mathbf{x}_2\right) = 0$$

$$\mathcal{D}_2 = \left(\int_{\mathbb{R}^3} \psi_2^*(\mathbf{x}_1)\psi_2(\mathbf{x}_1)\, d\mathbf{x}_1 \right) \left(\int_{\mathbb{R}^3} \psi_j^*(\mathbf{x}_2)\psi_1(\mathbf{x}_2)\delta(\mathbf{x}-\mathbf{x}_2)\, d\mathbf{x}_2 \right) = \psi_j^*(\mathbf{x})\psi_1(\mathbf{x})$$

so that we have

$$\left\langle \Psi_{1\mapsto j} \middle| \delta(\mathbf{x}-\mathbf{x}_2) \middle| \Psi_0 \right\rangle = \frac{1}{2}\psi_j^*(\mathbf{x})\psi_1(\mathbf{x})$$

which, when combined with (7.33), gives

$$\left\langle \Psi_{1\mapsto j} \middle| \mathfrak{n}(\mathbf{x}) \middle| \Psi_0 \right\rangle = \psi_j^*(\mathbf{x})\psi_1(\mathbf{x}) \tag{7.34}$$

To confirm the pattern, we instead consider promoting an electron from ψ_2 to ψ_j. This has the effect of switching $j \leftrightarrows 1$ and $2 \leftrightarrows j$ in (7.32), while Ψ_0 remains as before. In $\mathcal{A}_1$–$\mathcal{D}_2$, we make the replacements $\psi_j^* \mapsto \psi_1^*$ and $\psi_2^* \mapsto \psi_j^*$ because Ψ_j is the bra. This gives us that

$$\begin{aligned}
&\mathcal{A}_1 = 0 && \mathcal{B}_1 = 0 && \mathcal{C}_1 = 0 && \mathcal{D}_1 = \psi_j^*(\mathbf{x})\psi_2(\mathbf{x}) \\
&\mathcal{A}_2 = \psi_j^*(\mathbf{x})\psi_2(\mathbf{x}) && \mathcal{B}_2 = 0 && \mathcal{C}_2 = 0 && \mathcal{D}_2 = 0
\end{aligned}$$

so that

$$\left\langle \Psi_{2\mapsto j} \middle| \mathfrak{n}(\mathbf{x}) \middle| \Psi_0 \right\rangle = \psi_j^*(\mathbf{x})\psi_2(\mathbf{x}) \tag{7.35}$$

7.2.2.2 Bra-kets Involving $\mathfrak{n}(\mathbf{x})$: N-Electron Systems

The general pattern indicated by the results of (7.34) and (7.35) is apparent: when an excited state Ψ_j is created by moving an electron from orbital m to j, we have

$$\left\langle \Psi_j \middle| \mathfrak{n}(\mathbf{x}) \middle| \Psi_0 \right\rangle = \psi_j^*(\mathbf{x})\psi_m(\mathbf{x}) \tag{7.36}$$

$$\left\langle \Psi_0 \middle| \mathfrak{n}(\mathbf{x}) \middle| \Psi_j \right\rangle = \psi_m^*(\mathbf{x})\psi_j(\mathbf{x}) \tag{7.37}$$

The sum in (7.30) is over all excited states. A unique excited state can be generated by moving any originally occupied state m to an unoccupied one j [48, p.16]. Therefore, for each target j, there are m possible starting points, meaning each j induces a summation over m. In other words, (7.30) becomes

$$\chi_1(\mathbf{x},\mathbf{y},\omega) = \sum_j^{\text{unocc}} \sum_m^{\text{occ}} \left[\frac{\left\langle \Psi_0 \middle| \mathfrak{n}(\mathbf{x}) \middle| \Psi_j \right\rangle \left\langle \Psi_j \middle| \mathfrak{n}(\mathbf{y}) \middle| \Psi_0 \right\rangle}{\omega - \left(E_j - E_0\right) + i\eta} - \frac{\left\langle \Psi_0 \middle| \mathfrak{n}(\mathbf{y}) \middle| \Psi_j \right\rangle \left\langle \Psi_j \middle| \mathfrak{n}(\mathbf{x}) \middle| \Psi_0 \right\rangle}{\omega + \left(E_j - E_0\right) + i\eta} \right]$$

Applying the energy change (7.31) and simplifying the bra-kets with (7.36) and (7.37), the above becomes

$$\chi_1(\mathbf{x},\mathbf{y},\omega) = \sum_j^{\text{unocc}} \sum_m^{\text{occ}} \left[\frac{\psi_m^*(\mathbf{x})\psi_j(\mathbf{x})\,\psi_j^*(\mathbf{y})\psi_m(\mathbf{y})}{\omega - \varepsilon_j + \varepsilon_m + i\eta} - \frac{\psi_m^*(\mathbf{y})\psi_j(\mathbf{y})\,\psi_j^*(\mathbf{x})\psi_m(\mathbf{x})}{\omega + \varepsilon_j - \varepsilon_m + i\eta} \right]$$

By introducing occupation factors from Fermi-Dirac statistics, whereby $f_k = 1$ indicates that state k is occupied and $f_k = 0$ indicates it is unoccupied, we can write

$$\chi_1(\mathbf{x},\mathbf{y},\omega) = \sum_j^{\text{all}} \sum_m^{\text{all}} f_m(1-f_j) \left[\frac{\psi_m^*(\mathbf{x})\psi_j(\mathbf{x})\,\psi_j^*(\mathbf{y})\psi_m(\mathbf{y})}{\omega - \varepsilon_j + \varepsilon_m + i\eta} - \frac{\psi_m^*(\mathbf{y})\psi_j(\mathbf{y})\,\psi_j^*(\mathbf{x})\psi_m(\mathbf{x})}{\omega + \varepsilon_j - \varepsilon_m + i\eta} \right] \tag{7.38}$$

Finally, in the second term, we make the change of variables $j \leftrightarrows m$:

$$\sum_j \sum_m f_m(1-f_j) \frac{\psi_m^*(\mathbf{y})\psi_j(\mathbf{y})\,\psi_j^*(\mathbf{x})\psi_m(\mathbf{x})}{\omega + \varepsilon_j - \varepsilon_m + i\eta} = \sum_m \sum_j f_j(1-f_m) \frac{\psi_j^*(\mathbf{y})\psi_m(\mathbf{y})\,\psi_m^*(\mathbf{x})\psi_j(\mathbf{x})}{\omega + \varepsilon_m - \varepsilon_j + i\eta}$$

so that after switching the order of summation in the first term, we can combine the terms of (7.38):

$$\chi_1(\mathbf{x},\mathbf{y},\omega) = \sum_m \sum_j (f_m - f_j) \frac{\psi_m^*(\mathbf{x})\psi_m(\mathbf{y})\,\psi_j(\mathbf{x})\psi_j^*(\mathbf{y})}{\omega + \varepsilon_m - \varepsilon_j + i\eta} \tag{7.39}$$

7.2.3 Representation within Jellium Model

Within jellium, states correspond to the orbital's momentum[†] Restoring this notation in (7.39) yields

$$\chi_1(\mathbf{x},\mathbf{y},\omega) = \sum_{\mathbf{k}} \sum_{\mathbf{k}'} (f_{\mathbf{k}} - f_{\mathbf{k}'}) \frac{\psi_{\mathbf{k}}^*(\mathbf{x})\psi_{\mathbf{k}}(\mathbf{y})\,\psi_{\mathbf{k}'}(\mathbf{x})\psi_{\mathbf{k}'}^*(\mathbf{y})}{\varepsilon_{\mathbf{k}} - \varepsilon_{\mathbf{k}'} + \omega + i\eta} \tag{7.40}$$

Summation is more properly integration in momentum space, so it is more appropriate to write (7.40) as

$$\chi_1(\mathbf{x},\mathbf{y},\omega) = \int_{\mathbb{R}^3} f_{\mathbf{k}} \int_{\mathbb{R}^3} \frac{\psi_{\mathbf{k}}^*(\mathbf{x})\psi_{\mathbf{k}}(\mathbf{y})\,\psi_{\mathbf{k}'}(\mathbf{x})\psi_{\mathbf{k}'}^*(\mathbf{y})}{\varepsilon_{\mathbf{k}} - \varepsilon_{\mathbf{k}'} + \omega + i\eta}\, d\mathbf{k}'\, d\mathbf{k} - \int_{\mathbb{R}^3} f_{\mathbf{k}'} \int_{\mathbb{R}^3} \frac{\psi_{\mathbf{k}}^*(\mathbf{x})\psi_{\mathbf{k}}(\mathbf{y})\,\psi_{\mathbf{k}'}(\mathbf{x})\psi_{\mathbf{k}'}^*(\mathbf{y})}{\varepsilon_{\mathbf{k}} - \varepsilon_{\mathbf{k}'} + \omega + i\eta}\, d\mathbf{k}\, d\mathbf{k}'$$

In the second integral, we can make the change of variables $\mathbf{k} \leftrightarrows \mathbf{k}'$ and obtain that

$$\chi_1(\mathbf{x},\mathbf{y},\omega) = \int_{\mathbb{R}^3} f_{\mathbf{k}} \int_{\mathbb{R}^3} \frac{\psi_{\mathbf{k}}^*(\mathbf{x})\psi_{\mathbf{k}}(\mathbf{y})\,\psi_{\mathbf{k}'}(\mathbf{x})\psi_{\mathbf{k}'}^*(\mathbf{y})}{\varepsilon_{\mathbf{k}} - \varepsilon_{\mathbf{k}'} + \omega + i\eta}\, d\mathbf{k}'\, d\mathbf{k} + \int_{\mathbb{R}^3} f_{\mathbf{k}} \int_{\mathbb{R}^3} \frac{\psi_{\mathbf{k}}(\mathbf{x})\psi_{\mathbf{k}}^*(\mathbf{y})\,\psi_{\mathbf{k}'}^*(\mathbf{x})\psi_{\mathbf{k}'}(\mathbf{y})}{\varepsilon_{\mathbf{k}} - \varepsilon_{\mathbf{k}'} - \omega - i\eta}\, d\mathbf{k}'\, d\mathbf{k}$$

We recognize that the second integral is the complex conjugate of the first one with ω replaced by $-\omega$. It is therefore sufficient to work out the details of

$$\mathcal{I}(\mathbf{x},\mathbf{y},\omega) \triangleq \int_{\mathbb{R}^3} f_{\mathbf{k}} \int_{\mathbb{R}^3} \frac{\psi_{\mathbf{k}}^*(\mathbf{x})\psi_{\mathbf{k}}(\mathbf{y})\,\psi_{\mathbf{k}'}(\mathbf{x})\psi_{\mathbf{k}'}^*(\mathbf{y})}{\varepsilon_{\mathbf{k}} - \varepsilon_{\mathbf{k}'} + \omega + i\eta}\, d\mathbf{k}'\, d\mathbf{k}$$

[†]The true wavefunction in jellium is $\psi_{\mathbf{k}}(\mathbf{x})$. However, symmetry allows *computation* of the one-dimensional, scalar-indexed $\psi_k(x)$. The distinction between the computational tool of $\psi_k(x)$ and the actual wavefunction must not be forgotten.

Separating into components parallel (i.e., $\tilde{\mathbf{x}}$) and perpendicular to the surface as in Section 5.2, and applying the wavefunction decomposition (5.9), we can write

$$\mathcal{I}(\mathbf{x},\mathbf{y},\omega) = \int_{\mathbb{R}^3} f_{\mathbf{k}} \int_{\mathbb{R}^3} e^{i(\tilde{\mathbf{k}}'-\tilde{\mathbf{k}})(\tilde{\mathbf{x}}-\tilde{\mathbf{y}})} \frac{\psi_k^*(x)\psi_k(y)\,\psi_{k'}(x)\psi_{k'}^*(y)}{\varepsilon_{\mathbf{k}} - \varepsilon_{\mathbf{k}'} + \omega + i\eta}\, d\mathbf{k}'\, d\mathbf{k}$$

Define (formally) the Fourier transform parallel to the surface:

$$\tilde{\mathfrak{F}}\{f\}(\tilde{\mathbf{q}}) \triangleq \int_{\mathbb{R}^2} e^{-i\tilde{\mathbf{q}}\cdot(\tilde{\mathbf{x}})} f(\tilde{\mathbf{x}})\, d\tilde{\mathbf{x}} \tag{7.41}$$

Then the parallel Fourier transform of $\mathcal{I}$ is

$$\begin{aligned}
\tilde{\mathfrak{F}}\{\mathcal{I}\}(x,y,\tilde{\mathbf{q}};\omega) &= \int_{\mathbb{R}^3} f_{\mathbf{k}} \int_{\mathbb{R}^3} \delta\big(\tilde{\mathbf{q}} - \tilde{\mathbf{k}} + \tilde{\mathbf{k}}'\big) \frac{\psi_k^*(x)\psi_k(y)\,\psi_{k'}(x)\psi_{k'}^*(y)}{\varepsilon_{\mathbf{k}} - \varepsilon_{\mathbf{k}'} + \omega + i\eta}\, d\mathbf{k}'\, d\mathbf{k} \\
&= \int_{\mathbb{R}^3} f_{\mathbf{k}} \psi_k^*(x)\psi_k(y) \left[\int_{\mathbb{R}} \psi_{k'}(x)\psi_{k'}^*(y) \left[\int_{\mathbb{R}^2} \frac{\delta\big(\tilde{\mathbf{q}} - \tilde{\mathbf{k}} + \tilde{\mathbf{k}}'\big)}{\frac{1}{2}\mathbf{k}^2 - \frac{1}{2}\mathbf{k}'^2 + \varepsilon_k - \varepsilon_{k'} + \omega + i\eta}\, d\mathbf{k}' \right] dk' \right] d\mathbf{k} \\
&= \int_{\mathbb{R}^3} f_{\mathbf{k}} \psi_k^*(x)\psi_k(y) \left[\int_{\mathbb{R}} \frac{\psi_{k'}(x)\psi_{k'}^*(y)}{2\mathbf{k}\cdot\tilde{\mathbf{q}} - \frac{1}{2}\tilde{\mathbf{q}}^2 + \varepsilon_k - \varepsilon_{k'} + \omega + i\eta}\, dk' \right] d\mathbf{k}
\end{aligned}$$

We now employ a long-wavelength limit $|\tilde{\mathbf{q}}| \to 0$ relevant for incident photons [67, p.42] to obtain that

$$\begin{aligned}
\mathcal{I}(\mathbf{x},\mathbf{y},\omega) = \tilde{\mathfrak{F}}\{\mathcal{I}\}(x,y,0;\omega) &= \int_{\mathbb{R}^3} f_{\mathbf{k}} \psi_k^*(x)\psi_k(y) \left[\int_{\mathbb{R}} \frac{\psi_{k'}(x)\psi_{k'}^*(y)}{\varepsilon_k - \varepsilon_{k'} + \omega + i\eta}\, dk' \right] d\mathbf{k} \\
&= \int_{\mathbb{R}^3} f_{\mathbf{k}} \psi_k^*(x)\psi_k(y) G(x,y;\varepsilon_k + \omega)\, d\mathbf{k}
\end{aligned}$$

where we have used the spectral representation (6.17) of G. The $f_{\mathbf{k}}$ come from Fermi-Dirac statistics (5.6):

$$\mathcal{I}(\mathbf{x},\mathbf{y},\omega) = \int_{|\mathbf{k}|<k_F} \psi_k^*(x)\psi_k(y) G(x,y;\varepsilon_k + \omega)\, d\mathbf{k}$$

To resolve the integral over $\mathbf{k}$, we mirror the procedure that began with (5.8), went through (5.12), and produced (5.18). Doing so yields

$$\mathcal{I}(\mathbf{x},\mathbf{y},\omega) = \frac{1}{\pi^2} \int_0^{k_F} \big(k_F^2 - k^2\big) \psi_k(x)\psi_k(y) G(x,y;\varepsilon_k + \omega)\, dk$$

We have removed the conjugation from the wavefunction because it is real valued. Because $\chi_1(\mathbf{x},\mathbf{y},\omega) = \mathcal{I}(\mathbf{x},\mathbf{y},\omega) + \mathcal{I}^*(\mathbf{x},\mathbf{y},-\omega)$, we have the expression for the linear response function

$$\chi_1(x,y,\omega) = \frac{1}{\pi^2} \int_0^{k_F} \big(k_F^2 - k^2\big) \psi_k(x)\psi_k(y) \big[G(x,y;\varepsilon_k + \omega) + G^*(x,y;\varepsilon_k - \omega) \big]\, dk \tag{7.42}$$

Remark 7.3. The wavefunction decomposition (5.9) was again responsible for a reduction of dimension, allowing $\mathbf{x}$ and $\mathbf{y}$ to be replaced by x and y in (7.42). For the ground state density, the absolute value unilaterally eliminated the exponential factor. This time, the reduction is only allowed in the $\mathbf{q} \to 0$ limit, which is a macroscopic approximation that valid because of the symmetry of the jellium surface. ■

Remark 7.4. In Liebsch's derivation [67] of (7.42), he uses the summation

$$G(\mathbf{x}, \mathbf{y}; \varepsilon) = \sum_{\mathbf{k}} \frac{\psi_{\mathbf{k}}(\mathbf{x})\psi_{\mathbf{k}}^*(\mathbf{y})}{\varepsilon - \varepsilon_{\mathbf{k}} + i\eta}$$

which also appears in other sources too [78, p.182]. Because all the states are members of the continuous spectrum, this summation is an integral. His derivation is fundamentally correct as long as this interpretation is made; the above proceeds in proper rigor, even if the difference little more than a symbol. ■

7.3 Linear Response Density for Jellium Surface

We will now formulate how to compute the linear response density for the jellium system. We return to the integral equation for the linear response density $n_1(x;\omega)$ given in (7.22)

$$n_1(x;\omega) = \int_{-\infty}^{+\infty} \chi_1(x, y; \omega)\big[\phi_{\text{ext}}(y;\omega) + \phi_{\text{est}}(y;\omega) + \phi_{\text{xc}}(y;\omega)\big]\, dy \tag{7.43}$$

χ_1 is as in (7.42) and ϕ_{est} and ϕ_{xc} are as in (7.19) and (7.21), respectively, with dimension reduced. We assume that the source of the external potential is a uniform, normally incident time-varying electric field

$$\mathbf{E}_{\text{ext}}(t) = \big(\mathcal{E}_0 e^{i\omega t}, 0, 0\big)^T \tag{7.44}$$

or in frequency domain

$$\mathbf{E}_{\text{ext}}(\omega') = \big(\mathcal{E}_0, 0, 0\big)^T \delta(\omega - \omega')$$

If $\mathbf{E}_{\text{ext}}$ is monochromatic, then the only frequency contribution to n_1 from $\mathbf{E}_{\text{ext}}$ occurs at $\omega' = \omega$. If it is polychromatic, then we may write it as a sum of waves like (7.44) and consider each frequently separately. This explains the change of notation from (x, ω) in (7.22) to $(x;\omega)$ in (7.43)—now, we consider ω fixed.

Following elementary electromagnetics, there is a potential $\phi_{\text{ext}}(\mathbf{x};\omega)$ such that $-\nabla\phi_{\text{ext}}(\mathbf{x};\omega) = \mathbf{E}_{\text{ext}}(\omega)$. In this simple one-dimensional problem, it is easy to see that $\phi_{\text{ext}}(x;\omega) = -\mathcal{E}_0 x$ does the trick. However, to correspond to the long-wavelength limit of inelastic electron scattering [67], we choose the normalization

$$\phi_{\text{ext}}(x;\omega) = -2\pi x \tag{7.45}$$

We now see the motivation for the symbol swap performed at the end of Section 7.1.3. It desirable for the external potential to share the standard symbology of using ϕ for potentials in electromagnetics.

Much as long-range Coulomb interactions wreaked havoc in the ground state, necessitating the splitting of density described at length in Section 5.5, we cannot solve the Poisson equation (7.19) directly. We therefore construct another elaborate procedure that begins by defining the zeroth moment of the linear density:

$$\sigma(\omega) \triangleq \int_{-\infty}^{+\infty} n_1(x;\omega)\,dx \tag{7.46}$$

Because the normal component of the induced electric displacement $\mathbf{D}(x;\omega) = \varepsilon(\omega)\mathbf{E}(\mathbf{x};\omega)$ must be continuous across the metal/vaccuum interface, we have

$$\lim_{x\to 0^-} \varepsilon(\omega)\mathbf{E}_x(x;\omega) = \lim_{x\to 0^+} \varepsilon(\omega)\mathbf{E}_x(x;\omega)$$

where $\varepsilon(\omega)$ is the dielectric constant of the metal. In the Drude-Sommerfeld model,

$$\varepsilon(\omega) = 1 - \left(\frac{\omega_p}{\omega}\right)^2 \tag{7.47}$$

where ω_p denotes the plasma frequency (sometimes called the bulk-plasmon frequency)

$$\omega_p^2 = \frac{3}{r_s^3} \tag{7.48}$$

The limits denote approaching from inside the metal and vacuum, respectively. Then because

$$\lim_{x\to 0^-} \mathbf{E}_x(x) = -2\pi\big(1 - \sigma(\omega)\big)$$
$$\lim_{x\to 0^+} \mathbf{E}_x(x) = -2\pi\big(1 + \sigma(\omega)\big)$$

we have

$$\sigma(\omega) = \frac{\varepsilon(\omega) - 1}{\varepsilon(\omega) + 1} = \frac{\omega_p^2}{\omega_p^2 - 2\omega^2} \tag{7.49}$$

so that $\sigma(\omega)$ is always known *a priori* from the linear density. Next, we define

$$d_\perp(\omega) \triangleq \frac{1}{\sigma(\omega)} \int_{-\infty}^{+\infty} x n_1(x;\omega)\,dx \tag{7.50}$$

This quantity, first introduced by Feibelman, is a complex number (because n_1 is). The real part measures

the effective surface location of the normal component of the electric field, while the imaginary part represents the phase lag of this component in the surface region [31, p.325].

Following Liebsch [66], we now derive the splitting that filters out all those problematic bulk Coulomb effects by defining the bulk potential ϕ_b and quasi-electrostatic potential ϕ_1

$$\phi_b(x;\omega) \triangleq -2\pi\big(1-\sigma(\omega)\big)x + 2\pi\sigma(\omega)d_\perp(\omega) \tag{7.51}$$

$$\phi_1(x;\omega) \triangleq -4\pi \int_{-\infty}^{+\infty} (x-y)\Theta(x-y)n_1(y;\omega)\,dy \tag{7.52}$$

Recall that in one-dimension, $G_{\mathcal{L}}(x-y) = -2\pi\,|x-y| = -2\pi(x-y)\mathrm{sgn}(x-y)$. Consequently, as the solution to the Poisson equation (7.19), ϕ_{est} may be defined formally by integration against this Green's function

$$\phi_{\mathrm{est}}(x;\omega) = -2\pi \int_{-\infty}^{+\infty} (x-y)\mathrm{sgn}(x-y)n_1(y;\omega)\,dz$$

By writing $\mathrm{sgn}(x) = 2\Theta(x) - 1$, we can write the above formal solution as

$$\phi_{\mathrm{est}}(x;\omega) = \phi_1(x;\omega) + 2\pi \int_{-\infty}^{+\infty} (x-y)n_1(y;\omega)\,dy \tag{7.53}$$

Now we observe that

$$\begin{aligned}\int_{-\infty}^{+\infty} (x-y)\,n_1(y;\omega)\,dz &= x\int_{-\infty}^{+\infty} n_1(y)\,dy - \int_{-\infty}^{+\infty} y n_1(y;\omega)\,dy \\ &= \sigma(\omega)\big(x - d_\perp(\omega)\big)\end{aligned}$$

Combining this result with (7.53) and using (7.45), we have

$$\begin{aligned}\phi_{\mathrm{est}}(x;\omega) + \phi_{\mathrm{ext}}(x;\omega) &= \phi_1(x;\omega) + 2\pi\sigma(\omega)\big(x - d_\perp(\omega)\big) - 2\pi x \\ &= \phi_1(x;\omega) + \phi_b(x;\omega)\end{aligned} \tag{7.54}$$

Before we can go further, we need to break from the action to state and prove two lemmata.

Lemma 7.1. *If ψ_k is a Kohn-Sham wavefunction corresponding to ε_k, then*

$$\int_{-\infty}^{+\infty} \psi_k(y)G(x,y;\varepsilon)\,dy = \frac{\psi_k(x)}{\varepsilon - \varepsilon_k + i\eta}$$

Proof. Using the spectral representation of G given in (6.17), we have for any ε

$$\begin{aligned}\int_{-\infty}^{+\infty} \psi_k(y)G(x,y;\varepsilon)\,dy &= \int_{-\infty}^{+\infty} \psi_k(y) \int_{\mathbb{R}} \frac{\psi_\lambda(x)\psi_\lambda(y)}{\varepsilon-\varepsilon_\lambda+i\eta}\,d\lambda\,dy \\ &= \int_{\mathbb{R}} \frac{\psi_\lambda(x)}{\varepsilon-\varepsilon_\lambda+i\eta}\left[\int_{-\infty}^{+\infty} \psi_\lambda(y)\psi_k(y)\,dy\right]d\lambda \\ &= \int_{\mathbb{R}} \frac{\psi_\lambda(x)\delta(\lambda-k)}{\varepsilon-\varepsilon_\lambda+i\eta}\,d\lambda = \frac{\psi_k(x)}{\varepsilon-\varepsilon_k+i\eta}\end{aligned}$$

To obtain the final line, we have called upon the orthogonality of states (understood i.s.d.)

$$\int_{-\infty}^{+\infty} \psi_\lambda(y)\psi_k(y)\,dy = \delta(\lambda-k)$$ ∎

Lemma 7.2. *The linear response function $\chi_1(x,y;\omega)$ satisfies*

$$\int_{-\infty}^{+\infty} \chi_1(x,y;\omega)\,dy = 0$$

Proof. Recalling (7.42) and reversing the order of integration, we define

$$\mathcal{I} \triangleq \int_0^{k_F} \left(k_F^2-k^2\right)\psi_k(x) \int_{-\infty}^{+\infty} \psi_k(y)\big[G(x,y;\varepsilon_k+\omega)+G^*(x,y;\varepsilon_k-\omega)\big]\,dy\,dk$$

The conjugate from G^* in the second term filters out because $y\psi_k(y) \in \mathbb{R}$, so we have

$$\mathcal{I} = \int_0^{k_F} \left(k_F^2-k^2\right)\psi_k(x)\left[\int_{-\infty}^{+\infty} \psi_k(y)G(x,y;\varepsilon_k+\omega)\,dy + \left[\int_{-\infty}^{+\infty} \psi_k(y)G(x,y;\varepsilon_k-\omega)\,dy\right]^*\right]dk$$

Applying the result of Lemma 7.1 to the above, we have

$$\mathcal{I} = \int_0^{k_F} \left(k_F^2-k^2\right)\psi_k(x)\left[\frac{\psi_k(x)}{-\omega+i\eta}+\frac{\psi_k(x)}{\omega-i\eta}\right]dk = 0$$

which completes the proof. ∎

By definition,

$$\phi_1(x;\omega) = -4\pi\int_{-\infty}^{x}(x-y)n_1(y;\omega)\,dy \longrightarrow 0$$

as $x \to -\infty$, so all long-range Coulomb interaction from the bulk in (7.43) is contained in

$$\begin{aligned}\xi_1(x;\omega) &\triangleq \int_{-\infty}^{+\infty} \chi_1(x,y;\omega)\phi_b(y;\omega)\,dy \\ &= -2\pi\big(1-\sigma(\omega)\big)\int_{-\infty}^{+\infty} y\chi_1(x,y;\omega)\,dy + 2\pi\sigma(\omega)d_\perp(\omega)\int_{-\infty}^{+\infty}\chi_1(x,y;\omega)\,dy \qquad (7.55)\end{aligned}$$

Application of Lemma 7.2 to (7.55) gives a compact form for ξ_1:

$$\xi_1(x;\omega) = -2\pi\big(1-\sigma(\omega)\big)\int_{-\infty}^{+\infty} y\chi_1(x,y;\omega)\,dy \tag{7.56}$$

Juxtaposing (7.56) and (7.54) and substituting them into (7.43), we have

$$n_1(x;\omega) = \xi_1(x;\omega) + \int_{-\infty}^{\infty} \chi_1(x,y;\omega)\big[\phi_1(y;\omega) + \phi_{\mathrm{xc}}(y;\omega)\big]\,dy$$

We had dubbed ϕ_1 the "quasi-electrostatic potential." To see why this name is appropriate, we differentiate (7.52) twice with help from the Fundamental Theorem of Calculus and chain rule:

$$\phi_1'(x;\omega) = -4\pi\int_{-\infty}^{x} n_1(y;\omega)\,dy \quad\Longrightarrow\quad \phi_1'' = -4\pi n_1$$

Despite being related by the Poisson equation, ϕ_1 is obviously *not* the true linear electrostatic potential—the two differ by a term in the kernel of the operator $\frac{\partial^2}{\partial x^2}$. Because the operator annihilates the difference function, the two satisfy the same differential equation. However, because of this kernel term, ϕ_1 behaves inappropriately for an electrostatic potential as $x \to +\infty$, as will be shown in Section 7.5.

Even though we've made significant progress in isolating long-range Coulomb effects, we have not removed all of them—and, of course, we can only relocate them, not remove them from the system. ϕ_b contains the long-range effects from the *bulk material*, but does nothing to the Friedel oscillations in n_1. Those make computing ϕ_1 via direct integration unfeasible. A direct solve of the Poisson equation is possible [96], but great care must be taken to ensure numerical stability. Instead, we call upon the theorem below.

Theorem 7.3. *If u is a solution to the free Poisson equation over all of $\mathbb{R}$*

$$-u''(x) = 4\pi f(x)$$

then for any $\lambda > 0$, u also solves the integral equation

$$u(x) = \int_{-\infty}^{+\infty} e^{-\lambda|x-y|}\left[\frac{\lambda}{2}u(y) + \frac{2\pi}{\lambda}f(y)\right]dy$$

Proof. Let $\lambda > 0$. Then we may add $\lambda^2 u$ to both sides of the Poisson equation to give

$$\left(-\frac{\partial^2}{\partial x^2} + \lambda^2\right)u = 4\pi f + \lambda^2 u \tag{7.57}$$

We now compute the Green's function of the Helmholtz ("with the good sign") operator $\mathcal{Z} = -\frac{\partial^2}{\partial x^2} + \lambda^2$

$$\left(-\frac{\partial^2}{\partial x^2} + \lambda^2\right) G_{\mathcal{Z}}(x,y) = \delta(x-y)$$

by Fourier transform in x:

$$\hat{G}_{\mathcal{Z}}(\omega,y) = \frac{e^{-2\pi i\xi y}}{4\pi\xi^2+\lambda^2} \quad \Longrightarrow \quad G_{\mathcal{Z}}(x,y) = \frac{1}{2\lambda}e^{-\lambda|x-y|}$$

Consequently, the solution to the equivalent Poisson equation (7.57), treating the right-hand side as known, is given by integration against $G_{\mathcal{Z}}$:

$$u(x) = \int_{-\infty}^{+\infty} e^{-\lambda|x-y|}\left[\frac{\lambda}{2}u(y) + \frac{2\pi}{\lambda}f(y)\right]dy \qquad \blacksquare$$

Remark 7.5. Theorem 7.3 is precisely the technique used by Manninen [75] for computing ϕ in the ground state (cf. (5.29)). The technique is especially convenient here because a pair of coupled integral equations is easier solved than a system of an integral equation and a differential equation. $\blacksquare$

As a consequence of this theorem, we can obtain a pair of coupled integral equations for ϕ_1 and n_1:

$$n_1(x;\omega) = \xi_1(x;\omega) + \int_{-\infty}^{\infty} \chi_1(x,y;\omega)\Big[\phi_1(y;\omega) + f_{\mathrm{xc}}(y)n_1(y;\omega)\Big]dy \tag{7.58}$$

$$\phi_1(x;\omega) = \int_{-\infty}^{+\infty} e^{-\lambda|x-y|}\left[\frac{\lambda}{2}\phi_1(y;\omega) + \frac{2\pi}{\lambda}n_1(y;\omega)\right]dy \tag{7.59}$$

7.4 The Driving Function $\xi_1(x;\omega)$

Substituting the definition of χ_1 given in (7.42) into (7.56) and then interchanging the order of integration,

$$\xi_1(x) = -2\pi\big(1-\sigma(\omega)\big)\int_0^{k_F}\big(k_F^2-k^2\big)\psi_k(x)\int_{-\infty}^{+\infty} y\psi_k(y)\big[G(x,y;\varepsilon_k+\omega)+G^*(x,y;\varepsilon_k-\omega)\big]\,dy\,dk \tag{7.60}$$

We cannot perform a numerical computation over an infinite domain, so we decompose into three pieces:

$$\mathcal{B}^+(x,k;\omega) \triangleq \int_{-\infty}^{-R_1} y\psi_k(y)G(x,y;\varepsilon_k+\omega)\,dy \qquad \mathcal{B}^-(x,k;\omega) \triangleq \int_{-\infty}^{-R_1} y\psi_k(y)G^*(x,y;\varepsilon_k-\omega)\,dy$$

$$\mathcal{S}^+(x,k;\omega) \triangleq \int_{-R_1}^{R_2} y\psi_k(y)G(x,y;\varepsilon_k+\omega)\,dy \qquad \mathcal{S}^-(x,k;\omega) \triangleq \int_{-R_1}^{R_2} y\psi_k(y)G^*(x,y;\varepsilon_k-\omega)\,dy$$

$$\mathcal{V}^+(x,k;\omega) \triangleq \int_{R_2}^{\infty} y\psi_k(y)G(x,y;\varepsilon_k+\omega)\,dy \qquad \mathcal{V}^-(x,k;\omega) \triangleq \int_{R_2}^{\infty} y\psi_k(y)G^*(x,y;\varepsilon_k-\omega)\,dy$$

The symbols for these integrals have been selected to correspond to the physical region over which the integral is defined: the bulk metal, the surface, and the vacuum, respectively. Because both ψ_k and $G(x,\cdot;\varepsilon)$ decay exponentially into the vacuum, the contributions from $\mathcal{V}^+$ and $\mathcal{V}^-$ can be neglected. Therefore,

$$\xi_1(x;\omega) = -2\pi\big(1-\sigma(\omega)\big)\int_0^{k_F}\big(k_F^2-k^2\big)\psi_k(x)\big[\mathcal{B}^+(x,k;\omega)+\mathcal{S}^+(x,k;\omega)+\mathcal{B}^-(x,k;\omega)+\mathcal{S}^-(x,k;\omega)\big]\,dk$$

$\mathcal{B}^+$ and $\mathcal{B}^-$ can be computed analytically—and it is imperative to a correct result for ξ_1 that these contributions not be neglected—but $\mathcal{S}^+$ and $\mathcal{S}^-$ must be computed numerically from calculated solutions.

7.4.1 Contributions from the Bulk Metal

In this section, we will derive analytic expressions for the contributions to ξ_1 from deep within the bulk metal, encoded in $\mathcal{B}^+$ and $\mathcal{B}^-$. We are concerned only with $x \in [-R_1, R_2]$, so we may assume that $x \geq y$ in the integrals that define $\mathcal{B}^+$ and $\mathcal{B}^-$. This means that G does not "switch" in the middle of the integral, so

$$G(x,y;\varepsilon_k \pm \omega) = \frac{2}{W_k^{\pm}}\varphi_1(y;\varepsilon_k\pm\omega)\varphi_2(x;\varepsilon_k\pm\omega)$$

where the superscript plus indicates the value should be taken from $G(\cdot,\cdot;\varepsilon_k+\omega)$; minus, from $G(\cdot,\cdot;\varepsilon_k-\omega)$.

We open with the simpler "plus case," which requires computing

$$\begin{aligned}\mathcal{B}^+(x,k;\omega) &= \frac{2}{W_k^+}\int_{-\infty}^{-R_1} y\psi_k(y)\varphi_1(y;\varepsilon_k+\omega)\varphi_2(x;\varepsilon_k+\omega)\,dy \\ &= \frac{2}{W_k^+}\varphi_2(x;\varepsilon_k+\omega)\int_{-\infty}^{-R_1} y\psi_k(y)\varphi_1(y;\varepsilon_k+\omega)\,dy\end{aligned}$$

The interval of integration is contained in the asymptotic region, so the asymptotic expressions (5.17) and (6.5) may replace ψ_k and φ_1, respectively. Then

$$\mathcal{B}^+(x,k;\omega) = \frac{2}{W_k^+}\varphi_2(x;\varepsilon_k+\omega)\underbrace{\int_{-\infty}^{+\infty} y\Theta(-y-R_1)\sin(ky-\gamma_k)e^{-i\mu_k^+ y}\,dy}_{\triangleq\,\mathcal{I}}$$

Because $\mu_k^+ \in \mathbb{R}$, $\mathcal{I}$ does not converge to a function in k. However, because the result will be integrated against a smooth[†] function in k, we may compute $\mathcal{I}$ as a distribution with some help from the ordinary

[†]The integrand $\big(k_F^2-k\big)^2\psi_k$ is smooth enough in k, but the compact region of integration is equivalent to multiplying the integrand by the characteristic function $\chi_{[0,k_F]}(k) = \Theta(k-k_F)-\Theta(k)$, which is not smooth. For full rigor, the integral in momentum space should be taken in the limit against $C_c^\infty(\mathbb{R})$ functions that approximate the integrand. In the end, the distribution $\mathcal{I}$ can be applied to piecewise continuous functions, so the same result is obtained as when proper rigor is obeyed.

Fourier transform and the convolution derivative formula

$$\frac{\partial}{\partial \xi}\Big[f(\xi) * g(\xi)\Big] = f'(\xi) * g(\xi) = f(\xi) * g'(\xi)$$

By defining

$$f(y) \triangleq \Theta(-y - R_1) \qquad\qquad g(y) \triangleq \sin(ky - \gamma_k) = \sin\left(k\left(y - \gamma_k/k\right)\right)$$

we have that

$$\mathcal{I} = \frac{i}{2\pi}\frac{\partial}{\partial \xi}\Big[\hat{f}(\xi) * \hat{g}(\xi)\Big]_{\xi=\mu_k^+/2\pi} = \frac{i}{2\pi}\Big[\hat{f}'(\xi) * \hat{g}(\xi)\Big]_{\xi=\mu_k^+/2\pi}$$

where the derivative enters because of the y term. By making a change of variables $y \mapsto -y$ in the Fourier integral that defines $\hat{f}$ and applying shift rules, we have that

$$\hat{f}(\xi) = e^{2\pi i R_1 \xi}\,\mathcal{F}^*\Big\{\Theta(y)\Big\}(\xi)$$
$$\hat{g}(\xi) = e^{-2\pi i \gamma_k/k}\,\mathcal{F}\big\{\sin ky\big\}(\xi)$$

The transforms of the step and sine functions are well-known. Accordingly,

$$\hat{f}(\xi) = \frac{1}{2}e^{2\pi i R_1 \xi}\left(-\frac{1}{\pi i \xi} + \delta(\xi)\right)$$
$$\hat{g}(\xi) = \frac{1}{2i}\left[e^{-i\gamma_k}\delta\left(\xi - \frac{k}{2\pi}\right) - e^{i\gamma_k}\delta\left(\xi + \frac{k}{2\pi}\right)\right]$$

Then

$$\mathcal{I} = \frac{1}{4\pi}\left[e^{-i\gamma_k}\hat{f}'(\xi) * \delta\left(\xi - \frac{k}{2\pi}\right) - e^{i\gamma_k}\hat{f}'(\xi) * \delta\left(\xi + \frac{k}{2\pi}\right)\right]_{\xi=\mu_k^+/2\pi}$$
$$= \frac{1}{4\pi}\left[e^{-i\gamma_k}\hat{f}'\left(\frac{\mu_k^+ - k}{2\pi}\right) - e^{i\gamma_k}\hat{f}'\left(\frac{\mu_k^+ + k}{2\pi}\right)\right]$$

by the sifting property of the Dirac delta. Differentiating i.s.d directly, we have

$$\hat{f}'(\xi) = \frac{1}{2}e^{2\pi i R_1 \xi}\left[-\frac{2R}{\xi} + \frac{1}{i\pi\xi^2} + 2\pi i R\delta(\xi) + \delta'(\xi)\right]$$

Neither $k + \mu_k^+$ nor $k - \mu_k^+$ vanish, as that would require $k = \pm\sqrt{k^2 + 2\omega}$, which is impossible because $\omega > 0$.

Accordingly, the contributions from δ and δ' disappear and

$$\hat{f}'\left(\frac{\mu_k^+ \pm k}{2\pi}\right) = -2\pi e^{iR\mu_k^+ \pm iRk}\left[\frac{R_1}{\mu_k^+ \pm k} + \frac{i}{(\mu_k^+ \pm k)^2}\right]$$

Thus,

$$\mathcal{I} = \frac{1}{2}e^{iR_1\mu_k^+}e^{i(R_1k+\gamma_k)}\left[\frac{R_1}{\mu_k^+ + k} + \frac{i}{(\mu_k^+ + k)^2}\right] - \frac{1}{2}e^{iR_1\mu_k^+}e^{-i(R_1k+\gamma_k)}\left[\frac{R_1}{\mu_k^+ - k} + \frac{i}{(\mu_k^+ - k)^2}\right]$$

so that the desired computation is given by

$$\mathcal{B}_+ = \varphi_2(x;\varepsilon_k+\omega)\cdot\frac{e^{iR_1\mu_k^+}}{W_k^+}\left(e^{i(R_1k+\gamma_k)}\left[\frac{R_1}{\mu_k^+ + k} + \frac{i}{(\mu_k^+ + k)^2}\right] - e^{-i(R_1k+\gamma_k)}\left[\frac{R_1}{\mu_k^+ - k} + \frac{i}{(\mu_k^+ - k)^2}\right]\right) \tag{7.61}$$

The minus case is complicated by a $k_c = \sqrt{2\omega}$ at which μ_k^- will change from purely imaginary to real. Table 7.1 below gives the value of k_c for various input frequencies ω and choices of r_s. For inputs ω above the cutoff frequency $\omega_c = \frac{1}{2}k_F^2 = E_F$, we have $k_c > k_F$ so that μ_k^- remains real throughout the integral.

r_s	k_F	$0.1\omega_p$	$0.2\omega_p$	$0.3\omega_p$	$0.4\omega_p$	ω_c
2.0	0.9596	0.3500	0.4949	0.6062	0.6999	$0.7518\omega_p$
2.5	0.7677	0.2960	0.4187	0.5127	0.5921	$0.6725\omega_p$
3.0	0.6397	0.2582	0.3651	0.4472	0.5164	$0.6139\omega_p$
3.5	0.5483	0.2300	0.3253	0.3984	0.4600	$0.5683\omega_p$
4.0	0.4798	0.2081	0.2943	0.3604	0.4162	$0.5316\omega_p$

Table 7.1: Values of k_c and ω_c. The middle block lists the value of k_c for several frequencies per r_s value. For the listed frequencies, k_c always lies in $[0, k_F]$. The last column lists the ω above which $k_c > k_F$.

7.4.1.1 Case I: $k \geq \sqrt{2\omega}$

Because $\mu_k^- \in \mathbb{R}$ in this case, the analysis mirrors the plus case exactly. Therefore,

$$\mathcal{B}^- = \varphi_2(x;\varepsilon_k-\omega)\cdot\frac{e^{iR_1\mu_k^-}}{W_k^-}\left(e^{i(R_1k+\gamma_k)}\left[\frac{R_1}{\mu_k^- + k} + \frac{i}{(\mu_k^- + k)^2}\right] - e^{-i(R_1k+\gamma_k)}\left[\frac{R_1}{\mu_{\mathbf{k}}^- - k} + \frac{i}{(\mu_k^- - k)^2}\right]\right) \tag{7.62}$$

7.4.1.2 Case II: $k < \sqrt{2\omega}$

In this case, the asymptotic behavior of G is quantitatively different. Rather than become oscillatory, G decays exponentially as per (6.5), so

$$\mathcal{B}^-(x,k;\omega) = \frac{2}{W_k^-}\varphi_2(x;\varepsilon_k-\omega)\int_{-\infty}^{-R_1} y\sin(ky-\gamma_k)e^{\tilde{\kappa}_\omega^- y}\,dy$$

where $\tilde{\mu}_k^- \triangleq \operatorname{Im}\mu_k^-$. This integral can be computed using a tabular method to integrate by parts multiple times, but the process is tedious. Instead, by converting the sine term to an exponential

$$\mathcal{B}^-(x,k;\omega) = \frac{2}{W_k^-}\varphi_2(x;\varepsilon_k-\omega)\cdot\operatorname{Im}\underbrace{\int_{-\infty}^{+\infty} y\Theta(-y-R_1)e^{\tilde{\mu}_k^- y}e^{-iky}\,dy}_{\triangleq\mathcal{I}}$$

we can again use Fourier transforms to evaluate the integral by defining

$$f(y) \triangleq \Theta(-y-R)e^{\tilde{\mu}_k^- y} = e^{-\tilde{\mu}_k^- R}\Big[\Theta(-y-R_1)e^{\tilde{\mu}_k^-(y+R_1)}\Big]$$

and recognizing that

$$\mathcal{I} = \frac{i}{2\pi}\hat{f}'\left(\frac{k}{2\pi}\right)$$

By making a change of variables $y \mapsto -y$ and applying shift rules, $\hat{f}$ is expressed

$$\begin{aligned}\hat{f}(\xi) &= e^{-\tilde{\mu}_k^- R_1}\int_{-\infty}^{+\infty}\Theta(y-R_1)e^{-\tilde{\mu}_k^-(y-R)}e^{2\pi i\xi y}\,dy\\ &= e^{-\tilde{\mu}_k^- R_1}e^{2\pi i R_1\xi}\,\mathcal{F}^*\Big\{\Theta(y)e^{-\tilde{\mu}_k^- y}\Big\}(\xi)\end{aligned}$$

This time, $f \in L^2(\mathbb{R})$, so its Fourier transform is defined as a function:

$$\hat{f}(\xi) = e^{-\tilde{\mu}_k^- R_1}\frac{e^{2\pi i R_1\xi}}{\tilde{\mu}_k^- - 2\pi i\xi}$$

Differentiating directly, we have

$$\hat{f}'(\xi) = 2\pi i e^{-\tilde{\mu}_k^- R_1}e^{2\pi i R\xi}\left[\frac{R_1}{\tilde{\mu}_k^- - 2\pi i\xi} + \frac{1}{(\tilde{\mu}_k^- - 2\pi i\xi)^2}\right]$$

Then

$$\mathcal{I} = -e^{iR_1k - R_1\tilde{\mu}_k^-}\left[\frac{R_1}{\tilde{\mu}_k^- - ik} + \frac{1}{(\tilde{\mu}_k^- - ik)^2}\right]$$

gives us that

$$\mathcal{B}^-(x,k;\omega) = -\frac{2}{W_k^-}\varphi_2(x;\varepsilon_k-\omega)\cdot \operatorname{Im}\left(e^{i(R_1k+\gamma_k)-R_1\tilde{\mu}_k^-}\left[\frac{R_1}{\tilde{\mu}_k^- - ik}+\frac{1}{(\tilde{\mu}_k^- - ik)^2}\right]\right)$$

In order to draw parallels with (7.62), we make use of the identity $\operatorname{Im} z = \operatorname{Re}\left(\frac{z}{i}\right)$:

$$\begin{aligned}\operatorname{Im}\left(e^{i(R_1k+\gamma_k)-R_1\tilde{\mu}_k^-}\left[\frac{R_1}{\tilde{\mu}_k^- - ik}+\frac{1}{(\tilde{\mu}_k^- - ik)^2}\right]\right) &= \operatorname{Re}\left(e^{i(R_1k+\gamma_k)-R_1\tilde{\mu}_k^-}\left[\frac{R_1}{i\tilde{\mu}_k^- + k}+\frac{i}{(i\tilde{\mu}_k^- + k)^2}\right]\right)\\ &= \operatorname{Re}\left(e^{i(R_1k+\gamma_k)+iR_1\mu_k^-}\left[\frac{R_1}{\mu_k^- + k}+\frac{i}{(\mu_k^- + k)^2}\right]\right)\end{aligned}$$

with the last line coming by reversing $\tilde{\mu}_k^- = \operatorname{Im}\mu_k^-$ and that $\operatorname{Re}\mu_k^- = 0$. We then have

$$\mathcal{B}^-(x,k;\omega) = -\frac{2}{W_k^-}\varphi_2(x;\varepsilon_k-\omega)\cdot \operatorname{Re}\left(e^{i(R_1k+\gamma_k)+iR_1\mu_k^-}\left[\frac{R_1}{\mu_k^- + k}+\frac{i}{(\mu_k^- + k)^2}\right]\right) \tag{7.63}$$

Feibelman performed computations similar in nature to the ones in this section [29, 30], although his purpose was to find the asymptotic behavior of n_1. His methodology differed significantly from the one here: in evaluating integrals like the ones that define $\mathcal{B}^+$, he chose to do the integrals in k first. He converted the sine term to complex exponentials and then wrote

$$e^{-i(\mu_k^+\pm k)y} = \pm\frac{i}{y}\frac{\mu_k^+}{\mu_k^+\pm k}\cdot\frac{\partial}{\partial k}\left[e^{-i(\mu_k^+\pm k)y}\right]$$

From there, he iterated integration by parts twice. While functional, this method leads to an incredibly tedious and painstaking computation—the author of this thesis first attempted this method, with an incorrect solution resulting after nine dense pages of typeset text. Using Fourier transforms is in every way superior: it is easy to understand and produces an elegant solution with little effort.

7.4.2 Contributions from the Surface

Because no asymptotic behavior is needed to compute $\mathcal{S}^+$ and $\mathcal{S}^-$ there is no difference aside from a plus/minus symbol. We therefore handle the general expression

$$\mathcal{G}(x;\varepsilon) = \int_{R_1}^{R_2} y\psi_k(y)G(x,y;\varepsilon)\,dy$$

so that

$$\mathcal{S}^+(x,k;\omega) = \mathcal{G}(x;\varepsilon_k+\omega) \qquad\qquad \mathcal{S}^-(x,k;\omega) = \mathcal{G}(x;\varepsilon_k-\omega)$$

Because the real part of G has a cusp at $x = y$, accurate numerical integration requires breaking the integral at x and designing two quadrature rules, one for $[-R_1, x]$ and another for $[x, R_2]$. Computing these two integrals separately for each grid point x is incredibly inefficient, as the same computations are performed twice. We therefore seek to craft a more efficient method of computing $\mathcal{S}^+$ and $\mathcal{S}^-$. To this end, define

$$\mathcal{I}_1(x;\varepsilon) \triangleq \int_x^{R_2} y\psi_k(y)\varphi_1(y;\varepsilon)\,dy \tag{7.64}$$

$$\mathcal{I}_2(x;\varepsilon) \triangleq \int_x^{R_2} y\psi_k(y)\varphi_2(y;\varepsilon)\,dy \tag{7.65}$$

Then

$$\begin{aligned}\mathcal{G}(x;\varepsilon) &= \int_{-R_1}^{x} y\psi_k(y)G(x,y;\varepsilon)\,dy + \int_x^{R_2} y\psi_k(y)G(x,y;\varepsilon)\,dy \\ &= \frac{2}{W_\varepsilon}\left(\varphi_2(x)\left[\int_{-R_1}^{R_2} y\psi_k(y)\varphi_1(y)\,dy - \int_x^{R_2} y\psi_k(y)\varphi_1(y)\,dy\right] + \varphi_1(x)\int_x^{R_2} y\psi_k(y)\varphi_2(y)\,dy\right) \\ &= \frac{2}{W_\varepsilon}\left(\varphi_2(x;\varepsilon)\Big[\mathcal{I}_1(-R_1;\varepsilon) - \mathcal{I}_1(x;\varepsilon)\Big] + \varphi_1(x;\varepsilon)\,\mathcal{I}_2(x;\varepsilon)\right)\end{aligned} \tag{7.66}$$

Using the result of (7.66), the needed quantities $\mathcal{S}^+$ and $\mathcal{S}^-$ are

$$\mathcal{S}^+(x,k;\omega) = \frac{2}{W_k^+}\left(\varphi_2(x;\varepsilon_k+\omega)\Big[\mathcal{I}_1(-R_1;\varepsilon_k+\omega) - \mathcal{I}_1(x;\varepsilon_k+\omega)\Big] + \varphi_1(x;\varepsilon_k+\omega)\,\mathcal{I}_2(x;\varepsilon_k+\omega)\right) \tag{7.67}$$

$$\mathcal{S}^-(x,k;\omega) = \frac{2}{W_k^-}\left(\varphi_2(x;\varepsilon_k-\omega)\Big[\mathcal{I}_1(-R_1;\varepsilon_k-\omega) - \mathcal{I}_1(x;\varepsilon_k-\omega)\Big] + \varphi_1(x;\varepsilon_k-\omega)\,\mathcal{I}_2(x;\varepsilon_k-\omega)\right) \tag{7.68}$$

7.4.3 Summary

Figure 7.1 below displays several examples of ξ_1 as assembled from (7.61)–(7.63) and (7.67)–(7.68).

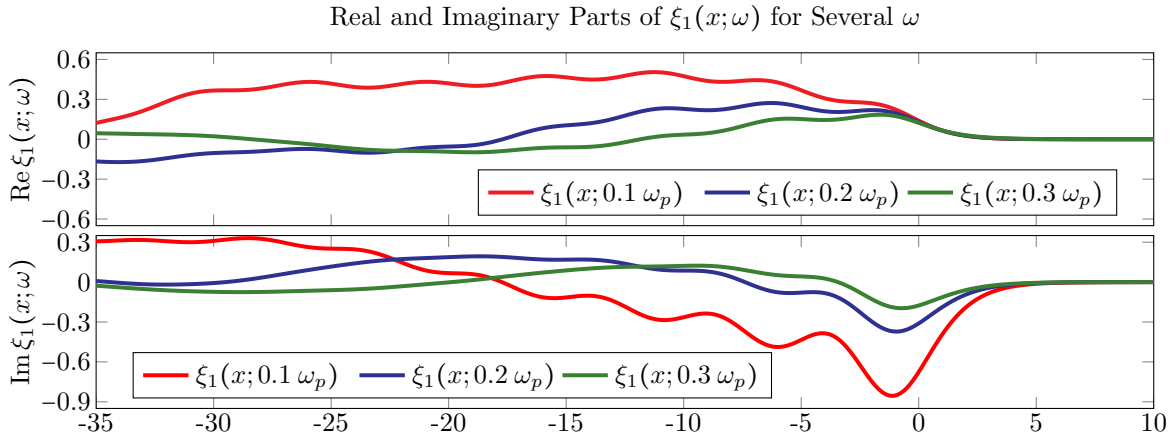

Figure 7.1: $\xi_1(x;\omega)$ for Several ω. This figure depicts the real (top) and imaginary (bottom) parts of $\xi_1(x;\omega)$ for $\omega = 0.1, 0.2, 0.3\omega_p$, all for $r_s = 3$.

Note that $\xi_1(x;\omega)$ displays rather unpredictable behavior and does not vanish as $x \to -\infty$. Because ξ_1 contributes only locally to $n_1(x;\omega)$, there are no concerns as there would be if ξ_1 were in an integral.

The importance of the analytic contributions $\mathcal{B}^+$ and $\mathcal{B}^-$ cannot be understated. Depicted below in Figure 7.2 is the result (for $\omega = 0.1\omega_p$) if these bulk contributions are not included.

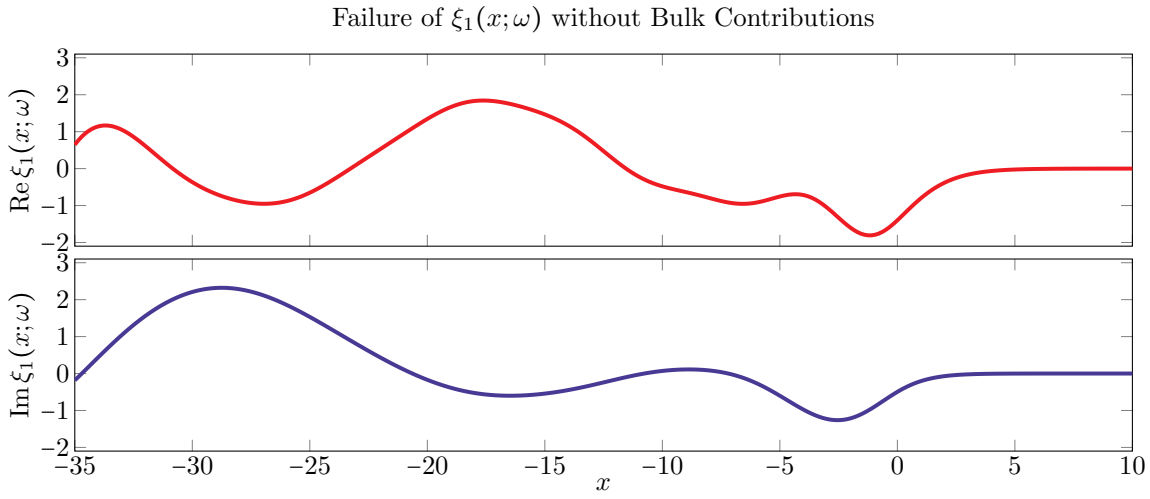

Figure 7.2: Incorrect $\xi_1(x;\omega)$. When the bulk contributions are not included, the result is a very different (and very wrong!) $\xi_1(x;\omega)$, shown for $\omega = 0.1\omega_p$ and $r_s = 3$.

7.5 Asymptotic Behavior of ϕ_1

We return to ϕ_1's integral definition, reproduced from (7.52) below:

$$\phi_1(x;\omega) = -4\pi \int_{-\infty}^{x} (x-y) n_1(y;\omega)\, dy$$

Because $n_1 \to 0$ exponentially [29], for $x \gg 0$ the integral in the above definition of ϕ_1 is well-approximated by one over all of $\mathbb{R}$. Consequently, we conclude that ϕ_1 behaves asymptotically like

$$\begin{aligned}\phi_1(x;\omega) &\sim -4\pi\left(x \int_{-\infty}^{+\infty} n_1(y;\omega)\, dy - \int_{-\infty}^{+\infty} y n_1(y;\omega)\, dy\right) \\ &\sim -4\pi\sigma(\omega)\big(x - d_\perp(\omega)\big)\end{aligned} \tag{7.69}$$

after applying the definitions (7.46) and (7.50). As a result, ϕ_1 grows unbounded. The electrostatic potential should approach a constant as we move farther and father away from the surface. Because ϕ_1 does not display

this behavior, it cannot represent the electrostatic potential. The cost of negating long-range Coulomb effects from the bulk by incorporating is that ϕ_1 inherited the external potential's linear growth.

One might expect the exponentially decaying kernels of (7.58) and (7.59) for $x \gg 0$ to snuff out (7.69), but failure to account for it results in a fantastically incorrect result, as depicted below in Figure 7.3.

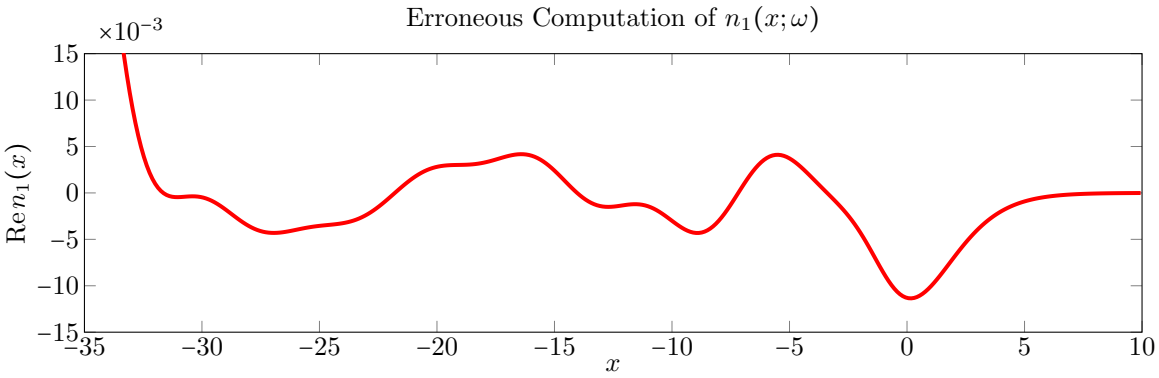

Figure 7.3: Spectacular Failure of Direct Solution. Attempt to solve (7.58) and (7.59) directly without consideration of the asymptotic behavior (7.69) of ϕ_1 results in this trainwreck of a solution.

Therefore, to avoid a disaster like the one depicted in the figure, we define

$$\tilde{\phi}_1(x) \triangleq \phi_1(x) + 4\pi\sigma(\omega)x\Theta(x) \tag{7.70}$$

which has $\tilde{\phi}_1 \to 4\pi\sigma(\omega)d_\perp(\omega)$ for $x \gg 0$. Substituting (7.70) into (7.58) and (7.59) gives

$$\begin{aligned}
n_1(x;\omega) &= \xi_1(x;\omega) - 4\pi\sigma(\omega)\int_0^{+\infty} y\chi_1(x,y;\omega)\,dy + \int_{-\infty}^{+\infty} \chi_1(x,y;\omega)\left[\tilde{\phi}_1(y;\omega) + f_{\mathrm{xc}}(y)n_1(y;\omega)\right]dy \\
\tilde{\phi}_1(x;\omega) &= 4\pi\sigma(\omega)x\Theta(x) - 2\pi\lambda\sigma(\omega)\int_0^{+\infty} ye^{-\lambda|x-y|}\,dy + \int_{-\infty}^{+\infty} e^{-\lambda|x-y|}\left[\frac{\lambda}{2}\tilde{\phi}_1(y;\omega) + \frac{2\pi}{\lambda}n_1(y;\omega)\right]dy
\end{aligned}$$

To clean up these cumbersome expressions, we define the function

$$\xi_2(x;\omega) \triangleq -4\pi\sigma(\omega)\int_0^{+\infty} y\chi_1(x,y;\omega)\,dy \tag{7.71}$$

and compute analytically the integral

$$-2\pi\lambda\sigma\int_0^{+\infty} ye^{-\lambda|x-y|}\,dy = -\frac{2\pi\sigma(\omega)}{\lambda}e^{-\lambda|x|} - 4\pi\sigma(\omega)x\Theta(x)$$

so that we can write more concisely

$$n_1(x;\omega) = \xi_1(x;\omega) + \xi_2(x;\omega) + \int_{-\infty}^{+\infty} \chi_1(x,y;\omega)\Big[\tilde{\phi}_1(y;\omega) + f_{\text{xc}}(y)n_1(y;\omega)\Big]dy \tag{7.72}$$

$$\tilde{\phi}_1(x;\omega) = -\frac{2\pi\sigma(\omega)}{\lambda}e^{-\lambda|x|} + \int_{-\infty}^{+\infty} e^{-\lambda|x-y|}\left[\frac{\lambda}{2}\tilde{\phi}_1(y;\omega) + \frac{2\pi}{\lambda}n_1(y;\omega)\right]dy \tag{7.73}$$

7.5.1 Computing $\xi_2(x;\omega)$

Just as in Section 7.4, we employ the definition (7.42) of χ_1 to expand ξ_2 as we did ξ_1:

$$\xi_2(x;\omega) = -2\pi\big(1-\sigma(\omega)\big)\int_0^{k_F}\left(k_F^2-k^2\right)\psi_k(x)\int_0^{+\infty} y\psi_k(y)\big[G(x,y;\varepsilon_k+\omega)+G^*(x,y;\varepsilon_k-\omega)\big]\,dy\,dk$$

Similar to what was done in Section 7.4.2, we focus on integrals of the form

$$\mathcal{G}(x;\varepsilon) = \int_0^{\infty} y\psi_k(y)G(x,y;\varepsilon)\,dy = \int_0^{R_2} y\psi_k(y)G(x,y;\varepsilon)\,dy$$

Because G's cusp at $x=y$ will occur within the domain of integration if $x>0$, we distinguish two cases.

Case I: $x \le 0$. Because $y \ge 0$ in the integral, we have $x \le y$ throughout, so G does not switch. Therefore,

$$\mathcal{G}(x;\varepsilon) = \frac{2}{W_\varepsilon}\varphi_1(x;\varepsilon)\int_0^{R_2} y\psi_k(y)\varphi_2(y;\varepsilon)\,dy = \frac{2}{W_\varepsilon}\varphi_1(x;\varepsilon)\mathcal{I}_2(0;\varepsilon)$$

Case II: $x \ge 0$. G will switch at x. Following the exact same procedure that led to (7.66), we have

$$\mathcal{G}(x;\varepsilon) = \frac{2}{W_\varepsilon}\left(\varphi_2(x;\varepsilon)\Big[\mathcal{I}_1(0;\varepsilon)-\mathcal{I}_1(x;\varepsilon)\Big]+\varphi_1(x;\varepsilon)\,\mathcal{I}_2(x;\varepsilon)\right)$$

Combining the results of the two cases, the complete recipe for $\xi_2(x;\omega)$ is

$$\xi_2(x;\omega) = -2\pi\big(1-\sigma(\omega)\big)\int_0^{k_F}\left(k_F^2-k^2\right)\psi_k(x)\mathcal{P}(x;k)\,dk \tag{7.74}$$

with

$$\mathcal{P} \triangleq \begin{cases} \dfrac{2}{W_\omega^+}\varphi_1(x;\varepsilon_k+\omega)\mathcal{I}_2(0;\varepsilon_k+\omega) + \dfrac{2}{W_\omega^-}\varphi_1(x;\varepsilon_k-\omega)\mathcal{I}_2(0;\varepsilon_k-\omega) & x \le 0 \\ \dfrac{2}{W_\omega^+}\left(\varphi_2(x;\varepsilon_k+\omega)\Big[\mathcal{I}_1(0;\varepsilon_k+\omega)-\mathcal{I}_1(x;\varepsilon_k+\omega)\Big]+\varphi_1(x;\varepsilon_k+\omega)\,\mathcal{I}_2(x;\varepsilon_k+\omega)\right)+ & \\ \qquad \dfrac{2}{W_\omega^-}\left(\varphi_2(x;\varepsilon_k-\omega)\Big[\mathcal{I}_1(0;\varepsilon_k-\omega)-\mathcal{I}_1(x;\varepsilon_k-\omega)\Big]+\varphi_1(x;\varepsilon_k-\omega)\,\mathcal{I}_2(x;\varepsilon_k-\omega)\right) & x \ge 0 \end{cases}$$

This formula for ξ_2 reuses things we must compute to obtain ξ_1, so we obtain it essentially "for free."

7.6 Putting It Together

We now summarize the results of the last ten pages or so of derivations and give a complete description of all the components necessary to determine the linear response density. To obtain n_1, we must solve the coupled system of inhomogeneous Fredholm integral equations of the second kind

$$\begin{aligned} n_1(x;\omega) &= \xi_1(x;\omega) + \xi_2(x;\omega) + \int_{-R_1}^{R_2} \chi_1(x,y;\omega)\Big[\tilde{\phi}_1(y;\omega) + f_{\mathrm{xc}}(y)n_1(y;\omega)\Big]\,dy \\ \tilde{\phi}_1(x;\omega) &= -\frac{2\pi\sigma(\omega)}{\lambda}e^{-\lambda|x|} + \int_{-R_1}^{R_2} e^{-\lambda|x-y|}\left[\frac{\lambda}{2}\tilde{\phi}_1(y;\omega) + \frac{2\pi}{\lambda}n_1(y;\omega)\right]dy \end{aligned} \tag{7.75}$$

where λ is freely chosen. (7.72) and (7.73) have been truncated to the finite domain $[-R_1, R_2]$. The driving function ξ_1 is

$$\xi_1(x;\omega) = -2\pi\big(1-\sigma(\omega)\big)\int_0^{k_F}\big(k_F^2-k^2\big)\psi_k(x)\big[\mathcal{B}^+(x,k;\omega)+\mathcal{S}^+(x,k;\omega)+\mathcal{B}^-(x,k;\omega)+\mathcal{S}^-(x,k;\omega)\big]\,dk$$

where $\mathcal{B}^+$ is given in (7.61); $\mathcal{B}^-$, in (7.62) for $k \geq \sqrt{2\omega}$ and (7.63) for $k < \sqrt{2\omega}$. $\mathcal{S}^+$ and $\mathcal{S}^-$ are given by (7.67) and (7.68), respectively. The helper functions $\mathcal{I}_1$ and $\mathcal{I}_2$ are written in (7.64) and (7.65), respectively. Finally, ξ_2 is listed above in (7.74), with its auxiliary function just beneath it.

The "correct" ϕ_1, of course, can be obtained from $\tilde{\phi}_1$ by reversing (7.70), but this is unnecessary. None of the potentials are terribly interesting, being little more than facilitators for obtaining the density.

Remark 7.6. As the Fourier transform of the time-dependent linear density, $n_1(x;\omega)$ is complex-valued except at zero-frequency. If $\hat{f}(\xi) \in \mathbb{R}$ for all ξ, then $f(x) = f^*(-x)$, which means that a real-valued f must be even. As $n_1(x,t) \equiv 0$ for $t < t_0$, it is certainly not even in t, so its Fourier transform must be complex.

Mathematically, the injection of complex numbers into an otherwise real system comes from two sources: the left and right boundary conditions of $G(x,y;\varepsilon_k+\omega)$. Because $\mu_k^+ \in \mathbb{R}$ for each k, $e^{ix\mu_k^+} \in \mathbb{C}$ and so $G(x,y;\varepsilon_k+\omega) \in \mathbb{C}$. On the right side, $(\nu_k^+)^2 = k^2 + 2\omega - 2\Delta V$, so for $k > \sqrt{2\Delta V - 2\omega}$, we have $\nu_k^- \in \mathbb{R}$. ∎

7.7 Numerical Implementation

7.7.1 The Nyström Method for Integral Equations

The goal of this section is to introduce a general method for solving Fredholm integral equations of the second kind called the Nyström method. The source of this presentation follows Atkinson [4, ch.4], although in slightly less generality. Let $f \in C[a,b]$ and suppose an N-point quadrature scheme of the form

$$\int_a^b f(x)\,dx \approx \sum_{q=1}^{N} w_q f(x_q) \tag{7.76}$$

is pre-defined. We assume that this scheme converges to the true value of the integral as $N \to \infty$ for every continuous f; it may come from Gaussian quadrature, as in Section 5.7.2, or a Newton-Cotes rule. Suppose $\mathcal{K}(x,y) \in C(\Omega)$ where $\Omega = [a,b] \times [a,b]$ and consider the integral equation for $x \in [a,b]$

$$\lambda u(x) = g(x) + \int_a^b \mathcal{K}(x,x')u(x')\,dx' \tag{7.77}$$

By applying the quadrature rule (7.76) to the integral of (7.77), we have an approximate solution $\tilde{u}$

$$\lambda \tilde{u}(x) = g(x) + \sum_{q=1}^{N} w_q \mathcal{K}(x,x_q)u(x_q)$$

Allowing x to be one of the x_q, we have

$$\lambda \tilde{u}(x_p) = g(x_p) + \sum_{q=1}^{N} w_q \mathcal{K}(x_p,x_q)u(x_q) \tag{7.78}$$

If p runs from 1 to N, the result is an $N \times N$ linear system of the form $A\tilde{\mathbf{u}} = \mathbf{g}$ with the system matrix

$$A \triangleq \lambda - \mathbf{KW} = \begin{pmatrix} \lambda - w_1\mathcal{K}(x_1,x_1) & -w_2\mathcal{K}(x_1,x_2) & \cdots & -w_N\mathcal{K}(x_1,x_N) \\ -w_1\mathcal{K}(x_2,x_1) & \lambda - w_2\mathcal{K}(x_2,x_2) & \cdots & -w_N\mathcal{K}(x_2,x_N) \\ \vdots & \vdots & \ddots & \vdots \\ -w_1\mathcal{K}(x_N,x_1) & -w_2\mathcal{K}(x_N,x_2) & \cdots & \lambda - w_N\mathcal{K}(x_N,x_N) \end{pmatrix} \tag{7.79}$$

where $\mathbf{K}$ is the matrix with elements $\mathbf{K}_{pq} = \mathcal{K}(x_p,x_q)$ and $\mathbf{W} = \operatorname{diag}\big(w_1,\ldots,w_N\big)$. The vectors $\tilde{\mathbf{u}}$ and $\mathbf{g}$ have entries $\tilde{\mathbf{u}}_p = \tilde{u}(x_p)$ and $\mathbf{g}_p = g(x_p)$.

Beyond its ease of implementation, the Nyström method has two benefits: first, its accuracy is the same as that of the underlying quadrature method. Second, it comes with a built in interpolation formula for

evaluation away from the quadrature points $x_1, \ldots, x_N$: if $\tilde{\mathbf{u}}$ is the numerical solution, then for any x

$$u(x) = \frac{1}{\lambda}\left[g(x) + \sum_{q=1}^{N} w_q \mathcal{K}(x, x_q)\tilde{\mathbf{u}}_q\right] \tag{7.80}$$

In practice, the above *Nyström interpolation formula* produces results superior to values from interpolation methods applied to the computed solution, such as splines.

7.7.2 Formulation with Simpson's Rule

Considering nothing but efficiency of the quadrature rule, the optimal choice for (7.76) would be a Gaussian rule. Unfortunately, the cusps in G, which in turn become cusps in χ_1 (see Figure 7.4), render it either impossible (if cusps are accommodated) or useless (if not) to formulate the Nyström method using Gaussian quadrature. Without special treatment of the cusps, the quadrature rule will not converge as $N \to \infty$.

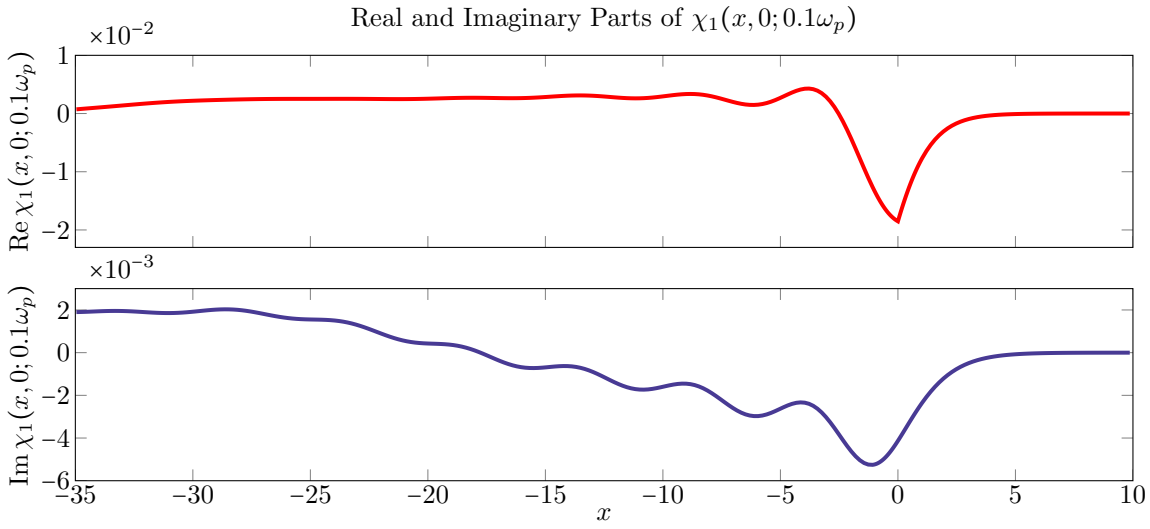

Figure 7.4: Linear Response Function $\chi_1(x, y; \omega)$. Plotted in this figure are the real (top) and imaginary (bottom) parts of $\chi_1(x, 0; 0.1\omega_p)$ for $r_s = 3$ ($\omega = 0.033$ a.u. or photons at 1367 nm). Note the cusp in the real part at $x = y = 0$; the imaginary part lacks this because δ affects only the real part of G.

Construction of the Nyström method begins by writing a N point composite Gauss rule for $[-R_1, R_2]$. Suppose these nodes are $\{x_q\}_{q=1}^{N}$. We generate the linear system determined by (7.79) by marching through the quadrature points, beginning at x_1. As described at the beginning of Section 7.4.2, to deal with the cusps at $y = x_1$, we must break the integrals of (7.75) into one over $[-R_1, x_1]$ and another over $[x_1, R_2]$. This necessitates writing two new quadrature rules: let $\{\zeta_q\}_{q=1}^{M}$ be the nodes for $[-R_1, x_1]$ and $\{\zeta_m\}_{q=M+1}^{N}$

for $[x_1, R_2]$, with weights w_q corresponding to ζ_q. Then the first equation for n_1 like (7.78) is

$$n_1(x_1) = \xi(x_1) + \sum_{q=1}^{N} w_q \chi_1(x_1, \zeta_q) \Big[\tilde{\phi}_1(\zeta_q) + V'_{\mathrm{xc}}(\zeta_q) n_1(\zeta_q) \Big]$$

Because of the nonlinear spacing of Gaussian points, we will have $\zeta_p \notin \{x_q\}_{q=1}^N$ for every p. Consequently, there are $N+1$ unknowns in the above equation. While using $N-1$ total ζ_m values momentarily fixes that issue, when we move to x_2 and write quadrature rules $\{\zeta'_q\}_{q=1}^M$ for $[-R_1, x_2]$ and $\{\zeta'_q\}_{m=M+1}^N$ for $[x_2, R_2]$, we will have $\zeta'_p \notin \{\zeta_q, x_q\}_{q=1}^N$, meaning we generate an entirely new set of unknowns. As a result, we cannot formulate a linear system using this approach to accommodating the cusps.

An alternative approach is to write rules for each interval $[x_q, x_{q+1}]$ so that the cusps in the integrand will always occur at endpoints. Because there are $N-1$ such intervals, to obtain N total unknowns for each of the N nodes x_q (for a square matrix A), we can only write one-point rules for each $[x_q, x_{q+1}]$, except for a single two-point rule to bring the total nodes to N. The one-point Gaussian rule coincides with the midpoint (rectangle) method, which offers only middling $\mathcal{O}(h^2)$ accuracy. As the primary benefit of Gaussian quadrature is its superb accuracy with respect to the number of points used, the large initial mesh being locked to one-point rules necessitates destroys any purpose for using Gaussian quadrature.

We instead consider a quadrature rule based on Simpson's rule. For N odd and $x_q = a + (q-1)h$ with $h = \frac{b-a}{N-1}$, the rule takes the form

$$\int_a^b f(x)\,dx \approx \frac{h}{3}\Bigg[f(x_1) + \sum_{\substack{q=2 \\ m \text{ even}}}^{N-1} 4f(x_q) + \sum_{\substack{q=3 \\ q \text{ odd}}}^{N-2} 2f(x_q) + f(x_{N+1}) \Bigg]$$

and is $\mathcal{O}(h^4)$ accurate, assuming $f \in C^4[a,b]$. Because this differentiability is lost only at $y = x$, at which point the integral is broken, we have the regularity necessary to guarantee this error estimate. Thus, in stark contrast to Gaussian quadrature, Simpson's rule cooperates with splitting at x.

Consider the abstract example (7.77). Let x_p be one of the Simpson nodes. Then we can write

$$\lambda u(x) = g(x) + \int_a^{x_p} \mathcal{K}(x, x') u(x')\,dx' + \int_{x_p}^b \mathcal{K}(x, x') u(x')\,dx'$$

First, suppose that p is odd with $p \geq 3$. Then the two subrules on $[a, x_p]$ and $[x_p, b]$ take the form

$$\int_a^{x_p} f(x)\,dx \approx \frac{h}{3}\Big[f(x_1) + 4f(x_2) + 2f(x_3) + \cdots + 4f(x_{p-1}) + f(x_p) \Big]$$

$$\int_{x_p}^{b} f(x)\,dx \approx \frac{h}{3}\Big[f(x_p) + 4f(x_{p+1}) + 2f(x_{p+2}) + \cdots + f(x_N)\Big]$$

when these result are combined, we get

$$\begin{aligned}\int_a^b f(x)\,dx &= \int_a^{x_p} f(x)\,dx + \int_{x_p}^b f(x)\,dx \\ &\approx \frac{h}{3}\Big[f(x_1) + \cdots + 4f(x_{p-1}) + 2f(x_p) + 4f(x_{p+1}) + \cdots + f(x_N)\Big]\end{aligned}$$

which is precisely the rule on the whole of $[a,b]$. This shows that the standard Simpson's rule automatically handles cusps that occur at odd numbered grid points inside the domain.

Next, suppose that p is even with $p \geq 4$. Simpson's rule requires an odd number of points (or even number of subintervals), and when p is even, there are an odd number of nodes each to the left and right of x_p. Assuming f is defined a bit beyond $[a,b]$, we instead write an approximation for the integral over $[a-h, b+h]$. Then $\{a-h, x_1, \ldots, x_p\}$ and $\{x_p, \ldots, x_N, b+h\}$ will both contain an odd number of elements and

$$\begin{aligned}\int_{a-h}^{x_k} f(x)\,dx &\approx \frac{h}{3}\Big[f(a-h) + 4f(x_1) + 2f(x_2) + \cdots + 4f(x_{p-1}) + f(x_k)\Big] \\ \int_{x_k}^{b+h} f(x')\,dx &\approx \frac{h}{3}\Big[f(x_p) + 4f(x_{p+1}) + 2f(x_{p+2}) + \cdots + 4f(x_N) + f(b+h)\Big]\end{aligned}$$

so that upon combination, we generate the rule on whole of $[a-h, b+h]$.

Naïvely gluing the even and odd cases together haphazardly would be unwise, as we would generate two different approximations to the same integral from splitting. If $f(a) = 0$ and $f(b) = 0$, then we define

$$\tilde{f}(x) \triangleq \begin{cases} f(x) & x \in [a,b] \\ 0 & x \notin [a,b] \end{cases}$$

so that

$$\int_a^b f(x)\,dx = \int_{a-2h}^b \tilde{f}(x)\,dx = \int_{a-h}^{b+h} \tilde{f}(x)\,dx$$

For splitting at the odd numbered points, we compute the integral after the first equals sign; for even numbered points, after the second equals sign. Assuming $\mathcal{K}(x,x')u(x')$ vanishes at the endpoints,

$$\begin{aligned} p \text{ even}: \quad \lambda u(x_p) &= g(x_p) + \frac{2h}{3}\sum_{q \text{ even}}^{N-1} \mathcal{K}(x_p,x_q)u(x_q) + \frac{4h}{3}\sum_{q \text{ odd}}^{N} \mathcal{K}(x_p,x_q)u(x_q) \\ p \text{ odd}: \quad \lambda u(x_p) &= g(x_p) + \frac{4h}{3}\sum_{q \text{ even}}^{N-1} \mathcal{K}(x_p,x_q)u(x_q) + \frac{2h}{3}\sum_{q \text{ odd}}^{N} \mathcal{K}(x_p,x_q)u(x_q) \end{aligned} \tag{7.81}$$

This modified scheme also handles the cases of $p = 1$ and $p = 2$, which were previously excluded. Note that the grid points should be taken so that $x_1 = a$ and $x_N = b$. The extended points outside $[a, b]$ are be numbered $x_{-2} = a - 2h$, $x_{-1} = a - h$, $x_{N+1} = b + h$. While $N + 2$ points were used to write each rule, only N of these contribute, so we may consider it an N point rule, since the spacing is still given by $h = \frac{b-a}{N-1}$.

As we saw in Figure 7.4, $\chi_1(-R_1, y; \omega) \approx 0$ and $\chi_1(x, y; \omega) \to 0$ exponentially for $x \gg 0$. $\tilde{\phi}_1 \to 0$ as $x \to -\infty$ and approaches a constant for $x \gg 0$. The kernel $e^{-\lambda|x-y|}$ clearly decays, so the only potential trouble spot is $f_{\text{xc}}(y)n_1(y; \omega)$. As n_1 and n_0 display similar decay properties as $x \to +\infty$, an invocation of Theorem 3.5, combined with the boundedness f_{xc} of $x \to -\infty$ and the decay of n_1 inside the metal let us conclude that both integrands of (7.75) vanish in y at $-R_1$ and R_2. Accordingly, (7.81) is applicable to (7.75).

Let $\{x_q\}_{q=1}^N$ uniformly spaced nodes on $[-R_1, R_2]$ such that $x_q = 0$ for some q. We need 0 to be a node because we require $\mathcal{I}_1(0; \varepsilon_k \pm \omega)$ to compute ξ_2 and it is much more efficient to include it as a node. Application of the scheme (7.81) to the system (7.75) yields the linear system

$$\begin{pmatrix} 1 - (\boldsymbol{\chi} \cdot \mathbf{W})\mathbf{F}_{\text{xc}} & -\boldsymbol{\chi} \cdot \mathbf{W} \\ -\frac{2\pi}{\lambda}\boldsymbol{\Lambda} \cdot \mathbf{W} & 1 - \frac{\lambda}{2}\boldsymbol{\Lambda} \cdot \mathbf{W} \end{pmatrix} \begin{pmatrix} \mathbf{n} \\ \tilde{\boldsymbol{\phi}} \end{pmatrix} = \begin{pmatrix} \boldsymbol{\xi} \\ \boldsymbol{\lambda} \end{pmatrix}$$

where $\mathbf{n}, \tilde{\boldsymbol{\phi}}, \boldsymbol{\xi}$, and $\boldsymbol{\lambda}$ are $N \times 1$ vectors with entries

$$\mathbf{n}_p = n_1(x_p; \omega) \qquad \boldsymbol{\xi}_p = \xi_1(x_p; \omega) + \xi_2(x_p; \omega)$$
$$\tilde{\boldsymbol{\phi}}_p = \tilde{\phi}_1(x_p; \omega) \qquad \boldsymbol{\lambda}_p = -\frac{2\pi\sigma(\omega)}{\lambda} e^{-\lambda|x_p|}$$

and $\boldsymbol{\chi}$, $\boldsymbol{\Lambda}$, and $\mathbf{W}$ are $N \times N$ matrices with entries

$$\boldsymbol{\chi}_{pq} = \chi_1(x_p, x_q; \omega) \qquad \mathbf{W}_{pq} = \begin{cases} \frac{2h}{3} & \text{if } p - q \text{ is even} \\ \frac{4h}{3} & \text{if } p - q \text{ is odd} \end{cases}$$
$$\boldsymbol{\Lambda}_{pq} = e^{-\lambda|x_p - x_q|}$$

Finally, $\mathbf{F}_{\text{xc}} = \text{diag}\big(f_{\text{xc}}(x_1), \ldots, f_{\text{xc}}(x_N)\big)$. The dot between matrices indicates *elementwise* multiplication (i.e., $C = A \cdot B$ has entries $C_{pq} = A_{pq}B_{pq}$).

7.7.3 Computing $G(x, y; \varepsilon_k + \omega)$ and $G(x, y; \varepsilon_k - \omega)$

The procedure for computing G is the same for both $\varepsilon_k + \omega$ and $\varepsilon_k - \omega$, just with different parameters. The basis functions φ_1 and φ_2 are found by applying Algorithm 2.3 to the following problems:

$$\left(-\frac{1}{2}\frac{\partial^2}{\partial x^2} + V(x) - \varepsilon_k \mp \omega\right)\varphi_1(x;\varepsilon_k \pm \omega) = 0 \qquad \left(-\frac{1}{2}\frac{\partial^2}{\partial x^2} + V(x) - \varepsilon_k \mp \omega\right)\varphi_2(x;\varepsilon_k \pm \omega) = 0$$

$$\varphi_1 \sim e^{i\nu_k^{\pm}x} \text{ as } x \to +\infty \qquad \varphi_2 \sim e^{-i\mu_k^{\pm}x} \text{ as } x \to -\infty$$

where, as has been lurking in the background of this chapter all along,

$$\mu_k^{\pm} = \sqrt{k^2 \pm 2\omega}$$
$$\nu_k^{\pm} = \sqrt{k^2 \pm 2\omega - 2\Delta V}$$

The infinite asymptotic conditions are imposed as starting values per Algorithm 2.2:

$$\varphi_1(x_{N-1};\varepsilon_k \pm \omega) = e^{i\nu_k^{\pm}x_{N-1}} \qquad \varphi_2(x_1;\varepsilon_k \pm \omega) = e^{i\mu_k^{\pm}x_1}$$
$$\varphi_1(x_N;\varepsilon_k \pm \omega) = e^{i\nu_k^{\pm}x_N} \qquad \varphi_2(x_2;\varepsilon_k \pm \omega) = e^{i\mu_k^{\pm}x_2}$$

7.7.4 Computing $\mathcal{I}_1(x;\varepsilon_k \pm \omega)$ and $\mathcal{I}_2(x;\varepsilon_k \pm \omega)$

Aside from the different basis functions in the integrand, $\mathcal{I}_1$ and $\mathcal{I}_2$ of (7.64) and (7.65) can be computed in an identical manner. Further, it makes no procedural difference whether we are calculating for $\varepsilon_k + \omega$ or $\varepsilon_k - \omega$, as there's no switching, changing realities, or other potential trouble spots that must be sidestepped.

Since all integrands are well-behaved and the spline method that computes ψ_k, φ_1, and φ_2 gives solutions that are known on all of $[-R_1, R_2]$, Gaussian quadrature may be used to perform the integrations. "Exact" integration, or multiplying out the spline representations and then integrating each polynomial analytically, is also an option. However, because ψ_k and φ_m are defined on different grids and the meshes for φ_m can be quite large, the multiplication will be quite slow (see Appendix C for details on spline multiplication). The gain in accuracy is marginal at best and cannot justify the protracted computational cost.

The Gauss rule of choice is the seven-point composite rule previously used in forming n_0 in Section 5.7.2. We chop up the domain of integration $[x, R_2]$ into d divisions, where $d = \left\lceil \frac{R_2 - x}{2} \right\rceil$, giving seven points per two units of space. While we have no alternative but to march through each x in the mesh for $[-R_1, R_2]$, at least we ensure that each step will be computed swiftly and accurately.

7.8 Computational Results

Finally, we present the culmination of all the hard work of this chapter by showing example numerical computations for the linear response density at a variety of input frequencies. For easier cross-comparison across different materials, it is natural to represent frequencies as fractions of ω_p, since atomic frequency units are rather enigmatic. Table 7.2 below lists equivalent wavelengths for photons.

r_s	$0.05\omega_p$	$0.1\omega_p$	$0.2\omega_p$	$0.3\omega_p$	$0.4\omega_p$	1064 nm	Example Material
2.0	1488	744	372	248	186	$0.0699\omega_p$	Platinum (1.99)
2.5	2080	1040	520	347	260	$0.0977\omega_p$	Cadmium (2.59)
3.0	2734	1367	683	456	342	$0.1285\omega_p$	Gold (3.01)
3.5	3445	1722	861	574	431	$0.1619\omega_p$	Strontium (3.56)
4.0	4209	2104	1052	701	526	$0.1978\omega_p$	Sodium (3.93)

Table 7.2: SI Wavelengths and Frequencies in Atomic Units. The energy of a photon in eV is $E(\text{eV}) = \frac{1239.841876 \text{ eV-nm}}{\lambda \text{ (nm)}}$. One a.u. of angular frequency is 27.211396 eV, so a photon with frequency ω a.u. has wavelength $\lambda = 45.563332\omega^{-1}$ nm. The fourth column gives the frequency that corresponds exactly to 1064 nm. The color of text indicates the color of light: infrared, red, green, blue, violet, and ultraviolet.

A case of particular interest is $\omega = 0.0428$ a.u., which is the frequency of photons at 1064 nm. This is most common variant of the venerable Nd:YAG laser, which has been one of the most widely available and commonly employed solid-state lasers since its invention at Bell Labs [41]. The fractions of the plasma frequency corresponding to this important wavelength are contained in the fourth column of Table 7.2.

The sample computations are all for $r_s = 3$. As seen in the table, the first four tenths of ω_p for this r_s value correspond to four different colors of light. This is more novelty than demonstrative, however; a stronger motivator for choosing this r_s value is that it closely approximates gold, always a material of interest.

For the sample computations presented in this section, an adaptive tolerance of $\tau_a = 5 \times 10^{-7}$ was selected for the spline methods used to compute the basis functions φ_1 and φ_2. This is slightly less than what was used for the ψ_k of the ground state, but as seen in Table 7.3, the number of splines required to reach even this tolerance is significantly higher. For all computations, a mesh of 901 points was used on the domain $[-35, 10]$, giving spacing $h = 0.05$ and including the origin as a mesh point as required.

Figure 7.5 below depicts the first example: $\omega = 0.1285\omega_p$, which corresponds to 1064 nm for $r_s = 3$.

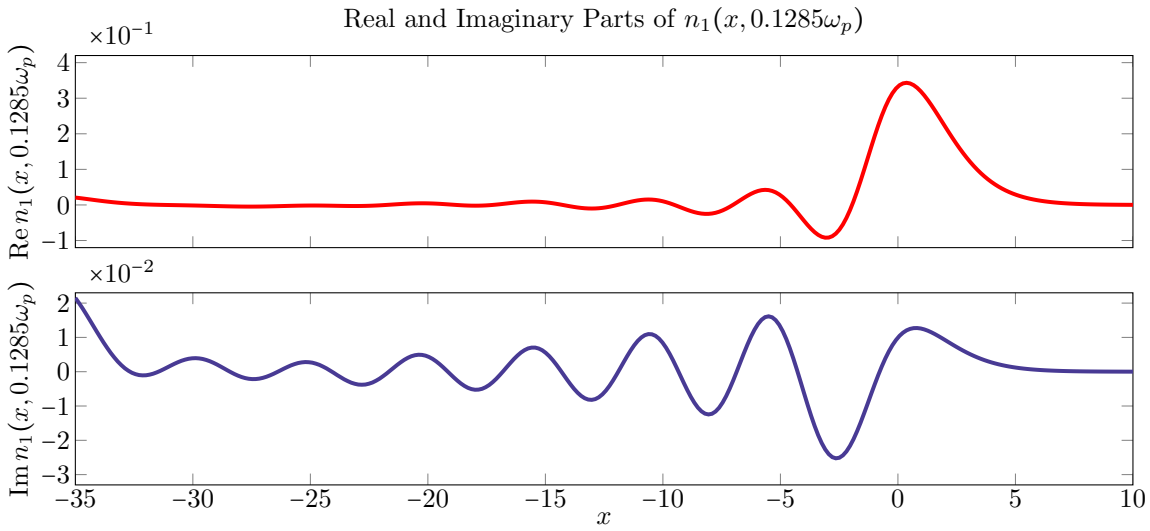

Figure 7.5: Linear Response for 1064 nm Incident Photons. This figure depicts the linear response density $n_1(x;\omega)$ for $r_s = 3$ and $\omega = 0.0482 = 0.1285\omega_p$, which corresponds to photons of wavelength 1064 nm.

The profile is quite different from what we see in the ground state. There is a large peak in the real part at approximately $x = 0.25$; this indicates that the maximum linear response occurs just *outside* the metal. The order of magnitude of the imaginary part is one less than the real part. Even this near the end of the IR spectrum (which ends around 700-750 nm), the real part is the primary contributor to the response.

A small amount of corruption in the solution can be see at the very left endpoint; it is more pronounced in the imaginary part than the real part. The lengthy discussion about accommodating the cusps in the space variable of χ_1 technically applies to the integral in k as well. Per Section 7.4.1, a fully proper treatment would involve splitting the integral in k at 2ω instead of plowing right through this singularity. To ensure consistency, the ψ_k constructing χ_1 must also construct n_0, so we cannot use different sets of k values. Consequently, we would have to customize the ground state computation for each ω. As the corruption is minor and confined near an arbitrarily chosen endpoint, repair is not worth doubling the computation time.

The results of runs for $\omega = 0.05$, 0.1, 0.2, 0.3, and $0.4\omega_p$ are shown on the composite figure on the next page. The real part of the response densities varies little in shape or magnitude until $0.4\omega_p$. The imaginary part increases steadily in magnitude with ω, finally becoming an equal contributor in the ultraviolet regime. In the infrared and visible regions of the spectrum, the response profile is dominated by the real part.

Physically, the induced dipole moment (first moment) of the imaginary part of n_1,

$$\alpha(\omega) = \int_{\mathbb{R}^d} x_d n_1(\mathbf{x};\omega)\, d\mathbf{x}$$

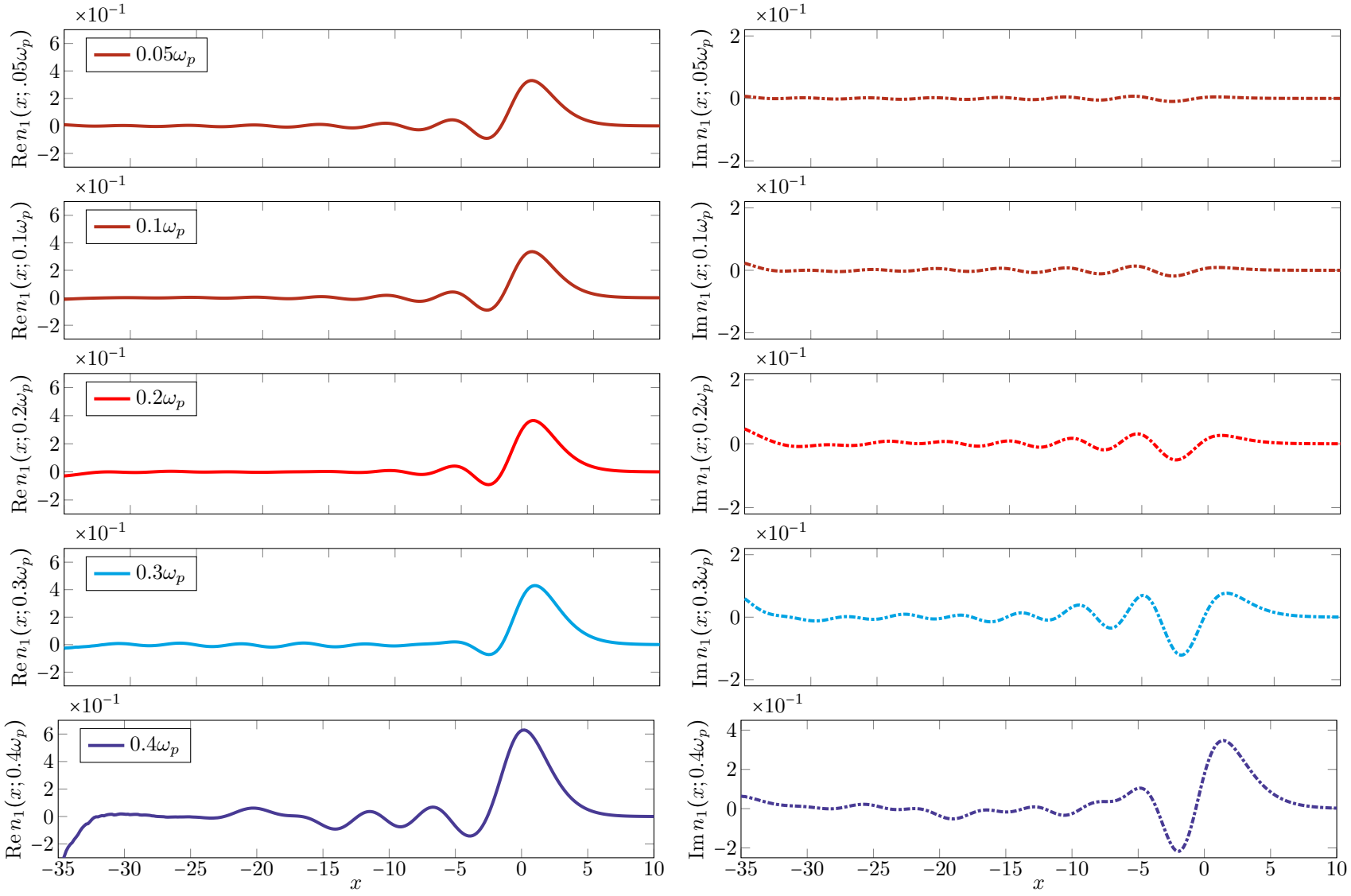

Figure 7.6: Linear Response at Various Frequencies, $r_s = 3$. The linear response densities are shown above for $0.05\omega_p$, $0.1\omega_p$, $0.2\omega_p$, $0.3\omega_p$, $0.4\omega_p$. The color of the plot indicates the corresponding photon wavelength, which are 1823 nm, 1367 nm, 683 nm, 456 nm, and 342 nm, respectively. Real parts are on the left in solid lines; imaginary parts, the right in broken lines. Note the different scale in y on the imaginary plot of $0.4\omega_p$.

gives the excitation spectrum [116]; in one-dimension, it is proportional to $d_\perp(\omega)$. The imaginary part of $\alpha(\omega)$ then gives the absorption, which is of course expected to be weaker at low frequencies.

An especially interesting comparison to make is among low-frequency responses and difference of screened and ground state densities $n_\varsigma - n_0$ from way back in Figure 5.12. The comparison is made in Figure 7.7.

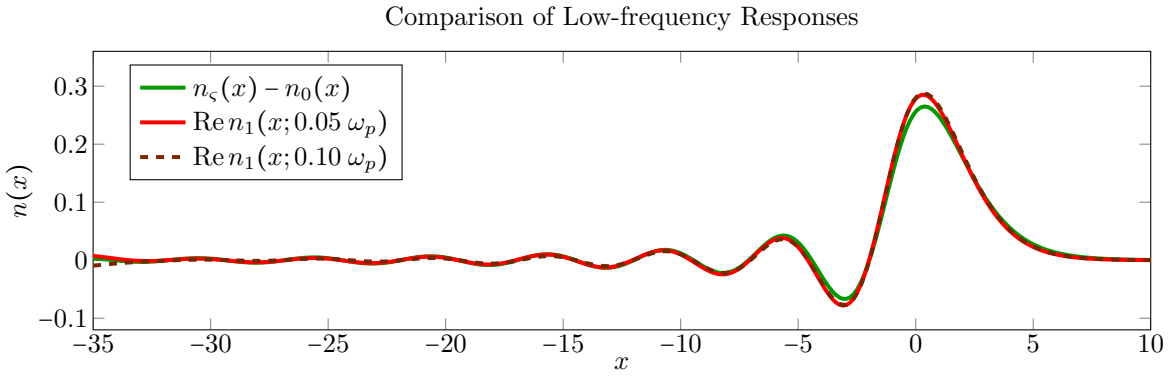

Figure 7.7: Comparison of Low-frequency Responses. To facilitate comparison, all quantities have been normalized to integrate to one. As in Figure 7.7, $\varsigma = 5 \times 10^{-4}$.

There are two striking observations to make in the above figure. First, there is very little difference in the responses at $0.05\omega_p$ and $0.10\omega_p$; further analysis puts their absolute difference on the order of 10^{-3}, which is also what it is between $0.10\omega_p$ and $0.1285\omega_p$. Second, the linear response at low-frequencies is remarkably similar to the difference $n_\varsigma - n_0$, except for the slightly smaller magnitude and slight offset in phase.

The more appropriate comparison for the low-frequency response is $n_\varsigma - n_{-\varsigma}$, normalized to integrate to one, and $\mathrm{Re}\, \frac{n_1(x;\omega)}{\sigma(\omega)}$, which also integrates to one per (7.46). Figure 7.8 below displays the striking outcome.

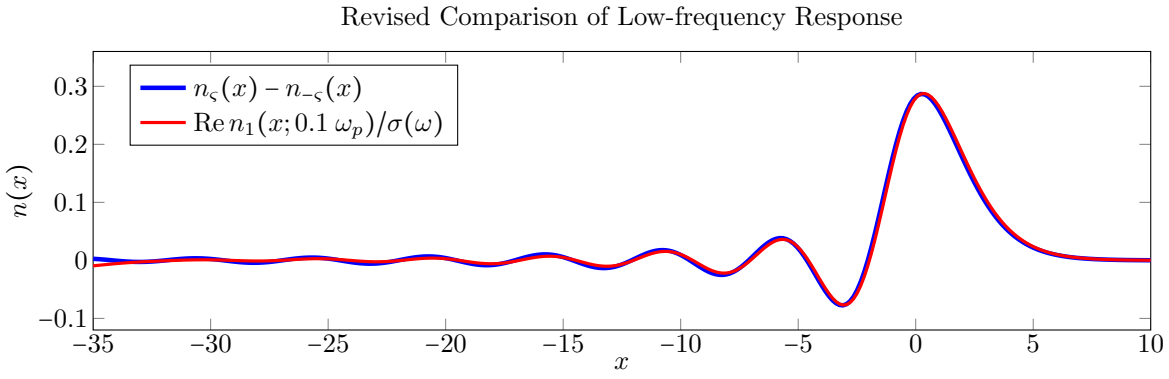

Figure 7.8: Comparison of Low-frequency Responses, Part II. All quantities have been normalized to have integral one. This figure justifies future claims of adiabacity we will make later.

Because $n_1(x; 0.05\omega_p)$ is nearly identical, Figure 7.8 shows only $n_1(x; 0.1\omega_p)$ for the sake of clarity. We see that $n_\varsigma - n_{-\varsigma}$ agrees with $n_1(x; 0.1\omega_p)$ magnificently, placing the peak in the correct location just beyond the surface and nearly matching in phase. Figure 7.8 will justify an adiabatic assumption in the next chapter.

The presentation of results concludes by once more highlighting the hard work of the adaptive spline method. Table 7.3 shows the number of splines required to compute φ_1 and φ_2 for both $\varepsilon_k + \omega$ and $\varepsilon_k - \omega$ for each frequency shown in a figure this section. The table shows that $\varphi_2(\cdot; \varepsilon_k + \omega)$ is always the hard one to compute, while $\varphi_2(\cdot; \varepsilon_k - \omega)$ dramatically increases in difficulty with ω, although only for low k. The large number of splines required can be attributed to exponentially growing behavior at one of the endpoints; for high k, the growth factor is smaller, so accurate solutions are easier to compute.

	k	$G(x,y;\varepsilon_k+\omega)$ φ_1	φ_2	$G(x,y;\varepsilon_k-\omega)$ φ_1	φ_2	$G(x,y;\varepsilon_k+\omega)$ φ_1	φ_2	$G(x,y;\varepsilon_k-\omega)$ φ_1	φ_2	
$0.05\omega_p$	0.0475	64579	2594	106681	6940	48139	3670	153143	239248	$0.20\omega_p$
	0.2723	52511	3604	62161	2602	38515	3636	121969	21176	
	0.5273	24949	5644	30069	4490	16037	5726	46637	3694	
$0.10\omega_p$	0.0475	57859	3214	124561	26866	39613	3664	225625	1101174	$0.30\omega_p$
	0.2723	47279	3688	76957	2562	27683	5104	151123	204336	
	0.5273	22065	5912	37691	3650	14219	5850	56651	3304	
$0.13\omega_p$	0.0475	55333	3436	133433	51242	28035	5028	294575	1602716	$0.40\omega_p$
	0.2723	44057	3732	93543	3008	22417	5900	219727	936386	
	0.5273	20217	5944	41621	3706	23267	6252	75275	2562	

Table 7.3: Adaptive Splines in Action, Part II. For $r_s = 3$ ($k_F = 0.6397$), this table shows the number of splines required to compute φ_1 and φ_2 for both $\varepsilon_k + \omega$ and $\varepsilon_k - \omega$ for various $f\omega$ with adaptive tolerance $\tau_a = 5 \times 10^{-7}$. The value of k extends across the thick center line.

Frequency	Computation Time	Frequency	Computation Time
$0.05\omega_p$	10 min, 36 sec	$0.20\omega_p$	16 min, 11 sec
$0.10\omega_p$	11 min, 14 sec	$0.30\omega_p$	36 min, 26 sec
$0.13\omega_p$	11 min, 47 sec	$0.40\omega_p$	52 min, 31 sec

Table 7.4: Computation Time for Linear Response. This table shows the time required to compute n_1. An adaptive tolerance of $\tau_a = 5 \times 10^{-7}$ was used. Time required to compute n_0 is not included.

Finally, Table 7.4 depicts the total computation time for determining the linear response density from start to finish. The workstation is the same as used for the ground state (a Core i7 at 3464 MHz with 16GB of

RAM). Table 7.3 indicated that an exceptional number of splines are required to reach the adaptive tolerance for certain ω; consequently, most of the CPU time is devoted to $G(x, y; \varepsilon_k + \omega)$ and $G(x, y; \varepsilon_k - \omega)$.

7.9 Conclusion

As attested to by the bevy of citations throughout this chapter, this thesis is certainly not the first to tackle linear response calculations for jellium surfaces. However, it contains a number of notable improvements in compution that make the contributions of this work significant.

Sections 7.1 and 7.2 contain a rigorous and complete derivation of linear response theory and the linear response function from first principles, a presentation with scope the author was unable to locate in any single publication. While the resultant formulas and hints of their origin are readily available in virtually every source discussing the concepts, the mathematically inclined will appreciate the effort made here.

In terms of analytic calculations, Section 7.4 presented a streamlined computation based on Fourier transforms that renders the cumbersome methods of Feibelman [29, 30] wholly obsolete. Authors such as Liebsch [67, p.170] have indicated the necessity of analytic-based contributions from inside the bulk metal, but none has provided a shred of the specifics of the execution aside from Feibelman.

Finally, the modifications of (7.58) and (7.59) of Section (7.5) that enable direct solution of the integral equations via (7.75) are a very welcome upgrade to the established iterative methods of Liebsch [65, 66, 67]. Continued use of the adaptive spline method to compute $G(x, y; \varepsilon_k \pm \omega)$ allows for seamless vertical integration with the ground state computations, as the grid for each G can be chosen independently.

Chapter 8

Second Harmonic Generation

Second Harmonic Generation (SHG), in which a material converts electromagnetic radiation at frequency ω to that at 2ω—for example, red light becomes green or green light becomes blue-violet—is the simplest yet perhaps most studied nonlinear optical phenomenon. The humbling story of its discovery is every bit as interesting as the numerous applications [47, 50, 82] SHG has found throughout the years.

In the early 1960s at the University of Michigan in Ann Arbor, Robert Terhune bet his colleague Peter Franken a nickel—the standard wager in physics at the time—that he could not generate optical harmonics. A favorite story among the co-discoverers [51], Franken never collected the monetary spoils from his victory, which Terhune did pay in the form of check never cashed, and was content to settle for the satisfaction of revolutionizing the world by birthing the field of nonlinear optics.

For the disarray he was willing to unleash upon Terhune's checkbook, Franken would not go without impunity. When the results of the celebrated experiment were first published in *Physical Review Letters* [37], the editor mistakingly erased the photographic evidence that proved their discovery, reproduced below.

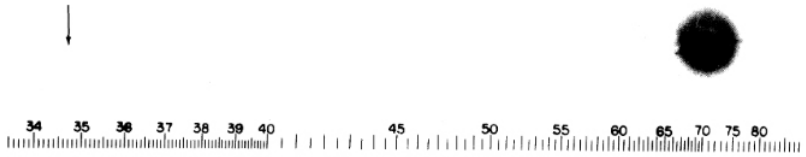

FIG. 1. A direct reproduction of the first plate in which there was an indication of second harmonic. The wavelength scale is in units of 100 A. The arrow at 3472 A indicates the small but dense image produced by the second harmonic. The image of the primary beam at 6943 A is very large due to halation.

Figure 8.1: "Demonstration" of SHG. Where the arrow points should be a small dot indicating the second harmonic. Its conspicuous absence is due to the editor's misguided assumption that the mark was blemish. Reproduced with express permission from the American Physical Society and Gabriel Weinreich.

8.1 The Mathematics of Second Harmonic Generation

Mathematically, SHG is modeled by the time-harmonic[†] Maxwell's equations in Gaussian units

$$\nabla \times \mathbf{E}(\mathbf{x},\omega') = -\frac{i\omega'}{c}\mathbf{B}(\mathbf{x},\omega') \qquad \nabla \times \mathbf{H}(\mathbf{x},\omega') = \frac{i\omega'}{c}\mathbf{D}(\mathbf{x},\omega')$$

where $\mathbf{E}$ is the electric field, $\mathbf{H}$ and $\mathbf{B}$ are the magnetic field and induction (respectively), and $\mathbf{D}$ is electric displacement; the frequency ω' is taken to be either ω or 2ω depending on whether the fundamental or second harmonic is of interest. For nonmagnetic materials, we have $\mathbf{B} = \mathbf{H}$. The nonlinearity necessary to describe nonlinear optical phenomena is contained in the constitutive relation for $\mathbf{D}$

$$\mathbf{D}(\mathbf{x},\omega') = \varepsilon(\omega')\mathbf{E}(\mathbf{x},\omega') + 4\pi\mathbf{P}^{\mathrm{NL}}(\mathbf{x},\omega')$$

$\mathbf{P}^{\mathrm{NL}}$ is the nonlinear polarization and has form highly dependent on the material under consideration.

Franken's first demonstration of SHG was in quartz, a dielectric material. The mathematical formulation for such materials is well-established [8, 98] and takes the polarization as a power series in the electric field,

$$\mathbf{P}^{\mathrm{NL}}(\mathbf{x},\omega') = \chi^{(2)}(\omega') : \mathbf{EE} + \chi^{(3)}(\omega') : \mathbf{EEE} + \cdots$$

The optical susceptibilities $\chi^{(k)}$ are $k+1$-rank tensors and are **not** to be confused with the response functions of TD-DFT, which are denoted with subscripts. As a rank-3 tensor, $\chi^{(2)}$ has twenty-seven components, many of which zero out with the crystal's symmetry structure. For centrosymmetric materials, $\chi^{(2)} \equiv 0$. As a second-order process, SHG is governed by $\chi^{(2)}$ and is theoretically impossible in centrosymmetric crystals.

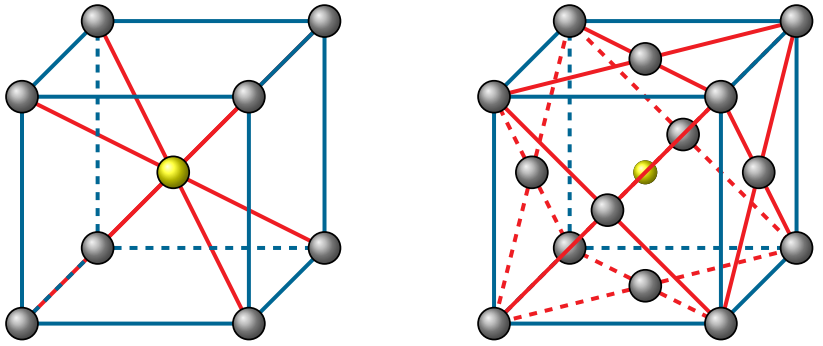

(a) **(b)**

Metal	Lattice
Chromium	bcc
Copper	fcc
Gold	fcc
Iron	bcc
Platinum	fcc
Silver	fcc

Figure 8.2: Examples of Metal Crystal Structure. Two common metal crystal lattice structures are shown here. **(a)** is a body-centered cubic (bcc) lattice and **(b)** shows a face-centered cubic (fcc) as Bravais lattice. In both cases, the middle of the cube (in yellow) is the point of inversion symmetry; in bcc, this point is a node in the lattice. The table on the very right indicates metals that have these structures.

[†]A time-harmonic quantity is of the form $\mathbf{A}(\mathbf{x},t) = \frac{1}{2}\mathrm{Re}\left(\mathbf{A}(\mathbf{x})e^{i\omega t}\right)$.

Of the thirty-two crystal classes, eleven of them display inversion symmetry, so SHG is not possible in every nonlinear optical material, although third-order effects are. All metals possess crystal classes among these, of which two examples and list of metals possessing them are displayed in Figure 8.2 on the previous page. Consequently, $\chi^{(2)}$ vanishes in metals, so SHG should not be possible. Despite this, Bloembergen *et al.* [6] experimentally demonstrated SHG in metals as a reflected wave. Figure 8.3 depicts the difference in process.

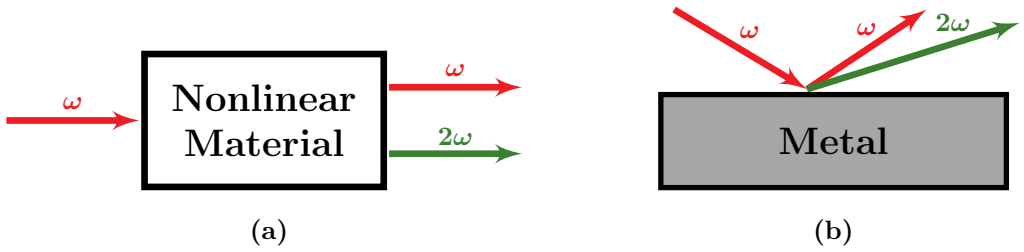

Figure 8.3: SHG in Dielectrics vs. Metals. (a) SHG in dielectrics: the dominant second-harmonic wave is a transmitted wave. **(b)** SHG in metals: it is a reflected wave because of attenuation.

The deficiency in describing SHG in centrosymmetrc materials is not an inherent limitation of the power series expansion. Rather, the polarization is taken in the electric dipole approximation, which ignores the much weaker contributions from electric quadrupoles and magnetic effects, and these dipole moments vanish in centrosymmetric materials. More properly, the nonlinear polarization should be [9, p.28]

$$\Pi^{\mathrm{NL}}(\mathbf{x},\omega') = \underbrace{\chi^{(2)}(\omega') : \mathbf{EE}}_{\mathbf{P}^{(2)}} - \nabla \cdot \Big[\underbrace{\chi_Q^{(2)}(\omega') : \mathbf{EE}}_{\mathbf{Q}^{(2)}}\Big] + \frac{\mu_0}{i\omega'} \nabla \times \Big[\underbrace{\chi_M^{(2)}(\omega') : \mathbf{EE}}_{\mathbf{M}^{(2)}}\Big] + \cdots$$

where $\chi_Q^{(2)}$ denotes the (electric) quadrupole susceptibility and $\chi_M^{(2)}$ denotes the magnetic dipole susceptibility. The unwieldiness of the above form and the difficulty of experimentally determining the additional susceptibilities means that different modeling techniques are needed for centrosymmetric materials.

8.1.1 The Classical Model

In seeking a revised theory that theoretically describe their experimental finding of SHG in metals, Bloembergen *et al.* considered the Drude-Sommerfeld free-electron model for metals and began with the classical hydrodynamic equation

$$\frac{\partial \mathbf{v}}{\partial t} + \big(\mathbf{v} \cdot \nabla\big)\mathbf{v} = -\frac{e}{m}\left(\mathbf{E} + \frac{1}{c}\mathbf{v} \times \mathbf{H}\right) \tag{8.1}$$

where e and m are the the electron charge and mass[†], respectively, and $\mathbf{v}$ is the average electron velocity. By expanding each quantity in powers of $e^{i\omega t}$, they obtained at the fundamental frequency

$$\mathbf{P}^{\mathrm{NL}}(\omega) = 0$$

and a complicated nonlinear polarization at the second harmonic

$$\mathbf{P}^{\mathrm{NL}}(2\omega) = \frac{\bar{n}e^3}{4m^2\omega^4}\big(\mathbf{E}(\omega)\cdot\nabla\big)\mathbf{E}(\omega) + \frac{e}{8\pi m\omega^2}\mathbf{E}(\omega)\big(\nabla\cdot\mathbf{E}(\omega)\big) + \frac{ie^3\bar{n}}{4m^2c\omega^3}\mathbf{E}(\omega)\times\mathbf{H}(\omega) \tag{8.2}$$

Applying the vector identity

$$\mathbf{E}\times\big(\nabla\times\mathbf{E}\big) = \frac{1}{2}\nabla\big(\mathbf{E}\cdot\mathbf{E}\big) - \big(\mathbf{E}\cdot\nabla\big)\mathbf{E}$$

in conjunction with the Faraday's law $-\dfrac{c}{i\omega}\nabla\times\mathbf{E}(\omega) = \mathbf{B}(\omega) = \mathbf{H}(\omega)$, (8.2) is more commonly written

$$\mathbf{P}^{\mathrm{NL}}(2\omega) = \frac{\bar{n}e^3}{2m^2\omega^4}\big(\mathbf{E}(\omega)\cdot\nabla\big)\mathbf{E}(\omega) + \frac{e}{8\pi m\omega^2}\mathbf{E}(\omega)\big(\nabla\cdot\mathbf{E}(\omega)\big) - \frac{e^3\bar{n}}{8m^2\omega^4}\nabla\big(\mathbf{E}(\omega)\cdot\mathbf{E}(\omega)\big)$$

While also appearing in Shen [98], Brevet [9, Ch.9] has a thorough presentation of the derivation of (8.2).

Bloembergen *et al.* argued that second harmonic waves originated from electric quadrupoles in the bulk and drown out the surface contributions in highly reflective media. A year later, Brown and Matsuoka [10] observed that "atomically clean silver surfaces generate approximately four times as much harmonic light as those subjected to adsorption" [10], indicating that domination of quadrupoles was not entirely correct.

Rudnick and Stern [93] examined the nature of second harmonic generation at metal surfaces and found that the response is composed of three currents: one from the bulk, one parallel to the surface, and one normal to the surface. The third of these had been incorrect in the established theory. The bulk current is expressed in the third term of (8.2) and contributes only because of the surface. The neglected quadrupoles had been pegged as the suspect for nearly ten years [104], so it was a remarkable flash of insight to argue that SHG is intrinsically due to the break in symmetry at the surface and not just predictive failure of previous models.

The hydrodynamic approach to SHG at metal surfaces has been improved a number of times since Rudnick and Stern's observations. To incorporate the surface effects lacking from Bloembergen's model, Sipe *et al.* [101] included a quantum pressure term $-\nabla p$ to the right-hand side of (8.1); Corvi and Schaich [19] further added an Ohmic damping term $-\frac{1}{\tau}\mathbf{v}$. Because of its simplicity and high level of customization, polarizations developed from hydrodynamic models are still regularly employed in studies today [16, 95].

[†]In order to present the original results verbatim, this subsection (and this subsection only) does not use atomic units

8.2 The Case for Density Functional Theory

Acknowledged in a multitude of sources [44, 93, 101], the hydrodynamic approach is a rather unrealistic approximation to electron dynamics at the metal surface. Its biggest flaw is that it must assume that the electron density is constant up to the surface (much like the background charge in jellium); of course, the profile should vary continuously as we've seen in DFT computations. While the hydrodynamic picture could be improved by incorporating the actual electron density, it would still remain a semi-classical model. If electron density is to be used, it is better to formulate a fully quantum mechanical approach.

The polarization $\mathbf{P}$ is related to the total current $\mathbf{J}$ by

$$\mathbf{J} = \mathbf{J}_f + \nabla \times \mathbf{M} + \frac{\partial \mathbf{P}}{\partial t}$$

where $\mathbf{J}_f$ is the free current injected into the system by external sources and $\mathbf{M}$ is the magnetization current density, a measure of the strength of magnetic dipoles. In non-magnetic materials, $\mathbf{M} = 0$, a fact implicitly assumed in writing the constitutive relation $\mathbf{B} = \mathbf{H}$, which is otherwise $\mathbf{B} = \mathbf{H} + 4\pi\mathbf{M}$. In nonmagnetic materials in the absence of free current, polarization is just the time-integral of the current.

Continuity of charge relates the current to the total charge $\rho(\mathbf{x}, t)$ via

$$\nabla \cdot \mathbf{J}(\mathbf{x}, t) + \frac{\partial \rho}{\partial t}(\mathbf{x}, t) = 0 \tag{8.3}$$

Using that $\mathbf{J} = \frac{\partial \mathbf{P}}{\partial t}$ and that in Fourier space, differentiation in t is equivalent to multiplication by $i\omega$, we can eliminate the current and have the relation

$$\nabla \cdot \mathbf{P}(\mathbf{x}, \omega') + \rho(\mathbf{x}, \omega') = 0$$

The total charge is easily given in terms of the electron density as $\rho(\mathbf{x}, t) = en(\mathbf{x}, t) = n(\mathbf{x}, t)$ so that if we can obtain the density in Fourier space, we can obtain the polarization via

$$\nabla \cdot \mathbf{P}(\mathbf{x}, \omega') = -n(\mathbf{x}, \omega')$$

Per previous discussion, in the case of second harmonic generation, we dub the part of the polarization at ω the "linear polarization" and the portion at 2ω the "nonlinear polarization" so that

$$\mathbf{P}^{\mathrm{NL}}(\omega) = 0$$
$$\nabla \cdot \mathbf{P}^{\mathrm{NL}}(2\omega) = -n(\mathbf{x}, 2\omega)$$

Once we have $\mathbf{P}^{\mathrm{NL}}(2\omega)$, we can solve a linear Maxwell equation with source term to obtain the field $\mathbf{E}(2\omega)$.

8.2.1 The Complete TD-DFT Approach

In the derivation of the TD-DFT linear response of Section 7.3, we saw that $n_1(x;\omega)$ contains all of the ω frequency content of $n(x,\omega')$, which is why we denoted it $n_1(x;\omega)$. Consequently, we cannot hope to extract the frequency information of $n(\mathbf{x},\omega')$ at 2ω from linear response theory alone.

The linear response density n_1 is the first term in the functional Taylor series (7.3). The second is given by

$$n_2(\mathbf{x},\omega) = \int_{\mathbb{R}^d} V_1(\mathbf{x}',\omega) \int_{\mathbb{R}^d} \Upsilon(\mathbf{x},\mathbf{x}',\mathbf{x}'',\omega,\omega) V_1(\mathbf{x}'',\omega)\, d\mathbf{x}''\, d\mathbf{x}' \tag{8.4}$$
$$\Upsilon(\mathbf{x},\mathbf{x}',\mathbf{x}'',\omega,\omega) \triangleq \left.\frac{\delta^2 n[V_{\mathrm{ext}}](\mathbf{x},\omega)}{\delta V_{\mathrm{ext}}(\mathbf{x}',\omega)\delta V_{\mathrm{ext}}(\mathbf{x}'',\omega)}\right|_{V_{\mathrm{ext}}=V_0}$$

In SHG, V_1 is solely due to the normally incident laser field and is given explicitly by the expression $V_1(\mathbf{x},t) = \mathcal{E}_0 x e^{i\omega t}$ so that $V_1(\mathbf{x},\omega') = \mathcal{E}_0 x \delta(\omega'-\omega)$. Therefore n_2 contains all the 2ω frequency content of $n(\mathbf{x},\omega')$.

Mimicking the procedures of Section 7.1.2 and 7.2, we can massage (8.4) into something computable for the jellium system. After considerable effort, we obtain a form comparable to what we had for n_1:

$$n_2(x;\omega) = \zeta(x;\omega) + \int_{-\infty}^{+\infty} \chi_1(x,y,2\omega)\big[\phi_2(y;\omega) + f_{\mathrm{xc}}(x) n_2(y;\omega)\big]\, dy \tag{8.5}$$
$$\zeta(x;\omega) \triangleq \int_{\mathbb{R}} \phi_{1,\mathrm{scf}}(y;\omega) \int_{\mathbb{R}} \chi_2(x,y,y';\omega,\omega)\phi_{1,\mathrm{scf}}(y';\omega)\, dy'\, dy + \frac{1}{2}\int_{\mathbb{R}} \chi_1(x,y;2\omega) g_{\mathrm{xc}}(y) n_1^2(y;\omega)\, dy$$

where $\phi_{1,\mathrm{scf}}(x;\omega) = \phi_{\mathrm{est}}(x;\omega) + \phi_{\mathrm{ext}}(x;\omega) + \phi_{\mathrm{xc}}(x;\omega)$ with these components of (7.19), (7.20), and (7.21), respectively; ϕ_2 is electrostatic potential corresponding to n_2 and therefore solves $\phi_2''(x;\omega) = -4\pi n_2(x;\omega)$. Finally, the nonlinear response function is given by the expression[†]

$$\begin{aligned}\chi_2(x,y,y';\omega,\omega) = \frac{1}{\pi^2}\int_0^{k_F} \big(k_F^2 - k^2\big)\big[&\psi_k(x)\psi_k(y)\, G(x,y;\varepsilon_k+2\omega)G(y,y';\varepsilon_k+\omega) + \\ &\psi_k(x)\psi_k(y)\, G(x,y;\varepsilon_k-2\omega)G(y,y';\varepsilon_k-\omega) + \\ &\psi_k(y)\psi_k(y')G(x,y;\varepsilon_k+\ \ \omega)G(y,y';\varepsilon_k-\omega)\big]\, dk\end{aligned}$$

We see that just like the linear response density, the nonlinear response density n_2 satisfies an inhomogeneous Fredholm integral equation of the second kind, identical in form to (7.58). Remember that we arrived at

[†]A slightly different expression appears in [68]. By switching dummy variables to combine two of the terms, one may obtain that the expression given here has identical *action* to the χ_2 of Liebsch and Schaich, although the two are not equal as functions. While the author did not complete his own derivation, he believes that anything with a minus ω' should be conjugated.

(7.43) from (7.58) by folding together ϕ_{est} and ϕ_{ext}. Because the external potential contains no frequency content at 2ω, the ϕ_2 of (8.5) *does* represent the electrostatic potential, unlike ϕ_1 of (7.58).

Not only are n_1 and n_2 determined by integral equations with the same kernel but also n_1 is an input in the source term $\zeta(x;\omega)$. The ground state also makes an appearance through the wavefunctions needed to compute χ_2. We thus have a hierarchal process: the nonlinear response requires the linear response, which requires the ground state. The progression is depicted visually in Figure 8.4 below.

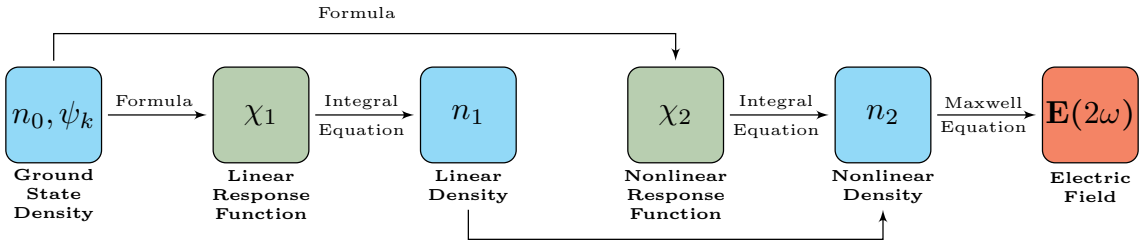

Figure 8.4: Complete TD-DFT Approach to SHG. This diagram illustrates the hierarchy clearly.

While the integral equation (8.5) can be solved in a manner as that for the linear density, the source term $\zeta(x;\omega)$ requires considerably more effort to obtain. Each of the three terms of χ_2 has a contribution deep within the bulk metal that must be determined analytically á la Section 7.4. That each term contains a product of Green's functions makes the analysis much more difficult. Numerically, we must compute an additional pair of Green's functions. The computation of Green's functions comprised nearly all the runtime for the linear response calculation. While reuse of $G(x, y; \varepsilon_k \pm \omega)$ from the previous step can prevent a true doubling of CPU time, it should be expected that the process will take at least as long as the linear response.

8.3 Intensity Formula

Figure 8.4 shows the procedure concluding with obtainment of the electric field via Maxwell's equations. In practice, the electric field does not provide much insight and what we really seek is just the field's intensity. It is possible to obtain the conversion efficiency without solving any partial differential equations.

The intensity formula is limited to giving information about the *p*-polarized component of the generated second harmonic field. The incident wave can be of mixed *s*-*p* polarization but must have a nonzero *p* component. Figure 8.5 illustrates clearly the geometry of incident and reflected fields.

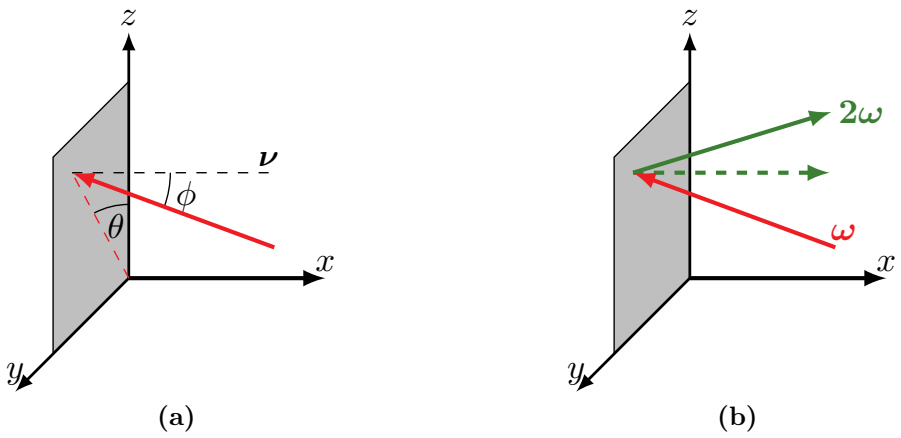

Figure 8.5: Geometry of Incidence and Reflection. In **(a)**, θ denotes the polar angle, or the angle with respect to the surface normal $\boldsymbol{\nu}$. ϕ denotes the angle with respect to the plane of incidence. (This ϕ is **not** electrostatic potential!) Radiation with $\phi = 0°$ is called p-polarized; with $\phi = 90°$, s-polarized. In **(b)**, the dashed green line is the p-polarized component of the second harmonic wave, in green.

Let $I_{2\omega}$ and I_ω be the intensities of the second- and first-harmonic electric fields just outside the surface:

$$I_{2\omega} \triangleq \frac{c}{2\pi}\left|\lim_{x\to 0^+}\mathbf{E}(x,2\omega)\right|^2 \qquad\qquad I_{\omega} \triangleq \frac{c}{2\pi}\left|\lim_{x\to 0^+}\mathbf{E}(x,\omega)\right|^2$$

The conversion ratio is given by a handy formula due to Sipe *et al.* [101], transcribed below in atomic units

$$\frac{I_{2\omega}}{I_\omega^2} = \frac{8\pi}{\omega^2 c^3}\left|\frac{\varepsilon(\omega)\big[\varepsilon(\omega)-1\big]\tan\theta}{\big[\varepsilon(2\omega)+s(2\omega)\big]\big[\varepsilon(\omega)+s(\omega)\big]^2}\left(A_p\cos^2\phi + A_s\sin^2\phi\right)\right|^2 \tag{8.6}$$

The amplitudes A_s and A_p, due to the s- and p-polarized components of the incident wave, are

$$A_p \triangleq a(\omega)\frac{\varepsilon(2\omega)}{\varepsilon(\omega)}\sin^2\theta + \frac{2s(\omega)s(2\omega)}{\varepsilon(\omega)}\cos^2\theta + \frac{1}{2} \tag{8.7}$$

$$A_s \triangleq \frac{\big[\varepsilon(\omega)+s(\omega)\big]^2}{2\varepsilon(\omega)\big[1+s(\omega)\big]^2} \tag{8.8}$$

where

$$s(\omega) = \sec\theta\sqrt{\varepsilon(\omega)-\sin^2\theta}$$

Two parameters, $b(\omega)$ and $d(\omega)$, which would be factors in the second and third terms of (8.7), respectively, and in (8.8), have been replaced by their values −1 and 1, per Corvi and Schaich [19], who also showed that the parameterization (8.6) is very nearly what is obtained from a full solution of Maxwell's Equations.

The parameter $a(\omega)$, which is linked to the normal component of the polarization at the second harmonic

frequency, is therefore all that is necessary to obtain the intensity via (8.6). It can be found via [67, p.230]

$$a(\omega) = -\frac{4\bar{n}}{\sigma^2(\omega)} \int_{-\infty}^{+\infty} x n_2(x;\omega)\, dx \tag{8.9}$$

8.4 Dynamical Force Sum Rules

Like n_0, n_1 and n_2 exhibit slowly decaying Friedel oscillations which make direct numerical evaluation of the integral in (8.9) impractical. Per (5.26), n_1 and n_2 behave something like $Ax^{-2}\cos(2k_F + \gamma)$ so that when multiplied by x and integrated in (7.50) or (8.9), the resultant integrals converge only conditionally. An accurate quadrature scheme would have to be written on an impractically enormous interval. This section contains two dynamical force sum rules that make it possible to find $d_\perp(\omega)$ and $a(\omega)$ from numerical solutions. The first of these is due to Liebsch [66] and the second is due to Liebsch and Schaich [68].

Lemma 8.1 (**Dynamical Force Sum Rule I**). *The parameter $d_\perp(\omega)$ is equivalently given by*

$$d_\perp(\omega) = \frac{\varepsilon(\omega) + 1}{\varepsilon(\omega)} \int_0^{\infty} x n_1(x;\omega)\, dx \tag{8.10}$$

assuming that the jellium surface occupies the negative half-space.

Proof. See Liebsch [66] or [67, p.172]. ∎

The second dynamical force sum rule is directly applicable to $a(\omega)$.

Lemma 8.2 (**Dynamical Force Sum Rule II**). *The first moment of $n_2(x;\omega)$ is equivalently given by*

$$\int_{-\infty}^{+\infty} x n_2(x;\omega)\, dx = \frac{\varepsilon(2\omega) - 1}{\varepsilon(2\omega)} \int_0^{\infty} x n_2(x;\omega)\, dx + \frac{\sigma^2(\omega)}{2\bar{n}} \tag{8.11}$$

assuming that the jellium surface occupies the negative half-space.

Proof. See Liebsch and Schaich [68] or Liebsch [67, p.232]. ∎

8.5 The Hybrid TD-DFT Approach

The first application of DFT to SHG was performed by Weber and Liebsch [113], who used KS-DFT to estimate $a(\omega)$. Chizmeshya and Zaremba [15] built upon that work by instead using Thomas-Fermi-Dirac-von Weizsäcker theory within OF-DFT, just as shown in Chapter 4. Both studies began with the electrostatic

perturbation expansion

$$\rho(x) = \rho_0(x) + \left(\frac{\mathcal{E}_0}{2\pi}\right)\rho_1(x) + \left(\frac{\mathcal{E}_0}{2\pi}\right)^2 \rho_2(x) + \cdots \tag{8.12}$$

where ρ_0 is the electron density in the absence of an external electric field and $\mathcal{E}_0 = 2\pi\varsigma$ is the magnitude of a static electric field normally incident upon the jellium surface. The induced densities can be found via

$$\rho_1(x) = \frac{1}{2\varsigma}\big[\rho_+(x) - \rho_-(x)\big] \tag{8.13}$$

$$\rho_2(x) = \frac{1}{2\varsigma^2}\big[\rho_+(x) + \rho_-(x) - 2\rho_0(x)\big] \tag{8.14}$$

where ρ_+ and ρ_- are computed with $\mathcal{E}_0 = 2\pi\varsigma > 0$ and $\mathcal{E}_0 = -2\pi\varsigma < 0$, respectively. If instead the applied field is of the form $\mathcal{E}(t) = \mathcal{E}_0 e^{i\omega t}$ with ω sufficiently low, say $\omega \lesssim 0.1\omega_p$, then the system may be assumed to respond adiabatically and the time varying quantity $\mathcal{E}(t)$ may replace $\mathcal{E}_0$ in (8.12):

$$\begin{aligned}\rho(x,t) &= \rho_0(x) + \left(\frac{\mathcal{E}(t)}{2\pi}\right)\rho_1(x) + \left(\frac{\mathcal{E}(t)}{2\pi}\right)^2 \rho_2(x) + \cdots \\ &= \rho_0(x) + \varsigma\rho_1(x)e^{i\omega t} + \varsigma^2\rho_2(x)e^{2i\omega t} + \cdots\end{aligned}$$

which after a Fourier transform in time becomes

$$\rho(x,\omega) = \rho_0(x)\delta(\omega') + \varsigma\rho_1(x)\delta(\omega' - \omega) + \varsigma^2\rho_2(x)\delta(\omega - 2\omega') + \cdots \tag{8.15}$$

In the macroscopic view, the bulk metal feels a screening charge of $\varsigma = \mathcal{E}_0/2\pi$. The applied field may be viewed as originating from a uniform sheet of charge parallel to the surface infinitely far away. Near infinity, the total electric field between the surface and this uniform sheet is $\mathbf{E}_{\text{tot}} = 4\pi\varsigma x\,\hat{\mathbf{x}}$. Since $\phi = -\nabla\mathbf{E}_{\text{tot}}$, the screening charge generates the boundary condition $\phi'(+\infty) = -4\pi\varsigma$. Consequently, in (8.12), ρ_0 corresponds to the ground state density n_0 and ρ_+ and ρ_- correspond to the screened densities n_ς and $n_{-\varsigma}$, respectively.

Via the preceding paragraph, (8.15) allows us to associate ρ_1 and ρ_2 with the TD-DFT linear and nonlinear response densities $n_1(x;\omega)$ and $n_2(x;\omega)$. To place the linear term ρ_1, first observe that from (8.13),

$$\int_{\mathbb{R}} \rho_1(x)\,dx = \frac{1}{2\varsigma}\left[\int_{\mathbb{R}} \big(n_\varsigma(x) - n_+(x)\big)\,dx - \int_{\mathbb{R}} \big(n_{-\varsigma}(x) - n_+(x)\big)\,dx\right] = 1$$

by the charge condition (5.28). Remember that $n_1(x;\omega)$ integrates to $\sigma(\omega)$ per (7.46). Consequently,

$$\rho_1(x) = -\frac{1}{\sigma(\omega)}n_1(x;\omega)$$

By making the appropriate replacements in ρ_2,

$$\int_{\mathbb{R}} \rho_2(x)\,dx = \frac{1}{2\varsigma^2}\left[\int_{\mathbb{R}} \big(n_\varsigma(x) - n_+(x)\big)\,dx + \int_{\mathbb{R}} \big(n_{-\varsigma}(x) - n_+(x)\big)\,dx - 2\int_{\mathbb{R}} \big(n_0(x) - n_+(x)\big)\,dx\right] = 0$$

It can be shown that $n_2(x;\omega)$ as defined in (8.5) integrates to zero, so there are no issues with normalization as there were for ρ_1 and $n_1(x;\omega)$. Accordingly, $\rho_2 = n_2(x;\omega)$ and we have the approximation

$$n_\varsigma(x) = n_0(x) + \frac{\varsigma}{\sigma(\omega)} n_1(x;\omega) + \varsigma^2 n_2(x;\omega) + \cdots$$

Liebsch and Schaich computed solutions to (8.5) in [68]. An inspection of the limited results presented there reveals that there are only small differences between low-frequency responses, just as we saw for $n_1(x;\omega)$ in Figure 7.7. Furthermore, in Figure 7.8, we saw very near agreement of the ρ_1 of (8.13) and $n_1(x;\omega)$ up to $0.1\omega_p$. It is not a stretch to conclude that a full solution of the nonlinear response equations is unnecessary and we can generate a reasonable approximation to $n_2(x;\omega)$ by rearranging (8.12):

$$n_2(x;\omega) \approx \frac{1}{\varsigma^2}\left[n_\varsigma(x) - n_0(x) - \frac{\varsigma}{\sigma(\omega)} n_1(x;\omega)\right] \tag{8.16}$$

We dub this method the *hybrid TD-DFT approach* because it combines linear response theory and electrostatics. A comparison of this method with a full solution to (8.5) is the subject of Section 8.5.2.

While the hybrid TD-DFT approach requires n_ς to be available, the complete TD-DFT approach must compute $n_1(x;\omega)$ and $n_2(x;\omega)$ for each frequency. The screened density n_ς is independent of the frequency and need only be computed once for a given r_s and ς, just like n_0. Therefore, the hybrid approach need only compute $n_1(x;\omega)$ once n_ς is available, requiring only half the work for subsequent inputs ω.

8.5.1 $a(\omega)$ in the Hybrid TD-DFT Approach

The nonlinear density is a means to the end; it is necessary only to compute the $a(\omega)$ parameter that appears in A_p. The dynamical force sum rules of Section 8.4 allow for direct expression of $a(\omega)$ without reference to $n_2(x;\omega)$ in the hybrid TD-DFT approach. First, by Lemma 8.2,

$$a(\omega) = -\frac{4\bar{n}}{\sigma^2(\omega)} \frac{\varepsilon(2\omega) - 1}{\varepsilon(2\omega)} \int_0^\infty x n_2(x;\omega)\,dx - 2$$

Then substituting (8.16) into the above and using Lemma 8.1, we have

$$\begin{aligned} a(\omega) &= -\frac{1}{\varsigma^2}\frac{4\bar{n}}{\sigma^2(\omega)}\frac{\varepsilon(2\omega)-1}{\varepsilon(2\omega)}\left[\int_0^\infty x\big(n_\varsigma(x)-n_0(x)\big)\,dx - \frac{\varsigma}{\sigma(\omega)}\int_0^\infty x n_1(x;\omega)\right]dx - 2 \\ &= -2 + \frac{1}{\varsigma^2}\frac{4\bar{n}}{\sigma^2(\omega)}\frac{\varepsilon(2\omega)-1}{\varepsilon(2\omega)}\left[\varsigma\frac{\varepsilon(\omega)d_\perp(\omega)}{\sigma(\omega)\big(\varepsilon(\omega)+1\big)} - \int_0^\infty x\big(n_\varsigma(x)-n_0(x)\big)\,dx\right] \end{aligned} \tag{8.17}$$

With the formula (8.17) in hand, we can bypass forming n_2 and proceed directly to the intensity formula. The diagram below is an updated version of Figure 8.4 to reflect the new procedure.

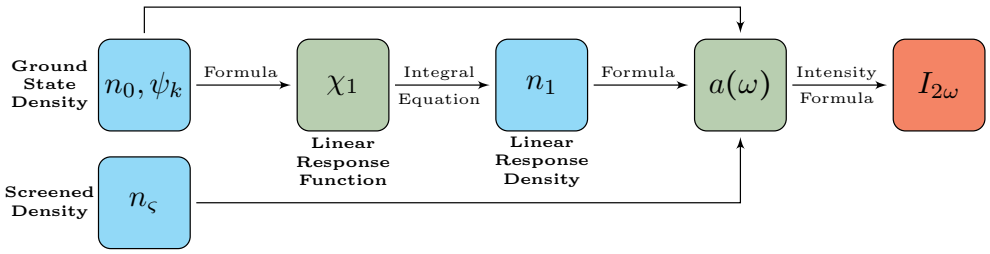

Figure 8.6: Hybrid TD-DFT Approach to SHG. The computational burden is significantly less than the complete approach once n_ς has been computed and stored permanently.

8.5.2 Comparison with Full Solution

The formula for $a(\omega)$ in (8.17) is handy, but an important consideration is its accuracy in comparison to a full solution to the nonlinear response equation (8.5). Below is the full solution for $r_s = 3$ and $\omega_p = 0.1\omega_p$:

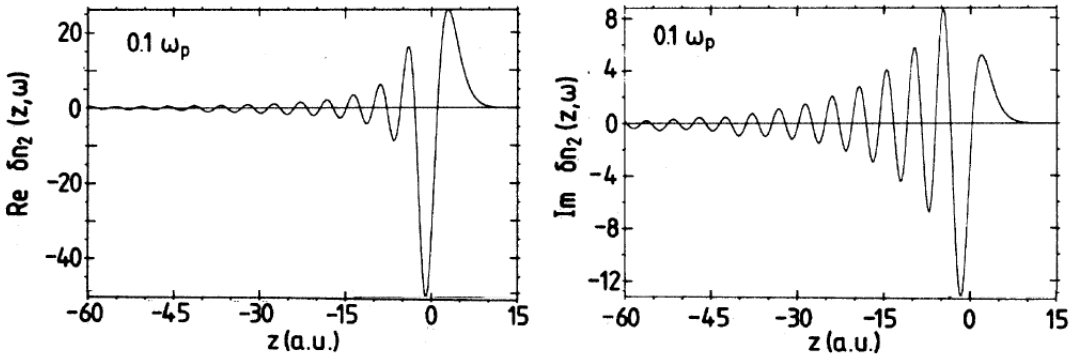

Figure 8.7: Nonlinear Response from Full TD-DFT Approach. This figure depicts the full solution $n_2(x;0.1\omega_p)$ to (8.5) computed by Liebsch and Schaich [68] for $r_s = 3$. Reproduced with express permission from the American Physical Society and Ansgar Liebsch.

Below in Figure 8.8 is the hybrid TD-DFT version of $n_2(x;\omega)$ from (8.16), assembled from the ground state density of Figure 5.6 and screening density with $\varsigma = 5\times10^{-4}$ of Figure 5.10.

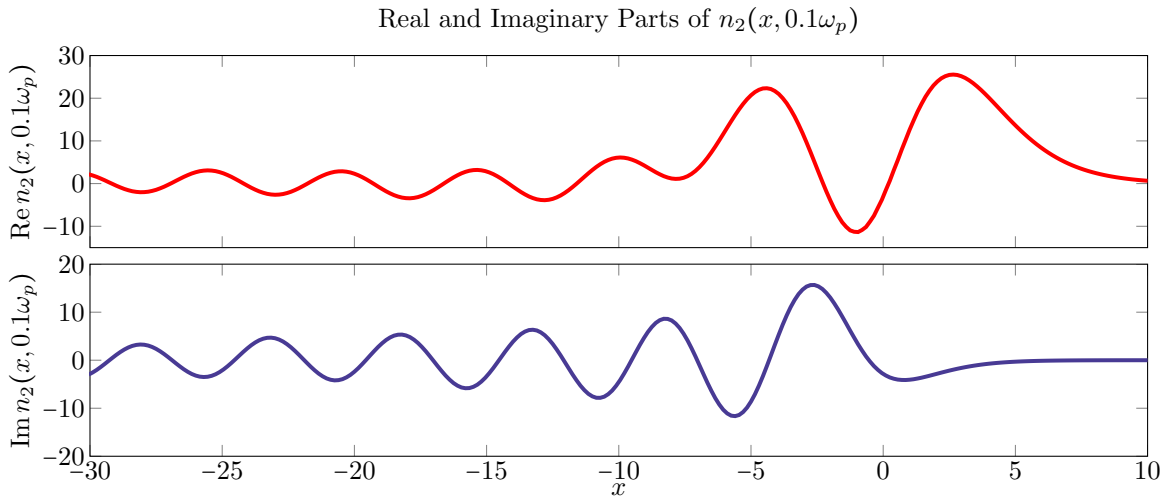

Figure 8.8: Nonlinear Response from Hybrid TD-DFT Approach. Shown is $n_2(x; 0.1\omega_p)$ for $r_s = 3$ and $\varsigma = 5 \times 10^{-4}$. Unlike the linear response density, which has a single spike just outside the surface, n_2 has three such peaks alternating in sign.

Comparing the real parts, we see that the hybrid TD-DFT method reproduces the spike just outside the surface nearly perfectly in both placement and magnitude but falters inside the metal. In particular, the negative spike occurring near the surface inside the metal is significantly weaker than it is in the full TD-DFT solution. The leftmost peaks match in location around $x \approx -5$ but differ slightly in magnitude. Friedel oscillations in the bulk material are equivalent phase and magnitude in both approaches.

The imaginary part of the hybrid TD-DFT's nonlinear density is significantly different than the full-solution's. As both n_0 and n_ς are real valued, the only contribution to $\mathrm{Im}\, n_2(x; \omega)$ in (8.16) comes from a scaled version of $n_1(x; \omega)$. As n_1 contributes to n_2 nonlinearly in (8.5), significant divergence is to be expected.

Because all of the quantities $\varepsilon(\omega')$, $\sigma(\omega)$, $\bar{n}$, and ς are real numbers, the real and imaginary parts of $a(\omega)$ are determined solely from the corresponding parts of $xn_2(x; \omega)$. Because of Lemma 8.2, the convergence of the real parts of the hybrid and full TD-DFT approaches in the region $[0, +\infty)$ means that we should expect good agreement between the real parts of $a(\omega)$ computed by both approaches.

8.6 Computational Results

The table below shows sample results for $a(\omega)$ computed via (8.17).

There is no "correct value" for $a(\omega)$. For $r_s = 3$, the Kohn-Sham based electrostatic approach of Weber and Liebsch [113] found $a(0) = -12.9$ and the TFDW techniques of Chizmeshya and Zaremba [15] placed

ς	$0.05\omega_p$	$0.10\omega_p$	$0.1285\omega_p$	**Average**
5.0×10^{-4}	$-16.3473 + 0.7321i$	$-14.0104 + 1.2906i$	$-15.3935 + 1.3427i$	-15.2504 + 1.1218i
2.5×10^{-4}	$-16.9031 + 1.4643i$	$-11.7983 + 2.5811i$	$-14.1679 + 2.6853i$	-14.2898 + 2.2436i
1.0×10^{-4}	$-21.4864 + 3.6607i$	$-8.1691 + 6.4528i$	$-13.5819 + 6.7133i$	-14.4125 + 5.6089i
Average	$-18.2456 + 1.9524i$	$-11.3259 + 3.4415i$	-14.3811 + 3.5804i	

Table 8.1: Computed Values for $a(\omega)$. This table shows the result of the hybrid TD-DFT method

$a(0) = -14.9$. The methodologies of both studies are unclear. Neither mentions how a single value of $a(0)$ was distilled from presumably many values of ς, just that "ς was taken on the order of 10^{-4}." To maintain a legitimate comparison with these studies, ς was chosen on the same order in Table 8.1.

Unfortunately, Liebsch and Schaich did not present a table of their values for $a(\omega)$ for the full TD-DFT approach, instead presenting only a small graph from which it is difficult to extract precise values. A careful inspection of their figure places $\mathrm{Re}\, a(0.05\omega_p) \approx -13$, $\mathrm{Re}\, a(0.10\omega_p) \approx -14$ and $\mathrm{Re}\, a(0.1285\omega_p) \approx -15$. This is more or less what we obtain from the hybrid TD-DFT method, although the result is a bit sensitive to ς.

8.7 Conclusion

The DFT approach for SHG is a truly multiphysics formulation, mixing together the quantum mechanics of DFT, the solid-state physics of jellium and other surface properties, and the optics of Maxwell's equations. The hybrid approach tosses one more ingredient—electrostatics—into the boiling cauldron.

A full solution of the nonlinear response equation (8.5) may be considered the optimal approach, but the hybrid TD-DFT approach presented in this chapter is certainly not without merit. If the fully static approaches of Weber and Liebsch and Chizmeshya and Zaremba produce values deemed acceptable, then incorporation of any frequency dependence can be considered an improvement. At the very least, the hybrid approach corrobrates the validity of the static approximation by confirming adiabacity up to the linear response.

The hybrid TD-DFT approach is well-suited to describe processes that depend on the response outside the surface, where there is excellent agreement with the full nonlinear response. In particular, because second harmonic generation at a metal surface is not a bulk phenomenon, the hybrid approach is up to the task. Insight into the nature of SHG that can be obtained from all this: the process is dominated by the linear response and ground state. Nonlinearity is largely a property of the bulk material and because of the dynamical force sum rules is not needed to describe all surface phenomena.

APPENDICES

Appendix A

Variational Calculus

This appendix provides a brief overview of the key results from variational calculus employed in the body of this thesis. For comprehensive instruction in the subject, see, for example, Gelfand and Fomin [39].

Let $\mathscr{F}(A;B)$ denote the set of functions from A to B. We will limit discussion here to the set $\mathscr{F}(\mathbb{R}^d;\mathbb{R})$. It is possible to generalize the results here to $\mathscr{F}(\mathbb{R}^d;\mathbb{R}^d)$, but doing so requires tensor calculus.

Definition A.1. *A* functional *is a map from a vector space of functions to its underlying scalar field. On* $\mathscr{F}(\mathbb{R}^d;\mathbb{R})$*, it is a rule that takes a function and returns an element in* $\mathbb{R}$*.*

On Hilbert spaces, the powerful Riesz Representation Theorem gives a complete characterization of all possible linear functionals. Here, we allow functionals to be nonlinear and define an analog to standard calculus on the space of functionals. Without delving into too much detail or rigor, we present some essential results from this variational calculus that are employed on several occasions in the body of this thesis.

Definition A.2 (**Variational (Functional) Derivative).** *For a functional* $F : \mathscr{F}(\mathbb{R}^d;\mathbb{R}) \to \mathbb{R}$*, the* variational (or functional) derivative *is defined by*

$$\int_{\mathbb{R}^d} \frac{\delta F}{\delta \rho}\, \varphi(\mathbf{x})\, d\mathbf{x} = \lim_{\eta \to 0} \frac{F[\rho + \eta\varphi] - F[\rho]}{\eta} = \left[\frac{\partial}{\partial \eta} F[\rho + \eta\varphi]\right]_{\eta=0}$$

where $\varphi \in \mathscr{F}(\mathbb{R}^d;\mathbb{R})$*.*

The functional derivative of a functional is again a functional, and $\dfrac{\delta F}{\delta \rho}$ is called the "first-variation of F" and is a funct*ion*. The process of taking a functional derivative is often called "taking the variation." It is also possible to compute variations of higher-order by nesting the above definition, which is equivalent to taking a derivative of the corresponding order in η on the very right side of the above definition.

For simple functionals defined by integration, a handy formula is available for the first variation:

Theorem A.1 (**Formula for First Variation**). *If $f : \mathbb{R}^3 \times \mathbb{R} \times \mathbb{R}^d \to \mathbb{R}$ is C^1 in its second and third arguments, then the functional $F : C^1(\mathbb{R}^d) \to C(\mathbb{R}^d)$ defined by*

$$F[\rho] = \int_{\mathbb{R}^d} f\big(\mathbf{x}, \rho(\mathbf{x}), \nabla\rho(\mathbf{x})\big)\, d\mathbf{x}$$

has first-variation

$$\frac{\delta F}{\delta \rho} = \frac{\partial f}{\partial \rho} - \nabla \cdot \frac{\partial f}{\partial \nabla \rho}$$

By letting $d_k \triangleq \dfrac{\partial \rho}{\partial x_k}$ and writing $f\big(\cdot, \cdot, \nabla\rho(\mathbf{x})\big) = f\big(\cdot, \cdot, d_1, \cdots, d_n\big)$, the derivative $\dfrac{\partial f}{\partial \nabla \rho}$ is interpreted

$$\frac{\partial f}{\partial \nabla \rho} = \left[\frac{\partial f}{\partial d_1}, \cdots, \frac{\partial f}{\partial d_n}\right]^T$$

One may also interpret this as "taking the gradient with respect to the gradient vector."

Proof. Let $\varphi : \mathbb{R}^d \to \mathbb{R}$ be such that $\varphi \to 0$ as $|\mathbf{x}| \to +\infty$ (e.g., φ is compactly supported). We proceed by direct computation, beginning with the definition:

$$\int_{\mathbb{R}^d} \frac{\delta F}{\delta \rho}\, \varphi(\mathbf{x})\, d\mathbf{x} = \left[\frac{\partial}{\partial \eta} \int_{\mathbb{R}^d} f\big(\mathbf{x}, \rho(\mathbf{x}) + \eta\varphi, \nabla\rho(\mathbf{x}) + \eta\nabla\varphi\big)\, d\mathbf{x}\right]_{\eta=0}$$

Differentiating under the integral by use of the chain rule, we have

$$\frac{\delta F}{\delta \rho} = \int_{\mathbb{R}^d} \left(\frac{\partial f}{\partial \rho}\varphi + \frac{\partial f}{\partial \nabla \rho} \cdot \nabla\varphi\right) d\mathbf{x}$$

To compute the derivatives $\dfrac{\partial f}{\partial \rho}$ and $\dfrac{\partial f}{\partial \nabla \rho}$ of $f\big(\mathbf{x}, \rho(\mathbf{x}) + \eta\varphi, \nabla\rho(\mathbf{x}) + \eta\nabla\varphi\big)$, we differentiate f in its second and third arguments, respectively, and then evaluate at $\rho + \eta\varphi$ and $\nabla\rho + \eta\nabla\varphi$, respectively. By the product rule for divergence,

$$\nabla \cdot \left[\frac{\partial f}{\partial \nabla \rho}\varphi\right] = \frac{\partial f}{\partial \nabla \rho} \cdot \nabla\varphi + \varphi\nabla \cdot \left[\frac{\partial f}{\partial \nabla \rho}\right]$$

so that

$$\begin{aligned}\int_{\mathbb{R}^d} \frac{\partial f}{\partial \nabla \rho} \cdot \nabla\varphi\, d\mathbf{x} &= \int_{\mathbb{R}^d} \left(\nabla \cdot \left[\frac{\partial f}{\partial \nabla \rho}\varphi\right] - \varphi\nabla \cdot \frac{\partial f}{\partial \nabla \rho}\right) d\mathbf{x} \\ &= -\int_{\mathbb{R}^d} \varphi\nabla \cdot \frac{\partial f}{\partial \nabla \rho}\, d\mathbf{x}\end{aligned}$$

with the second line coming from the Divergence Theorem and that φ vanishes at infinity. Then

$$\int_{\mathbb{R}^d} \frac{\delta F}{\delta \rho}\, \varphi \, d\mathbf{x} = \int_{\mathbb{R}^d} \left(\frac{\partial f}{\partial \rho} - \nabla \cdot \frac{\partial f}{\partial \nabla \rho} \right) \varphi \, d\mathbf{x}$$

Because φ was chosen arbitrary, we conclude that $\dfrac{\delta F}{\delta \rho}$ is exactly as claimed in the theorem statement. ■

Of great use in the derivation of linear response theory are the following two chain rules.

Theorem A.2 (**Variational Chain Rule for Functions**). *If $f : \mathbb{R} \to \mathbb{R}$ is a differentiable function, then the* functional chain rule *of $F[f(\rho)]$ is given by the expression*

$$\frac{\delta F[f(\rho)]}{\delta \rho(\mathbf{x})} = \frac{\delta F[f(\rho)]}{\delta f(\rho(\mathbf{x}))} \frac{\partial f(\rho)}{\partial \rho}(\mathbf{x})$$

The symbol chasing of the above might be a bit confusing. The variational derivative of F should be taken in the symbol f and the partial of f should be taken in the symbol ρ. For example, if $\varphi, \rho : \mathbb{R}^d \to \mathbb{R}$ and

$$F[\varphi] = \int_{\mathbb{R}^d} \varphi^2(\mathbf{x})\, d\mathbf{x} \qquad\qquad f(\rho(\mathbf{x})) = e^{-\rho(\mathbf{x})}$$

Then the variational derivative of $F[f(\rho)]$ is

$$\begin{aligned} \frac{\delta F[f(\rho)]}{\delta \rho(\mathbf{x})} &= \left[\frac{\delta}{\delta f} \int_{\mathbb{R}^d} f^2(\rho(\mathbf{x}))\, d\mathbf{x} \right] \cdot \frac{\partial f}{\partial \rho}(\mathbf{x}) \\ &= 2 f(\rho(\mathbf{x})) \cdot (-e^{-\rho(\mathbf{x})}) \\ &= -2e^{-2\rho(\mathbf{x})} \end{aligned}$$

We can confirm the result by direct computation:

$$F[\rho] = \int_{\mathbb{R}^d} e^{-2\rho(\mathbf{x})}\, d\mathbf{x} \quad \Longrightarrow \quad \frac{\delta F[\rho]}{\delta \rho}(\mathbf{x}) = -2e^{-2\rho(\mathbf{x})}$$

We can extend the chain rule for functionals. Suppose that F is a functional that depends on some function $G(\varphi)$, which itself is a functional $G[\rho](\varphi)$, so that F is a functional of ρ: $F[G[\rho](\varphi)]$

Theorem A.3 (**Variational Chain Rule for Functionals**). *The* variational chain rule for functionals *of $F[G[\rho](\varphi)]$ is given by the expression*

$$\frac{\delta F[\rho]}{\delta \rho(\mathbf{x})} = \int \frac{\delta F[G]}{\delta G(\varphi)} \frac{\delta G[\rho](\varphi)}{\delta \rho(\mathbf{x})}\, d\varphi$$

There is a special case of the above theorem worth investigating. Consider the functional $F[G[\rho(\mathbf{x})](\mathbf{y})] = \rho(\mathbf{x}_0)$. Then the variational chain rule for functionals yields

$$\begin{aligned}\delta(\mathbf{x}-\mathbf{x}_0) = \frac{\delta\rho(\mathbf{x}_0)}{\delta\rho(\mathbf{x})} &= \frac{\delta F[\rho]}{\delta\rho(\mathbf{x})} \\ &= \int_{\mathbb{R}^d} \frac{\delta F[G]}{\delta G[\mathbf{y}]}\frac{\delta G[\rho](\mathbf{y})}{\delta\rho(\mathbf{x})}\,d\mathbf{y} \\ &= \int_{\mathbb{R}^d} \frac{\delta\rho(\mathbf{x}_0)}{\delta G[\mathbf{y}]}\frac{\delta G[\rho](\mathbf{y})}{\delta\rho(\mathbf{x})}\,d\mathbf{y}\end{aligned}$$

We state one final result of great relevance to us—it forms the backbone of linear response theory in time-dependent density functional theory:

Theorem A.4 (**Functional Taylor Series**). *Given a functional* $F[y(\mathbf{x})] : \mathscr{F}\left(\mathbb{R}^d;\mathbb{R}\right) \to \mathbb{R}$, *its* functional Taylor series *is*

$$\begin{aligned}F[y+\delta y] = F[y] + \int K_1(\mathbf{x}_1)\delta y(\mathbf{x}_1)\,d\mathbf{x}_1 + \frac{1}{2!}\iint K_2(\mathbf{x}_1,\mathbf{x}_2)\delta y(\mathbf{x}_1)\delta y(\mathbf{x}_2)\,d\mathbf{x}_1 d\mathbf{x}_2 \\ + \frac{1}{3!}\iiint K_2(\mathbf{x}_1,d\mathbf{x}_2,d\mathbf{x}_3)\delta y(\mathbf{x}_1)\delta y(\mathbf{x}_2)\delta y(\mathbf{x}_3)\,d\mathbf{x}_1\mathbf{x}_2\mathbf{x}_3 + \cdots\end{aligned}$$

where the n*-th kernel* K *is the* n*-th variation of* F*:*

$$K_n(\mathbf{x}_1,\ldots,\mathbf{x}_n) \triangleq \frac{\delta^n F[y]}{\delta y(\mathbf{x}_1)\cdots\delta y(\mathbf{x}_n)}$$

Again, note that the coefficients are given as integrals against variations, very different from Taylor's Theorem for functions on $\mathbb{R}^d$.

Appendix B

Solid State Constants

The Wigner-Seitz radius r_s, Fermi wavevector k_F, and average electron density $\bar{n}$ recur extraordinarily frequently throughout this thesis. These critical values can all be expressed in terms of one another:

$$k_F = \left(3\pi^2\bar{n}\right)^{1/3} = \left(\frac{9\pi}{4r_s^3}\right)^{1/3}$$
$$\bar{n} = \frac{3}{4\pi r_s^3} = \frac{k_F^3}{3\pi^2}$$
$$r_s = \left(\frac{3}{4\pi\bar{n}}\right)^{1/3} = \left(\frac{9\pi}{4k_F^3}\right)^{1/3}$$

The table below gives the numerical values, along with the Fermi energy E_F, for common materials.

r_s	k_F	$\bar{n}$	E_F	Example Material (actual r_s)
2.0	0.9596	2.9842×10^{-2}	0.4604	Platinum (1.99)
2.5	0.7677	1.5279×10^{-2}	0.2947	Cadmium (2.59)
3.0	0.6397	8.8419×10^{-3}	0.2046	Gold (3.01)
3.5	0.5483	5.5681×10^{-3}	0.1503	Strontium (3.56)
4.0	0.4798	3.3730×10^{-3}	0.1151	Sodium (3.93)
4.5	0.4265	2.2620×10^{-3}	0.0909	Potassium (4.86)
5.0	0.3838	1.9099×10^{-3}	0.0737	Rubidium (5.20)

Table B.1: Values of r_s, k_F, and $\bar{n}$ for Common Materials.

Appendix C

The Spline Class

The adaptive spline methods of this this thesis are powered by a custom MATLAB class called `Spline`. While MATLAB provides some built-in spline functionality, this self-developed class is far more flexible, powerful, and broad in scope than provided code. This appendix details the capabilities of `Spline`.

The `Spline` class operates on splines are written in the shifted form

$$s_k(x) = a_d^{(k)}(x - x_k)^d + a_{d-1}^{(k)}(x - x_k)^{d-1} + \cdots + a_1^{(k)}(x - x_k) + a_0^{(k)} \tag{C.1}$$

for $x \in [x_k, x_{k+1}]$. It is critical for correct operation that coefficients passed in via the first class constructor be consistent with this form. If the second class constructor is used, compatible coefficients will be generated.

Class Constructors

The `Spline` provides two configurations of the class constructor:

- `Spline(X_L,X_R,C)`

  `X_L` and `X_R` are column vectors of length `num` that represent the left and right endpoints of the splines. `C` is a `(deg+1)×num` column vector that contains the coefficients of the splines. The member variables `deg` and `num` are set automatically from the lengths of these input vectors. `C` may be complex-valued.

- `Spline(x,f,fp0,fpn)`

  `x` and `f` are vectors of equal length that represent a mesh and set of function values on that mesh. The `make` method is used perform cubic spline interpolation on the values `f`. The other two inputs `fp0` and `fpn` represent the value of the function's derivative at the first and last entries of `x`, respectively.

Creation of `null` objects is possible by passing no arguments into the constructor. Such functionality is useful in preallocating memory for arrays of `Spline` objects.

Member Variables

- `C:` Column vector of length `(deg+1)×num` that contains the coefficients of the splines.
- `deg:` Scalar value giving the degree of this instance of the `Spline` object
- `num:` Total number of splines contained in this instance of the `Spline` object.
- `X_L:` Column vector of length `num` that contains the left endpoints defining the splines.
- `X_R:` Column vector of length `num` that contains the right endpoints defining the splines.

Member Functions

- `antidiff:` Takes an input value a and a location as a string, which must be `'begin'` or `'end'`, and returns the antiderivative $\mathcal{S}$ of S, given piecewise by

$$\mathcal{S}(x) = \left\{ \frac{1}{d+1} a_d^{(k)} (x - x_k)^{d+1} + \frac{1}{d} a_{d-1}^{(k)} (x - x_k)^d + \cdots + a_0 (x - x_k) + \alpha_k \qquad x \in \left[x_k, x_{k+1} \right] \right.$$

  The values α_k are computed to make $\mathcal{S}$ continuous to give it regularity one higher than S has. These values are found by making $\mathcal{S}(x_1) = a$ if `'begin'` was input or $\mathcal{S}(x_{\texttt{num+1}}) = a$ if the input was `'end'`. Then the method then marches spline by spline from either `2:num` or `num-1:1` to set the remaining α_k by enforcing C^0 conditions at the nodes. Consequently, the method will be slow if the mesh is large.

- `diff:` Takes an input k and returns the k^{th} derivative of S. If $k > \deg S$, the user is warned that the requested derivative vanishes identically but the operation is still allowed. Unless a high-order spline is created by an external method or as a result of `antidiff`, S is only C^2. The `diff` method will allow inputs of $k > 2$ and will return the correct piecewise result, which may not be continuous. However, if further `Spline` methods are called upon a discontinuous S, incorrect results may be produced.

- `evaluate:` For *sorted* vector input $\mathbf{x} = \left(x_1, \cdots, x_M\right)$, returns the vector $\left(S(x_1), \cdots, S(x_M)\right)^T$. The method can accept either a column or a row vector for $\mathbf{x}$ but always returns a column.

- `integrate:` Takes two input values a and b and returns the value of the definite integral from a to b. First, the method calls the `shrink` method to temporarily downsize the domain to $[a, b]$ so that the

reduced spline has $x_1 = a$ and $x_M = b$. The definite integral is computed exactly by the formula

$$\int_a^b S(x)\,dx = \sum_{k=1}^{N-1} \int_{x_k}^{x_{k+1}} s_k(x)\,dx = \sum_{k=1}^{M-1} \sum_{m=1}^{d} \frac{1}{d+2-m} a_m^{(k)} h_k^{d+2-m}$$

where $h_k = x_{k+1} - x_k$. If called with no arguments, integration over the whole domain is performed; if called with just a, integration is performed from a to the end of the domain. The method is vectorized so that it runs quickly even if `num` is large, in contrast to `antidiff`.

- `get_domain:` Returns the two-vector [`X_L(1)`, `X_R(end)`].
- `get_mesh:` Returns the set of complete set of nodes [`X_L`; `X_R(end)`] as an `num`+1 column vector.
- `make:` Takes inputs of a vector **x** (of length N) and corresponding function values **f** along with values f_0' and f_N' that represent derivative information at the first and last values of **x**. The `make` method performs cubic spline interpolation on the input data and creates a $4N$ vector of coefficients. This method's primary function is as a helper method for one of the class constructors.
- `plot:` A highly flexible method for plotting that may be called in a variety of argument configurations:
  - No arguments: The method generates its own test mesh with help from `get_mesh`; if the mesh contains more than 2000 points, then a uniformly spaced mesh of 2000 points is used instead.
  - One argument: A column or row vector **x** specifies the points to use to generate the plot.
  - Two arguments: Two configurations are possible. The first argument may be either an empty vector `[ ]`, in which case a test mesh will be automatically generated, or a vector **x** of points to use. The second may be either a string compatible with the MATLAB `plot` command, such as `'--r'`, *or* a 3×1 row-vector containing values in $[0, 1]$ specifying the color in the RGB palette.
  - Three arguments: The first argument is either **x** or `[ ]` as above. The second argument must be a 3×1 vector specifying a standard RGB color. The third must be a string specifying a standard MATLAB line style: `-`, `:`, `-.`, `--`, `.'`, `o`, `x`, `+`, `*`, `s`, `d`, `v`, `^`, `<`, `>`, `p`, or `h`.
  - Four arguments: The first three are as above. The fourth is a number that specifies the line width.

  If S is complex-valued, then the plot will display as a 2×1 subplot with the real part on the top and imaginary part on the bottom, both with the same user-specified mesh, color, and style options.
- `respline:` Takes an input value N and transfers S from its current mesh to an N-point uniformly spaced mesh (on the same domain) by re-interpolating values from `evaluate`.
- `shrink:` Takes input values a and b and permanently reduces the domain to $[a, b]$. Information on the original domain outside $[a, b]$ is discarded. This method was designed as a helper for `integrate`.

- `times_power:` Takes an input k (which must be an integer) and performs the multiplication $x^k S$, preserving continuity. This method iteratively calls `times_x` k times.
- `times_x:` Globally multiplies S by x without using spline arithmetic. The regularity is preserved.

Spline Arithmetic

`Spline` objects may be added, subtracted, and multiplied using the standard binary operators `+`, `-`, and `*`. Addition and subtraction of scalar constants is also supported, as is multiplication by scalar values. Division in any form is not supported; to divide a `Spline` by a constant value a, instead multiply by $1/a$.

The primary challenge in performing spline arithmetic is that splines may be defined on different meshes. Accordingly, both splines must be transferred to the same mesh before any arithmetic can be done. It is highly desirable to preserve the original precision, so transfer must be done without loss of information (e.g., via `respline`). The process is best explained visually, shown below in Figure C.1.

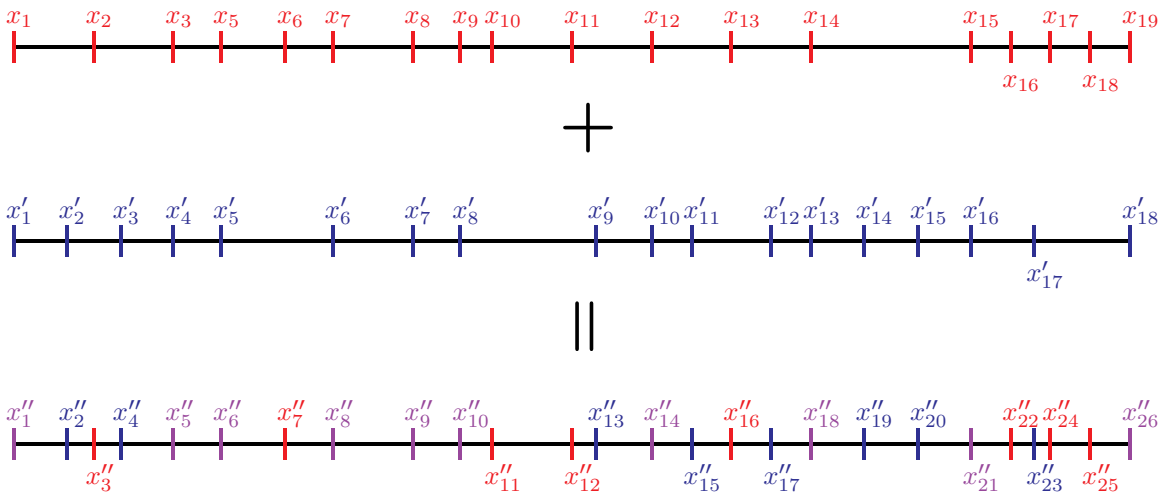

Figure C.1: Combining Spline Meshes. Addition of meshes is performed by including all unique points between the two meshes. The bottommost mesh is the "sum" of the two above it. Points in red are unique to the top mesh, points in blue are unique to the bottom, and points in purple are shared by both.

Because the coefficients assume the shifted form (C.1), coefficients cannot merely be copied to new subintervals. For example, for S defined on the red mesh in Figure C.1, a new point x'_2 was added between x_1 and x_2 in transferring to the bottom mesh. For such an S and a point $y \in [x'_2, x_2]$, $S(y)$ was originally given by

$$S(y) = a_d^{(1)}(y - x_1)^d + a_{d-1}^{(1)}(y - x_1)^{d-1} + \cdots + a_1^{(1)}(y - x_1) + a_0^{(1)}$$

On the combined mesh, S should be evaluated by an expression of the form

$$S(y) = b_d^{(2)}(y - x_2')^d + b_{d-1}^{(2)}(y - x_2')^{d-1} + \cdots + b_1^{(2)}(y - x_2') + b_0^{(2)}$$

because y now falls within the interval that defines the second spline. The new $b_m^{(2)}$ coefficients are computed from the $a_m^{(1)}$ by first using the age-old trick of adding and subtracting the same thing

$$S(y) = a_d^{(1)}\big(y - x_2' - (x_1 - x_2')\big)^d + a_{d-1}^{(1)}\big(y - x_2' - (x_1 - x_2')\big)^{d-1} + \cdots + a_1^{(1)}\big(y - x_2' - (x_1 - x_2')\big) + a_0^{(1)}$$

and then expanding each power with the binomial formula. In general, if x_m is the largest point from the original mesh such that $x_m \le x_k''$, where x_k'' is a point from the combined mesh, then

$$\begin{pmatrix} b_d^{(k)} \\ \vdots \\ b_0^{(k)} \end{pmatrix} = \Big[\mathbf{A} \cdot \mathbf{Z}\Big] \begin{pmatrix} a_d^{(m)} \\ \vdots \\ a_0^{(m)} \end{pmatrix}$$

where $\mathbf{A}$ and $\mathbf{Z}$ are $(d+1) \times (d+1)$ matrices with entries

$$\mathbf{A}_{pq} = \begin{cases} \binom{d-q+1}{d-p+1} & \text{if } p \ge q \\ 0 & \text{else} \end{cases} \qquad \mathbf{Z}_{pq} = \begin{cases} (x_k'' - x_m)^{p-q} & \text{if } p \ge q \\ 0 & \text{else} \end{cases}$$

and the dot indicates elementwise multiplication (i.e., $\Big[\mathbf{A} \cdot \mathbf{Z}\Big]_{pq} = \mathbf{A}_{pq}\mathbf{Z}_{pq}$). The algorithm must march element by element through the new mesh, although it remembers the smallest x_m from the original mesh from x_{k-1}'' so that the original mesh need not be searched each time. Consequently, spline arithmetic can run slowly, especially when splines on large meshes containing many mutually disjoint points are combined.

Once the same mesh, arithmetic on splines of different degrees is slightly complicated by the different dimensions of the corresponding `C` vectors. Fortunately, this issue is much easier resolved than the matter of different meshes. To add or subtract, the spline of the lower degree is converted to "higher degree" by padding zeros. For example, if `S` of degree three and `T` of degree five are to be combined, `S.C` is replaced by

$$\Big[0, 0, a_3^{(1)}, a_2^{(1)}, a_1^{(1)}, a_0^{(1)}, 0, 0, a_3^{(2)}, a_2^{(2)}, a_1^{(2)}, a_0^{(2)}, \cdots, 0, 0, a_3^{(\texttt{num})}, a_2^{(\texttt{num})}, a_1^{(\texttt{num})}, a_0^{(\texttt{num})}\Big]^T$$

Because `S` and `T` are on the same mesh, `num = S.num = T.num`. The coefficients of the sum or difference of `S` and `T` is then given by the corresponding operation applied to `T.C` and the new `S.C`.

Multiplication is slightly less efficient. First, a new vector to represent the coefficients of the product of

length `(S.deg+T.deg+1)×num` is preallocated. Then the entries of `P.C`, where `P` is the product spline, on each $[x_k, x_{k+1}]$ for `k = 1:num` are found by circularly convolving the appropriate entries of `S.C` and `T.C`:

```
P.C(p:p+S.deg+T.deg) = conv(S.C(s:s+S.deg),T.C(t:t:T.deg))
```

where `p = 1+(S.deg+T.deg+1)×(k-1)`, `s = 1+(S.deg+1)×(k-1)`, and `t = 1+(T.deg+1)×(k-1)`.

Addition and subtraction of a scalar value a from `S` is handled without creation of a spline to represent the constant: all that need be done is to correspondingly add or subtract a from `S.C(S.deg+1:S.deg+1:end)`. Multiplication of a scalar requires nothing more than scaling `S.C` by the desired value.

Child Classes

The spline method is used to compute several different types of functions in this thesis, each with a different set of parameters associated with it. `Spline` serves as a parent class for each of these data types, which add additional member variables to store these distinguishing values. The child classes of `Spline` are:

- `Density:` used for representing electron densities n_0.

  Additional member variables:

  - `rs:` Stores the Wigner-Seitz radius r_s.
  - `sigma:` Stores the screening charge ς.
  - `type:` A string, generally `'OF'` or `'KS'`, that indicates the DFT formulation.
  - `kvals:` For KS-DFT densities, contains the values of k that index the wavefunctions ψ_k generating the density. For OF-DFT densities, this field is left empty.
  - `weights:` For KS-DFT densities, contains the Gaussian quadrature weights of the corresponding entries of `kvals`. For OF-DFT densities, this field is left empty.
  - `lambdas:` For KS-DFT densities, contains the exponents λ_k of right boundary conditions of the wavefunctions ψ_k generating the density. For OF-DFT densities, this field is left empty.
  - `alphas:` For KS-DFT densities, contains the coefficients α_k of right boundary conditions of the wavefunctions ψ_k generating the density. For OF-DFT densities, this field is left empty.
  - `gammas:` For KS-DFT densities, contains the phase shifts γ_k of wavefunctions ψ_k generating the density. For OF-DFT densities, this field is left empty.
  - `gamma_kF:` For KS-DFT densities, contains the phase shift at $k = k_F$ (which is not used to generate the density). For OF-DFT densities, this field is left empty.

Additional functionality:

- When arithmetic is performed two `Density` objects, the result is a `Density` object. The values of `rs`, `kvals`, `weights`, and `lambdas`—which are assumed to be the same—are preserved in the result. When a `Density` object is multiplied by a scalar, all member fields are preserved.

- `ExcitedState:` used for representing the linear response density $n_1(x;\omega)$

  Additional member variables:

  - `rs:` Stores the Wigner-Seitz radius r_s.
  - `type:` A string that indicates the nature of the response (e.g., `'LR'` for linear response)
  - `f_omega_p:` Frequency as a fraction of the plasma frequency, $\omega = f\omega_p$. The f is stored here.

- `WaveFun:` used for representing Kohn-Sham wavefunctions ψ_k.

  Additional member variables:

  - `k:` Value of k of this wavefunction.
  - `gamma:` Value of phase shift γ_k of this wavefunction.
  - `alpha:` Value of coefficient α_k in right-hand asymptotic behavior.
  - `lambda:` Exponential factor λ_k appearing in right-hand asymptotic behavior.

REFERENCES

REFERENCES

[1] E. L. Albasiny and W. D. Hoskins. Cubic spline solutions to two-point boundary value problems. *The Computer Journal*, 12(2):151–153, 1969.

[2] N. W Ashcroft and N. D. Mermin. *Solid State Physics*. Saunders, 1976.

[3] K. E. Atkinson. *An Introduction to Numerical Analysis*. John Wiley & Sons, 2nd edition, 1989.

[4] K. E. Atkinson. *The Numerical Solution of Integral Equations of the Second Kind*. Cambridge Monographs on Applied and Computational Mathematics. Cambridge University Press, 1997.

[5] C. M. Bender and S. A. Orszag. *Advanced Mathematical Methods for Scientists and Engineers: Asymptotic Methods and Perturbation Theory*. Springer, 1999.

[6] N. Bloembergen, R. K. Chang, S. S. Jha, and C. H. Lee. Optical second-harmonic generation in reflection from media with inversion symmetry. *Physical Review*, 174(3):813–822, Oct 1968.

[7] W. E. Boyce and R. C. DiPrima. *Elementary Differential Equations and Boundary Value Problems*. John Wiley & Sons, 7th edition, 2001.

[8] R. W Boyd. *Nonlinear Optics*. Academic Press, 2nd edition, 2003.

[9] P. F. Brevet. *Surface Second Harmonic Generation*. Presses Polytechniques et Universitaires Romandes, 1997.

[10] F. Brown and M. Matsuoka. Effect of adsorbed surface layers on second-harmonic light from silver. *Physical Review*, 185:985–987, Sep 1969.

[11] H. Bruus and K. Flesberg. *Many-body Quantum Theory in Condensed Matter Physics: An Introduction*. Oxford Graduate Texts. Oxford University Press, 2004.

[12] H. F. Budd and J. Vannimenus. Surface forces and the jellium model. *Physical Review Letters*, 31:1218–1221, Nov 1973.

[13] M. Causley. A method of lines transpose approach for the one dimensional wave equation. Preprint.

[14] D. M. Ceperley and B. J. Alder. Ground state of the electron gas by a stochastic method. *Physical Review Letters*, 45:566–569, 1980.

[15] A. Chizmeshya and E. Zaremba. Second-harmonic generation at metal surfaces using an extended Thomas–Fermi–von Weizsäcker theory. *Physical Review B*, 37(6):2805–2811, Feb 1988.

[16] Cristian Ciracì, Ekaterina Poutrina, Michael Scalora, and David R. Smith. Second-harmonic generation in metallic nanoparticles: Clarification of the role of the surface. *Phys. Rev. B*, 86:115451, Sep 2012.

[17] L. A. Cole and J. P. Perdew. Calculated electron affinities of the elements. *Physical Review A*, 25:1265–1271, 1982.

[18] J. Conway. *A Course in Functional Analysis*, volume 96 of *Graduate Texts in Mathematics*. Springer, 1990.

[19] M. Corvi and W. L. Schaich. Hydrodynamic-model calculation of second-harmonic generation at a metal surface. *Physical Review B*, 33:3688–3695, Mar 1986.

[20] P. A. M. Dirac. Note on exchange phenomena in the thomas atom. *Proceedings of the Cambridge Philosophical Society*, 26:376–385, 1930.

[21] D. G Duffy. *Green's Functions with Applications*. CRC Press, 2001.

[22] E. N. Economou. *Green's Functions in Quantum Physics*, volume 7 of *Springer Series in Solid-State Sciences*. Springer-Verlag, 3rd edition, 2006.

[23] E. N. Economou. *The Physics of Solids: Essentials and Beyond*. Graduate Texts in Physics. Springer-Verlag, 2010.

[24] E. Engel and R. Dreizler. *Density Functional Theory: An Advanced Course*. Theoretical and Mathematical Physics. Springer-Verlag, 2011.

[25] H. Eschrig. The Fundamentals of Density Functional Theory (Revised and Extended Version). `http://www.ifw-dresden.de/userfiles/groups/itf_folder/Helmut_Eschrig/dft.pdf`.

[26] L. Evans. *Partial Differential Equations*, volume 19 of *Graduate Studies in Mathematics*. American Mathematical Society, 1993.

[27] R. A. Evarestov. *Quantum Chemistry of Solids: LCAO Treatment of Crystals and Nanostructures*, volume 153 of *Springer Series in Solid-State Sciences*. 2nd edition, 2012.

[28] P. P. Ewald and H. Juretschke. *Structure and Properties of Solid Surfaces* (editors R. Gomer and C. Stanley), chapter "Atomic Theory of Surface Energy", pages 82–119. University of Chicago Press, 1952.

[29] P. J. Feibelman. Microscopic calculation of surface-plasmon dispersion and damping. *Physical Review B*, 9:5077–5098, Jun 1974.

[30] P. J. Feibelman. Microscopic calculation of electromagnetic fields in refraction at a jellium-vacuum interface. *Physical Review B*, 12:1319–1336, Aug 1975.

[31] P. J. Feibelman. Surface electromagnetic fields. *Progress in Surface Science*, 12(4):287–407, 1982.

[32] E. Fermi. Un metodo statistice per la determinazione di alcune proprieta dell'atomo. *Rendiconti Accademia dei Lincei*, 6:602–607, 1927.

[33] E. Fermi. A statistical method for the determinination of some atomic properties and the application of this method to the theory of periodic system of elements. *Zeitschrift für Physik*, 48:73–79, 1928. English translation in *Self-Consistent Fields in Atoms* by N. H. March, Oxford:Pergamon, 1975.

[34] E. Fermi. Sulla deduzione statistica di alcune proprieta dell'atomo. *Rendiconti Accademia dei Lincei*, 7:342–346, 1928.

[35] A. L. Fetter and J. D Walecka. *Quantum Theory of Many-Particle Systems*. McGraw-Hill, 1971. Reprinted by Dover in 2003.

[36] The Wolf Foundation. Conyers herring winner of wolf prize in physics - 1985, Accessed May 25, 2014. `http://www.wolffund.org.il/index.php?dir=site&page=winners&cs=353`.

[37] P. Franken, A. Hill, C. Peters, and G. Weinreich. Generation of optical harmonics. *Physical Review Letters*, 7(4):118–119, Aug 1961. Copyright 1961 by the American Physical Society.

[38] J. Friedel. Xiv. the distribution of electrons round impurities in monovalent metals. *Philosophical Magazine Series 7*, 43(337):153–189, 1952.

[39] I. M. Gelfand and S. V. Fomin. *Calculus of Variations*. Prentice-Hall, 1963. Reprinted by Dover in 2000. Translated by R.A. Silverman.

[40] M. Gell-Mann and K. A. Brueckner. Correlation energy of an electron gas at high density. *Physical Review*, 106:364–368, Apr 1957.

[41] J. E. Geusic, H. M. Marcos, and L. G. Van Uitert. Laser oscillations in nd-doped yttrium aluminum, yttrium gallium, and gadolinum garnets. *Applied Physics Letters*, 4(10):182–184, 1964.

[42] P. Gies and R. R. Gerhardts. Self-consistent calculation of the electron distribution at a jellium surface in a strong static electric field. *Physical Review B*, 31:6843–6845, May 1985.

[43] L. Grafakos. *Classical Fourier Analysis*, volume 249 of *Graduate Texts in Mathematics*. Springer, 2nd edition, 2008.

[44] A. Griffin and H. Kranz. Plasmon contribution to surface energies. *Physical Review B*, 15:5068–5072, May 1977.

[45] E. K. U. Gross, J. F. Dobson, and M. Petersilka. *Density Functional Theory II: Relativistic and Time Dependent Extensions* (editor Nalewajski, R. F.), volume 181 of *Topics in Current Chemistry*, chapter "Density Functional Theory of Time-Dependent Phenomena". Springer-Verlag, 1996.

[46] E. K. U Gross and N. T Maitra. *Fundamentals of Time-Dependent Density Functional Theory* (editors Marques, M. A. L., Maitra, N. T., Nogueira, F., Gross, E. K. U. and Rubio, A.), volume 837 of *Lecture Notes in Physics*, chapter 4: Introduction to TDDFT. Springer-Verlag, 2012.

[47] M. Han, G. Giese, and J. Bille. Second harmonic generation imaging of collagen fibrils in cornea and sclera. *Optics Express*, 13(15):5791–5797, Jul 2005.

[48] J. Harl. *The Linear Response Function in Density Functional Theory: Optical Spectra and Improved Description of the Electron Correlation*. PhD thesis, Universität Wein, Germany, October 2008.

[49] D. R. Hartree. *The Calculation of Atomic Structures*. John Wiley & Sons, 1957.

[50] R. Hellwarth and P. Christensen. Nonlinear optical microscope using second harmonic generation. *Applied Optics*, 14(2):247–248, Feb 1975.

[51] A. Hill. "Memories of the Discovery of Optical Harmonics and of Peter Franken". Nonlinear Optics At 50: Celebrating the 50$^{\text{th}}$ Anniversary of Nonlinear Optics. University of Michigan, Ann Arbor, MI, October 26, 2011.

[52] P. Hohenberg and W. Kohn. Inhomogeneous electron gas. *Physical Review*, 136:B864–B871, 1964.

[53] H. K. Khalil. *Nonlinear Systems*. Prentice Hall, 3rd edition, 2002.

[54] A. Kiejna and K. F. Wojciechowski. *Metal Surface Electron Physics*. Elsevier Science, 1996.

[55] W. Kohn and L. J. Sham. Self-consistent equations including exchange and correlation effects. *Physical Review*, 140:A1133–A1138, 1965.

[56] N. D. Lang and W. Kohn. Theory of metal surfaces: Charge density and surface energy. *Physical Review B*, 1:4555–4568, Jun 1970.

[57] N. D. Lang and W. Kohn. Theory of metal surfaces: Work function. *Physical Review B*, 3:1215–1223, Feb 1971. Copyright 1971 by the American Physical Society.

[58] N. D. Lang and W. Kohn. Theory of metal surfaces: Induced surface charge and image potential. *Phys. Rev. B*, 7:3541–3550, Apr 1973.

[59] M. Levy. Universal variational functionals of electron densities, first-order density matrices, and natural spin-orbitals and solution of the v-representability problem. *Proceedings of the National Academy of Sciences USA*, 76:6062–6065, 1979.

[60] M. Levy. Electron densities in search of Hamiltonians. *Physical Review A*, 26:1200–1208, 1982.

[61] M. Levy and J. P. Perdew. *Density Functional Methods in Physics* (editors Dreizler, R. M and da Providencia, J.), chapter "The constrained search formulation of density functional theory", pages 11–30. Plenum Press, 1985.

[62] E. H. Lieb. Thomas-fermi and related theories of atoms and molecules. *Reviews of Modern Physics*, 53:603–641, 1981.

[63] E. H Lieb. *Physics as Natural Philosophy, Essays in Honor of Laszlo Tisza on his 75th Birthday* (editors Feshbach, M. and Shimony, A.), chapter "Density functionals for Coulomb systems", pages 111–149. MIT Press, 1982. [Revised in *International Journal of Quantum Chemistry*, 24:243–277].

[64] E. H. Lieb. Density functionals for coulomb systems. *International Journale of Quantum Chemistry*, XXIV:243–277, 1983.

[65] A. Liebsch. Density functional approach to the dynamic response at metal surfaces: van der Waals reference plane position and excitation of electron-hole pairs. *Journal of Physics C: Solid State Physics*, 19:5025–5047, 1986.

[66] A. Liebsch. Dynamical screening at simple-metal surfaces. *Physical Review B*, 36:7378–7388, 1987.

[67] A. Liebsch. *Electronic Excitations at Metal Surfaces*. Physics of Solids and Liquids. Plenum Press, 1997.

[68] A. Liebsch and W. L. Schaich. Second-harmonic generation at simple metal surfaces. *Physical Review B*, 40:5401–5410, Sep 1989. Copyright 1989 by the American Physical Society.

[69] M. J. Lighthill. *An Introduction to Fourier Analysis and Generalized Functions*. Cambridge University Press, 1958.

[70] F. R. Loscalzo and T. D. Talbot. Spline function approximations for solutions of ordinary differential equations. *Bulletin of the American Mathematical Society*, 73(3):438–442, May 1967.

[71] G. D. Mahan. *Many-Particle Physics*. Kluwer Academic/Plenum Publishers, 3rd edition, 2000.

[72] G. D. Mahan and K. R Subbaswamy. *Local Density Theory of Polarizability*. Physics of Solids and Liquids. Plenum Press, 1990.

[73] N. T. Maitra. Undoing static correlation: Long-range charge transfer in time-dependent density-functional theory. *The Journal of Chemical Physics*, 122(23), 2005.

[74] N. T. Maitra, F. Zhang, R. J. Cave, and K. Burke. Double excitations within time-dependent density functional theory linear response. *The Journal of Chemical Physics*, 120(13):5932–5937, 2004.

[75] M. Manninen, R. Nieminen, P. Hautojärvi, and J. Arponen. Electrons and positrons in metal vacancies. *Physical Review B*, 12:4012–4022, Nov 1975.

[76] N. H. March and B. V. Paranjape. High-density jellium-model calculation of force between half-planes of a nearly-free-electron metal at small separation. *Physical Review B*, 30:3131–3135, Sep 1984.

[77] M. A. L Marques, C. A. Ullrich, F. Nogueira, A. Rubio, K. Burke, and E. K. U Gross, editors. *Time-Dependent Density Functional Theory*, volume 706 of *Lecture Notes in Physics*. Springer-Verlag, 2006.

[78] R. G. Newton. *Scattering Theory of Waves and Particles*. Springer-Verlag, 2nd edition, 1982.

[79] T. T. Nguyen-Dang, R. F. W. Bader, and H. Essen. Some properties of the Lagrange multiplier μ in density functional theory. *International Journal of Quantum Chemistry*, 22(5):1049–1058, Nov 1982.

[80] P. Nozières and D. Pines. Correlation energy of a free electron gas. *Physical Review*, 111:442–454, Jul 1958.

[81] B. Numerov. Note on the numerical integration of $\frac{d^2x}{dt^2} = f(x,t)$. *Astronomische Nachrichten*, 230(19):359–364, 1927.

[82] P. Pantazis, J. Maloney, D. Wu, and S.E. Fraser. Second harmonic generating (shg) nanoprobes for in vivo imaging. *Proceedings of the National Academy of Science*, 1071:14535–14540, Jul 2010.

[83] R. G. Parr and W. Yang. *Density-Functional Theory of Atoms and Molecules*, volume 16 of *The International Series of Monographs on Chemistry*. Oxford University Press, 1989.

[84] J. P. Perdew. Comments on the metal surface from a simple analytic model. *Physical Review B*, 21:869–873, Jan 1980.

[85] J. P. Perdew and Y. Wang. Accurate and simple analytic representation of the electron-gas correlation energy. *Physical Review B*, 45:13244–13249, Jun 1992.

[86] J. P. Perdew and A. Zunger. Self-interaction correction to density-functional approximations for many-electron systems. *Physical Review B*, 23:5048–5079, May 1981.

[87] D. V. Posvyanskii and A. Y. Shul'Man. Self-consistent solution of kohn-sham equations for infinitely extended systems with inhomogeneous electron gas. *Soviet Journal of Experimental and Theoretical Physics*, 109:145–168, July 2009.

[88] K. Promislow and T. Kapitula. *Spectral and Dynamical Stability of Nonlinear Waves*, volume 185 of *Applied Mathematical Sciences*. Springer, 2013.

[89] D. Rocca. *Time-Dependent Density Functional Perturbation Theory: New Algorithms with Applications to Molecular Spectra*. PhD thesis, Scuola Internazionale Superiore di Studi Avanzati, Italy, October 2007.

[90] H. L. Royden. *Real Analysis*. 3rd. Macmillan, 1988.

[91] W. Rudin. *Real and Complex Analysis*. McGraw-Hill, 3rd edition, 1987.

[92] W. Rudin. *Functional Analysis*. McGraw Hill, 2nd edition, 1991.

[93] J. Rudnick and E. A. Stern. Second-harmonic radiation from metal surfaces. *Physical Review B*, 4(15):4274–4290, 1971.

[94] E. Runge and E. K. U. Gross. Density-functional theory for time-dependent systems. *Physical Review Letters*, 52:997–1000, Mar 1984.

[95] M. Scalora, M. A. Vincenti, D. de Ceglia, V. Roppo, M. Centini, N. Akozbek, and M. J. Bloemer. Second- and third-harmonic generation in metal-based structures. *Physical Review A*, 82(4):043828, Oct 2010.

[96] W. L. Schaich. Crystallinity effects on the surface optical response in metals: Model calculations of the effect of surface states on $d_\perp$. *Physical Review B*, 50:17587–17596, Dec 1994.

[97] G. Senatore and K. R. Subbaswamy. Nonlinear response of closed-shell atoms in the density-functional formalism. *Physical Review A*, 35:2440–2447, Mar 1987.

[98] Y. R. Shen. *The Principles of Nonlinear Optics*. Wiley Classics Library. John Wiley & Sons, 2003. Reprint of 1984 original.

[99] A. Y. Shul'Man. Genuine converging solution of self-consistent field equations for extended many-electron systems. *Journal of Physics: Conference Series*, 35(1):163, 2006.

[100] B. Simon. *Trace Ideals and Their Applications*, volume 120 of *Mathematical Surveys and Monographs*. American Mathematical Society, 2nd edition, 2005.

[101] J. E. Sipe, V. C. Y. So, M. Fukui, and G. I. Stegeman. Analysis of second-harmonic generation at metal surfaces. *Physical Review B*, 21:4389–4402, May 1980.

[102] A. Sommerfeld. Zur elektronentheorie der metalle. *Naturwissenschaften*, 15(41):825–832, 1927.

[103] J. Stoer and R. Bulirsch. *Introduction to Numerical Analysis*, volume 12 of *Texts in Applied Mathematics*. Springer, 2nd edition, 1993.

[104] R. W. Terhune, P. D. Maker, and C. M. Savage. Optical harmonic generation in calcite. *Physical Review Letters*, 8:404–406, May 1962.

[105] G. Teschl. *Mathematical Methods in Quantum Mechanics with Applications to Schrödinger Operators*, volume 99 of *Graduate Studies in Mathematics*. American Mathematical Society, 2009.

[106] A. K. Theophilou. An analytic estimate of the field penetration into metal surfaces. *Journal of Physics F: Metal Physics*, 2(6):1124–1136, 1972.

[107] L. H. Thomas. The calculation of atomic fields. *Mathematical Proceedings of the Cambridge Philosophical Society*, 23:542–548, 1 1927.

[108] C. A. Ullrich. Time-dependent density-functional theory beyond the adiabatic approximation: Insights from a two-electron model system. *The Journal of Chemical Physics*, 125(23):234108, 2006.

[109] C. A. Utreras-Diaz. Metallic surfaces in the Thomas-Fermi-von Weizsäcker approach: Self-consistent solution. *Physical Review B*, 36:1785–1788, Jul 1987.

[110] R. van Leeuwen. *Introduction to Time-Dependent Density Functional Theory*. Second International Workshop and School on Time-Dependent Density Functional Theory. Benasque, Spain, Aug. 27–Sept. 11, 2006.

[111] C. F. von Weizsacker. Zur theorie dier kernmassen. *Zeitschrift für Physik*, 96:431–458, 1935.

[112] S. H. Vosko, L. Wilk, and M. Nusair. Accurate spin-dependent electron liquid correlation energies for local spin density calculations: a critical analysis. *Canadian Journal of Physics*, 58(8):1200–1211, 1980.

[113] M. Weber and A. Liebsch. Density-functional approach to second-harmonic generation at metal surfaces. *Physical Review B*, 35(14):7411–7416, May 1987.

[114] R. P Wehrum and H. Hermeking. On the response of arbitrary finite order and its relation to imaginary-time correlation functions. *Journal of Physics C: Solid State Physics*, 7(6):L107–110, 1974.

[115] E. Wigner. On the interaction of electrons in metals. *Physical Review*, 46:1002–1011, Dec 1934.

[116] A. Zangwill and P. Soven. Density-functional approach to local-field effects in finite systems: Photoabsorption in the rare gases. *Physical Review A*, 21:1561–1572, May 1980.

[117] J. M. Ziman. *Principles of the Theory of Solids*. Cambridge University Press, 2nd edition, 1972.